Applications of Synchrotron Radiation to the Structure, Localization, and Quantitation of Zinc in Biological Systems

by

Jesse Dylan Ward

A dissertation submitted in partial fulfillment
of the requirements for the degree of
Doctor of Philosophy
(Chemistry)
in The University of Michigan
2009

Doctoral Committee:

Professor James E. Penner-Hahn, Chair
Professor Mark M. Banaszak Holl
Professor Carol A. Fierke
Professor Robert T. Kennedy
Associate Professor Michal R. Zochowski

Acknowledgements

First and foremost, I would like to thank my advisor, Dr. Jim Penner-Hahn, for taking me on as a Ph.D. student and for teaching me a great deal about X-ray science and research in general. I had already completed the two standard rotations in the University of Michigan graduate chemistry program without much success when I decided to give biophysics research in the Penner-Hahn lab a try. I probably would have left the program if Jim had not given me my second chance, so I am extremely grateful. It is hard to imagine a boss who could match Jim in both kindness and intelligence. I consider myself very fortunate to have worked with him.

Thanks also to the rest of my committee members, Dr. Carol Fierke, Dr. Mark Banaszak Holl, Dr. Robert Kennedy, and Dr. Michal Zochowski, for attending various events, sometimes on relatively short notice, required for my graduate advancement.

There are several members of the Penner-Hahn lab who deserve special mention. Of these, Dr. Becky Kelly stands out as one of the most significant figures, not only in the Penner-Hahn lab, but in my whole graduate school experience. She taught me a great deal of what I know about EXAFS data collection and analysis, and her stories, personality, and sense of humor made my first couple of years in the Penner-Hahn lab all the more bearable, especially when certain elements of graduate life were bringing me down. Dr. Suranjana Haldar, another former student in the Penner-Hahn lab, was also very kind and helpful to me. I only wish that my time here had overlapped with theirs a little longer. Special thanks to Dr. Jay Stasser and Dr. Sam Pazicni, two postdocs who are

both very knowledgeable and terrific to work with. Thanks also to Dr. Aniruddha Deb, who helped in the XES data collection and who pointed out to me some of the electronic structure programs used in this thesis. Thanks to Jeff Harding, an undergraduate who was able to quickly ship a lot of XES samples to SSRL on short notice. Some of these samples proved key to unraveling the mysteries of the $K\beta_{2,5}$ peaks. Finally, special thanks to Diana Hilton and Jenna Welby, who were beginning their graduate careers in the Penner-Hahn lab right as I was ending mine. Their company made my final year as a graduate student a lot more fun than it otherwise would have been. Best of luck to you all!

Several members of the Fierke lab also deserve recognition. Everyone in the Fierke lab that I have met has been both extremely helpful and extremely knowledgeable of all matters biological. Of these, Dr. Nathan Zahler has probably been the most instrumental to my success. He taught me half of what I know about the X-ray imaging sample preparation, data collection, and analysis. Thanks also to Andrea Stoddard, one of the nicest and most helpful people I have met as a graduate student. Imaging trips with Nathan and Andrea were always a treat. I would also like to thank Dr. John Hsieh, Dr. Terry Watt, Dr. Jimmy Hougland, Dr. Kristin Smith, and Sam Gattis for various conversations, scientific and otherwise. I am extremely impressed by each and every one of them.

I would like to thank several collaborators of mine. Becky Marvin and her advisor Dr. Thomas O'Halloran at Northwestern University provided the malaria samples for X-ray imaging and X-ray spectroscopy. Dr. Chris Kelly, a former student of Dr. Mark Banaszak Holl, grew the KB cell samples used in the apoptosis imaging study. I also feel

privileged to have participated in the iron oxide nanoparticle imaging project, a collaboration that led to my first publication as a graduate student, led primarily by Dr. Kevin Landmark, another former student of the Banaszak Holl lab. Also, thanks to Dr. Jonathan Melnick and his advisor Dr. Gerard Parkin at Columbia University for providing the zinc scorpionates for the X-ray emission project.

Thanks to the staff members at the Stanford Synchrotron Radiation Lightsource for their collaboration and support on several beam trips taken throughout my graduate career. Dr. Matthew Latimer, Dr. Allyson Aranda, and Dr. Erik Nelson were very timely and helpful in setting up on beamlines 9-3 and 7-3 for various EXAFS and XANES experiments. Dr. Uwe Bergmann was instrumental in setting up the Rowland circle detector at beamline 6-2 that we used for the X-ray emission project.

Special thanks also to the staff at the Advanced Photon Source, including Dr. Stefan Vogt, Dr. Lydia Finney, and Dr. Barry Lai at Sector 2, and Dr. Raul Barrea at Sector 18. Barry was the one who first taught me how to make sense of the intimidating user interface for the imaging projects. Stefan taught me a great deal about X-ray fluorescence imaging in general, as well as how to use his extremely useful program, Maps, which was used for the imaging data analysis. He also hooked me up with my first post-graduate job, which I am very grateful for. Lydia has made the last year or so of beam trips at Sector 2 extremely pleasant. I look forward to working with them all.

The acknowledgements would not be complete if I did not thank the One who has sustained me throughout my degree: the late, great Dr. Carl Sagan. Although I did not know him personally, reading *The Demon-Haunted World* as a freshman in college was *the* event that made me want to become a scientist. The road has not always been easy,

but it has always been rewarding.

Finally, I extend a heartfelt thank-you to my parents, Dennis and Linda Ward. My father fostered a love of learning in me from a young age, and has been a hero and role model to me in my personal and professional life. My parents were able to send me to a number of very good private schools, including a very good, but very expensive, private college, the tuition for which my mother delayed her retirement in order to pay. They provided a safe haven for me amidst a sea of uncertainty, and worried about me more than I worried about myself. I love them both.

Table of Contents

Acknowledgements ii

List of Figures viii

List of Tables xiii

Abstract xiv

Chapter 1. Introduction 1

Metals in Biology 1
- Zinc in Biology 3
- The Role of Metals in Malaria 4
- The Role of Metals in Apoptosis 6
- Spectroscopically Quiet Metals 8

Techniques Used in this Thesis 9
- X-Ray Absorption Spectroscopy (XAS) 9
- X-Ray Emission Spectroscopy (XES) 13
- X-Ray Fluorescence (XRF) Imaging 16

Overview of This Thesis 20
References 28

Chapter 2. X-Ray Fluorescence Imaging of Chelator-Treated Erythrocytes Infected with the Malaria Parasite *Plasmodium falciparum* 33

Introduction 33
Materials and Methods 39
- Sample Preparation 39
- X-Ray Fluorescence (XRF) Imaging 39
- Data Analysis 40

Results 41
Discussion 44
References 60

Chapter 3. X-Ray Absorption Spectroscopy of the Zinc Environment in Erythrocytes Infected with the Malaria Parasite *Plasmodium falciparum* 63

Introduction 63

Materials and Methods....67
Sample Preparation....67
X-Ray Absorption Spectroscopy....68
Data Analysis....69
Results....70
Discussion....75
References....92

Chapter 4. X-Ray Fluorescence Imaging of Human KB Cells Undergoing Staurosporine-Induced Apoptosis....94

Introduction....94
Materials and Methods....99
Sample Preparation....99
X-Ray Fluorescence Imaging....99
Data Analysis....100
Propidium Iodide Staining....101
Results....101
Discussion....104
References....122

Chapter 5. X-Ray Emission Spectroscopy of Zinc Active Site Mimics....126

Introduction....126
Materials and Methods....129
Sample Preparation....129
High-Resolution XES....131
X-Ray Absorption Fine Structure (EXAFS) Spectroscopy....132
Electronic Structure Calculations....134
Results....135
Discussion....147
References....175

Chapter 6. Summary and Future Directions....178

The Role of Zinc in Malaria....178
The Bioinorganic Chemistry of Apoptosis....180
XES of Zinc Active Site Mimics....182
References....184

List of Figures

Figure 1.1 Example X-ray absorption spectrum of zinc oxide, showing the division between the XANES (blue) and EXAFS (green) regions 24

Figure 1.2 Example EXAFS spectrum after data work-up (left) and the pseudo-radial distribution function (right) for zinc oxide 24

Figure 1.3 $K\beta_{2,5}$ emission spectrum of zinc oxide 25

Figure 1.4 Schematic of Rowland circle geometry 25

Figure 1.5 Comparison of the zinc $K\beta_{1,3}$ fluorescence obtained using an energy-dispersive detector (blue) vs. a wavelength-dispersive detector (green) 26

Figure 1.6 A fitted spectrum, using NIST thin-film standard NBS-1832 as an example 27

Figure 2.1 Schematic of the *Plasmodium* life cycle 52

Figure 2.2 Schematic of erythrocytic stage 52

Figure 2.3 IC_{50} of various zinc chelators as a function of zinc binding affinity 53

Figure 2.4 XRF images of untreated schizont-stage infected red blood cells 54

Figure 2.5 XRF images of schizont-stage infected red blood cells grown in 0.5 μM TPEN 55

Figure 2.6 XRF images of schizont-stage infected red blood cells grown in 347 μM EDTA 56

Figure 2.7 Individual zinc totals for each treatment condition 57

Figure 2.8 Individual iron totals for each treatment condition 57

Figure 2.9 Individual phosphorous totals for each treatment condition 58

Figure 2.10 Percentage of total iron present in the hemozoin crystal for individual cells for each treatment condition 58

Figure 2.11 Percentage of total zinc present in the hemozoin crystal for individual cells for each treatment condition 59

Figure 2.12 Zn/Fe weight ratio within the hemozoin crystal for individual cells for each treatment condition 59

Figure 3.1 Normalized XANES of red blood cell samples 81

Figure 3.2 Detail on normalized XANES of RBC samples 81

Figure 3.3 Comparison of model compound XANES 82

Figure 3.4 Comparison of Fourier transforms derived from biological EXAFS 82

Figure 3.5 Comparison of Fourier transforms derived from model compound EXAFS 83

Figure 3.6 EXAFS fit for untreated uninfected sample, 5 N/O....83

Figure 3.7 EXAFS fit for untreated uninfected sample, 3.5 N/O, 1S 84

Figure 3.8 EXAFS fit for untreated schizont sample, 5 N/O 84

Figure 3.9 EXAFS fit for untreated schizont sample, 3.5 N/O, 1 S 84

Figure 3.10 EXAFS fit for TPEN-treated sample, 5 N/O 85

Figure 3.11 EXAFS fit for TPEN-treated sample, 3.5 N/O, 1 S 85

Figure 3.12 EXAFS fit for EDTA-treated sample, 2.5 N/O, 1.5 S 85

Figure 3.13 Sensitivity of resolved first-shell distance to increased Zn-TPEN fraction 86

Figure 3.14 Two-component fit for TPEN-treated XANES 86

Figure 3.15 Three-component fit for TPEN-treated XANES 87

Figure 4.1 Sample XRF images for control sample 112

Figure 4.2 Sample XRF images after 30 minutes of STS exposure....113

Figure 4.3 Sample XRF images after 60 minutes of STS exposure....114

Figure 4.4 Sample XRF images after 90 minutes of STS exposure.....115

Figure 4.5 Sample XRF images after 140 minutes of STS exposure.....116

Figure 4.6 Total potassium levels as a function of staurosporine exposure.....117

Figure 4.7 Total chloride levels as a function of staurosporine exposure.....117

Figure 4.8 Chloride-to-potassium ratio as a function of staurosporine exposure 118

Figure 4.9 Total calcium levels as a function of staurosporine exposure 118

Figure 4.10 Total zinc levels as a function of staurosporine exposure 119

Figure 4.11 Total iron levels as a function of staurosporine exposure.....119

Figure 4.12 Total copper levels as a function of staurosporine exposure 120

Figure 4.13 Propidium iodide fluorescence from an untreated culture.....120

Figure 4.14 Propidium iodide fluorescence after 120 minutes of exposure to 2 μM STS.....121

Figure 4.15 Percent KB cells stained by propidium iodide as a function of staurosporine exposure time 121

Figure 5.1 Schematic of Rowland circle geometry 155

Figure 5.2 Comparison between zinc emission spectra 155

Figure 5.3 XES of Zinc Chalcogenides.....156

Figure 5.4 XES of Zinc Halides 156

Figure 5.5 XES of 3^{rd}-Row Zinc Salts 157

Figure 5.6 XES of 4^{th}-Row Zinc Salts.....157

Figure 5.7 Comparison of $K\beta_{1,3}$ spectra of various zinc compounds.....158

Figure 5.8 Variation of XES with geometry 158

Figure 5.9 Comparison of XES and XANES for zinc bromide 159

Figure 5.10 Comparison between XES and DOS calculations for $ZnBr_2$.....159

Figure 5.11 Comparison between XES and DOS calculations for $ZnCl_2$ 160

Figure 5.12 Comparison between XES and DOS calculations for ZnF_2.....160

Figure 5.13 Comparison between XES and DOS calculations for ZnSe 161

Figure 5.14 Comparison between XES and DOS calculations for ZnS 161

Figure 5.15 Comparison between XES and DOS calculations for ZnO 162

Figure 5.16 Comparison of XES for 4-coordinate zinc carboxylates 162

Figure 5.17 Comparison of XES for anhydrous zinc acetate and the corresponding dihydrate 163

Figure 5.18 Comparison of zinc acetate dihydrate with fluorinated form 163

Figure 5.19 Comparison of zinc acetate and zinc acetylacetonate.....164

Figure 5.20 Comparison of zinc acetylacetonates.....164

Figure 5.21 XES of hydrated zinc salts.....165

Figure 5.22 Comparison of zinc compounds dominated by Zn-N ligation.....165

Figure 5.23 XES of zinc-organosulfur complexes 166

Figure 5.24 XES comparison of zinc compounds in carboxylate, imidazole, and thiolate environments.....166

Figure 5.25 XES of (dipropionato-O)(dithiourea-S)zinc(II).....167

Figure 5.26 XES of (dipropionato-O)(dithiourea-S)zinc(II) and fit.....167

Figure 5.27 XES comparison of mixed oxygen/sulfur zinc environments 168

Figure 5.28 XES comparison of bis(2-aminopyridine-N)bis(benzoato-O)zinc(II) and bis(benzoato-O)bis(thiourea-S)zinc(II).....168

Figure 5.29 XES of bis(1-methylimidazole)bis(thiophenolato)zinc(II).....169

Figure 5.30 XES of bis(1-methylimidazole)bis(thiophenolato)zinc(II) and fit 169

Figure 5.31 Input models used in cluster calculations 170

Figure 5.32 Stick spectrum for thioformaldehyde ligation 171

Figure 5.33 Stick spectrum for imidazole ligation 171
Figure 5.34 Stick spectrum for formaldehyde ligation.....172
Figure 5.35 Stick spectrum for methanol interaction 172
Figure 5.36 Stick spectrum for formate interaction 173
Figure 5.37 Stick spectrum for furan interaction 173
Figure 5.38 Stick spectrum for hexaqua zinc 174

List of Tables

Table 3.1 Fit Results of the EXAFS Data for Untreated Uninfected Sample.....88

Table 3.2 Fit Results of the EXAFS Data for Untreated Schizont Sample 89

Table 3.3 Fit Results of the EXAFS Data for TPEN-Treated Sample.....90

Table 3.4 Fit Results of the EXAFS Data for EDTA-Treated Sample.....91

Table 4.1 Whole-cell total elemental concentrations for human KB cells 111

Table 4.2 Primary components of RPMI 1640 media 111

Table 5.1 CHN Analysis of Synthesized Compounds.....150

Table 5.2 CHN Analysis of Zinc Carboxylates and Acetylacetonates 150

Table 5.3 Best Fits for EXAFS of Synthesized Compounds.....151

Table 5.4 Best Fits for EXAFS of Zinc Carboxylates and Acetylacetonates 151

Table 5.5 Positions and Intensities for XES Peaks.....152

Abstract

Applications of Synchrotron Radiation to the Structure, Localization, and Quantitation of Zinc in Biological Systems

by

Jesse Dylan Ward

Chair: James E. Penner-Hahn

This thesis describes the application of synchrotron X-ray sources for localization, quantification and characterization of biological zinc sites. Erythrocytes infected with the malaria parasite *Plasmodium falciparum* are known to accumulate zinc ~3-fold over basal levels. Attempts to reduce parasite viability through the use of zinc chelators had shown previously that the membrane permeable chelator TPEN was several hundred-fold more effective than the impermeable chelator EDTA, despite these having similar zinc binding affinities. XRF imaging data presented here indicates that both chelators were able to prevent zinc uptake in infected erythrocytes and suggests that parasites cope with the lack of extracellular zinc by making greater use of host zinc stores. EXAFS studies indicated that zinc sites in zinc-depleted, but viable, EDTA-treated samples were significantly more sulfur-rich compared to TPEN-treated samples and untreated controls, suggesting that changes in zinc speciation are another method of coping with zinc loss.

Apoptotic cells exhibit early characteristic volume decrease, thought to be linked to small ion fluxes. These fluxes are commonly studied through the use of fluorophores, which lack element specificity and which probe only the labile ion pools. XRF imaging revealed increases in chloride and decreases in calcium not previously recorded in the literature. Within 140 minutes after exposure to staurosporine, potassium and chloride levels were identical to those of the surrounding media. In addition, calcium was observed to co-localize with zinc in the cytosol, although the target of this localization could not be determined.

Although EXAFS can yield accurate zinc active site structures, the technique lacks sensitivity to ligand identity. $K\beta_{2,5}$ (valence-to-core) X-ray fluorescence was used to study structurally-characterized zinc active site mimics. Zinc carboxylates, imidazoles, and thiolates were all found to have characteristic $K\beta_{2,5}$ lineshapes, which open up the possibility of site-selective EXAFS.

Chapter 1

Introduction

Metals in Biology

Biologically relevant metals can be divided into two broad classes—the bulk metals, such as K^+, Na^+, Mg^{2+} and Ca^{2+}, which are involved in signal transduction and in the maintenance of osmotic pressure, ionic strength, and charge balance, and the transition metals, such as copper, iron, and zinc, which form complexes with proteins and are involved in catalysis, electron transfer, structure stabilization, and oxygen storage and transport. While the transition metals comprise less than 0.01% of the human body by mass [1], life as we know it would not be possible without them. Between one fourth and one third of all structurally characterized proteins either bind metals or require metals for normal functioning [2], and cells contain intricate machinery for efficient uptake, transport and delivery of transition metal ions to their target proteins [3-6]. Indeed, several disease states are associated with failure of this machinery, such as Wilson's disease [7] and Menkes disease [8], caused by errors in copper transport, and hemochromatosis, caused by excessive iron uptake [9]. Metal-induced protein aggregates also contribute to certain diseases. For example, binding of copper and zinc is thought to induce formation of the amyloid β plaques that characterize Alzheimer's disease [10].

Levels of transition metals are tightly regulated within the cell. It is crucial to avoid toxic excesses of free redox-active metal ions such as iron, copper and manganese, which can generate damaging reactive oxygen species if left unchecked. In yeast, the free

copper concentration in unstressed cells has been estimated to be not more than approximately one attomolar [6]. This would correspond to less than one free copper ion per yeast cell. Free zinc levels are similarly regulated despite the relatively low toxicity of Zn(II). By varying the thermodynamically-defined free zinc concentration using the chelator TPEN, the O'Halloran lab at Northwestern University has found that half-maximal repression of the transcription of the *E. coli* gene *znuC*, which encodes one subunit of the zinc importer protein ZnuABC, occurs when $[Zn(II)]_{free}$ reaches approximately 0.2 fM. That same study determined that the half-maximal activation of the *E. coli* zinc exporter ZntR occurred at a free zinc concentration of approximately 1.2 fM. Since the free zinc concentration would, presumably, be close to these binding constants, these data suggest a "set point" of free zinc of approximately 0.7 fM, which corresponds to less than one free zinc ion per cell in *E. coli* [5]. This conclusion has been challenged by experiments with carbonic anhydrase-based zinc sensors, which have determined an exchangeable zinc concentration of approximately 5-10 pM in PC-12 cells [11]. Nonetheless, for a eukaryotic cell with a volume of approximately 3 pL, this would correspond to tens to hundreds of zinc atoms per cell, suggesting that the pool of labile or readily exchangeable zinc is small compared to the total zinc.

Somewhat surprisingly, concentrations of total zinc, iron, and copper seem to be relatively invariant across a variety cell lines, at least to within about an order of magnitude [12]. Straight lines are obtained when the average number of moles of zinc, iron, and copper per cell are plotted against cell volume for cell lines as diverse as *E. coli*, *S. cerevisiae*, mouse fibroblasts, *Xenopus* oocytes and chicken egg yolks. Average cellular concentrations of zinc and iron are approximately 100-300 μM, and

approximately 10 μM for total copper. X-ray fluorescence measurements on human KB cells presented later in this thesis are in line with these results, with approximately 300 μM total zinc and 150 μM total iron. However, exceptions to this trend do exist. In red blood cells, for example, total zinc levels tend to be 200-300 μM, consistent with the concentrations presented above, while total iron levels are close to 20 mM, several orders of magnitude higher than in the average cell. Large deviations from the expected total concentrations for a given metal ion may indicate a special function for that metal within the cell, as is the case for iron in erythrocytes, where heme iron binds oxygen for transport.

Zinc in Biology

The bulk of this thesis is concerned with the structure and localization of biological zinc sites. Of the transition metals, zinc is the second most abundant in the human body, following iron, and the most abundant if the iron contribution from hemoglobin is not included [13]. More than 300 enzymes [14] and 500 gene regulatory proteins [15] have been found which must bind zinc for proper functioning, and there is at least one zinc metalloprotein present in every major enzyme class recognized by the International Union of Biochemistry, these being oxidoreductases, transferases, hydrolases, lyases, isomerases, and ligases [13]. Zinc's ubiquity is due to the unique chemical properties of Zn(II) compared to the other transition metal ions. It is redox inactive and amphoteric. Furthermore, it has intermediate chemical hardness and a closed-shell electron configuration, so it can assume a variety of coordination geometries and ligation environments. In proteins, zinc assumes four-, five-, or six-coordinate

environments, with four-coordinate being the most common, and can interact with nitrogen from histidine imidazoles, oxygen from aspartate and glutamate carboxylates, and sulfur from cysteine thiolates [13].

Zinc metalloenzymes can be broadly divided into three classes: catalytic, co-catalytic, and structural [13]. Catalytic zinc sites are most commonly four-coordinate tetrahedral, with the zinc bound to the protein through interaction with three amino acid residues, these usually being histidine, aspartate, or glutamate. The fourth site is occupied by a water molecule, which either is displaced by ligand docking so that the zinc interacts directly with the ligand in the transition state, or primed for deprotonation to carry out acid-catalyzed reactions. In co-catalytic sites, the zinc does not participate directly in the reaction, but its presence enhances the catalytic activity of a second metal center. These sites tend to be the most geometrically diverse, as examples of four-, five-, and six-coordinate ligation are known, and with the zinc ion most commonly bound through aspartate, glutamate or histidine residues. Finally, structural zinc sites do not participate directly or indirectly in catalysis other than their role in maintaining tertiary structure. These tend to be four-coordinate sites with primarily cysteine ligation. Also of note are the so-called zinc finger, zinc twist and zinc cluster proteins, which bind DNA and RNA and are involved in transcription regulation and nucleotide repair [16]. These are also four-coordinate, and exhibit mixed sulfur/nitrogen ligation through bound cysteines and histidines, respectively.

The Role of Metals in Malaria

Malaria is a blood-borne illness caused by four species of the *Plasmodium* genus

and transmitted by the *Anopheles* mosquito [17], the most deadly of which is *Plasmodium falciparum* [17, 18]. The malaria parasite spends much of its life cycle reproducing asexually in the human bloodstream, where it invades host erythrocytes prior to growth and division [19-21]. The parasite digests the erythrocyte cytosol, where it uses hemoglobin as its primary protein source [22]. Degradation of hemoglobin releases heme, which can participate in Fenton chemistry, generating toxic hydroxyl and peroxyl radicals [23]. Consequently, the heme must be detoxified. This is done by sequestering heme within the parasite's food vacuole, where it crystallizes as a non-toxic hemozoin crystal [22]. Some of the earliest and most effective drugs for treating malaria, quinine and chloroquine, are believed to work by disrupting the formation of this hemozoin crystal, killing the parasite through heme cytotoxicity [24]. However, chloroquine resistant strains of *P. falciparum* have evolved that can recognize and export quinoline antimalarials, as well as promote heme crystallization even in the presence of chloroquine, prompting a search for alternative treatment strategies [25].

One such alternative strategy is to disrupt the parasite's metal homeostasis, particularly its zinc homeostasis, through the use of chelators. As the parasite grows and feeds, it modifies the host membrane to import essential nutrients. During this time, the parasite synthesizes transporters for the accumulation of metal ions from the bloodstream. These include homologues for both the cation diffusion facilitator (CDF) transporter and the ZIP zinc transporter [12]. Ginsburg and co-workers determined that red blood cells infected with *P. falciparum* accumulate zinc approximately 2-3 fold over the normal erythrocyte zinc concentration [26]. Recently, a collaboration between the Penner-Hahn and O'Halloran labs has confirmed this result and furthermore determined that the

parasite concentrates chelatable zinc approximately 20-fold in localized sub-regions [12, 27]. The exact function of that zinc is unknown, but the use of membrane-permeable chelators has proven effective at reducing parasitemia in *P. falciparum* cultures. The high affinity chelator TPEN has proven particularly effective, exhibiting an IC_{50} of 500 nM. This is comparable to that of the quinoline antimalarials, which have IC_{50} values—the concentration at which growth is inhibited by 50%—of 29-138 nM for chloroquine, and 90-338 nM for quinine [28].

The Role of Metals in Apoptosis

Apoptosis is a type of programmed cell death used by multicellular organisms to dispose of unwanted or damaged cells [29-32]. The process is interesting not only because it is necessary for normal body plan development, but for medical reasons as well. Many disease states are associated with disruption of the apoptotic machinery, most notably cancer [33, 34], where many of the genes that encode factors crucial to the apoptotic process fail to express properly. Thus, there is a great deal of interest in elucidating the factors that control the onset of apoptosis.

Apoptosis is not characterized by a single biochemical pathway, but by several different pathways that terminate with the cell breaking down its nucleotides and proteins in an orderly fashion and dividing into numerous so-called apoptotic bodies, which are recognized and phagocytosed by the surrounding tissue [29, 35]. The process is characterized by numerous biochemical and morphological markers, including cysteine-aspartic acid protease (caspase) activity, DNA laddering, and changes in the plasma membrane composition and morphology [29]. One of the earliest of these markers is the

apoptotic volume decrease (AVD), a 50% drop in cell volume that occurs within one hour of induction of apoptosis, independent of the cell's normal osmotic response [36]. AVD is believed to be controlled by small ion fluxes, particularly of the bulk metal ions K^+ and Na^+, as well as chloride, since inhibitors that block channels that are specific for these ions have been found in many cases to protect the cell from apoptotic stimuli [37-41]. Altering the ionic composition of the cytosol in this manner is believed to promote maximal caspase and nuclease activity [42].

Intracellular calcium is also believed to play a large role in apoptosis. Free calcium is stored in the endoplasmic reticulum (ER), and certain cell signalling pathways involve transient release of Ca(II) from the ER, where it serves as a second messenger [43]. On the other hand, apoptotic induction involves a much more pronounced and sustained increase in intracellular free calcium [44, 45], as judged through the use of calcium-specific fluorophores. High levels of free calcium relocalizing to the mitochondria seem to be able to trigger certain pathways for cytochrome c release [35]. Cytochrome c released from the mitochondria can combine with the apoptosis inducing factor (AIF) in the cytosol to form the apoptosome, which activates certain caspases and thereby certain intrinsic apoptosis pathways [35].

The role, if any, that transition metal ions play in this process is less clear. Of the transition metals, zinc has received the most attention, because of the relationship between zinc levels and caspase-3 activity [46]. Both deficiency and toxic excesses of zinc potentiate cells for apoptosis [47]. On the other hand, mild zinc supplementation has a protective effect. While many of the details of the apoptotic process depend on the particular cell line and inducer under study, the protective effect of mild zinc

supplementation has been noted under many different conditions [47]. Zinc is believed to protect cells from apoptosis by protecting them from oxidative stress that would otherwise trigger apoptosis, although this is not believed to be mediated through Cu/Zn-SOD activity, since treatment with the membrane-permeable zinc chelator N,N,N',N'-tetrakis-(2-pyridylmethyl)-ethylenediamine (TPEN) can induce apoptosis while leaving Cu/Zn-SOD activity unaltered [48]. Rather, the focus has been on zinc's ability to prevent oxidation of cysteine thiolates, since interaction of Zn(II) with cysteine thiolates is believed to present a barrier to the oxidation of these thiolates to form disulfide bridges [47]. This would prevent certain kinds of damage to the cell that may result in apoptosis. Furthermore, excess zinc has been found in some cases to block the release of cytochrome c from the mitochondria [49], a crucial step in many apoptotic pathways, though whether this phenomenon occurs under physiological conditions is unclear.

Spectroscopically Quiet Metals

Zinc is interesting not only for its utility and ubiquity, but for the spectroscopic challenge it presents. Biologically relevant metal ions such as Zn(II) and Cu(I) are examples of so-called "spectroscopically quiet" metals [50]. These metals have a closed-shell, $3d^{10}$ configuration and so are unable to be studied by conventional spectroscopies such as UV/Vis, MCD and EPR. In the case of Zn(II), several other spectroscopic probes exist for studying zinc metalloproteins, each with their own advantages and disadvantages. ^{67}Zn NMR has been successfully applied to distinguish between several carbonic anhydrase active site mimics [51]. However, this technique currently requires highly concentrated and symmetric solid state samples and is currently not widely used

for biological applications. Protein crystallography can help determine the local geometry with a resolution of ~1 Å at best [52], which may help to determine the immediate interacting residues, but lacks the resolution for a detailed local structure. Furthermore, this technique is only accessible to the fraction of metalloproteins that can actually be crystallized, and there is no guarantee that the crystal structure thus obtained is the biologically relevant one. Substituting the Zn(II) ion for a more spectroscopically active metal such as Co(II) and Cd(II) can often be done, but again there is no guarantee that the metal-substituted complex is isostructural to the native zinc site [53].

In contrast to other zinc spectroscopic probes, X-ray spectroscopy can yield high-resolution structural information on the order of 0.02 Å [50, 54]. In addition, these spectroscopies can be performed on disordered, amorphous samples, and with an X-ray source with high-enough flux—as present in synchrotron X-ray sources—zinc can be studied in its native environment. The bulk of this thesis will be devoted to the use of synchrotron X-ray sources to probe the structure and localization of biological zinc sites.

Techniques Used in this Thesis

X-Ray Absorption Spectroscopy (XAS)

The X-ray absorption spectrum can be divided into two broad regions, the X-ray absorption near-edge structure (XANES) and the extended X-ray absorption fine structure (EXAFS). The division between the two is somewhat arbitrary, but the XANES is conventionally taken to be the absorption spectrum within 50 eV of the edge—the sudden jump in the X-ray absorption cross section that occurs when the incident X-ray energy exceeds the binding energy of one of the electrons in the sample [50, 54]. The

EXAFS region covers everything above that point (Figure 1.1).

The XANES spectrum consists primarily of transitions between bound states. For the K edge of biologically relevant transition metals, this corresponds to the 1s → 4p transition and various associated satellite transitions, for example, the 1s → 4p shakedown and shakeup transitions [55, 56]. For many of the transition metals, a pre-edge peak is present within a few electronvolts below the edge. This corresponds to the 1s → 3d transition. This transition carries information about the geometry around the metal center, since in complexes lacking inversion symmetry (i.e. tetrahedral symmetry), the 4p can mix with the 3d, making this transition dipole-allowed and increasing its intensity [57-59]. Additionally, the 1s → 3d lineshape is sensitive to the metal's spin state [57-59]. However, these pre-edge features are not present in metals with closed-shell configurations like Zn(II) and Cu(I). The edge position itself contains information about the metal's oxidation state. It is more difficult to remove an electron from highly oxidized metal centers, and in transition metals, this translates to an increase in edge energy of approximately 5 eV for every unit increase in oxidation state [60].

The 1s electron can be liberated from a metal center if an incident photon has high enough energy. In principle, for a completely isolated atom the X-ray absorption cross section would decrease monotonically after the edge as the incident X-ray energy is increased. However, the presence of neighboring atoms causes a modulation of the absorption cross section. This modulation is caused by scattering of the photoelectron off the neighboring atoms, such that the final state is not merely a photoelectron wave, but the photoelectron wave interfering with itself due to the presence of neighboring atoms. The modulation of the absorption is determined by whether this wave undergoes

constructive or destructive interference at the absorbing atom, as determined by the photoelectron energy and the site geometry. Constructive interference causes an increase in absorption cross section, while destructive interference causes a decrease [56].

A complete description of the EXAFS would require a full multiple scattering formalism [61]. However, for samples lacking significant long-range order, as is the case in most metalloproteins, the EXAFS can often be approximated with a single-scattering theory [56]. The EXAFS is extracted from the absorption spectrum by fitting the post-edge region to a spline function and then subtracting this function from the post-edge spectrum. The resulting spectrum, which resembles a damped sine wave, is fit with the EXAFS equation [54, 56]:

$$\chi(k) = -S_0^2 \times \sum_j \frac{N_j}{kR_j^2} | f(k) | \exp(\frac{-2R_j}{\lambda_e}) \exp(-2k^2\sigma_j^2) \sin(2kR_j + \varphi(k))$$

where S_0^2 is an amplitude reduction factor, N_j is the number of neighboring atoms, R_j is the absorber-scatterer distance, $|f(k)|$ is the scattering amplitude, λ_e is the photoelectron mean free path, σ^2 is the Debye-Waller factor (the mean squared deviation of the metal-ligand bond lengths), and $\varphi(k)$ is a phase shift function that comes from the interaction of the photoelectron with the absorber and scatterer potentials. The summation is taken over all shells—groupings of similar atoms at similar distances from the absorbing atom. The photoelectron wavenumber, *k*, is defined as

$$k = \sqrt{\frac{2m_e(E - E_0)}{\hbar^2}}$$

where m_e is the electron mass and E_0 is the threshold energy.

Since the EXAFS is proportional to sin(2*k*R), the data can be Fourier transformed over R to yield a pseudo-radial distribution function, so termed because the amplitudes

are not directly proportional to the coordination number and because the absorber-scatterer distances are shifted by approximately -0.5 Å due to the phase shift function $\varphi(k)$ [50, 54]. See Figure 1.2 for an example of a processed EXAFS spectrum and its corresponding pseudo-radial distribution function. Fitting the EXAFS equation using a theoretically calculated or empirically derived phase function yields the proper bond distance.

One problem with fitting EXAFS data is that the fit parameters can be highly correlated with each other [50]. For example, the coordination number is positively correlated with the Debye-Waller factor and negatively correlated with the amplitude reduction factor. In addition, R and E_0 are correlated since E_0 defines *k*. The latter problem is especially important because there is no universally agreed-upon definition for what energy E_0 should correspond to, and a number of different conventions exist [56].

Furthermore, there is the danger of over-fitting the data, particularly if the *k* range is low and the number of shells one wishes to fit is high. The number of independent data points, N_{idp}, in any given EXAFS data set is given by [50, 62]:

$$N_{idp} = \frac{2\Delta k \Delta R}{\pi}$$

where Δk is the *k* range of the data set, typically between 2-10 $Å^{-1}$ and 2-16 $Å^{-1}$, and ΔR is the useful R range. The definition of this range is somewhat ambiguous, but is usually between approximately 0.5-2.0 Å, and never more than approximately 5 Å, where the experimental noise starts to dominate the spectrum [50].

When using EXAFS to determine the structure of an unknown, the uncertainty in E_0 and S_0 can largely be ameliorated by first fitting the EXAFS equation to data derived from well-characterized model compounds—that is, compounds with known N and R—

believed to be similar in nature to the unknown. The threshold energy, scattering amplitudes, and phase shifts derived from this fit then become constants when fitting the unknown. This effectively reduces the number of fit parameters and decreases the likelihood of obtaining a fit that is mathematically reasonable but physically unrealistic [63].

In general, the detailed shape of the XANES region is even more sensitive than EXAFS to scattering effects and to scattering from more distant atoms, since the lower photoelectron energies are less affected by inelastic losses, allowing the photoelectron to sample a larger volume [64]. The sensitivity of the XANES region to multiple scattering effects can be used to perform minute structural refinements on metalloproteins whose structure is already reasonably well-known. This approach has been used to refine the bond lengths and angles around the zinc site in Cu/Zn-SOD [65]. However, this approach is not as useful when studying complete unknowns or complex mixtures, and so will not be further discussed here.

X-Ray Emission Spectroscopy (XES)

EXAFS is a powerful tool for determining accurate active site geometries. However, this technique suffers from significant limitations. The most serious of these is its inability to distinguish between ligands with similar atomic numbers, since the phase function $\varphi(k)$ is too similar to make much of a difference in the EXAFS [50, 54]. This means that it is impossible to use single-shell fits to distinguish between most of the biologically relevant ligands, namely histidine, glutamate, aspartate, and water. Furthermore, it is often difficult to obtain a unique fit for sites with mixed sulfur and

nitrogen ligation, since in these cases the scattering from the sulfur is almost exactly out of phase with the scattering from nitrogen for most of the useful *k* range [63]. To compensate for this difficulty, we employed X-ray emission spectroscopy on a variety of zinc compounds. Specifically, we examined the valence-to-core transitions, which were expected to offer increased chemical sensitivity.

X-ray emission spectroscopy is the complementary technique to the X-ray absorption spectroscopy described above. Whereas XAS is concerned primarily with the effects of oxidation state, spin state, ligation and geometry on the intensity and position of the core-to-valence transitions, XES is concerned with the effect that these factors have on fluorescence energies and intensities after a core hole has been created. In some respects, the XES spectrum is more straightforward to interpret than the XAS, since while the XANES region depends on both absorption and scattering effects, the XES consists solely of bound state transitions [66].

The Kα (2p → 1s) and $K\beta_{1,3}$ (3p → 1s) transitions have been extensively studied in transition metal complexes, and of these, manganese, nickel and iron minerals have received the most attention [66]. These spectra are sensitive to oxidation state, spin state, and chemical environment, and the variety of lineshapes thus obtained has been exploited for some interesting applications. For example, site-selective EXAFS and XANES can be performed by windowing the detector on characteristic features in the XES spectrum [66, 67]. This allows determination of the local geometry and electronic structure around a single type of metal center in a complex mixture of different complexes of the same element, rather than a single average geometry over all the metal centers of a given element in the mixture. This approach has been applied, for instance, to distinguish

between the high-spin and low-spin iron sites in Prussian blue ($Fe_4[Fe(CN)_6]_3$) [68].

In contrast, the Kα and $K\beta_{1,3}$ XES of zinc compounds has received relatively little attention. Since there is only one significant oxidation and spin state, these spectra are relatively uniform, and because of the filled 3d shell there is no significant multiplet structure. However, advances in high-resolution X-ray optics and synchrotron radiation flux have made it possible to study the Kβ satellite transitions, namely the $K\beta_{2,5}$ and Kβ'', where the $K\beta_{2,5}$ is the transition from the valence molecular orbitals to metal 1s, and the Kβ'' is the so-called "crossover" transition, a charge transfer transition between the ligand valence orbitals and the metal 1s [69]. Since these transitions involve the ligand orbitals and molecular orbitals that include the ligand orbitals, these spectra are expected to be very sensitive to ligand identity (Figure 1.3).

Obtaining useful information from the XES spectra depends crucially on the type of detector used. The standard germanium detector used in the X-ray absorption and imaging studies offers too low a resolution for this purpose. These detectors have a resolution of approximately 150 eV [70]. The Kβ satellite peaks are within 100 eV of the $K\beta_{1,3}$ peak and about a hundred times weaker, so instrumental broadening would blur out any informative features. Instead, a wavelength-dispersive detector is employed for this purpose. Rather than being sent directly to the detector, the fluorescent photons are first reflected off a set of bent analyzer crystals at a backscattering angle of close to 180°. The Rowland circle geometry is employed, such that the sample, analyzer crystals, and detector are situated on a circle with the analyzer crystals equidistant between the sample and the detector, and with the analyzer crystals possessing a radius of curvature equal to the Rowland circle diameter (Figure 1.4) [71, 72]. When these conditions are met, the

fluorescent photons entering and leaving the analyzer crystals simultaneously satisfy Bragg's law and the law of reflection. Thus, the analyzer crystals function as both a mirror and a monochrometer, efficiently collecting photons from weak transitions with very high resolution. For the zinc $K\beta_{2,5}$ transition with an energy of approximately 9655 eV, Ge(555) analyzer crystals give a resolution of approximately 1.2 eV. See Figure 1.5 for an example of the improvement in resolution this setup provides.

Interpretation of the XES spectra is accomplished not only through qualitative comparison of the spectra derived from similar compounds, but through electronic structure calculations. When calculating the X-ray emission spectrum, it is commonly assumed that the ground state density of states is a reasonable approximation to the actual density of states and that the presence of the core hole has a negligible effect [73]. For transitions between core states with energies ε_{c1} and ε_{c2}, fluorescence energy $\hbar\omega = \varepsilon_{c2} - \varepsilon_{c1}$ gives the difference in binding energies. The lineshapes of these transitions can be reasonably well-approximated by calculating the dipole couplings between states with energies calculated from multiplet theory [74, 75]. Transitions from the valence band give the occupied density of states, with the photon energy equal to the valence band energy minus the core electron energy [73]. The calculated density of states does not accurately reproduce the experimental spectrum, but is useful for making rough peak assignments and general comparisons.

X-Ray Fluorescence (XRF) Imaging

X-ray fluorescence imaging of metal distributions in biological systems has received increasing attention in recent years, with improvements in synchrotron radiation

flux and X-ray optics allowing detection limits as little as one part per ten million for transition metals. This is more than sufficient to study iron, zinc, and copper *in situ*, though other essential elements like nickel, vanadium and cobalt are typically undetectable at biological concentrations except in certain special cases. X-ray fluorescence imaging offers simultaneous, quantitative, and element-specific determination of the amounts and distribution of each element in the sample.

The technique has features in common with both fluorescence-detected X-ray absorption spectroscopy and scanning electron microscopy. The sample is exposed to a monochromatic beam with sufficiently high energy to remove a core electron, and an energy-dispersive detector is used to measure the fluorescence from the atoms in the sample as they relax to the ground state. The fluorescence energies depend on the elemental makeup of the sample. Elemental specificity is due to the fact that each element has its own characteristic fluorescence lines (see Figure 1.6). The fluorescence intensities are proportional to the concentration of the corresponding element within the sample. Quantitation can be achieved through the use of standards of known elemental composition. For sufficiently thin samples, the concentration of any given element in the sample can be determined using the equation [76]:

$$[unk] = [std] \times \frac{F_{unk}}{F_{std}}$$

where [unk] is the unknown sample concentration for a given element, [std] is the concentration of the corresponding element in the standard, F_{unk} is the number of fluorescence counts per second of a given fluorescence line, normalized to the incident beam intensity, and F_{std} is the corresponding normalized fluorescence intensity in the standard.

The fluorescence counts at the detector depend on the incident intensity, the absorbing elements' photoelectric cross sections and quantum yields, the absorption of the fluorescent photons by the surrounding air, the sensitivity of the detector material to the fluorescent photons, and the detector solid angle. The sample matrix itself also has an effect, but this can be ignored as long as the sample is sufficiently thin. By normalizing the fluorescence intensity of a given element in the standard to the incident intensity, the standard's absorbance (determined by the standard concentration and the photoelectric cross section), the quantum yield, and the absorbance of the surrounding air and the detector material, one obtains a number that depends only on the detector geometry. Since absorption cross sections and quantum yields are tabulated for most elements, this information can be used to create a calibration curve that can be used to calculate the ratio $[std]/F_{std}$ for elements not actually present in the standard. Thus, one can quantify elements in the sample for which one does not have a suitable standard [76].

As in other scanning probe microscopies, images of the elemental distribution of each element are built up by raster-scanning the sample across the beam and plotting the fluorescence intensity as a function of position. The resolution is determined by the spot size. Tissue-level images can be obtained by using slits to define the beam size, yielding a resolution on the order of 100-1000 μm. Cellular and sub-cellular imaging can be attained by focusing the incident beam. Because the index of refraction for most materials is close to one at hard X-ray energies [70], it is impractical to focus the beam with a lens as in traditional microscopy. Focusing is achieved either through reflection off a bent multilayer at grazing incidence or through diffraction. The former is the basis for the Kirkpatrick-Baez mirror, a pair of orthogonally oriented, parabolically curved multilayers

that can focus the incident beam to a spot size of approximately 0.8 μm x 0.8 μm at 10 keV with little loss of flux [77]. The latter is the basis of zone plate optics. The zone plate is a circular diffraction grating that can focus the incident beam to a typical spot size of 0.3 μm x 0.3 μm at 10 keV, although work is underway to achieve spot sizes as low as 30 nm x 30 nm [78]. The trade-off, however, is that the zone plate is relatively inefficient—approximately 10% of the incident beam is focused to the desired focal length, while the other 90% is either absorbed or diffracted to other diffraction orders [70].

A spot size of 0.3 μm x 0.3 μm allows sub-cellular imaging and the ability to quantify metals in individual cells. The images thus obtained can also be used to quantify metals within certain sub-regions within individual cells without having to perform sub-cellular fractionation, though the resolution is currently only good enough to perform this analysis on the nucleus and the larger organelles, such as the vacuole in yeast cells and the food vacuole in malaria-infected red blood cells. These abilities provide complementary information to techniques such as ICP-MS and ICP-AES, which can determine the average metal contents of a population of cells to a high degree of accuracy, but which lose information about the distribution of those metals both within individual cells and within the population of cells. The trade-off is the relatively small sample sizes obtained through X-ray fluorescence imaging. A typical eukaryotic cell has a diameter of approximately 20 μm after freeze drying in preparation for imaging. With a spot size of 0.3 μm x 0.3 μm, the resulting image is 60 x 60 pixels, or 3600 pixels in total. A dwell time of one second per pixel means that it takes approximately one hour to image one eukaryotic cell, even if the motor move and settle times during the raster scanning

process are not taken into account. As a consequence, the sample size of a single XRF imaging experiment is typically limited to tens of cells for each sample condition.

The information obtained from X-ray fluorescence imaging is complementary to that derived from the use of element-specific fluorophores—fluorescent molecules whose fluorescence intensity increases upon interaction with a metal ion due to a decrease in nonradiative quenching. Consider zinc as an example. Dissociation constants for zinc-specific fluorophores range from nanomolar to tens of micromolar [12, 79], whereas dissociation constants for protein zinc binding sites are in the nanomolar to picomolar range [80]. Thus, zinc fluorophores probe the fraction of zinc that is free or weakly bound. In contrast, hard X-ray fluorescence imaging probes the entire zinc contents of the sample. Fluorescent probes are well suited for the task when one is interested specifically in free or weakly bound zinc; however, changes in fluorescence intensity from zinc probes are not necessarily indicative of global changes in zinc distribution.

Overview of This Thesis

Broadly, this thesis is concerned with the use high flux synchrotron radiation X-ray sources to study the contents, localization, and structure of biologically relevant zinc sites, with some attention to the other transition metals and to the bulk elements where appropriate. Chapter 2 is an X-ray fluorescence imaging study of red blood cells infected with the malaria parasite *Plasmodium falciparum*. Red blood cells infected with *P. falciparum* are known to accumulate zinc 2-3 fold as the parasite matures. We hypothesized that this zinc plays an essential role in the parasite's growth and survival, and examined the effect of zinc chelators on the same. The membrane-permeable chelator

TPEN was found to be very effective at inhibiting parasite growth, while the membrane-impermeable chelator EDTA was relatively ineffective, despite these having similarly-high zinc binding affinities. To determine what effect these chelators may have on metal homeostasis, we employed XRF imaging to study the zinc and iron contents and distribution in EDTA- and TPEN-treated schizont-stage infected red blood cells, with untreated samples as a control. An analysis of the contents of the hemozoin crystal suggested some ways in which the parasite may deal with zinc-deprived conditions, by both consuming more of the host cytosol and by making use of relatively more of the host zinc.

Chapter 3 complements Chapter 2, and is an X-ray absorption spectroscopy study of red blood cells infected with *P. falciparum* and subjected to various chelator treatments. The X-ray imaging study in Chapter 2 revealed some puzzling features of the zinc uptake in *P. falciparum*. In particular, the membrane-impermeable chelator EDTA seems to be able to abolish zinc uptake without a concomitant decrease in viability. This suggests that the parasite does not require extracellular zinc for survival, although it seems to have some use for it, since the imported zinc is not confined to the parasite food vacuole. This raises the question as to why the parasite imports this excess zinc at all. XAS was employed in order to determine the average zinc environment in EDTA- and TPEN-treated schizont-stage infected red blood cells, with untreated schizont-stage and uninfected red blood cell samples as controls, in order to gain a broad view of how the parasite partitions the available zinc between structural, catalytic and co-catalytic sites under the different treatment conditions. Surprisingly, the TPEN-treated sample was similar to the uninfected and untreated schizont-stage infected samples in terms of its

average zinc environment, whereas the EDTA-treated sample was significantly different, exhibiting much greater zinc-sulfur interactions.

Chapter 4 switches the focus to apoptosis, or programmed cell death. Apoptotic cells exhibit a phenomenon called apoptotic volume decrease (AVD), a 50% reduction of cell volume that occurs within one hour of introduction of an apoptotic stimulus. AVD is believed to be related to small ion fluxes, which are believed to be crucial for optimizing protease and nuclease activity. These fluxes are commonly studied using element-specific fluorophores, which have certain limitations when it comes to quantification and element specificity. To gain this information, we employed X-ray fluorescence imaging on human KB cells undergoing staurosporine-induced apoptosis. Using this method, we found changes in the chloride and calcium levels that either contradict previous reports or were not previously noted in the literature. In addition, we noted unexpected changes in the calcium, zinc, and copper distributions in the early stages following the introduction of the apoptotic stimulus.

Chapter 5 is an X-ray emission spectroscopy study of a series of zinc minerals, salts, and metalloprotein active site mimics. Well-characterized zinc compounds are used to identify the main transitions and how they change in energy and intensity as the ligand identity is systematically varied. Zinc carboxylates, thiolates and imidazoles are found to have characteristic shapes that can be used to determine ligand identities and stoichiometry, which is often difficult to determine by EXAFS analysis. The Kβ'' crossover peak seems to be largely absent in the zinc thiolates and imidazoles, suggesting that this peak would be a unique marker for glutamate, aspartate, or water, which would allow site-selective EXAFS to be performed in some instances.

Much of the work presented in this thesis was a collaborative effort. In Chapter 2, *P. falciparum* samples were grown and mounted for imaging by Becky Marvin from the O'Halloran lab at Northwestern University, while I performed the quantification and analysis. Data acquisition was handled by both. In Chapter 3, *P. falciparum* samples for XAS were also prepared by Becky Marvin, while I performed the data acquisition and analysis. In Chapter 4, human KB cells were grown by Chris Kelly from the Banaszak Holl lab at the University of Michigan, while I performed the plunge freezing, data acquisition, quantification and analysis. In Chapter 5, the zinc scorpionates $[Tm^{t\text{-}Bu}]ZnSPh$, $[Tm^{t\text{-}Bu}]ZnSCH_2C(O)N(H)Ph$, and $[Tp^{t\text{-}Bu,Me}]ZnOH$ were prepared by Jonathan Melnick from the Parkin lab at Columbia University. All other samples that were not purchased were prepared by me. In addition, I performed the data acquisition and analysis, as well as the electronic structure calculations. The X-ray emission spectrometer utilized in Chapter 5 was built by Dr. Uwe Bergmann at beamline 6-2 at the Stanford Synchrotron Radiation Lightsource. X-ray absorption spectroscopy of the red blood cell samples featured in Chapter 3 was also performed at the Stanford Synchrotron Radiation Lightsource, at beamline 9-3. The X-ray fluorescence imaging in Chapter 2 and Chapter 4 was performed at the Advanced Photon Source at beamline 2-ID-E, which is maintained by Dr. Stefan Vogt and Dr. Lydia Finney.

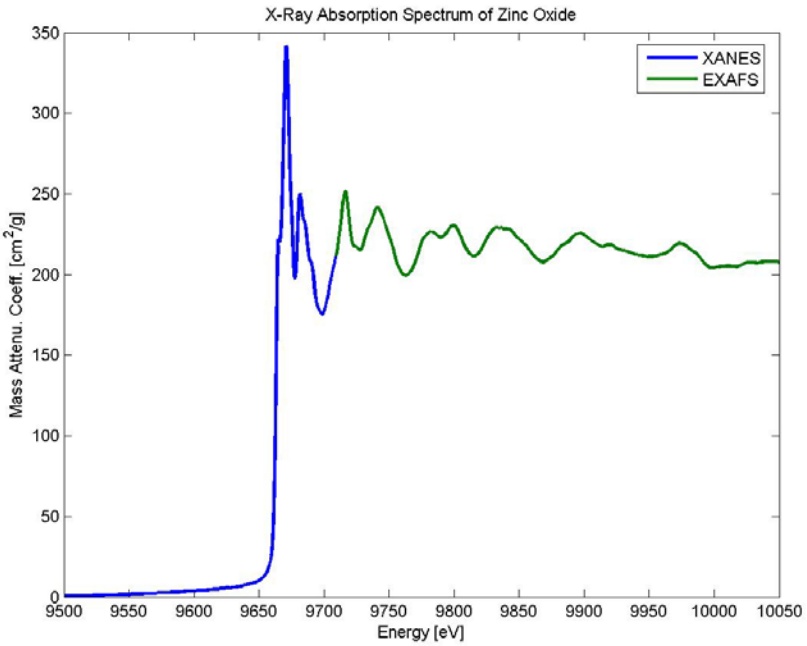

Figure 1.1: Example X-ray absorption spectrum of zinc oxide, showing the division between the XANES (blue) and EXAFS (green) regions.

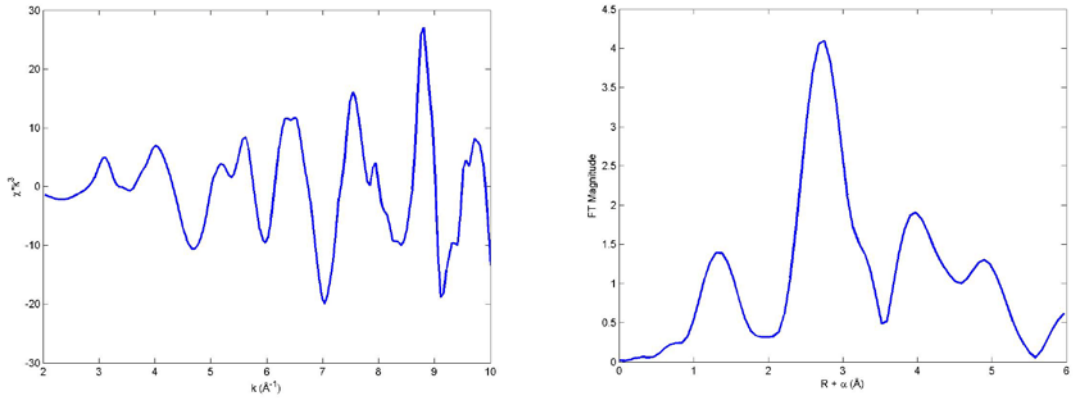

Figure 1.2: Example EXAFS spectrum after data work-up (left) and the pseudo-radial distribution function (right) for zinc oxide.

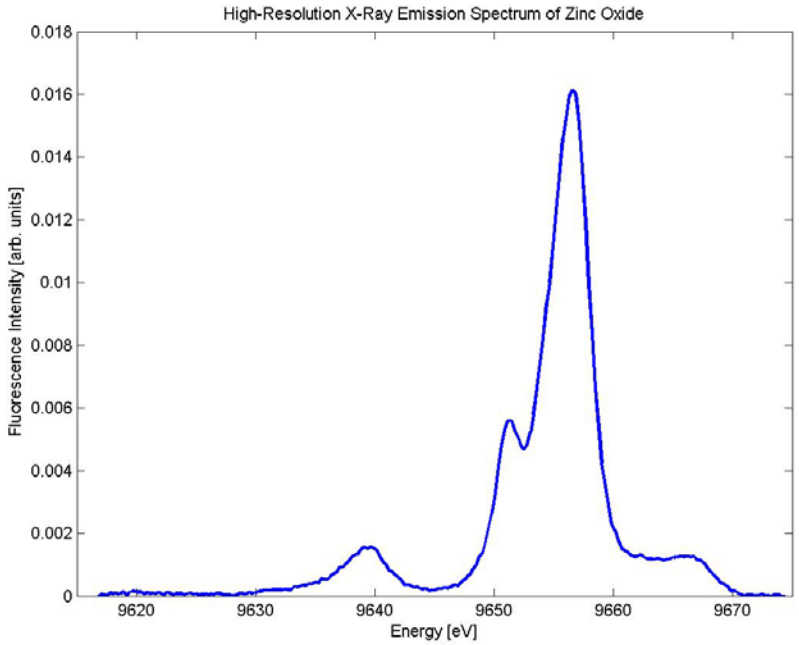

Figure 1.3: $K\beta_{2,5}$ emission spectrum of zinc oxide. The spectrum has been normalized to the $K\beta_{1,3}$ intensity, meaning the tallest peak in this spectrum is approximately 60 times less intense than the $K\beta_{1,3}$ transition. The Kβ'' crossover peak is the small peak at approximately 9640 eV.

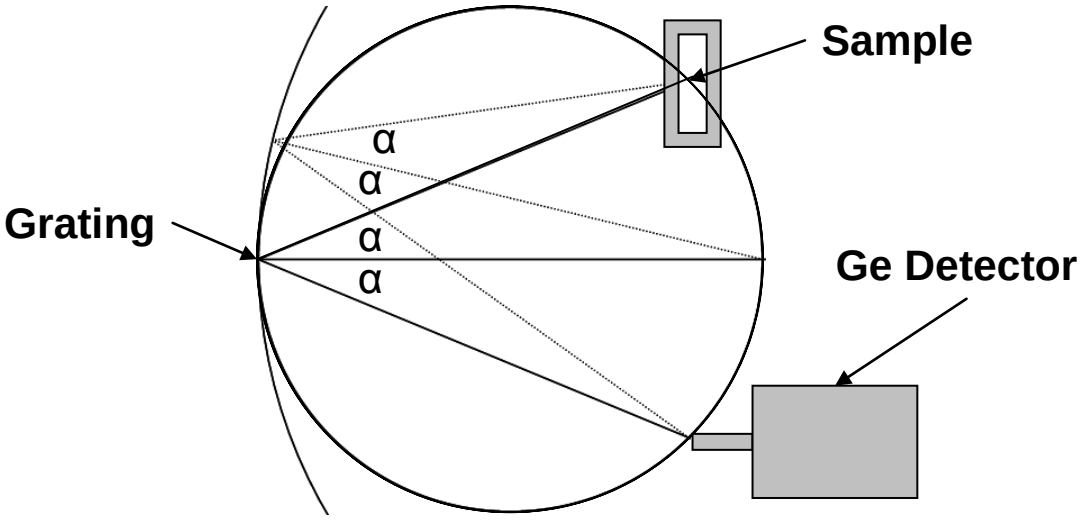

Figure 1.4: Schematic of Rowland circle geometry. Here, all angles α are equal, so all fluorescence from the sample will end up at the detector regardless of what point it hits the grating.

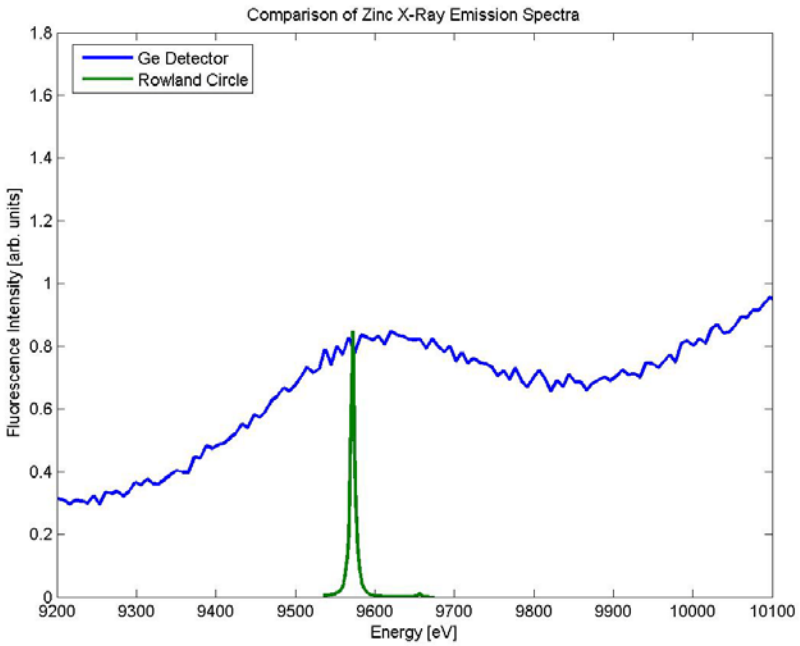

Figure 1.5: Comparison of the zinc $K\beta_{1,3}$ fluorescence obtained using an energy-dispersive detector (blue) vs. a wavelength-dispersive detector (green). The rising background in the former spectrum is due to the presence of the inelastic scatter peak when the incident energy is 12 keV. The high-resolution spectrum was collected with incident energy of 10.4 keV, and despite this being closer to the $K\beta_{1,3}$ peak there is no apparent background distortion.

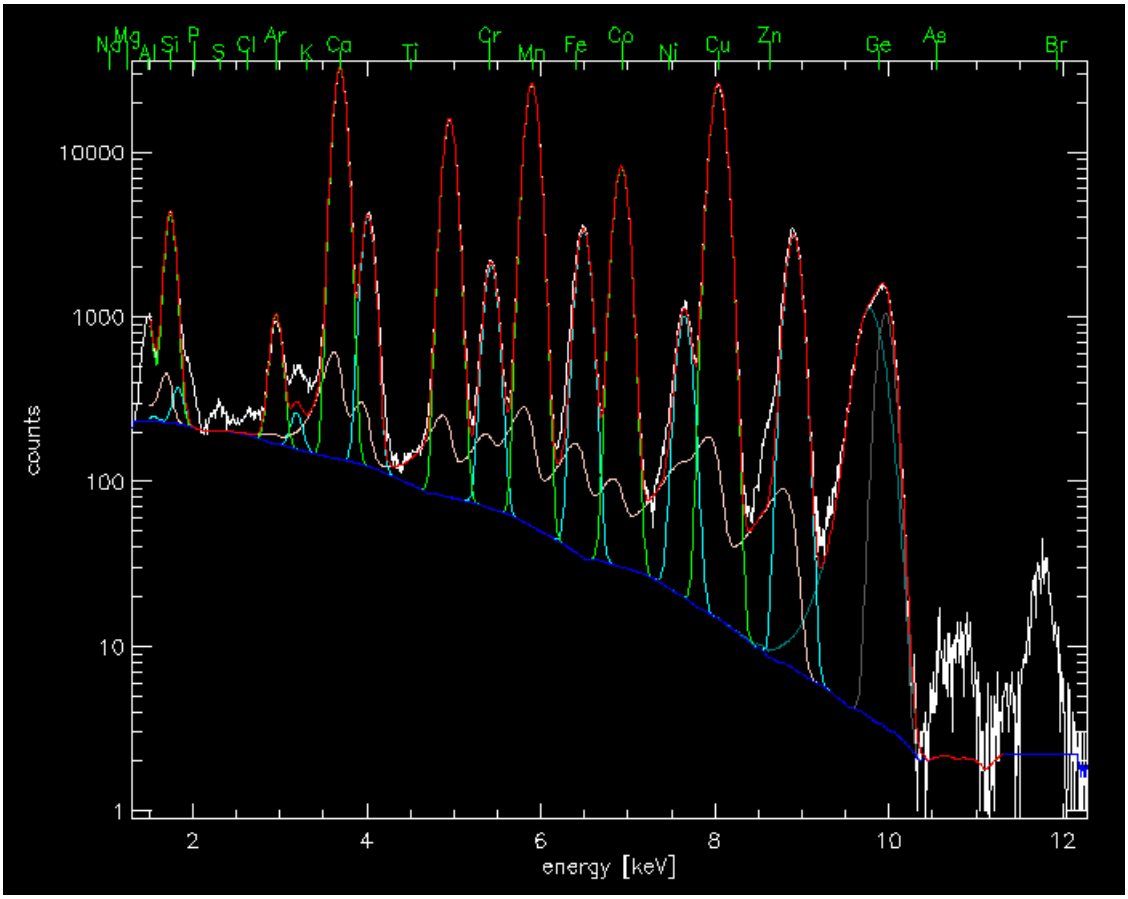

Figure 1.6: A fitted spectrum, using NIST thin-film standard NBS-1832 as an example. NBS-1832 contains known amounts of copper, cobalt, manganese, vanadium, and calcium. The white spectrum is the raw data, and the red is the best fit. Individual components of the fit are also visible. The dark blue spectrum is the background function, defined by applying a peak stripping algorithm to the raw data. The green peaks are the Kα peaks, while the turquoise peaks are the $K\beta_{1,3}$ lines. The beige line is the sum of the low-energy tail functions for all the fluorescence lines, required because the detector is more efficient at collecting the photons at the low-energy side of the peaks. The incident energy was 10keV, and the fitted elastic and inelastic peaks (in dark grey) are visible at the right hand side. Fits and figure were produced using Maps software [81].

References

1. Kaim, W. and B. Schwederski, *Bioinorganic Chemistry: Inorganic Elements in the Chemistry of Life: An Introduction and Guide*. 1994, San Francisco, CA: John Wiley & Sons.
2. Ibers, J. and R. Holm, *Modeling coordination sites in metallobiomolecules.* Science, 1980. **209**(4453): p. 223.
3. Finney, L.A. and T.V. O'Halloran, *Transition Metal Speciation in the Cell: Insights from the Chemistry of Metal Ion Receptors.* Science, 2003. **300**(5621): p. 931-936.
4. McMahon, R.J. and R.J. Cousins, *Mammalian zinc transporters.* Journal of Nutrition, The, 1998. **128**(4): p. 667.
5. Outten, C.E. and T.V. O'Halloran, *Femtomolar Sensitivity of Metalloregulatory Proteins Controlling Zinc Homeostasis.* Science, 2001. **292**(5526): p. 2488-2492.
6. Rae, T.D., et al., *Undetectable Intracellular Free Copper: The Requirement of a Copper Chaperone for Superoxide Dismutase.* Science, 1999. **284**(5415): p. 805-808.
7. Bull, P.C., et al., *The Wilson disease gene is a putative copper transporting P–type ATPase similar to the Menkes gene.* Nature Genetics, 1993. **5**(4): p. 327.
8. Chelly, J., et al., *Isolation of a candidate gene for Menkes disease that encodes a potential heavy metal binding protein.* Nature Genetics, 1993. **3**(1): p. 14.
9. Hanson, E.H., *HFE gene and hereditary hemochromatosis: a HuGE review.* American Journal of Epidemiology, 2001. **154**(3): p. 193.
10. Curtain, C.C., et al., *Alzheimer's Disease Amyloid-beta Binds Copper and Zinc to Generate an Allosterically Ordered Membrane-penetrating Structure Containing Superoxide Dismutase-like Subunits.* J. Biol. Chem., 2001. **276**(23): p. 20466-20473.
11. Bozym, R.A., et al., *Measuring picomolar intracellular exchangeable zinc in PC-12 cells using a ratiometric fluorescence biosensor.* ACS chemical biology, 2006. **1**(2): p. 103.
12. Wolford, J.L., *Zinc localization and quantitation in specialized cells and tissues*. 2006, Northwestern University.
13. Vallee, B.L., *The biochemical basis of zinc physiology.* Physiological reviews, 1993. **73**(1): p. 79.
14. Coleman, J.E., *Zinc Proteins: Enzymes, Storage Proteins, Transcription Factors, and Replication Proteins.* Annual Review of Biochemistry, 1992. **61**(1): p. 897-946.
15. Huntley, S., *A comprehensive catalog of human KRAB-associated zinc finger genes: Insights into the evolutionary history of a large family of transcriptional repressors.* Genome research, 2006. **16**(5): p. 669.
16. Vallee, B.L., J.E. Coleman, and D.S. Auld, *Zinc fingers, zinc clusters, and zinc twists in DNA-binding protein domains.* Proceedings of the National Academy of Sciences of the United States of America, 1991. **88**(3): p. 999-1003.
17. Bogitsh, B.J., *Human Parasitology*. 1998, San Diego: Academic Press.

18. Murphy, G. and E. Oldfield, *Falciparum malaria.* Infectious disease clinics of North America, 1996. **10**(4): p. 747.
19. Sherman, I.W., *Biochemistry of Plasmodium (malarial parasites).* Microbiology and molecular biology reviews, 1979. **43**(4): p. 453.
20. Fujioka, H. and M. Aikawa, *Malaria Parasites and Disease: Structure and Life Cycle.* Chem Immunol, 2002. **80**: p. 1.
21. Aikawa, M., *Variations in structure and function during the life cycle of malarial parasites.* World Health Organization. Bulletin of the World Health Organization, 1977. **55**(2-3): p. 139.
22. Francis, S.E., D.J. Sullivan, and a.D.E. Goldberg, *Hemoglobin metabolism in the malaria parasite Plasmodium falciparum.* Annual Review of Microbiology, 1997. **51**(1): p. 97.
23. Muller, S., *Redox and antioxidant systems of the malaria parasite Plasmodium falciparum.* Molecular microbiology, 2004. **53**(5): p. 1291.
24. Foley, M., *Quinoline antimalarials mechanisms of action and resistance and prospects for new agents.* Pharmacology & therapeutics, 1998. **79**(1): p. 55.
25. Hyde, J., *Mechanisms of resistance of Plasmodium falciparum to antimalarial drugs.* Microbes and infection, 2002. **4**(2): p. 165.
26. Ginsburg, H., R. Gorodetsky, and M. Krugliak, *The status of zinc in malaria (Plasmodium falciparum) infected human red blood cells: stage dependent accumulation, compartmentation and effect of dipicolinate.* Biochimica et Biophysica Acta (BBA) - Molecular Cell Research, 1986. **886**(3): p. 337.
27. Kidd, M.J. 2006, University of Michigan.
28. Wongsrichanalai, C., *In vitro susceptibility of Plasmodium falciparum isolates in Vietnam to artemisinin derivatives and other antimalarials.* Acta Tropica, 1997. **63**(2-3): p. 151.
29. Bowen, I.D., S.M. Bowen, and A.H. Jones, *Mitosis and Apoptosis: Matters of Life and Death*. 1998, New York, NY: BIOS Scientific Publishers.
30. Elmore, S., *Apoptosis: a review of programmed cell death.* Toxicologic pathology, 2007. **35**(4): p. 495.
31. Zhang, A., et al., *Apoptosis-a brief review.* Neuroembryology, 2004. **3**(1): p. 47.
32. Fadeel, B. and S. Orrenius, *Apoptosis: a basic biological phenomenon with wide-ranging implications in human disease.* Journal of internal medicine, 2005. **258**(6): p. 479.
33. Bold, R.J., P.M. Termuhlen, and D.J. McConkey, *Apoptosis, cancer and cancer therapy.* Surgical Oncology, 1997. **6**(3): p. 133.
34. Lee, J.M. and A. Bernstein, *Apoptosis, cancer and the p53 tumour suppressor gene.* Cancer and Metastasis Reviews, 1995. **14**(2): p. 149.
35. Orrenius, S., B. Zhivotovsky, and P. Nicotera, *Regulation of cell death: the calcium–apoptosis link.* Nature Reviews. Molecular Cell Biology, 2003. **4**(7): p. 552.
36. Hessler, J.A., et al., *Atomic force microscopy study of early morphological changes during apoptosis.* Langmuir, 2005. **21**(20): p. 9280.
37. Bortner, C.D., *Uncoupling Cell Shrinkage from Apoptosis Reveals That Na+ Influx Is Required for Volume Loss during Programmed Cell Death*.* The Journal of biological chemistry, 2003. **278**(40): p. 39176.

38. Porcelli, A.M., et al., *Apoptosis induced by staurosporine in ECV304 cells requires cell shrinkage and upregulation of Cl− conductance.* Cell Death and Differentiation, 2004. **11**(6): p. 655.
39. Heimlich, G., *Selective role of intracellular chloride in the regulation of the intrinsic but not extrinsic pathway of apoptosis in Jurkat T-cells.* The Journal of biological chemistry, 2005. **281**(4): p. 2232.
40. Bortner, C.D. and Bortner, *Cell shrinkage and monovalent cation fluxes: role in apoptosis.* Archives of biochemistry and biophysics, 2007. **462**(2): p. 176.
41. Park, I.S., *Potassium efflux during apoptosis.* Journal of biochemistry and molecular biology, 2002. **35**(1): p. 41.
42. Segal, M.S., *Effect of pH, ionic charge, and osmolality on cytochrome c-mediated caspase-3 activity.* American journal of physiology. Cell physiology, 2001. **281**(4): p. 1196.
43. Alberts, B., et al., *Molecular Biology of the Cell*. 2002, London: Garland Science.
44. Nicotera, P. and S. Orrenius, *The role of calcium in apoptosis.* Cell calcium, 1998. **23**(2-3): p. 173.
45. Tanaka, T., *Blockade of calcium influx through L-type calcium channels attenuates mitochondrial injury and apoptosis in hypoxic renal tubular cells.* Journal of the American Society of Nephrology, 2004. **15**(9): p. 2320.
46. Perry, D.K., *Zinc is a potent inhibitor of the apoptotic protease, caspase-3 A novel target for zinc in the inhibition of apoptosis.* The Journal of biological chemistry, 1997. **272**(30): p. 18530.
47. Truong-Tran, A.Q., et al., *The role of zinc in caspase activation and apoptotic cell death.* Biometals, 2001. **14**(3/4): p. 315.
48. Parat, M.O., et al., *Involvement of zinc in intracellular oxidant/antioxidant balance.* Biological Trace Element Research, 1997. **60**(3): p. 187.
49. Zamzami, N., *Mitochondrial control of nuclear apoptosis.* The Journal of experimental medicine, 1996. **183**(4): p. 1533.
50. Penner-Hahn, J.E., *Characterization of "spectroscopically quiet" metals in biology.* Coordination Chemistry Reviews, 2005. **249**(1-2): p. 161.
51. Lipton, A.S., et al., *Solid-State 67Zn NMR Spectroscopic Studies and ab Initio Molecular Orbital Calculations on a Synthetic Analogue of Carbonic Anhydrase.* Journal of the American Chemical Society, 2003. **125**(13): p. 3768.
52. Strange, R.W., M. Ellis, and S.S. Hasnain, *Atomic resolution crystallography and XAFS.* Coordination Chemistry Reviews, 2005. **249**(1-2): p. 197.
53. Kimblin, C., et al., *Bis (mercaptoimidazolyl)(pyrazolyl) hydroborato Complexes of Zinc, Cadmium, and Cobalt: Structural Evidence for the Enhanced Tendency of Zinc in Biological Systems to Adopt Tetrahedral M [S4] Coordination.* Inorganic chemistry, 2000. **39**(19): p. 4240.
54. Penner-Hahn, J.E., *X-ray absorption spectroscopy in coordination chemistry.* Coordination Chemistry Reviews, 1999. **190-192**: p. 1101.
55. Bianconi, A., et al., *Multielectron excitations in the K-edge x-ray-absorption near-edge spectra of V, Cr, and Mn 3d compounds with tetrahedral coordination.* Physical Review B, 1991. **43**(9): p. 6885.
56. Teo, B.K., *EXAFS: Basic Principles and Data Analysis*. 1986, Berlin: Springer-Verlag.

57. Westre, T.E., et al., *A multiplet analysis of Fe K-edge 1s→ 3d pre-edge features of iron complexes.* Journal of the American Chemical Society, 1997. **119**(27): p. 6297.
58. Glaser, T., et al., *Ligand K-Edge X-ray Absorption Spectroscopy: A Direct Probe of Ligand− Metal Covalency.* Accounts of chemical research, 2000. **33**(12): p. 859.
59. Roe, A.L., et al., *X-ray absorption spectroscopy of iron-tyrosinate proteins.* Journal of the American Chemical Society, 1984. **106**(6): p. 1676.
60. Knauth, P. and J. Schoonman, *Nanocomposites: Ionic Conducting Materials and Structural Spectroscopies*. 2007, New York, NY: Springer.
61. Boland, J.J., *Theory of extended x-ray absorption fine structure: Single and multiple scattering formalisms.* The Journal of chemical physics, 1982. **77**(1): p. 142.
62. Bunker, G., S. Hasnain, and D. Sayers, *X-Ray Absorption Fine Structure*. 1991, New York, NY: Ellis Horwood.
63. Clark-Baldwin, K., et al., *The Limitations of X-ray Absorption Spectroscopy for Determining the Structure of Zinc Sites in Proteins. When Is a Tetrathiolate Not a Tetrathiolate?* Journal of the American Chemical Society, 1998. **120**(33): p. 8401.
64. Benfatto, M. and S. Della Longa, *Geometrical fitting of experimental XANES spectra by a full multiple-scattering procedure.* Journal of synchrotron radiation, 2001. **8**(4): p. 1087.
65. Benfatto, M., et al., *MXAN: a new software procedure to perform geometrical fitting of experimental XANES spectra.* Journal of synchrotron radiation, 2001. **8**(2): p. 267.
66. Glatzel, P. and U. Bergmann, *High resolution 1s core hole X-ray spectroscopy in 3d transition metal complexes—electronic and structural information.* Coordination chemistry reviews, 2005. **249**(1-2): p. 65.
67. Hayashi, H., et al., *Selective XANES spectroscopy from RIXS contour maps.* The Journal of Physics and Chemistry of Solids, 2005. **66**(12): p. 2168.
68. Glatzel, P., et al., *Site-selective EXAFS in mixed-valence compounds using high-resolution fluorescence detection: A study of iron in Prussian Blue.* Inorganic chemistry, 2002. **41**(12): p. 3121.
69. Bergmann, U., et al., *High-resolution X-ray spectroscopy of rare events: a different look at local structure and chemistry.* Journal of Synchrotron Radiation, 2001. **8**(2): p. 199.
70. Thompson, A., et al., *X-Ray Data Booklet*, ed. U.o.C. Lawrence Berkeley National Laboratory, Berkeley, CA. 2001.
71. Bergmann, U. and S.P. Cramer. *Proceedings of SPIE: High-resolution large-acceptance analyzer for x-ray fluorescence and Raman spectroscopy*. 1998. San Diego, CA.
72. Born, M. and E. Wolf, *Principles of Optics*. 7th ed. 2005: Cambridge University Press.
73. de Groot, F.M.F. and A. Kotani, *Core Level Spectroscopy of Solids*. 2008, Boca Raton: CRC Press, Taylor & Francis Group.
74. de Groot, F.M.F., *Multiplet effects in X-ray spectroscopy.* Coordination chemistry reviews, 2005. **249**(1/2): p. 31.

75. de Groot, F.M.F., *High-resolution x-ray emission and x-ray absorption spectroscopy.* Chemical Reviews, 2001. **101**(6): p. 1779.
76. Van Grieken, R.E. and A.A. Markowicz, eds. *Handbook of X-Ray Spectrometry*. 2002, Marcel Dekker: New York, NY.
77. Tamura, S., et al., *Development of a multilayer Fresnel zone plate for high-energy synchrotron radiation X-rays by DC sputtering deposition.* Journal of Synchrotron Radiation, 2002. **9**(3): p. 154.
78. Vogt, S., et al., *Imaging Trace Elements in Cells with X-Ray Fluorescence Microscopy.* Microscopy and Microanalysis, 2007. **13**(s02): p. 40.
79. Haugland, R.P., *The Handbook—A Guide to Fluorescent Probes and Labeling Technologies*. 2005, Eugene, OR: Molecular Probes.
80. Auld, D.S., *The ins and outs of biological zinc sites.* Biometals, 2009. **22**(1): p. 141.
81. Vogt, S., *MAPS: a set of software tools for analysis and visualization of 3D X-ray fluorescence data sets.* Journal de Physique IV (Proceedings), 2003. **104**(2): p. 635.

Chapter 2

X-Ray Fluorescence Imaging of Chelator-Treated Erythrocytes Infected with the Malaria Parasite *Plasmodium falciparum*

Introduction

Despite being largely eradicated in North America and Europe, globally malaria still takes an enormous human and economic toll. The disease affects an estimated 300-500 million people worldwide and is the cause of 1-3 million deaths annually [1], mostly in sub-Saharan Africa, but also in South America, India, and Southeast Asia [2, 3]. Infection rates correlate with poverty, as countries with high malaria endemicity also tend to have a lower average GDP per capita and a lower annual rate of increase of GDP per capita [4]. This has led some to postulate that high infection rates exacerbate poverty and vice versa, not only through direct medical costs, but also through the impact of malaria on trade, tourism, schooling, and foreign investment [4].

Malaria is a blood-borne illness caused by protozoan parasites of the genus *Plasmodium*. Four species are known to cause malaria in humans: *Plasmodium falciparum*, *Plasmodium vivax*, *Plasmodium malariae*, and *Plasmodium ovale*. Of these, *Plasmodium falciparum* is the most prevalent and deadly, accounting for 80% of all cases [5] and the majority of deaths [6]. *Plasmodium* has a complex life cycle that requires two hosts—humans and the female *Anopheles* mosquito. The *Plasmodium* life cycle has been reviewed extensively in other sources [5, 7-10], and will be covered briefly here. See Figure 2.1 for a schematic of the overall process. During the mosquito's blood meal,

threadlike sporozoites in the mosquito's saliva enter the bloodstream and invade the liver within one hour, where they develop into trophozoites and feed on the host cytosol for 1-2 weeks. After this time, the trophozoites divide numerous times, producing thousands of merozoites which burst from their host cells and enter the bloodstream. At this point the erythrocytic life cycle begins (Figure 2.2). Host invasion begins when the apical end of the merozoite comes into contact with a red blood cell membrane. The merozoite contains three apical organelles—micronemes, rhoptries, and dense granules—specialized to aid in the invasion process [11]. First, micronemes excrete adhesive proteins that help form a gliding junction between the parasite and host, and the volume contained between the merozoite and host form the beginnings of the parasitophorous vacuole. The rhoptries then expel material that is believed to aid in parasitophorous vacuole development. The host membrane deforms, and the parasite is internalized. Finally, the dense granules expel their contents into the parasitophorous vacuole. The function of this last step is unclear, but seems to involve modifications to the parasitophorous vacuole membrane [12]. At this point, the parasite has been completely internalized and enters a period of relative dormancy called the ring stage.

Twenty-four hours after a *P. falciparum* merozoite invades an erythrocyte host, the parasite enters a metabolically active stage called the trophozoite stage. During this stage, the parasite feeds on the host cytoplasm, using hemoglobin as its primary source of amino acids. Approximately 60-80% of the host cell hemoglobin is degraded in this fashion [13]. Of key importance is detoxifying the heme released in this process, which can react with O_2 to generate superoxide anions which lead to the formation of hydrogen peroxide and hydroxyl radicals [14]. The parasite accomplishes this by crystallizing the

released heme into a nontoxic hemozoin crystal within its food vacuole [13]. During this time, the parasite also makes extensive modifications to the parasitiphorous vacuole and host membranes. The parasite builds a tubovesicular membrane network that connects the parasitophorous vacuole and host membrane and aids in importing essential nutrients not present in sufficient amounts within the host [15]. For example, the amino acids methionine, cysteine, glutamine, glutamic acid, and isoleucine are poorly represented or absent within the red blood cell and must be imported from the serum [13].

The trophozoite stage lasts twelve hours in the *P. falciparum* life cycle. Eventually, the parasite enters the schizont stage, where it divides 4-5 times, producing 16-32 daughter merozoites. Forty-eight hours post-invasion, these daughter merozoites rupture their host cell and invade new erythrocytes within 30 minutes [16], where the cycle continues for the majority of merozoites. A fraction of these will differentiate into male and female gametocytes [5, 10], and enter the sexual phase of their life cycle when they are taken into an uninfected *Anopheles* mosquito that takes a blood meal from an infected human. Invasion and rupture cycles are highly synchronized within the human host, thought to be timed by circadian melatonin secretion and hypothesized to aid the parasite in evading the host's immune system [17]. This feature is common to all *Plasmodium* strains.

Symptoms of malaria present themselves during the erythrocytic cycle and are flu-like in nature, including chills, fever, nausea, vomiting and headache [5]. Complications that lead to death almost always have their roots in severe lactic acidosis caused by insufficient oxygen delivery to tissues [8]. In *P. falciparum* infection, hypoxia is not only due to destruction of red blood cells and hemoglobin, but also to obstruction

of capillaries due to adhesion of infected erythrocytes to the capillary walls [8]. This capillary obstruction is thought to contribute to cerebral malaria, a condition that results in coma and leaves only a 50% chance of survival even with optimal care [18, 19].

Some of the earliest and most successful treatments for malaria were the quinoline-based antimalarials such as quinine and chloroquine. The mechanism of action is somewhat unclear, but these are believed to accumulate in the parasite's food vacuole and interfere with hemozoin crystallization [19, 20]. While these have enjoyed widespread use for many decades, chloroquine-resistant *Plasmodium* strains have emerged that have rendered them largely ineffective in many regions. A second line of drugs meant to interfere with the parasite's folate biosynthesis have been adopted as a first line of defense in many countries; however, resistance to these emerged soon after deployment [20, 21]. Thus, there is a need for alternative effective, cheaply available therapies.

One such strategy is to interfere with the *Plasmodium* metal ion homeostasis through the use of chelators. Cells need a certain base concentration of iron, copper, and zinc to survive [22], and metal levels are tightly regulated within the cell [23, 24]. Furthermore, metal ion deficiencies are known to be harmful to organisms. Therefore, this approach is expected to be effective in treating *P. falciparum*. Chelating the extracellular zinc is expected to be particularly effective, given the parasite's known propensity for accumulating zinc [22, 25, 26]. In this regard, zinc chelation therapy would be somewhat analogous to the use of iron chelators to treat *Legionella pneumophila*, the causative agent of Legionnaire's disease [27].

Zinc accumulation by *P. falciparum* was first noted in 1986 by Ginsburg and co-

workers, who found a 2.3-fold increase in total zinc in infected red blood cells as the parasite matures to schizont stage [26]. The reason for this zinc increase was unclear, but the excess zinc was postulated to be associated partially with the parasite and host membranes, and partially to be incorporated into the parasite's DNA and RNA polymerase. A recent collaboration between the Penner-Hahn and O'Halloran labs confirmed a zinc increase in infected red blood cells, measuring a 3-fold increase in red blood cells infected with mature schizont-stage parasites compared to uninfected red blood cell zinc levels [22, 25]. That same study also found increases in free zinc, as measured by the fluorophore Zinbo-5, that began during the trophozoite stage approximately 24 hours post-infection and that appeared to be located within the daughter parasites, but excluded from the nuclei. Although the mechanism of zinc uptake is unknown, a database search revealed the presence of homologues to both the cation diffusion facilitator (CDF) and ZIP zinc transporters [22]. These are postulated to be expressed during the trophozoite stage as the parasite modifies the host membrane.

While the role of this excess and free zinc has yet to be established, the O'Halloran group has found that the addition of certain zinc chelators to the culture medium is effective at reducing parasitemia—the percentage of infected red blood cells within the culture—after 48 hours of treatment. Figure 2.3 shows a plot of the chelator IC_{50}, the concentration at which parasitemia decreases by 50%, as a function of the zinc-chelator dissociation constant. For the membrane-permeable chelators, there is a negative correlation between IC_{50} and zinc binding affinity—the stronger the chelator, the lower the concentration that is sufficient to inhibit parasite growth. On the other hand, the membrane-impermeable chelators proved less effective. Of special note here is the

relative efficacy of the high-affinity chelators EDTA and TPEN. These two have similar zinc binding affinities at physiological pH—the Zn-TPEN complex has a K_d of $10^{-16.2}$ at pH 7.4, while the corresponding Zn-EDTA dissociation constant is $10^{-15.3}$. However, the TPEN IC_{50} is dramatically lower than that for EDTA. The IC_{50} for TPEN (0.5 μM) is approximately 700-fold smaller than the IC_{50} initially reported for EDTA (345μM). Subsequent measurements have shown that the IC_{50} for EDTA is even larger (8 mM), thus making the TPEN:EDTA IC_{50} ratio even smaller. Under the latest IC_{50} measurements, the original EDTA IC_{50} of 347 μM produced no measurable decrease in parasitemia (Becky Marvin and Tom O'Halloran, Northwestern University, personal communication).

This difference in IC_{50} is especially striking when one considers the maximum concentration of hydrated free zinc that ought to be present in the media at each treatment condition. In the above study, the concentration of total zinc in the media was found to be 1.0 ± 0.1 μM by ICP-MS, so in the presence of 0.5 μM TPEN, the maximum free zinc levels will be approximately 0.5 μM. In the presence of 347 μM EDTA, this number drops to 1.4 attomolar. If both chelators functioned through a method of general zinc starvation, a much lower EDTA concentration (0.5 μM) ought to be sufficient to decrease parasitemia by 50%. On the other hand, it may be that the ability of TPEN to cross cell membranes is the significant factor, and would suggest that EDTA and TPEN are functioning through separate mechanisms, though the nature of these mechanisms is unknown.

To address this issue, we employed X-ray fluorescence imaging to study red blood cells infected with *P. falciparum* in the presence of EDTA and TPEN. XRF

imaging not only allows determination of average cellular zinc contents in the overall culture, but also allows measurement of the composition of the food vacuole. This measurement should provide a clue as to how *Plasmodium* copes with metal starvation.

Materials and Methods

Sample Preparation

Slides for X-ray fluorescence imaging were prepared by Becky Marvin at the O'Halloran Lab at Northwestern University. The 3D7 strain of *Plasmodium falciparum* was cultured in 10% human serum in RPMI-1640 according to literature methods [28]. Cultures were synchronized with 5% sorbitol, transferred to fresh culture media to 1.5% parasitemia, and grown at 37^{o}C for 48 hours, either untreated or in the presence of 0.5 μM TPEN (Sigma-Aldrich) or 347 μM EDTA (Sigma-Aldrich). After 48 hours, schizonts were isolated using a 60% Percoll gradient. Infected cells were pelleted and washed in PBS, then re-suspended in PBS at 5% hematocrit—the fraction of the total sample volume occupied by red blood cells. A 2 μL volume of suspended cells was spotted onto 200-nm thick silicon nitride windows obtained from Structure Probe, Inc (West Chester, PA). After allowing the cells to settle, slides were frozen by submerging in liquid nitrogen for 20 seconds. Samples were dehydrated by submerging in liquid acetone just above its freezing point for 20 seconds and air drying.

X-Ray Fluorescence (XRF) Imaging

X-ray fluorescence imaging was performed at Sector 2-ID-E at the Advanced Photon Source at Argonne, IL. A Leica DMXRE optical microscope was used to locate

appropriate cells for imaging (Leica Microsystems, Wetzlar, Germany). Undulator-derived X-rays were monochromatized to 10 keV incident energy using a single-bounce Si(111) monochromator and focused to a spot size of 0.5 μm horizontal by 0.3 μm vertical using Fresnel zone plate optics (X-radia, Concord, CT). Samples were raster-scanned through the X-ray beam using 0.5 μm horizontal and 0.3 μm vertical steps. Fluorescence spectra were collected for one second per pixel using a single-element Ge detector (Canberra Industries, Meriden, CT).

Data Analysis

Quantitation and image processing were performed using MAPS software [29]. Normalized fluorescence intensities for each element at each pixel were converted to a two-dimensional concentration in micrograms per square centimeter by fitting spectra against the spectra obtained from the NIST thin-film standards NBS-1832 and NBS-1833 (National Institute of Standards and Technology, Gaithersberg, MD). Iron and zinc levels were quantified by defining a region of interest (ROI) around an infected cell and another around a section of the background. The average concentrations in $\mu g/cm^2$ were calculated for both the cell and background ROIs. The average background concentration was subtracted from the average cell concentration, and the total elemental contents of each cell were calculated by multiplying the background-subtracted two-dimensional concentrations by the cell ROI area. The composition of the food vacuole was determined by defining an ROI around the hemozoin crystal, calculating the average concentration in $\mu g/cm^2$, subtracting the background concentration, and multiplying by the hemozoin crystal ROI area.

The presence of outliers was detected by examining a box plot for each data set. Points that lay more than three times the interquartile range (IQR) above the third quartile or more than three times the IQR below the first quartile were rejected as extreme outliers [30]. No more than one point per data set was rejected in this manner. Statistical analysis was performed using the Mann-Whitney *U* test [31]. Differences were taken to be significant if $p < 0.05$.

Results

Sample XRF images and their corresponding visual light microscope images for the untreated control, TPEN-treated, and EDTA-treated samples are shown in Figures 2.4, 2.5, and 2.6, respectively. Sample sizes were 14, 28, and 12 cells, respectively, so Figures 2.4 through 2.6 represent approximately one fifth of the imaged cells. The hemozoin crystal is clearly seen as an opaque spot in the visual light microscope images, and this correlates with the bright spot in the iron maps. No obvious systematic differences in overall cell and hemozoin crystal morphology were noted between the different sample conditions.

Zinc totals for the individual infected red blood cells are depicted in Figure 2.7. The average total zinc for untreated, TPEN-treated, and EDTA-treated samples was 4.4 ± 0.9 fg ($n = 14$), 1.28 ± 0.09 fg ($n = 27$), and 1.3 ± 0.1 fg ($n = 11$), respectively, where the intervals represent one standard error of the mean. Also provided for the sake of comparison are the zinc totals for individual uninfected red blood cells, obtained from [25], where the average zinc contents were determined to be 1.31 ± 0.05 fg ($n = 27$). The Mann-Whitney *U* test revealed no significant differences between the uninfected, EDTA-

treated and TPEN-treated samples, while the untreated schizont-stage infected sample zinc totals were significantly higher than the other sample conditions ($p < 0.01$).

Iron totals for the individual red blood cells are depicted in Figure 2.8. The average iron totals for the untreated schizont, TPEN-treated schizont and EDTA-treated schizont were 91 ± 5 fg (n = 14), 99 ± 6 fg (n = 27), and 128 ± 9 fg (n = 12), respectively. The average iron contents of an uninfected red blood cell was 70 ± 2 fg (n = 27), taken from [25]. The EDTA-treated sample had significantly higher iron on average ($p < 0.05$) in all cases. There were no significant differences between the TPEN-treated and untreated schizont average iron totals, but both were significantly higher than the uninfected sample iron totals ($p < 0.01$), as judged by the Mann-Whitney *U* test.

Phosphorous totals for the individual red blood cells are shown in Figure 2.9. The average phosphorous totals for the untreated schizont, TPEN-treated schizont and EDTA-treated schizont were 230 ± 10 fg (n = 14), 200 ± 30 fg (n = 27), and 190 ± 20 fg (n = 12), respectively. The Mann-Whitney *U* test indicated no significant differences between the average phosphorous contents of the EDTA-treated and TPEN-treated samples. The phosphorous totals for the chelator-treated samples were not found to be significantly lower than in the untreated schizont sample.

The approximate percentage of the total iron that is present in the hemozoin crystal can be calculated for each cell by dividing the hemozoin crystal iron content by the total cellular iron content. The result is shown in Figure 2.10. Average percentages for untreated schizont, TPEN-treated schizont and EDTA-treated schizont samples were 72 ± 2% (n = 13), 86 ± 1% (n = 27), and 87 ± 2% (n = 12), respectively. The TPEN-treated and EDTA-treated schizont samples were not found to be significantly different,

while the percentage of the total iron present in the food vacuole in the untreated schizont sample was significantly lower than in the other two conditions ($p < 0.01$). The percentage of total zinc in the food vacuole can also be determined in this way, and the result is shown in Figure 2.11. The average food vacuole zinc percentages were 15 ± 1% ($n = 14$) for the untreated schizont sample, 26 ± 2% ($n = 28$) for the TPEN-treated sample, and 21 ± 2% ($n = 12$) for the EDTA-treated sample. The TPEN-treated sample and EDTA-treated sample were not found to be significantly different, while both were significantly higher than the untreated sample ($p < 0.05$).

The ratio of femtograms zinc to femtograms iron within the food vacuole was calculated for individual cells for each treatment condition, and the results are shown in Figure 2.12. Average weight ratios were determined to be 0.011 ± 0.002 ($n = 14$) for untreated schizont-stage infected red blood cells, 0.0040 ± 0.0002 ($n = 27$) for TPEN-treated samples, and 0.0028 ± 0.0004 ($n = 12$) for EDTA-treated samples. Whole-cell Zn/Fe weight ratios from uninfected cells are also provided for the sake of comparison. These were found to have a Zn/Fe weight ratio of 0.0190 ± 0.0006 ($n = 27$). Food vacuoles from the EDTA-treated sample were found to have a Zn/Fe ratio significantly lower than the hemozoin Zn/Fe ratio in the TPEN-treated samples ($p < 0.05$), while the Zn/Fe ratio in the TPEN-treated sample was significantly lower than in the untreated sample ($p < 0.01$). The food vacuoles from all three samples had a Zn/Fe ratio significantly lower than that of the overall Zn/Fe ratio in intact, uninfected red blood cells ($p < 0.01$).

Discussion

As reported above, untreated schizont-stage infected red blood cells are able to take up zinc from the media, with the total zinc increasing from ~1.3 fg per cell to ~4.4 fg per cell. A typical malaria culture is 5% hematocrit and is maintained at infection levels of approximately 5% parasitemia, so for every 1 L of total culture, 0.0025 L represents infected red blood cells. Since the median red blood cell volume is approximately 88.9 ± 0.5 fL [32], this translates to approximately (2.81 ± 0.02) x 10^{10} infected red blood cells per culture. On the other hand, 1.0 ± 0.1 μM total zinc in a 1 L culture translates to approximately (6.6 ± 0.7) x 10^{10} fg total extracellular zinc, or a ratio of 2.4 ± 0.2 fg zinc available for each infected red blood cell, which is within the range of increase found in this study (3.1 ± 0.9 fg zinc per cell).

Both 347 μM EDTA and 0.5 μM TPEN were found to prevent zinc uptake in schizont-stage infected red blood cells, decreasing the metal loading after 48 hours of incubation from 4.4 fg per cell to approximately 1.3 fg per cell, the same zinc levels reported previously in uninfected red blood cells [25, 26]. That 347 μM EDTA can accomplish this comes as no surprise. Since the concentration of total zinc in the media was measured to be 1.0 μM by ICP-MS and since the dissociation constant for the Zn-EDTA complex is approximately $10^{-15.3}$, 347 μM EDTA would result in attomolar levels of free zinc in the media. On the other hand, the ability of 0.5 μM TPEN to prevent zinc uptake is not intuitively obvious, since 0.5 μM TPEN should be able to sequester at most half the available zinc.

One potential explanation for this is that even though the total zinc in the media may be 1.0 μM, the amount of zinc available for uptake may be significantly less due to

interactions with other components in the media. The media contains 10% human serum. One component of this serum is human serum albumin (HSA), a plasma protein that is present at levels of approximately 43 g/L in the human bloodstream, or 640 μM [33], which would translate to 64 μM in the growth media used in this study. HSA has two zinc-binding sites, with dissociation constants of 0.84 μM and 2 μM at 37°C and pH 7.3 [34]. Considering only the relatively high-affinity site, a solution with 1.0 μM total zinc and 64 μM total HSA would have expected free zinc levels of approximately 13 nanomolar. However, it appears that under normal conditions the off rate of the Zn-HSA interaction is rapid enough that infected red blood cells are able to sequester almost all of the zinc in the culture media as they mature over 48 hours, as evidenced by the fact that the untreated schizont-stage infected red blood cells appear to take up all of the media zinc.

Another possibility is that exposure to 0.5 μM TPEN suppresses expression of some of the parasite's zinc transporters, either as a result of TPEN-induced damage or as a result of the parasite's specific feedback mechanisms. Normally, one would expect increased expression of zinc importers as a result of zinc depletion through TPEN exposure; however, there seems to be some variability as to what transporters are up-regulated or down-regulated. Cousins and co-workers observed a 27-fold increase in expression of the zinc importer Zip-2 in human macrophage THP-1 cells in response to exposure to 10 μM TPEN [35]. The same authors also noted a ~75% decrease in expression of the zinc importer Zip-1 for the same cell line and treatment condition [36]. In contrast, Rezaei and co-workers noted a 2-fold decrease in Zip-2 expression when cultured human retinal pigment epithelial cells were treated with 2-4 μM TPEN [37].

However, much is still unknown about metal transport within *P. falciparum*, so it is difficult to say whether or not this sort of phenomenon is relevant in this case.

A third possibility is that the TPEN-induced decrease in zinc uptake is an indirect consequence of TPEN exposure, and is not caused directly by zinc chelation. This would be consistent with the observation that 0.5 μM TPEN is sufficient to decrease parasitemia by half. This would also be consistent with reports that both TPEN and Zn-TPEN are able to induce apoptosis in PC-12 cells, which suggests that TPEN toxicity may not be exclusively due to its ability to chelate zinc [38]. It is possible that the decreased *Plasmodium* viability is the cause rather than the consequence of decreased zinc uptake. This would explain the observation that EDTA-treated cells, while similarly zinc depleted, show no decrease in viability.

Notable increases in total iron were apparent in comparing uninfected red blood cells to the untreated schizont-stage infected and TPEN-treated schizont-stage infected samples, and in comparing the untreated schizont stage infected and TPEN-treated schizont-stage infected samples to the EDTA-treated schizont-stage infected sample. However, the biological relevance of these increases is difficult to establish. Comparing the previous XRF studies on the average zinc and iron levels in malaria-infected red blood cells, although the average zinc contents in uninfected red blood cells were relatively consistent—1.28 ± 0.03 fg per cell reported by Ginsburg *et al*, compared to 1.31 ± 0.05 fg per cell reported by Kidd and Wolford—the average iron contents of the same varied considerably—97 ± 3 fg per cell reported by Ginsburg *et al*, compared to 70 ± 2 fg per cell reported by Kidd and Wolford [22, 25, 26]. Both studies reported small but statistically significant increases in iron contents upon infection—from 93.4 fg per cell to

96.7 fg per cell reported by Ginsburg, and from 70 fg per cell to 78 fg per cell as reported by Kidd and Wolford [22, 25, 26]. Since malarial parasites apparently lack heme oxygenase [39], it may be that they have to import some non-heme iron to meet their iron requirements. However, the apparent increases in Figure 2.8—20-30 fg per cell—seem too large to be reasonable, since the iron levels in RPMI 1640 with 10% human serum are approximately 1 μM, similar to the media zinc concentration (Becky Marvin and Tom O'Halloran, Northwestern University, personal communication). Even if all of the media iron were transported into infected red blood cells, this would translate to an increase of approximately 2 fg per cell, similar to the observed zinc increases. Given the variability in the previously reported results and the only modest increases in total iron upon infection, it seems more likely that the differences in iron seen in Figure 2.8 are simply due to different iron loadings in different blood samples. Whole-blood hemoglobin levels can vary based on age, race, and gender [40, 41]. While the average whole-blood hemoglobin levels have been measured to be 14 ± 1 g per 100 mL in males and 13 ± 1 g per 100 mL in females, individual whole-blood hemoglobin measurements ranged between 8.1-18.0 g per 100 mL of blood in males, and 7.4-17.0 g per 100 mL of blood in females [41].

Whole-cell phosphorous totals were not significantly different in TPEN- and EDTA-treated samples compared to the untreated controls. In organisms, phosphorous is present mostly in DNA, RNA, and in phospholipids. In *P. falciparum,* phosphorous content can be taken as an indicator for growth activity, not only due to the fact that the parasite divides 4-5 times as it matures to schizont stage, but also due to increased phospholipid content as it builds the tubovesicular membrane network during the

trophozoite stage. Since zinc is required for both cell division and differentiation [42] and for certain phospholipid synthesis pathways [43], one might expect total phosphorous to decrease along with zinc. Interestingly, this does not appear to be the case.

Untreated, schizont-stage infected red blood cells were found to sequester roughly 70% of the total iron into the food vacuole. Since most of the iron in the infected cell will come from hemoglobin, this is consistent with literature reports of 60-80% of the total hemoglobin being consumed by the end of the schizont stage [13]. A significantly higher percentage of the total iron ends up in the food vacuole under zinc-starved conditions, increasing from 70% to close to 85% (Figure 2.10). If one assumes that the hemoglobin is more or less homogeneously distributed throughout the uninfected red blood cell, consuming 85% of the hemoglobin would correlate to consuming 85% of the host cytosol. It is possible that the increased cytosol digestion may represent an effort on the part of the parasite to compensate for the loss of extracellular zinc. If so, this would imply that the parasite must be able to use zinc stores that are liberated by cytosol digestion.

The hemozoin Zn/Fe weight ratios shown in Figure 2.12 are consistent with the hypothesis that the parasite makes increasing use of the host zinc stores as extracellular zinc is depleted via chelators. In the original paper by Ginsburg *et al*, hemozoin crystals were collected by sub-cellular fractionation, and the Zn/Fe weight ratio was determined to be 1.11×10^{-2}. This was found to be similar to the Zn/Fe weight ratio in intact, uninfected red blood cells—namely, 1.23×10^{-2}—and the conclusion drawn from this was that the parasite was using little if any of the host zinc stores, preferring to import zinc from the serum [26]. The values determined in this study for the untreated schizont-stage sample roughly confirms Ginsburg's earlier observation, with a Zn/Fe weight ratio

of $(1.1 \pm 0.2) \times 10^{-2}$ on average. On the other hand, the food vacuole Zn/Fe weight ratios for the chelator-treated samples were significantly lower—$(4.0 \pm 0.2) \times 10^{-3}$ and $(2.8 \pm 0.4) \times 10^{-3}$ TPEN-treated and EDTA-treated samples, respectively.

The decrease in the food vacuole Zn/Fe ratio following chelator treatment could result either from a decrease in zinc or an increase in iron. It is likely that the observed decrease in hemozoin Zn/Fe ratios represents a decrease in zinc and not an increase in iron loading. Figure 2.10 indicates that for the untreated sample approximately 72% of the host hemoglobin has been processed and converted into nontoxic hemozoin. Assuming that the majority of host hemoglobin and zinc metalloenzymes were well-mixed throughout the red blood cell cytosol to begin with, the fact that 72% of the host hemoglobin has been processed means that roughly 72% of the host zinc has also undergone some sort of processing. Assume for the time being that all of the host zinc ends up in the food vacuole along with the hemozoin crystal, and that none of it is redistributed for the parasite's use. If an uninfected red blood cell contains 1.3 fg zinc on average, 0.94 fg would end up in the food vacuole. Since in this experiment, the average schizont-stage red blood cell has imported enough zinc to raise the total to 4.4 fg, one would expect on average approximately 21% of the total zinc to reside in the hemozoin crystal area. Artifacts due to parasite or host zinc pools overlapping above or below the food vacuole could raise this apparent percentage slightly, but the only way to lower this percentage would be a net removal of zinc from the food vacuole. In fact, the average zinc contents of the food vacuole in the untreated schizont-stage case was determined to be 15% (Figure 2.11), which would correspond to the parasite making use of approximately 30% of the host's zinc pool even when extracellular zinc is available. The

effect is even more pronounced in the chelator-treated cases. In those cases, approximately 85% of the host hemoglobin has been processed, and if all of the host zinc were also being stored in the food vacuole, the hemozoin crystal area should contain approximately 85% of the total zinc, since there is no net increase in total zinc in the chelator treated cases compared to the uninfected red blood cells. On the contrary, in both cases the food vacuole contains approximately 25% of the total zinc (Figure 2.12), which translates into the parasite making use of approximately 70% of the host's zinc stores, or 0.92 fg. The XRF images of the chelator-treated samples confirm this (Figures 2.5 and 2.6), since if the bulk of the host zinc were being stored in the food vacuole, one would expect the zinc to co-localize with the hemozoin crystal. In fact, it tends to be distributed uniformly throughout the sample, suggesting that the parasite can process the host zinc, at least under certain treatment conditions.

To summarize, both EDTA and TPEN were found to prevent zinc uptake in red blood cells infected with *P. falciparum*. The parasite seems to cope with this zinc starvation through two mechanisms. First, it consumes a greater percentage of the host cytosol, presumably in order to obtain metal ions from the host cell that it cannot obtain extracellularly. Secondly, the parasite transports a greater percentage of the host zinc out of the food vacuole. Since 0.5 μM TPEN should be able to sequester at most 50% of the available extracellular zinc, and since the parasite apparently sequesters close to 100% of the extracellular zinc if given the opportunity, it is unclear why 0.5 μM TPEN should be equally effective as 347 μM EDTA at preventing zinc uptake, given their similar binding affinities for zinc. If the mode of action for both were through binding extracellular zinc, it should take either a lot more TPEN or a lot less EDTA to damage the parasite than is

actually needed.

The data in Figure 2.3 suggest that the ability of TPEN to cross cell membranes may be important. It is possible that only a fraction of the parasite's zinc pool is critically important to its survival, and that it is this zinc that is chelated by TPEN (and not by EDTA). In this model, TPEN could function by interfering with the distribution of the zinc that the parasite extracts from the red blood cell cytosol. If this interference decreases the viability of the parasite, it could be responsible for the lack of zinc uptake, since under these conditions the parasite would be unable to synthesize the necessary zinc transporters to import the extracellular zinc.

There is much about the *P. falciparum* metal homeostasis that is still unknown, and more work is needed to identify the malarial zinc transporters and what conditions regulate their expression. In addition, it would be worthwhile investigating why the parasite imports extracellular zinc if, as shown by the EDTA treatment, it can apparently receive its zinc quota from the host cell itself. In an average untreated schizont-stage infected cell, the parasite receives approximately 0.4 fg zinc from the host cell, and 3.1 fg from the extracellular environment, or an increase of approximately 3.5 fg per parasite. In contrast, chelator treated schizonts receive 0.9 fg zinc from the host on average and none from the extracellular environment. If the parasite is able to survive off of the 0.9 fg zinc it receives from the host, one wonders what use it has for the additional 2.6 fg, since it certainly is not being shuttled to the food vacuole for storage, as is postulated to occur for other unneeded heavy metals in *P. falciparum* [44]. Some knowledge of not only the contents and localization, but the speciation of the zinc within the sample under the different treatment conditions would be desirable, and that will be the aim of Chapter 3.

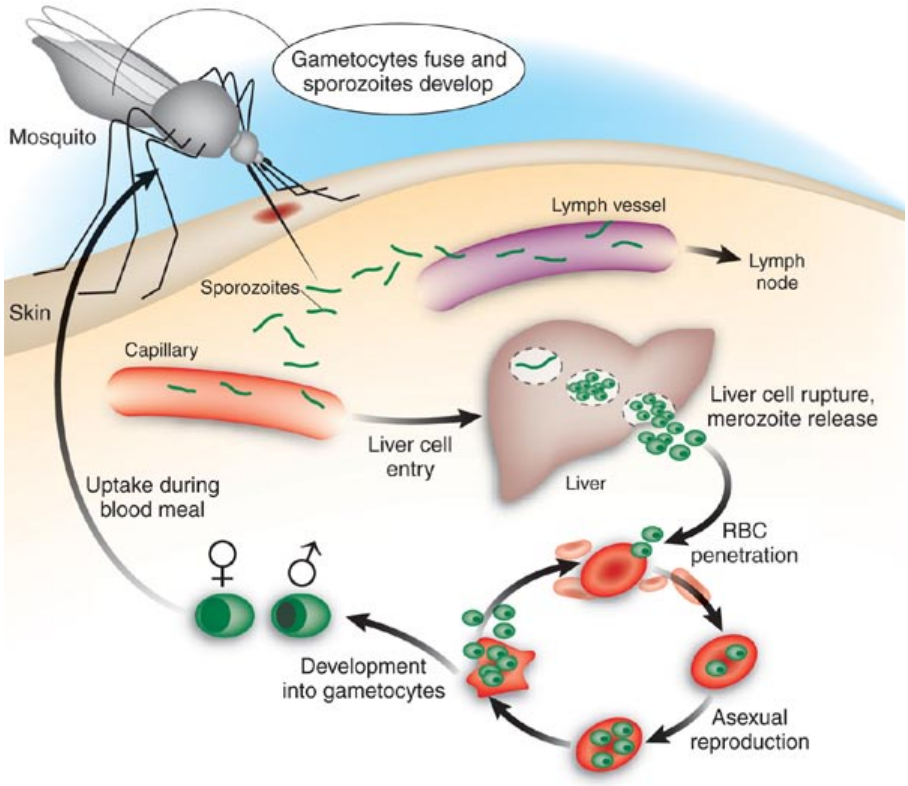

Figure 2.1: Schematic of the *Plasmodium* life cycle. Reprinted by permission from Macmillan Publishers Ltd: *Nature* [45], copyright 2006.

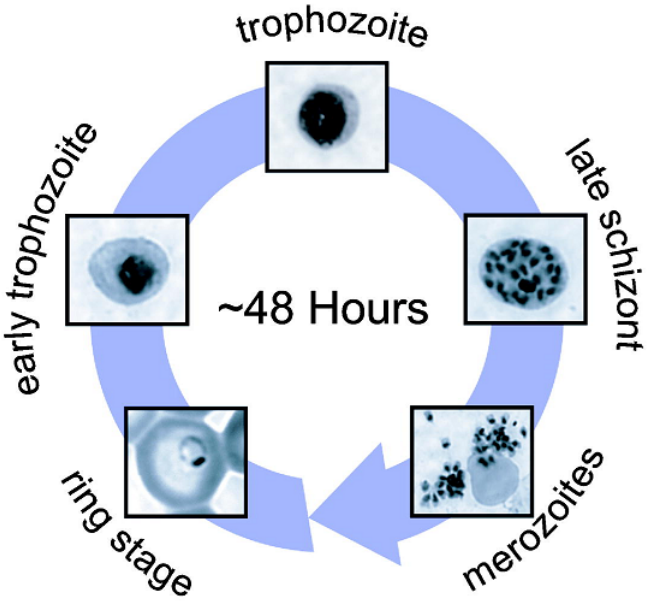

Figure 2.2: Schematic of erythrocytic stage. Taken from *PLoS Biology* [46], whose content is published under the Creative Commons "by attribution" license.

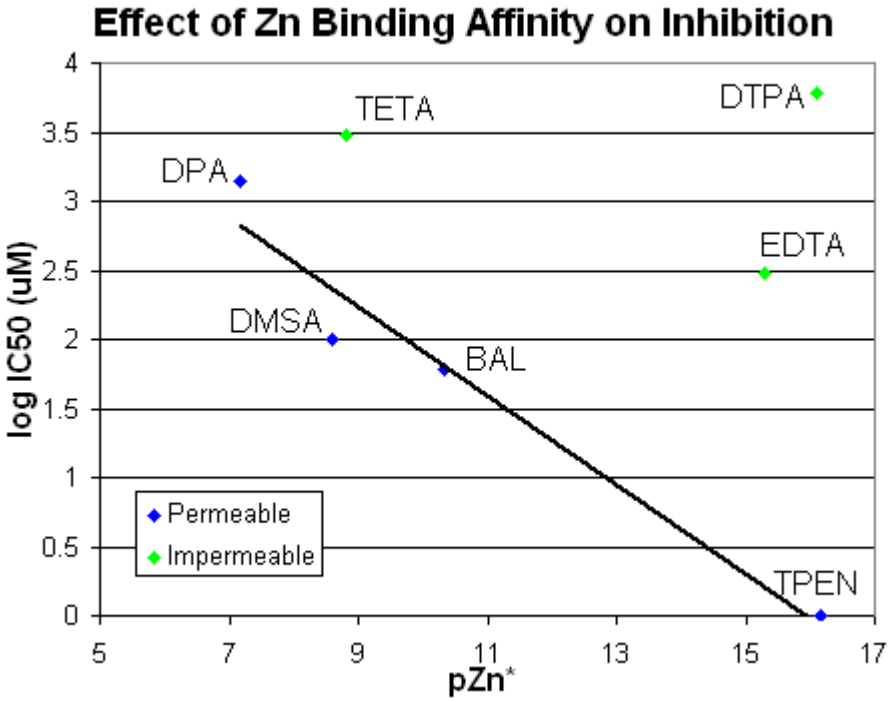

Figure 2.3: IC_{50} of various zinc chelators as a function of zinc binding affinity. Image provided by Becky Marvin, Northwestern University.

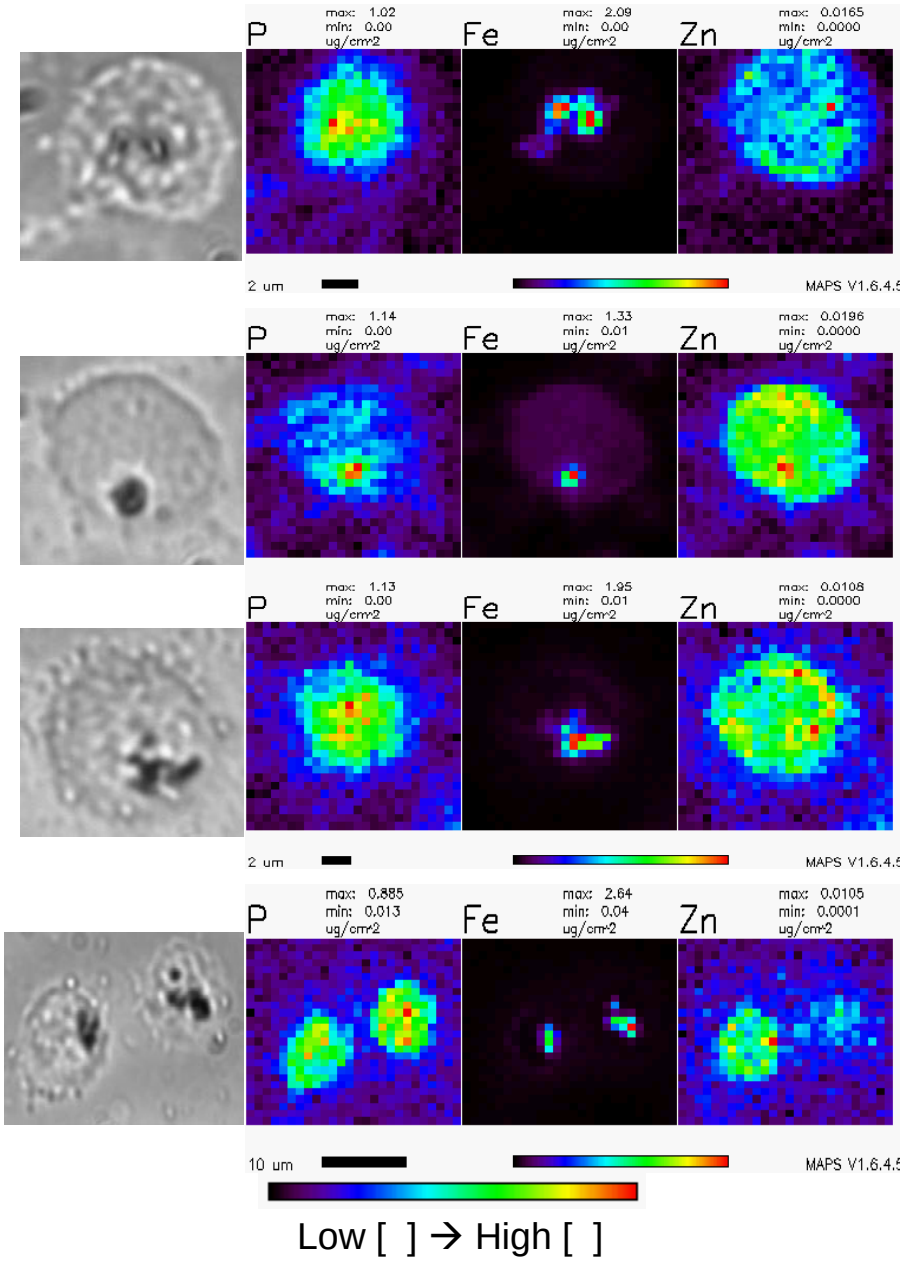

Figure 2.4: XRF images of untreated schizont-stage infected red blood cells.

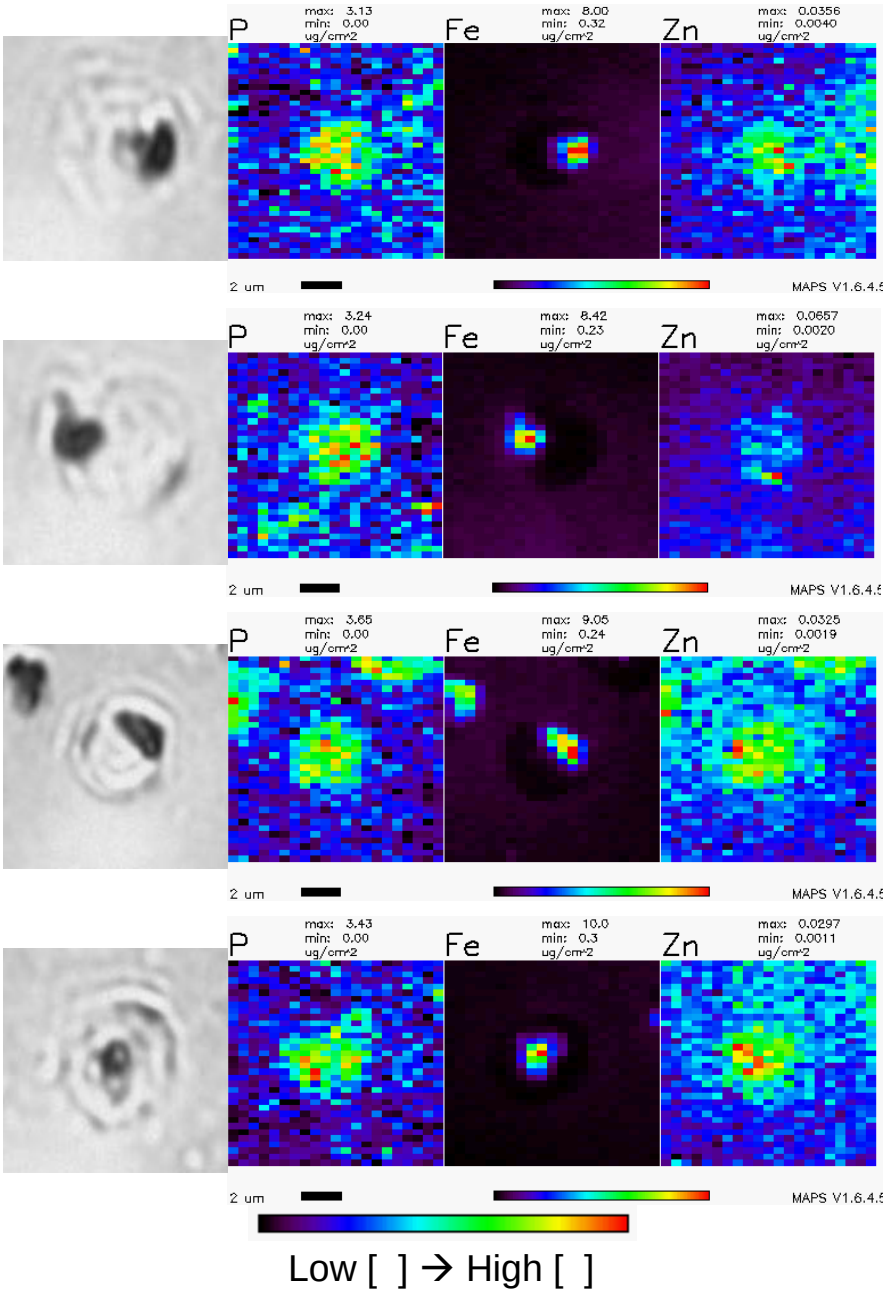

Figure 2.5: XRF images of schizont-stage infected red blood cells grown in 0.5 μM TPEN.

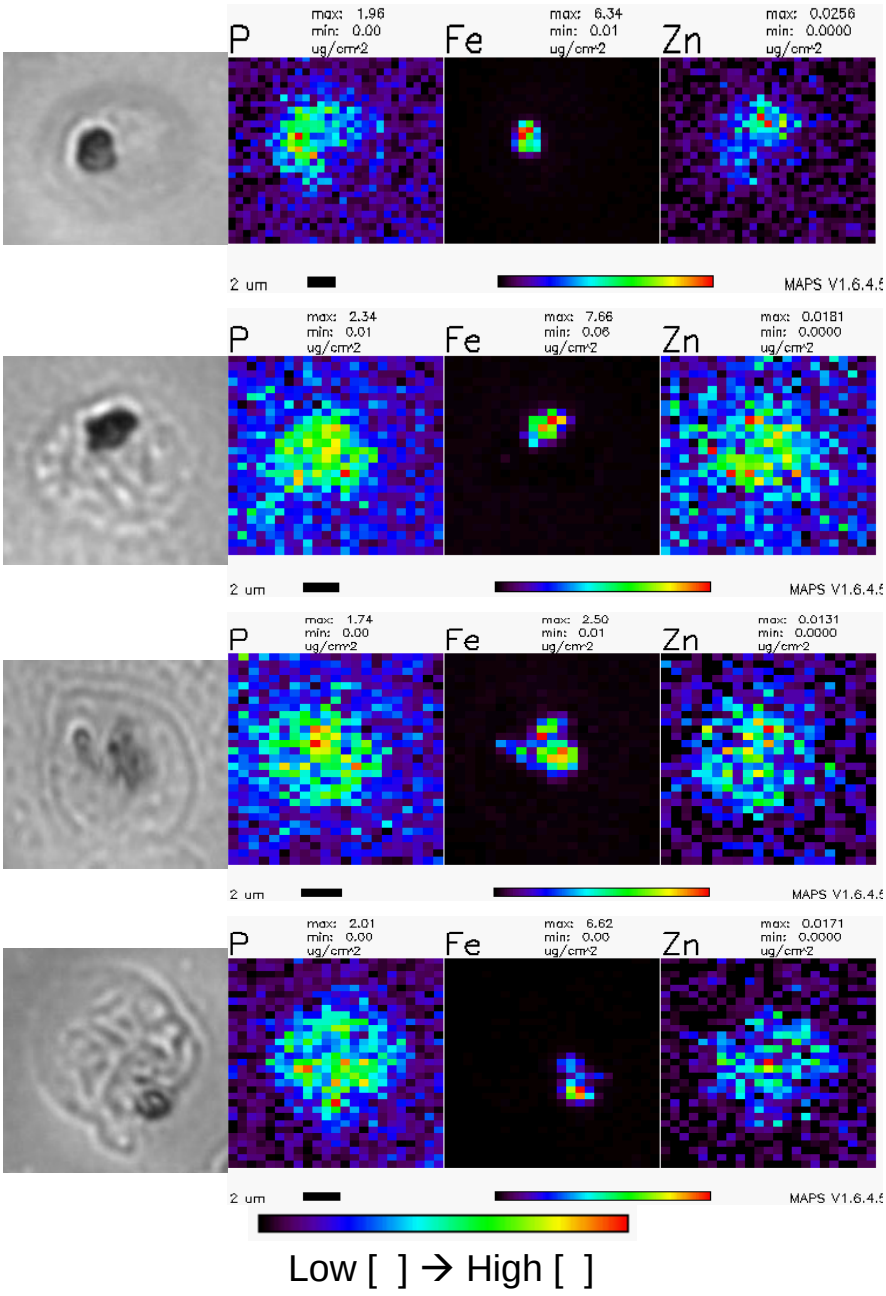

Figure 2.6: XRF images of schizont-stage infected red blood cells grown in 347 μM EDTA.

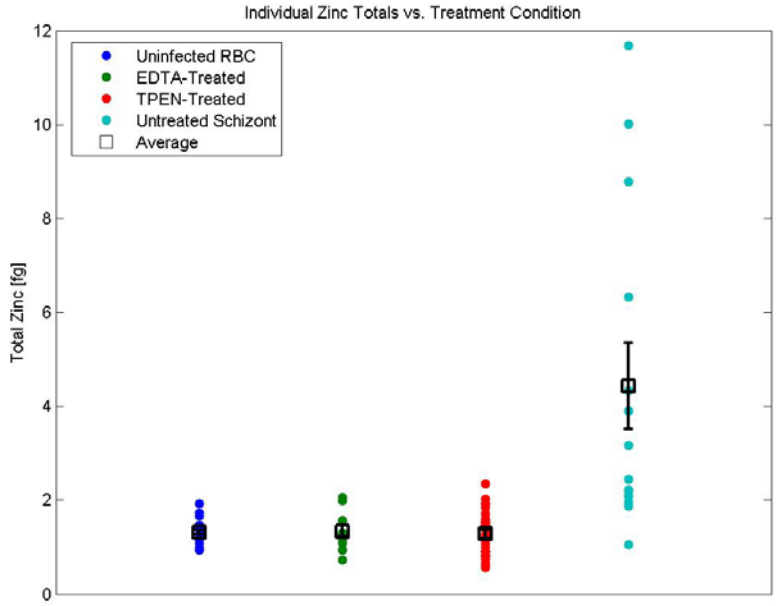

Figure 2.7: Individual zinc totals for each treatment condition. The error bars represent one standard error of the mean. Individual values for the uninfected sample were taken from [25].

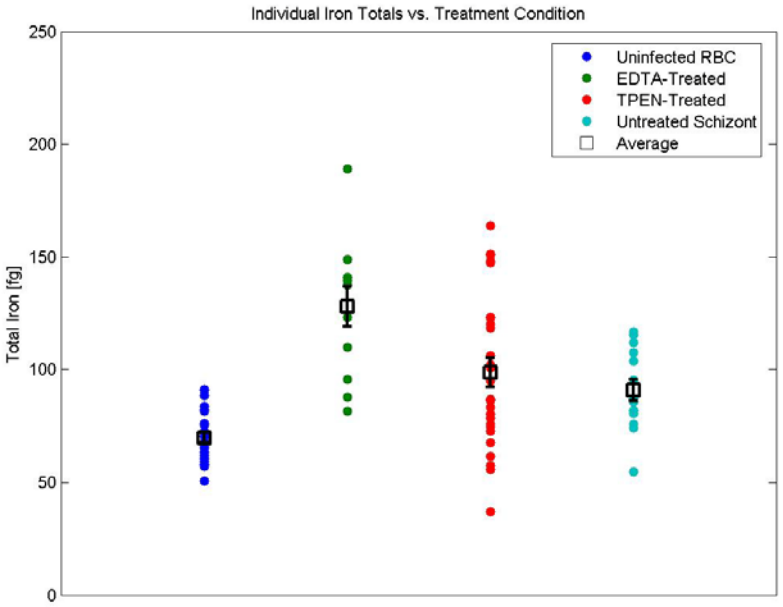

Figure 2.8: Individual iron totals for each treatment condition. The error bars represent one standard error of the mean. Individual values for the uninfected sample were taken from [25].

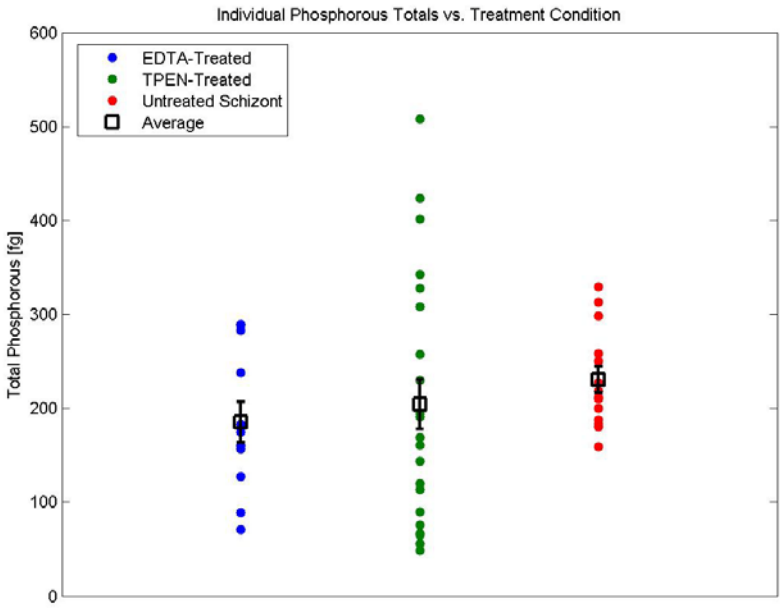

Figure 2.9: Individual phosphorous totals for each treatment condition. The error bars represent one standard error of the mean.

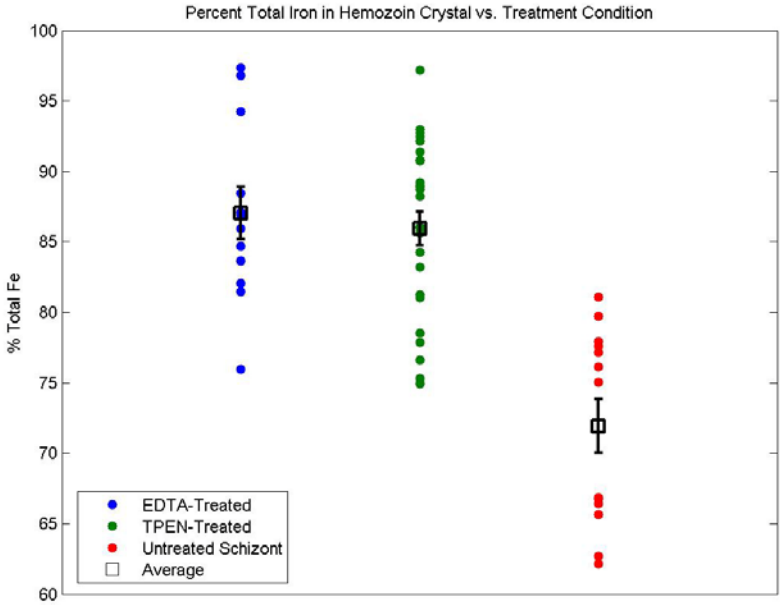

Figure 2.10: Percentage of total iron present in the hemozoin crystal for individual cells for each treatment condition. The error bars represent one standard error of the mean.

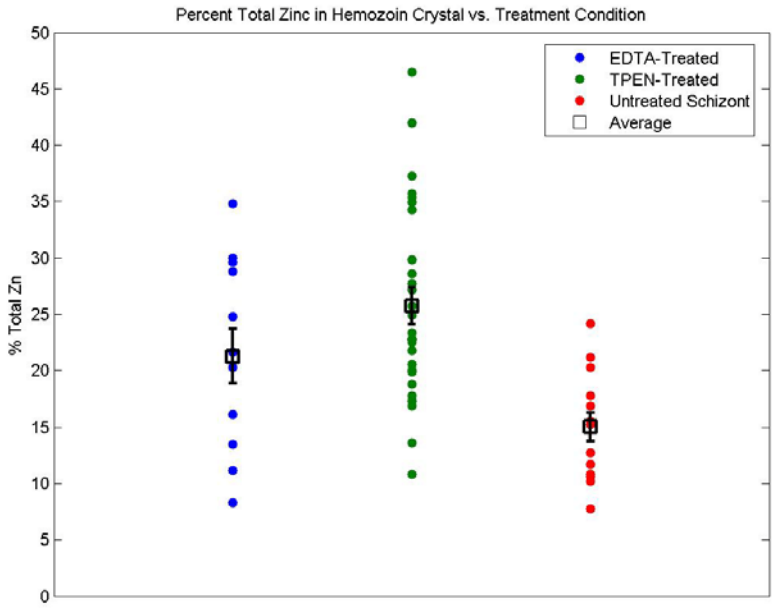

Figure 2.11: Percentage of total zinc present in the hemozoin crystal for individual cells for each treatment condition. The error bars represent one standard error of the mean.

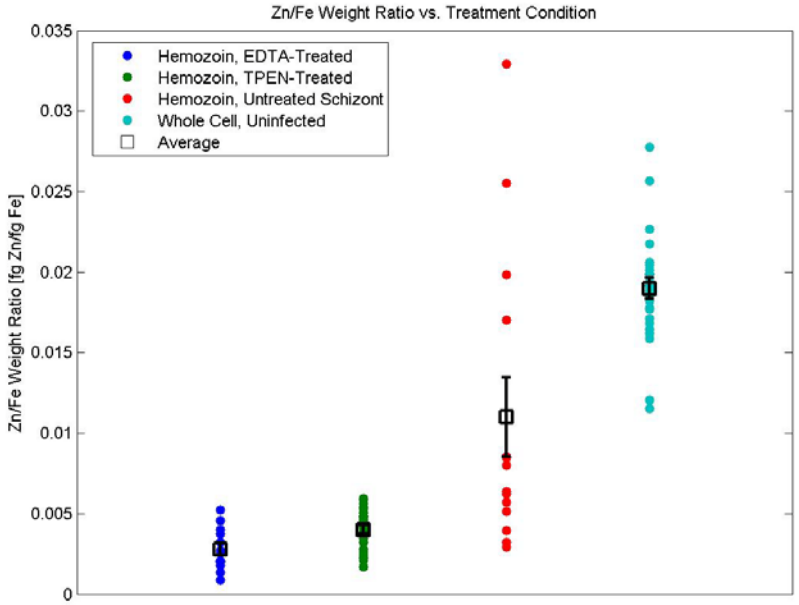

Figure 2.12: Zn/Fe weight ratio within the hemozoin crystal for individual cells for each treatment condition. The whole-cell Zn/Fe ratios, calculated from the data in [25], are provided for comparison. The error bars represent one standard error of the mean.

References

1. Breman, J.G., *The ears of the hippopotamus: manifestations, determinants, and estimates of the malaria burden.* The American journal of tropical medicine and hygiene, 2001. **64**(1/2; SUPP): p. 1.
2. Guerra, C.A., et al., *The limits and intensity of Plasmodium falciparum transmission: implications for malaria control and elimination worldwide.* PLoS medicine, 2008. **5**(2): p. e38.
3. Mendis, K., *The neglected burden of Plasmodium vivax malaria.* The American journal of tropical medicine and hygiene, 2001. **64**(90010): p. 97.
4. Sachs, J. and P. Malaney, *The economic and social burden of malaria.* Nature, 2002. **415**(6872): p. 680.
5. Bogitsh, B.J., *Human Parasitology*. 1998, San Diego: Academic Press.
6. Murphy, G. and E. Oldfield, *Falciparum malaria.* Infectious disease clinics of North America, 1996. **10**(4): p. 747.
7. Aikawa, M., *Variations in structure and function during the life cycle of malarial parasites.* World Health Organization. Bulletin of the World Health Organization, 1977. **55**(2-3): p. 139.
8. Miller, L.H., et al., *The pathogenic basis of malaria.* Nature, 2002. **415**(6872): p. 673.
9. Sherman, I.W., *Biochemistry of Plasmodium (malarial parasites).* Microbiology and molecular biology reviews, 1979. **43**(4): p. 453.
10. Fujioka, H. and M. Aikawa, *Malaria Parasites and Disease: Structure and Life Cycle.* Chem Immunol, 2002. **80**: p. 1.
11. Dubremetz, J., *Invited review Apical organelles and host-cell invasion by Apicomplexa.* International journal for parasitology, 1998. **28**(7): p. 1007.
12. Miller, L.H., et al., *Pf155/RESA antigen is localized in dense granules of Plasmodium falciparum merozoites.* Experimental Parasitology, 1990. **71**(3): p. 326.
13. Francis, S.E., D.J. Sullivan, and a.D.E. Goldberg, *Hemoglobin metabolism in the malaria parasite Plasmodium falciparum.* Annual Review of Microbiology, 1997. **51**(1): p. 97.
14. Muller, S., *Redox and antioxidant systems of the malaria parasite Plasmodium falciparum.* Molecular microbiology, 2004. **53**(5): p. 1291.
15. Haldar, K., *Intracellular trafficking in Plasmodium-infected erythrocytes.* Current opinion in microbiology, 1998. **1**(4): p. 466.
16. Mamoun, C.B., et al., *Co-ordinated programme of gene expression during asexual intraerythrocytic development of the human malaria parasite Plasmodium falciparum revealed by microarray analysis.* Molecular microbiology, 2001. **39**(1): p. 26.
17. Garcia and C.T. Hotta, *Calcium-dependent modulation by melatonin of the circadian rhythm in malarial parasites.* Nature Cell Biology, 2000. **2**(7): p. 466.
18. Aikawa, M., *The pathology of human cerebral malaria.* The American journal of tropical medicine and hygiene, 1990. **43**(2 Pt 2): p. 30.
19. Foley, M., *Quinoline antimalarials mechanisms of action and resistance and prospects for new agents.* Pharmacology & therapeutics, 1998. **79**(1): p. 55.

20. Hyde, J., *Mechanisms of resistance of Plasmodium falciparum to antimalarial drugs.* Microbes and infection, 2002. **4**(2): p. 165.
21. Yuthavong, Y., *Basis for antifolate action and resistance in malaria.* Microbes and infection, 2002. **4**(2): p. 175.
22. Wolford, J.L., *Zinc localization and quantitation in specialized cells and tissues*. 2006, Northwestern University.
23. Outten, C.E., *Femtomolar sensitivity of metalloregulatory proteins controlling zinc homeostasis.* Science, 2001. **292**(5526): p. 2488.
24. Finney, L.A., *Transition metal speciation in the cell: insights from the chemistry of metal ion receptors.* Science, 2003. **300**(5621): p. 931.
25. Kidd, M.J. 2006, University of Michigan.
26. Ginsburg, H., R. Gorodetsky, and M. Krugliak, *The status of zinc in malaria (Plasmodium falciparum) infected human red blood cells: stage dependent accumulation, compartmentation and effect of dipicolinate.* Biochimica et Biophysica Acta (BBA) - Molecular Cell Research, 1986. **886**(3): p. 337.
27. Gebran, S.J., *Macrophage permissiveness for Legionella pneumophila growth modulated by iron.* Infection and immunity, 1994. **62**(2): p. 564.
28. Trager, W. and J. Jensen, *Human malaria parasites in continuous culture.* Science, 1976. **193**(4254): p. 673.
29. Vogt, S., *MAPS: a set of software tools for analysis and visualization of 3D X-ray fluorescence data sets.* Journal de Physique IV (Proceedings), 2003. **104**(2): p. 635.
30. Walpole, R.E., et al., *Probability & Statistics for Engineers & Scientists, 8th ed.* 2006, Upper Saddle River, NJ: Prentice Hall.
31. Sheskin, D., *Handbook of parametric and nonparametric statistical procedures, 3rd ed*. 2004, Boca Raton, FL: Chapman & Hall/CRC.
32. McLaren, C.E., *Analysis of red blood cell volume distributions using the ICSH reference method: detection of sequential changes in distributions determined by hydrodynamic focusing.* Clinical and laboratory haematology, 1993. **15**(3): p. 173.
33. Zunszain, P.A., et al., *Crystal structural analysis of human serum albumin complexed with hemin and fatty acid.* BMC structural biology, 2003. **3**(1): p. 6.
34. Andr, C. and Y.C. Guillaume, *Zinc-human serum albumin association: testimony of two binding sites.* Talanta, 2004. **63**(2): p. 503.
35. Cousins, R.J., et al., *A global view of the selectivity of zinc deprivation and excess on genes expressed in human THP-1 mononuclear cells.* Proceedings of the National Academy of Sciences of the United States of America, 2003. **100**(12): p. 6952-6957.
36. Cousins, R.J., *Regulation of Zinc Metabolism and Genomic Outcomes 1 2.* Journal of Nutrition, The, 2003. **133**(5): p. 1521.
37. Rezaei, K.A., et al., *Modulation of Nrf2-Dependent Antioxidant Functions in the RPE by Zip2, a Zinc Transporter Protein.* Investigative ophthalmology & visual science, 2008. **49**(4): p. 1665.
38. Bozym, R.A., et al., *Measuring picomolar intracellular exchangeable zinc in PC-12 cells using a ratiometric fluorescence biosensor.* ACS chemical biology, 2006. **1**(2): p. 103.

39. Slater, A., *An iron-carboxylate bond links the heme units of malaria pigment.* Proceedings of the National Academy of Sciences of the United States of America, 1991. **88**(2): p. 325.
40. Perry, G.S., *Iron nutrition does not account for the hemoglobin differences between blacks and whites.* Journal of Nutrition, The, 1992. **122**(7): p. 1417.
41. Hawkins, W.W., *Variation of the hemoglobin level with age and sex.* Blood, 1954. **9**(10): p. 999.
42. Vallee, B.L., *The biochemical basis of zinc physiology.* Physiological reviews, 1993. **73**(1): p. 79.
43. Carman, G.M., *Regulation of phospholipid synthesis in yeast by zinc.* Biochemical society transactions, 2005. **33**(5): p. 1150.
44. Rosenberg, E., et al., *pfmdr2 Confers Heavy Metal Resistance to Plasmodium falciparum.* J. Biol. Chem., 2006. **281**(37): p. 27039-27045.
45. Jones, M.K. and M.F. Good, *Malaria parasites up close.* Nature Medicine, 2006. **12**(2): p. 220.
46. Bozdech, Z., et al., *The Transcriptome of the Intraerythrocytic Developmental Cycle of Plasmodium falciparum.* PLoS Biology, 2003. **1**(1): p. e5.

Chapter 3

X-Ray Absorption Spectroscopy of the Zinc Environment in Erythrocytes Infected with the Malaria Parasite *Plasmodium falciparum*

Introduction

Red blood cells infected with the malaria parasite *Plasmodium falciparum* accumulate an excess of zinc during the course of the parasite's life cycle, increasing the red blood cell's zinc total from approximately 1.3 fg per cell—the baseline total in uninfected cells—to approximately 3-4 fg per cell during late schizont-stage infection [1-3]. Since the median red blood cell volume is approximately 90 fL [4], this corresponds to an increase in total zinc concentration from approximately 220 μM to approximately 510-680 μM during parasite maturation. Living cells tightly regulate total metal levels, and with the exception of certain specialized cells, metal levels tend to be relatively constant for a variety of cell lines [3, 5, 6]. Therefore, it has been hypothesized that the increased zinc levels present in schizont-stage *P. falciparum* are necessary to perform some critical role in the parasite's normal functioning, though the nature of that role remains uncertain. If this is the case, then preventing this zinc accumulation through the use of zinc chelators could provide a cheap and effective treatment for this disease.

The O'Halloran group at Northwestern University has examined the effects of a variety of zinc chelators on parasite growth and has observed a direct relationship between zinc binding affinity and parasite growth inhibition. However, this is only true if one restricts the search to membrane-permeable chelators. The membrane-permeable

chelator TPEN proved effective at inhibiting parasite growth, with an IC_{50}—the concentration at which parasitemia decreases twofold—of 0.5 μM. In contrast, a much higher concentration of the membrane-impermeable chelator EDTA was required for 50% growth inhibition despite having a similarly high zinc binding affinity ($K_d \approx 10^{-15}$ for EDTA, compared to 10^{-16} for TPEN). The EDTA IC_{50} was initially determined to be 347 μM, the concentration used for the imaging study in Chapter 2, though this number has been subsequently determined to be closer to 8 mM. An IC_{50} of 347 μM would place EDTA between the membrane-permeable chelators DPA and DMSA in terms of effectiveness (IC_{50} values of 1397 μM and 98 μM, respectively) despite these two having much lower zinc binding affinities ($K_d \approx 10^{-7}$ for DPA, and 10^{-8} for DMSA), while an IC_{50} of 8 mM would make EDTA less effective than even DPA despite having a zinc affinity at least one hundred million times greater.

In Chapter 2, we found that both 347 μM EDTA and 0.5 μM TPEN were able to significantly decrease zinc uptake in cultured *P. falciparum* over a 48-hour period. These results were surprising, given the expected amount of free zinc under the given treatment conditions. The concentration of free zinc in chelator-supplemented media can be calculated from the total chelator concentration, total zinc concentration, and the pH-dependent binding constant [6]. The Zn-EDTA complex has a dissociation constant of $10^{-15.3}$ at pH 7.4, while the corresponding Zn-TPEN dissociation constant is $10^{-16.2}$. The total media zinc levels were measured to be 1.0 ± 0.1 μM by ICP-MS. Under these conditions, there should be approximately one attomolar free zinc in the presence of 347 μM EDTA, which would explain the lack of zinc uptake in EDTA-treated schizonts. On the other hand, 0.5 μM TPEN should only be able to sequester half the available zinc.

Since the parasites were found to take up close to 100% of the media zinc in the absence of chelator, chelating half the available zinc would be expected to decrease the zinc uptake by half, at most. Yet uptake has been completely abolished under these conditions. One explanation may involve a down-regulation of zinc transporters targeted to the host cell membrane and an up-regulation of zinc transporters targeted to the food vacuole in response to low-zinc conditions. Consistent with this view, the food vacuoles in chelator-treated samples were found to contain less zinc than expected based on the fraction of the host cytosol consumed.

Several open questions remain regarding the phenomenon of zinc uptake and the effect of zinc chelation in *P. falciparum*. Since carrying out the XRF imaging studies described in Chapter 2, the EDTA IC_{50} has been re-evaluated and determined to be 8 mM, while no growth inhibition was observed at the previously-determined IC_{50} of 347 μM. Thus, it would seem that the parasite is able to cope with external zinc deprivation and that the zinc taken from the host cell is sufficient for the parasite's needs. This raises two questions. First, why does the parasite import external zinc if it is able to meet its quota by transporting additional zinc out of the food vacuole? The additional zinc does not appear to localize to the food vacuole, which implies that the parasite is able to make use of it. Secondly, given that the EDTA-treated and TPEN-treated schizonts were found to have similar zinc content, phosphorous content, and food vacuole composition, what is the essential difference between the two zinc chelators that makes TPEN relatively more effective at reducing parasitemia?

One explanation for the efficacy of TPEN is the possibility that it can diffuse into infected red blood cells and disrupt the parasite's metal homeostasis in addition to

preventing zinc uptake. TPEN is known to induce apoptosis in T cells [7, 8], and this effect is thought to be caused by intracellular zinc chelation, though the concentrations of TPEN in that case were much higher (10 mM) than that used here. One line of evidence in support of this hypothesis in our system is the observation that TPEN treatment was found to decrease fluorescence from the ratiometric zinc probe Zinbo-5 in infected schizonts pre-loaded with that dye (Becky Marvin and Tom O'Halloran, Northwestern University, personal communication). However, the precise zinc pools targeted by TPEN remain a mystery, as is the percentage of the total zinc that these zinc pools represent.

If one assumes that the membrane-permeable TPEN becomes evenly distributed throughout the culture, including within the red blood cells, there will be an effective concentration of 0.5 μM TPEN in each infected red blood cell. Since a typical TPEN-treated schizont-stage infected red blood cell contains approximately 220 μM total zinc, indistinguishable from an uninfected RBC, 0.5 μM TPEN can bind at most 0.2% of the total intracellular zinc. However, since cells represent a metal-rich environment relative to the surrounding media [5] and since metal-bound TPEN would be unable to cross cell membranes due to a net positive charge, it is possible that TPEN diffuses into cells and is then trapped as a metal-TPEN complex. This would result in the selective enrichment of TPEN within red blood cells, increasing its effective concentration. The malaria cultures we use are approximately 5% hematocrit, or 5% red blood cell by volume, so if all of the TPEN selectively accumulates within red blood cells, this would result in a maximum 20-fold enrichment. The effective concentration would then be 10 μM, and the Zn-TPEN complex would account for approximately 5% of the total intracellular zinc at maximum. In the extreme limiting case, one could imagine all of the TPEN selectively accumulating

in infected red blood cells. In our system, typical infection levels are approximately 5% of the total red blood cells in culture, so there could be at most another 20-fold enrichment if the TPEN were all localized in infected cells. Under these conditions, the effective TPEN concentration would be 200 μM, similar to the IC_{50} values demonstrated by some of the other zinc chelators, and the Zn-TPEN complex would account for approximately 90% of the total intracellular zinc.

In order to determine the effect that zinc chelation has on the zinc speciation and to determine how the parasite may use its apparently superfluous imported zinc, we performed X-ray absorption spectroscopy on uninfected and schizont-stage infected red blood cells, as well as EDTA- and TPEN-treated schizont-stage infected samples. The XANES spectra were compared in order to assess minute changes in the average zinc environment, and the EXAFS was analyzed in order to determine average first-shell ligation and bond lengths. We show that at most 15% of the total zinc is present as Zn-TPEN in the TPEN-treated samples, and the data are consistent with little or no Zn-TPEN present.

Materials and Methods

Sample Preparation

All biological samples were prepared by Becky Marvin at the O'Halloran Lab at Northwestern University. The 3D7 strain of *Plasmodium falciparum* was cultured in 10% human serum in RPMI-1640 according to literature methods [9]. Cultures were synchronized with 5% sorbitol and grown at 37^{o}C for 48 hours, either untreated or in the presence of 0.5 μM TPEN (Sigma-Aldrich) or 347 μM EDTA (Sigma-Aldrich). After 48

hours, schizonts were isolated using a 60% Percoll gradient. Infected cells were pelleted and washed in PBS, and loaded into Lucite sample cells with Kapton windows. An uninfected red blood cell sample was used as a control. A 100 mM sample of the Zn-TPEN complex was prepared from TPEN and zinc nitrate (Sigma-Aldrich) and loaded into a Lucite sample cell.

X-Ray Absorption Spectroscopy

X-ray absorption spectra were taken at beamline 9-3 at the Stanford Synchrotron Radiation Lightsource. Samples were placed in a He-cooled cryostat maintained at 12 K to reduce thermal disorder. The incident beam was scanned between 9430 eV and 10325 eV using a Si(220) monochrometer in the $\varphi = 0^{o}$ orientation, with a rhodium-coated mirror upstream for harmonic rejection. The pre-edge region (9430 eV-9630 eV) was scanned in 10 eV steps, the edge region (9630 eV-9690 eV) in 0.35 eV steps, and the EXAFS region (between $k = 1.62$ Å^{-1} and $k = 13$ Å^{-1}) in 0.05 Å^{-1} steps. Integration times were 1 s per data point in the pre-edge and edge regions, and between 1s and 25 s (k^3-weighted) in the EXAFS region, for a total scan time of approximately 35 minutes per sweep. Three N_2-filled ion chambers were placed in the beam path, one prior to the cryostat in order to measure the incident beam intensity, and two placed after the cryostat. Energy calibration was achieved by use of a zinc foil between the second and third ion chambers, with the first inflection point of the zinc foil scan defined to be 9659 eV. Zinc fluorescence was detected using a 30-element Ge detector (Canberra Industries, Meriden, CT) windowed on the zinc Kα peak (8638 eV). The incoming count rate was approximately 13 kHz per detector element, and the zinc fluorescence count rate was

approximately 3 kHz per detector element.

Data Analysis

For all samples, each detector element was examined for artifacts and good channels (~28) were averaged. All fluorescence spectra were normalized to the tabulated X-ray absorption cross sections using the program *MBACK* [10, 11]. Least-squares fitting of the XANES spectra were carried out using the SIXPack suite of programs [12]. Normalization, spline fitting, and Fourier transforms for EXAFS analysis were carried out using EXAFSPAK. The pre-edge region was fit to a Gaussian tail, and the post-edge was fit to a cubic spline with three regions. The data were converted to *k*-space using the equation $k = [(8\pi^2 m_e/h^2)(E-E_0)]^{1/2}$. The threshold energy, E_0, was taken to be 9666 eV, as determined by fitting EXAFS spectra to zinc compounds of known structure [13]. After extracting the EXAFS, the data were Fourier transformed over the *k* range of 2-12 $Å^{-1}$ to obtain the pseudo-radial distribution function.

The k^3-weighted EXAFS were fit to the EXAFS equation [14] with a non-linear least-squares algorithm, keeping the coordination numbers and the threshold energy constant while allowing the bond lengths and Debye-Waller factors to vary. A variety of N/O and S coordination numbers were tested, based on the types of zinc coordination environments found in metalloproteins [15, 16]. Fits were constrained so that the total coordination number varied between 4 and 6, that the number of bound sulfurs never exceeded four, and that the coordination environment could only include four sulfurs if no other ligands were present. Combinations of N/O and S environments that met these criteria were also rejected if they could only arise from N/O environments with

unreasonably high coordination numbers. For example, a fit with 2.5 sulfurs and 3.0 low-Z ligands was rejected, because if it is assumed that all the zinc-sulfur interactions come from ZnS_4 sites, then a physically unreasonable $Zn(N/O)_8$ site would be required to yield an average coordination environment of 2.5 sulfurs and 3.0 low-Z ligands. If, instead, it is assumed that the sulfur in this example comes from an average $S_3(N/O)$ environment, the apparent average N/O coordination number would increase to 13.

The best fit was determined partly by the combination of parameters that minimize the fit parameter F reported by EXAFSPAK, defined as the sum of the squares of the differences between the data and the fit. However, some fits with a low fit parameter were rejected if the refined quantities were physically unreasonable—for example, fits with negative Debye-Waller factors or fits with bond lengths that are too short for the corresponding coordination number [17]. A reduced chi-squared statistic, F', was also computed to account for the improvement of fit quality that inevitably results from including more fit parameters. For this purpose, F' is defined as F/ν, where $\nu = N_{idp} - N_{par}$, N_{par} is the number of variable parameters, and N_{idp} is the number of independent data points, which for an EXAFS spectrum is $N_{idp} = 2\Delta k \Delta R/\pi$ [18].

Results

A comparison of the X-ray absorption near-edge structure (XANES) spectra for the biological samples is shown in Figures 3.1 and 3.2. The spectra for the untreated uninfected, untreated schizont-stage infected, and TPEN-treated schizont-stage infected samples were all similar in shape, with a split peak after the rising edge. The schizont-stage infected sample showed a smaller additional peak at approximately 9685 eV. In

contrast to these, the XANES for the EDTA-treated schizont-stage infected sample consisted of a single broad peak. The Zn-TPEN model and hexaqua zinc have similar spectra, with a sharp main peak at 9669 eV, a secondary peak at 9685 eV, and, for Zn-TPEN, a prominent post-edge peak at 9672 eV (Figure 3.3). An intense main peak in the XANES, as seen in hexaqua zinc, has been suggested to be a characteristic of highly symmetric metal centers. For example, in a study of dimanganese compounds, the XANES peak maximum varied inversely with the root mean square variation in the metal-ligand bond lengths [19]. The relatively weaker and broader main peak for the Zn-TPEN spectrum is consistent with this, as this compound, though six-coordinate, binds zinc through a mixture of pyridine groups and tertiary amines. The TPEN-treated schizont spectrum does not show any of the features present in Zn-TPEN, which suggests that the Zn-TPEN complex, if present at all, constitutes a relatively small percentage of the total zinc in the TPEN-treated sample. Furthermore, none of the spectra have the characteristic shape of hexaqua zinc (Figure 3.3), which shows a single prominent peak at 9700 eV and a secondary peak at 9685 eV [20], indicating that this too is a minor component of the biological samples.

The Fourier transforms derived from the biological sample extended X-ray absorption fine structure (EXAFS) are compared in Figure 3.4. Once again, the untreated uninfected, untreated schizont-stage infected, and TPEN-treated schizont-stage infected samples were all similar, with the first peak at ~1.5 Å in the non-phase-shifted spectra. The EDTA-treated sample showed a significantly less intense peak at ~1.5 Å as well as a second peak at ~1.8 Å. A comparison with the Zn-TPEN model compound, shown in Figure 3.5, can be used to suggest the type of zinc sites that would give rise to these

Fourier transforms. Zn-TPEN is a six-coordinate complex with exclusively nitrogen ligation and an average Zn-N first shell distance of 2.161 Å [21]. This is the longest reasonable Zn-(O/N) first-shell distance. In Figure 3.5, this corresponds to the Fourier transform peak at ~1.6 Å. Thus, peaks lower than 1.6 Å likely correspond to O/N-ligation. Lower-distance peaks indicate shorter Zn-(O/N) bonds, and since bond length correlates with coordination number, the peaks present at ~1.5 Å most likely indicate a 4- or 5-coordinate site. In contrast, peaks at larger distances would correspond to Zn-S interactions. Under these criteria, it would appear as if the EDTA-treated sample contains significantly more Zn-S ligation than in the other three biological samples.

The EXAFS fits support these conclusions, and the fit results for the untreated uninfected, untreated schizont, TPEN-treated schizont and EDTA-treated schizont are shown in Tables 3.1 through 3.4, respectively. The untreated uninfected, untreated schizont and TPEN-treated schizont all refined to a 3.5 O/N, 1 S average environment using a two-shell fit, and a 5 O/N environment with a one-shell fit. For the one-shell fits, the Debye-Waller factors lie in the range (7.0-8.1) x 10^{-3} $Å^2$, whereas the Debye-Waller factor for a typical zinc compound lies in the range (2.0-4.0) x 10^{-3} $Å^2$ [17]. The Debye-Waller factor tends to be positively correlated with coordination number, and an abnormally high Debye-Waller factor is often indicative of a fit with an abnormally high coordination number. For the two-shell fits, the Debye-Waller factors for both the O/N and the S shells all lie within the typical range. This would argue that the two-shell fits are the more physically reasonable ones, even though the calculated F' parameter is higher for these fits. In contrast to the other biological samples, the EDTA-treated sample showed relatively higher ratio of sulfur to low-Z ligands, with the best fit refining to a 2.5

O/N, 1.5 S average zinc environment. The corresponding EXAFS, Fourier transforms and fits are shown in Figures 3.6 through 3.12.

The similarity in the fits for the uninfected, untreated schizont, and TPEN-treated schizont samples for both the one- and two-shell fits is surprising given that the latter presumably has some fraction of its zinc present as six-coordinate Zn-TPEN, which would be expected to raise both the coordination number and bond length of the O/N shell. It is possible that the Zn-TPEN complex is present in the TPEN-treated sample, but at levels undetectable above the contributions from the other zinc species in the sample. Estimating this detection limit would place an upper bound on the amount of zinc that can be present as Zn-TPEN in the TPEN-treated sample. One estimate for this upper bound can be obtained by taking advantage of the fact that bond length tends to increase with coordination number and the fact that the precision of EXAFS bond length measurements (~0.004 Å) is significantly better than the precision for determining the coordination number using EXAFS (approximately ± 25%) [22, 23]. This upper bound can be established by constructing various linear combinations of the untreated schizont and Zn-TPEN model spectra, fitting the EXAFS of the composite spectrum, and finding the point where the Zn-(O/N) bond length differs from that of the untreated schizont sample by 0.012 Å, which would roughly correspond to the detection limit if the precision in the bond length determination is 0.004 Å.

To estimate this upper bound, the EXAFS was extracted from the untreated schizont spectrum, Fourier transformed over the *k* range of 2-12 $Å^{-1}$, and fit to a single shell as described above, allowing N, R, and σ to float. Next, a series of hypothetical data sets were constructed from the untreated schizont and Zn-TPEN spectra by summing *n*

times the untreated schizont spectrum and (1-*n*) times the Zn-TPEN spectrum, where $1.0 \geq n \geq 0.5$. The EXAFS was extracted from these hypothetical data sets as described above, and the spectra were fit allowing R to float while keeping N, σ, and ΔE_0 held constant. The cutoff for the minimum detectable fraction of Zn-TPEN was determined by finding the point where the R for the fit hypothetical data differs from the R for the fit untreated schizont data by 0.012 Å, which corresponds to three times the precision of determining R from EXAFS measurements [23].

The results of the sensitivity analysis for determining the lowest possible detectable Zn-TPEN levels are shown in Figure 3.13. Comparing the resolved Zn-(N/O) distances to the known limits of the technique, we can see that approximately 15% of the total zinc content would have to be present as a Zn-TPEN complex in order to have a significant effect on the fit results. The first-shell fits for the untreated schizont and TPEN-treated schizont were very similar, being 2.010 Å and 2.015 Å, respectively, for a one-shell fit, and 1.994 Å and 1.999 Å, respectively, in a two-shell fit (Tables 3.2 and 3.3). This similarity, combined with the sensitivity analysis shown in Figure 3.13, suggests an upper limit (~15%) for the amount of Zn-TPEN in the TPEN-treated sample.

An attempt to model the TPEN-treated sample XANES as a linear combination of the untreated schizont and Zn-TPEN complex failed to completely account for the observed lineshape (Figure 3.14). The best two-component fit was obtained with 90.4% schizont and 9.6% Zn-TPEN, which is consistent with the upper limit on the Zn-TPEN fraction determined by the EXAFS analysis. A significantly better fit was obtained by including the untreated uninfected spectrum (Figure 3.15). In that case, the best fit was determined to be 47.3% uninfected, 40.4% schizont-stage infected, and 12.3% Zn-TPEN

complex. Although the residual retains some features above the noise level, this fit is able to reproduce most of the features of the TPEN-treated schizont sample. Taken together, these fits suggest that less than 10-12% of the zinc in the TPEN-treated sample could be present as Zn-TPEN.

Discussion

Broadly speaking, zinc metalloenzymes can be divided into three classes: catalytic, coactive, and structural [16]. The zinc is present at the enzyme's active site in both catalytic and coactive sites, and the distinction between these two depends on whether activity is completely or partially abolished upon stripping away the bound zinc. These sites tend to be dominated by histidine, aspartate and glutamate ligation, with histidine being the most common. However, examples of catalytic sites with cysteine ligation do exist, notably the catalytic site of alcohol dehydrogenase, which is $(Cys)_2His(H_2O)$. In contrast, structural zinc sites do not participate in enzyme activity other than their role in maintaining the required tertiary structure. These sites are dominated by tetrahedral cysteine ligation. Also of note are the so-called zinc finger proteins, a class of nucleoproteins involved in DNA binding, transcription regulation and repair, and which tend to have $(Cys)_4$, $(Cys)_3His$, or $(Cys)_2(His)_2$ zinc sites [24]. Finally, mention should be made of metallothionein, a cysteine-rich polypeptide that can bind up to seven zinc atoms. Metallothionein is involved primarily in heavy metal detoxification, but has been postulated to also be involved in metal trafficking *in vivo*, as evidenced by its ability to restore function to inactive apoenzymes *in vitro* [25].

The uninfected and untreated schizont spectra were surprisingly similar in both

the XANES and the EXAFS, given the fact that the untreated schizont samples contain significantly more zinc than present in uninfected red blood cells and the fact that the infected red blood cells are metabolically active and contain DNA. In the original paper by Ginsburg *et al.*, the authors postulated that most of the increase in zinc would be associated with the tubovesicular and host cell membranes, with the rest associating with zinc finger proteins [1]. Specifically, the authors note that in uninfected red blood cells, approximately 5-8% of the total zinc is associated with the membrane and that the phospholipid content increases 3-5-fold as the parasite builds the tubovesicular membrane network (TVM). If one assumes that the additional membranes would have a similar zinc:phosphate ratio, then one can calculate the percentage of the zinc that is likely to be bound to the TVM. For an uninfected red blood cell with 1.30 fg total zinc, 5-8% of the zinc corresponds to approximately 0.07-0.10 fg Zn that will be bound to one "unit" of phospholipid. Adding 2-4 units of phospholipid would potentially bind 0.14-0.40 fg of Zn. Since the total zinc increase is 3.1 fg, then approximately 5-13% of the imported zinc could be phospholipid-bound. Furthermore, Ginsburg *et al.* found that the zinc bound to the host cell membrane increases 1.5-2-fold, which was postulated to be due to a histidine-rich protein that the parasite is known to target to the host membrane [1]. In the case presented here, this would be an increase in host membrane zinc of approximately 0.04-0.10 fg, or another 1-3% of the total increase associated with these histidine-rich proteins. This would leave the remaining 84-94% of the zinc increase for DNA and RNA polymerase. The membrane-associated zinc could be between 4- to 6-coordinate low-Z, whereas zinc bound in zinc fingers would be between 2-coordinate S, 2-coordinate low-Z and 4-coordinate S. Assuming 2-coordinate S, 2-coordinate low-Z for

the zinc finger proteins and 6-coordinate low-Z for the membrane-associated zinc, this would give a low-Z:S ratio of between 1.2:1 and 1.6:1 at the lowest, which is still considerably more sulfur-rich than the observed ratio of 3.5:1. Clearly, there are more low-Z sites present in the schizont-stage infected red blood cells than this model accounts for. The *P. falciparum* genome is known to contain genes for such catalytic zinc metalloenzymes as carbonic anhydrase [26] and farnesyl transferase [27], which are both low-Z and may be partially responsible for the observed low-Z:sulfur ratio.

Uninfected red blood cells showed mostly low-Z first-shell zinc coordination, whereas EDTA-treated schizont-stage erythrocytes showed increased zinc-sulfur coordination. This observation, combined with the observation from Chapter 2 that EDTA-treated samples do not have total zinc levels significantly higher than uninfected red blood cells, is consistent with the idea that the parasite is able to metabolize and make use of the host cell's zinc stores under zinc-starved conditions. Host cell zinc metalloproteins are taken into the parasite's food vacuole as part of normal parasite feeding. Zinc acquired in this manner was previously thought to play a relatively minor role in meeting the parasite's zinc requirements. Ginsburg *et al* found that the Zn/Fe weight ratio in the food vacuole (1.11×10^{-2}) was similar to the Zn/Fe weight ratio in the uninfected host (1.23×10^{-2}) [1], which was suggested to mean that the host zinc was largely being shuttled to the food vacuole without prior processing. However, that study did not measure this ratio for samples grown under zinc-starved conditions. Furthermore, it was found in Chapter 2 that for samples grown under 347 μM EDTA or 0.5 μM TPEN, the Zn/Fe ratio within the food vacuole was significantly lower—0.28×10^{-2} and 0.40×10^{-2}, respectively—lending support to the notion that the parasite is able to process the

host zinc pool, at least under certain conditions. The X-ray absorption spectra of the EDTA-treated sample suggest that the parasite removes zinc from (O/N)-dominated zinc sites in the host cell and places it in sulfur-rich zinc sites in the parasite.

Treatment with TPEN did not result in the same sort of zinc relocalization as observed in the EDTA-treated samples. The TPEN-treated EXAFS was similar to the uninfected and untreated infected spectra in both the one- and two-shell fits. However, the specific distribution of zinc among the different zinc sites in the TPEN-treated case is, from the XANES results, at least somewhat different from the uninfected and untreated infected samples. As noted in Chapter 2, the zinc distribution in this instance appears spread out through the cell, not concentrated in the food vacuole, which suggests that the red blood cell zinc has undergone some form of processing. Furthermore, a fraction of this zinc is likely Zn-TPEN, since TPEN treatment has been noted to quench Zinbo-5 fluorescence whereas EDTA treatment does not. Unfortunately, the study performed here did not have enough sensitivity to determine exactly how much of the total intracellular zinc was present as Zn-TPEN, only that this fraction is unlikely to be more than 15%. The exact zinc pools affected by the presence of TPEN are also unknown.

The observation that 347 μM EDTA prevents zinc uptake without a concomitant decrease in parasite viability demonstrates that the parasite is able to cope with zinc starvation. Taken together, the results of Chapters 2 and 3 suggest that there are three requirements to survive in low-zinc conditions. First, the parasite consumes relatively more of the host cytosol. This by itself would compensate somewhat for the loss of extracellular zinc, since the results of the XRF imaging suggest that the parasite is able to utilize a portion of the host zinc pool even under normal zinc conditions. Secondly,

relatively more of the host zinc is transported out of the food vacuole. Finally, based on the EXAFS data, there seems to be a redistribution of zinc in EDTA-treated schizonts that results in relatively more of the total zinc being placed in sulfur-rich sites, compared to untreated schizonts. This redistribution would not need to be a specific response to zinc deprivation. It is possible that relocation of zinc to fill sulfur-rich sites also occurs in untreated schizonts, but this change is obscured by the 2-3-fold excess zinc imported by the parasite. That is, if the imported zinc occupies primarily low-Z sites, preventing this uptake may increase the apparent Zn-S coordination number. As for the effects of TPEN treatment, treatment with 0.5 μM TPEN seems to trigger many of the same low-zinc responses as 347 μM EDTA with regards to the total amount of zinc present, the percentage of cytosol consumed, and amount of zinc removed from the food vacuole. The primary difference between the two cases appears to be the effect that each has on the zinc speciation within the cells. We suggest here that this difference in zinc speciation is the basis for TPEN cytotoxicity, where TPEN treatment prevents zinc from being delivered to crucially important sulfur-rich sites. However, whether TPEN is intercepting zinc directly or working indirectly by preventing expression of those factors required for proper zinc delivery in *Plasmodium* has yet to be determined.

It is difficult to determine the identity of these essential sulfur-rich sites, given that living systems represent a complex mixture of multiple different zinc sites, although it is possible to make some guesses. In principle, increased expression of alcohol dehydrogenase, aspartate transcarbamylase, and protein kinase C can all raise the ratio of sulfur to low-Z ligands, as can zinc fingers and metallothionein. Metallothionein presents an attractive option for EDTA-treated cells, since it has been found that mouse fibroblasts

adapted to low-zinc conditions have adapted metallothionein for zinc scavenging purposes [25]. However, a database search of the *P. falciparum* genome for the presence of metallothioneins did not support the existence of these proteins within the parasite [28]. Of the remaining options, increased expression of zinc finger transcription factors and DNA repair proteins would be reasonable as part of the parasite's stress response. Two A20/AN1 zinc-finger domain-containing proteins have been identified in *P. falciparum* [29]. These sequences are present in a variety of plant and animal species and are responsive to several different stresses, including cold, salt, dehydration and heavy metal exposure. However, the exact function of these proteins in *P. falciparum* has yet to be determined. Overall, the *P. falciparum* genome encodes a greater number of $(Cys)_3His$ zinc finger sequences than most eukaryotes—28 genes per 10,000 compared to 17 per 10,000—although it contains many fewer zinc finger sequences in total [30]. Thus, one possibility is that *P. falciparum* is viable as long as it can deliver enough zinc to fill sulfur-rich zinc finger sites, either as a stress response, or to fulfill its normal requirements of DNA and RNA polymerase. The host erythrocyte may contain sufficient zinc to meet these requirements, whereas intracellular TPEN seems to prevent proper delivery.

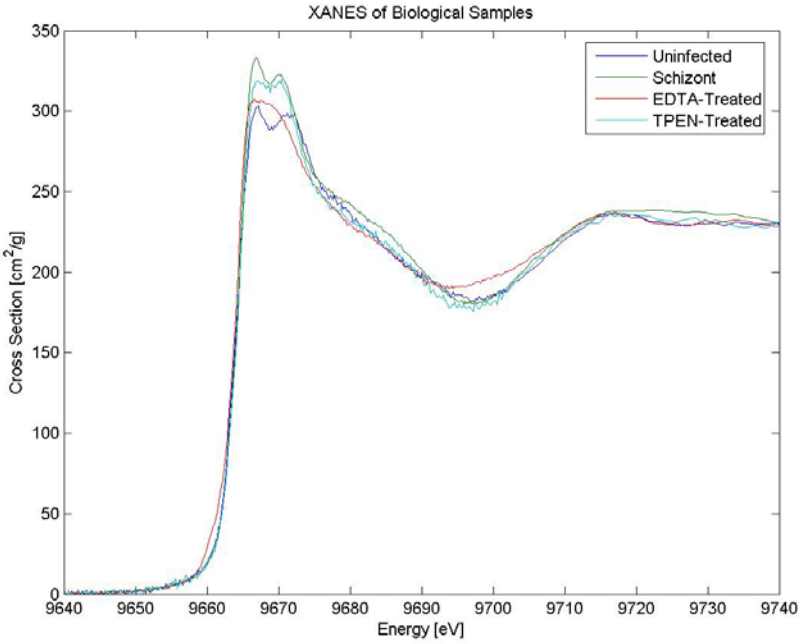

Figure 3.1: Normalized XANES of red blood cell samples.

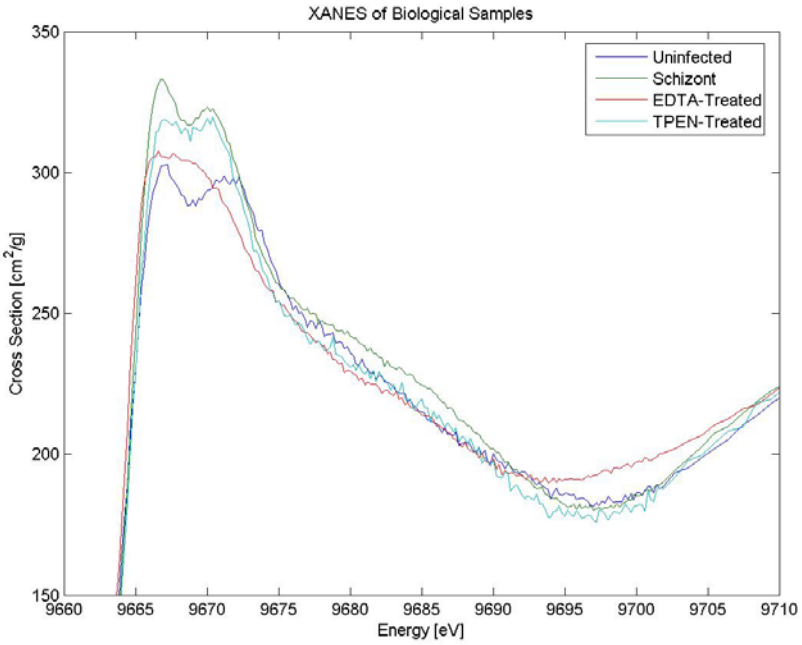

Figure 3.2: Detail on normalized XANES of RBC samples.

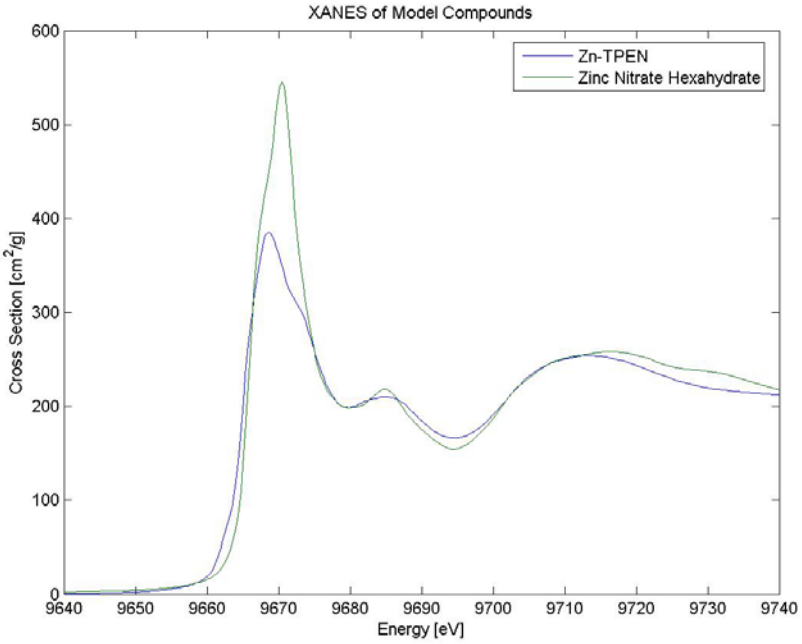

Figure 3.3: Comparison of model compound XANES. Water comprises the first coordination shell of zinc nitrate hexahydrate, and the XANES spectrum looks similar to hexaqua zinc [20].

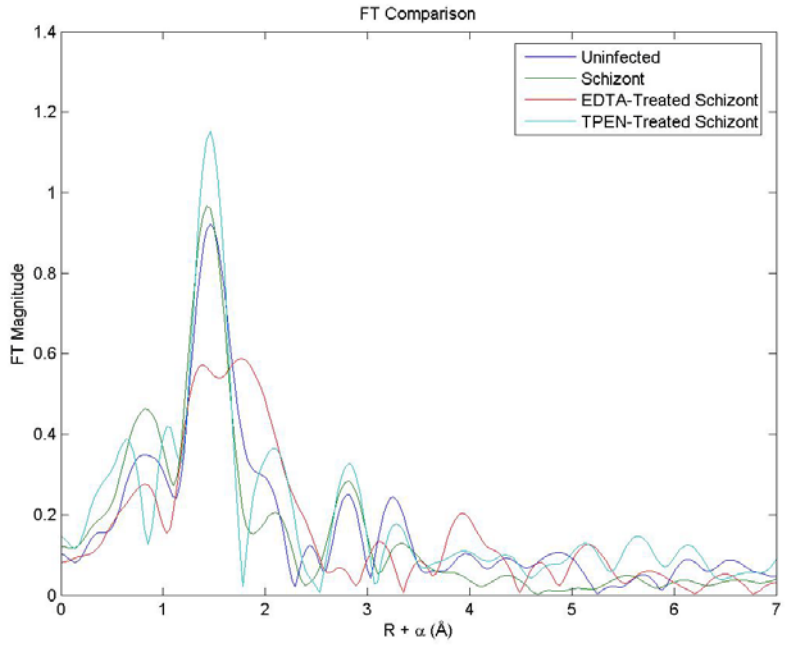

Figure 3.4: Comparison of Fourier transforms derived from biological EXAFS.

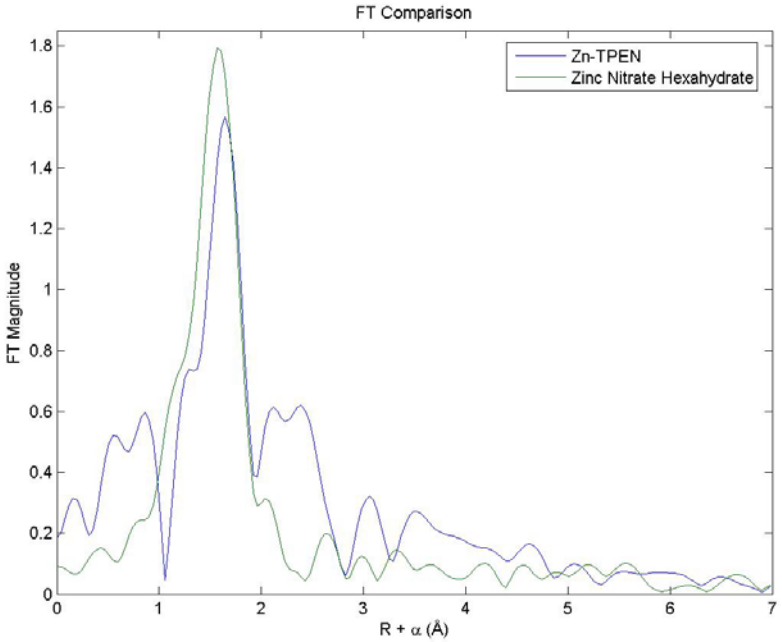

Figure 3.5: Comparison of Fourier transforms derived from model compound EXAFS.

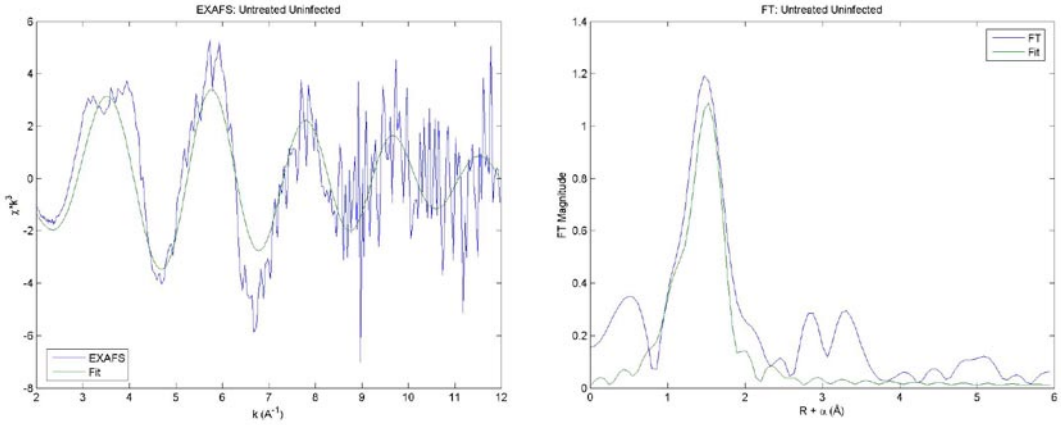

Figure 3.6: EXAFS fit for untreated uninfected sample, 5 N/O.

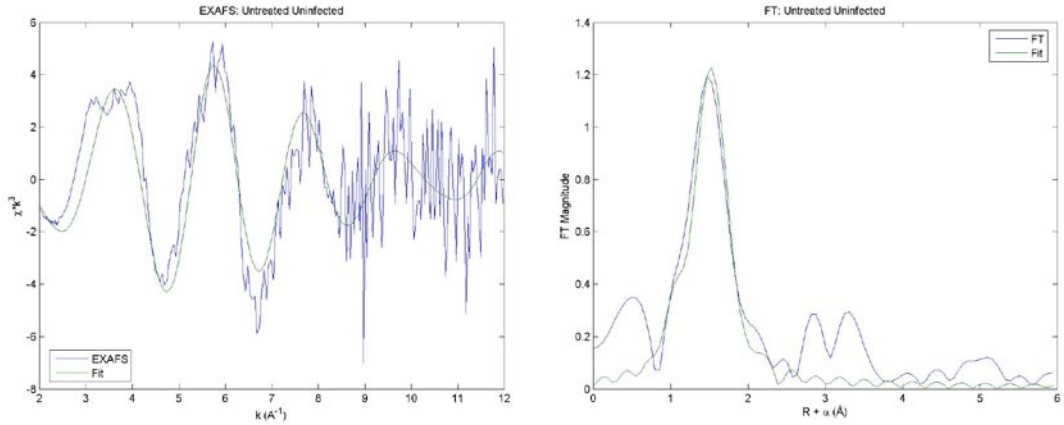

Figure 3.7: EXAFS fit for untreated uninfected sample, 3.5 N/O, 1S.

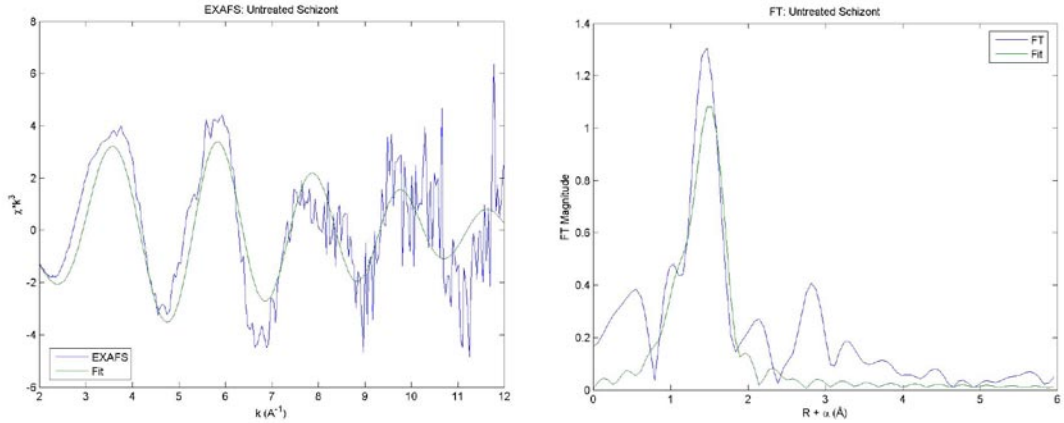

Figure 3.8: EXAFS fit for untreated schizont sample, 5 N/O.

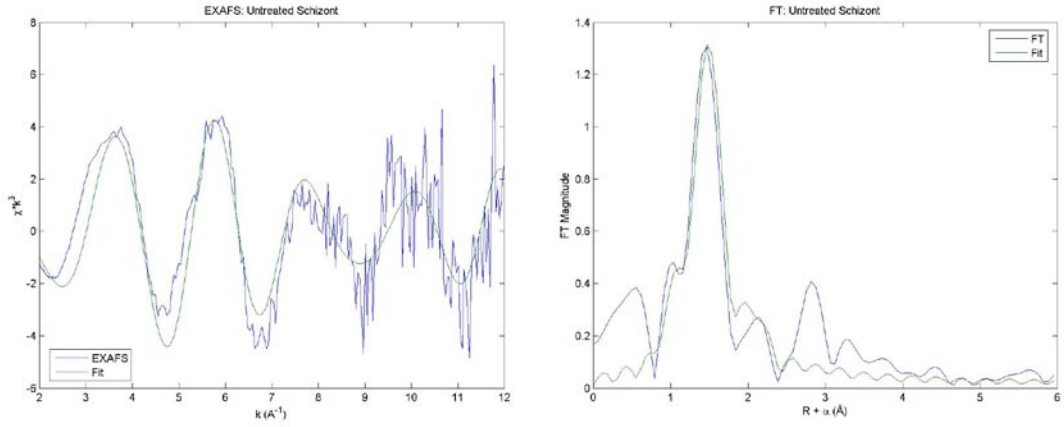

Figure 3.9: EXAFS fit for untreated schizont sample, 3.5 N/O, 1 S.

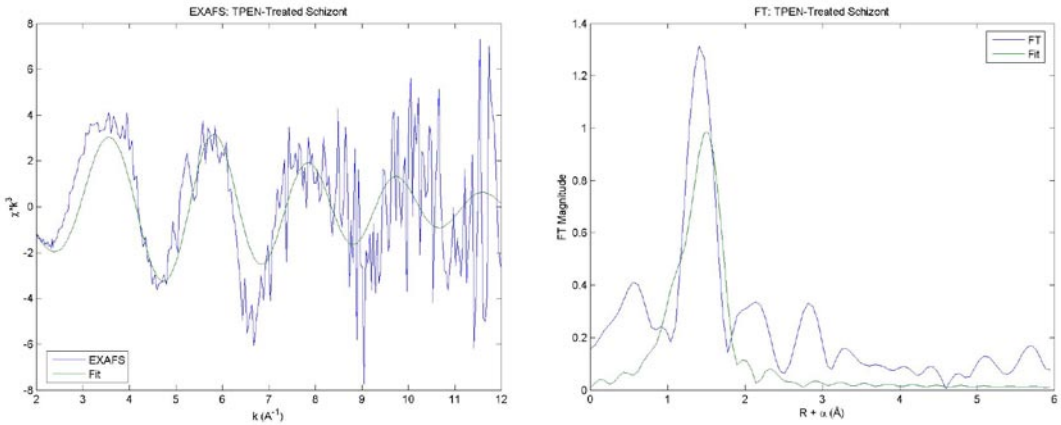

Figure 3.10: EXAFS fit for TPEN-treated sample, 5 N/O.

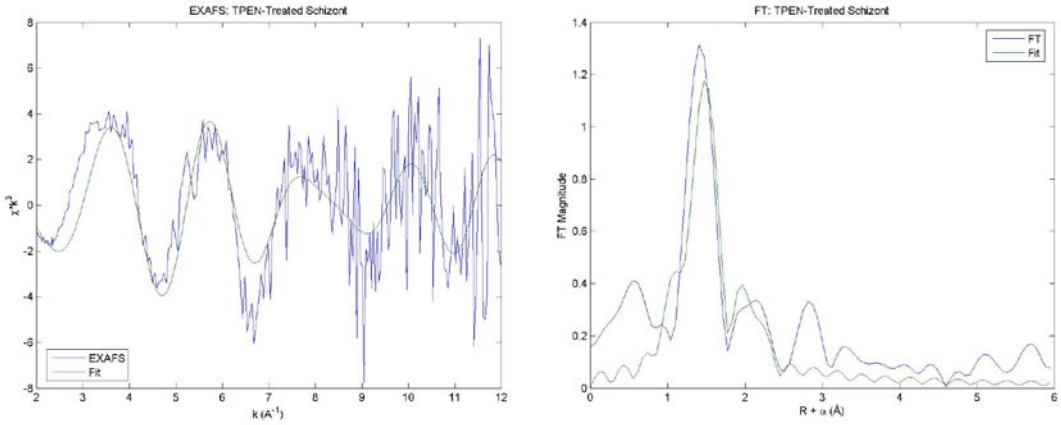

Figure 3.11: EXAFS fit for TPEN-treated sample, 3.5 N/O, 1 S.

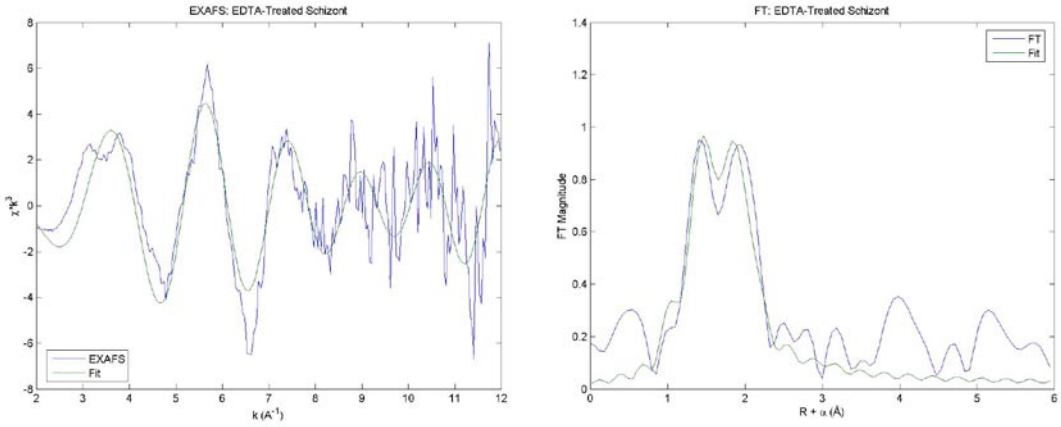

Figure 3.12: EXAFS fit for EDTA-treated sample, 2.5 N/O, 1.5 S.

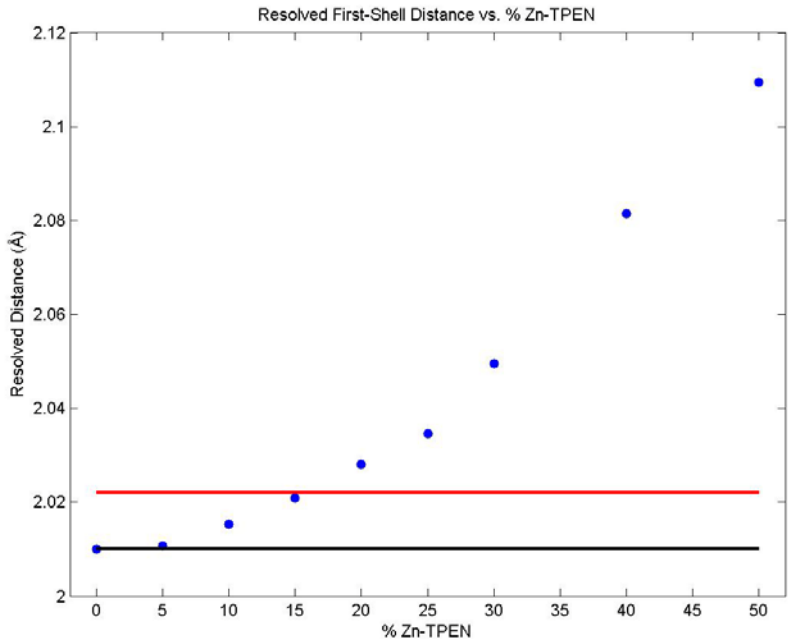

Figure 3.13: Sensitivity of resolved first-shell distance to increased Zn-TPEN fraction. The black line indicates the resolved single-shell distance for the untreated schizont sample, while the red line shows the same incremented by 0.012 Å, three times the precision of EXAFS measurements [23].

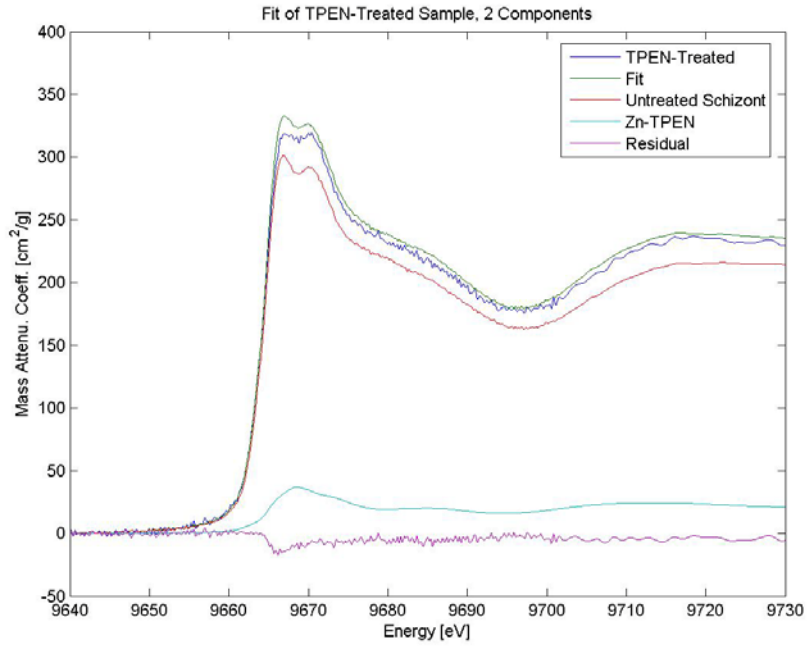

Figure 3.14: Two-component fit for TPEN-treated XANES.

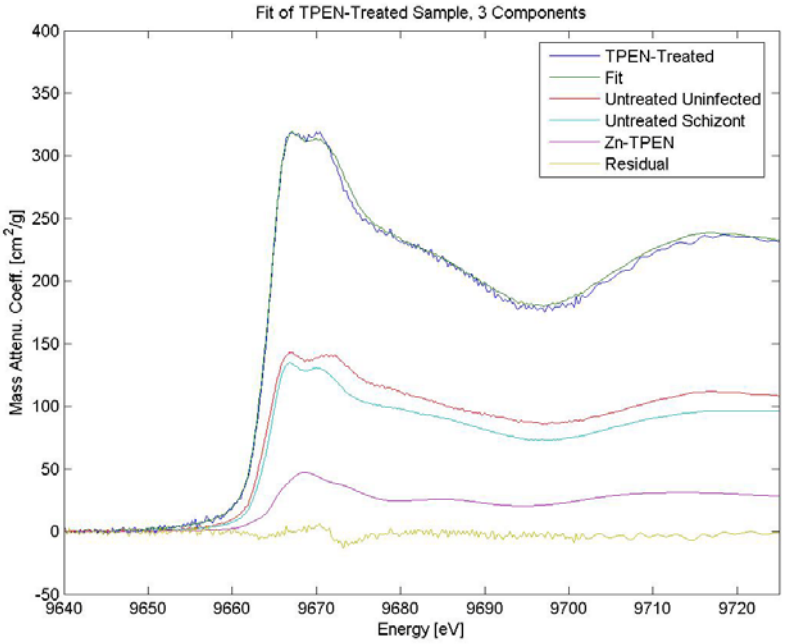

Figure 3.15: Three-component fit for TPEN-treated XANES.

Table 3.1: Fit Results of the EXAFS Data for Untreated Uninfected Sample

O/N			S				
N	**R (Å)**	**σ^2 x 10^3 (Å^2)**	**N**	**R (Å)**	**σ^2 x 10^3 (Å^2)**	**F[a]**	**F'[b]**
6.0	2.03	8.4	0.0			571	71
5.5	2.03	7.7	0.0			572	71
5.0	2.02	6.0	0.5	2.30	1.5	527	88
5.0	**2.03**	**7.0**	**0.0**			**578**	**72**
4.5	2.01	4.9	0.5	2.30	0.6	518	86
4.0	2.01	4.9	1.0	2.29	4.9	528	88
3.5	2.01	4.4	1.5	2.28	7.6	538	90
3.0	2.01	4.0	2.0	2.28	9.9	550	92
4.5	2.03	6.3	0.0			591	74
4.0	2.01	3.9	0.5	2.29	0.0	519	86
3.5	**2.01**	**3.8**	**1.0**	**2.28**	**4.0**	**526**	**88**
3.0	2.00	3.3	1.5	2.28	6.6	539	90
2.5	2.00	2.7	2.0	2.27	8.7	554	92
2.0	2.00	1.9	2.5	2.27	10.3	573	95
1.5	2.00	0.7	3.0	2.26	11.5	596	99
4.0	2.03	5.5	0.0			612	76
3.5	2.01	3.0	0.5	2.29	-0.5	526	88
3.0	2.00	2.6	1.0	2.28	3.4	531	88
2.5	2.00	2.0	1.5	2.28	5.8	547	91
2.0	2.00	1.3	2.0	2.27	7.8	566	94
1.5	1.99	0.3	2.5	2.26	9.4	590	98
1.0	1.99	-1.2	3.0	2.26	10.5	621	103
0.5	1.99	-3.8	3.5	2.25	11.6	665	111
0.0			4.0	2.24	13.4	822	103

[a] Goodness-of-fit parameter. [b] Reduced goodness-of-fit parameter.
Best one- and two-shell fits are highlighted in bold.

Table 3.2: Fit Results of the EXAFS Data for Untreated Schizont Sample

O/N			S				
N	**R (Å)**	**σ^2 x 10^3 (Å^2)**	**N**	**R (Å)**	**σ^2 x 10^3 (Å^2)**	**F[a]**	**F'[b]**
6.0	2.01	8.8	0.0			504	63
5.5	2.01	8.0	0.0			501	63
5.0	2.01	5.3	0.5	2.32	-0.5	404	67
5.0	**2.01**	**7.2**	**0.0**			**503**	**63**
4.5	2.00	4.4	0.5	2.32	-0.7	394	66
4.0	2.00	3.7	1.0	2.31	3.4	412	69
3.5	1.99	3.1	1.5	2.31	6.4	428	71
3.0	1.99	2.4	2.0	2.30	9.1	440	73
4.5	2.01	6.3	0.0			510	64
4.0	2.00	3.5	0.5	2.31	-0.9	389	65
3.5	**1.99**	**2.7**	**1.0**	**2.31**	**3.1**	**406**	**68**
3.0	1.99	2.0	1.5	2.30	6.0	422	70
2.5	1.98	1.3	2.0	2.29	8.5	437	73
2.0	1.98	0.3	2.5	2.29	10.5	453	76
1.5	1.98	-0.9	3.0	2.28	12.1	473	79
4.0	2.01	5.4	0.0			523	65
3.5	2.00	2.5	0.5	2.31	-1.2	390	65
3.0	1.99	1.7	1.0	2.30	2.8	406	68
2.5	1.99	0.9	1.5	2.29	5.7	424	71
2.0	1.98	0.0	2.0	2.29	8.1	443	74
1.5	1.98	-1.1	2.5	2.28	10.1	466	78
1.0	1.97	-2.8	3.0	2.27	11.9	496	83
0.5	1.97	-5.6	3.5	2.26	13.1	544	91
0.0			4.0	2.25	16.4	863	108

[a] Goodness-of-fit parameter. [b] Reduced goodness-of-fit parameter.
Best one- and two-shell fits are highlighted in bold.

Table 3.3: Fit Results of the EXAFS Data for TPEN-Treated Sample

O/N			S				
N	**R (Å)**	**σ^2 x 10^3 (Å^2)**	**N**	**R (Å)**	**σ^2 x 10^3 (Å^2)**	**F[a]**	**F'[b]**
6.0	2.02	10.0	0.0			1092	137
5.5	2.02	9.0	0.0			1092	137
5.0	2.01	6.5	0.5	2.35	-0.1	967	161
5.0	**2.01**	**8.1**	**0.0**			**1093**	**137**
4.5	2.01	5.6	0.5	2.34	-0.1	963	160
4.0	2.00	4.5	1.0	2.34	3.6	963	160
3.5	2.00	3.6	1.5	2.33	6.4	968	161
3.0	1.99	2.7	2.0	2.33	8.9	975	162
4.5	2.01	7.1	0.0			1099	137
4.0	2.01	4.6	0.5	2.34	-0.1	964	161
3.5	**2.00**	**3.5**	**1.0**	**2.33**	**3.6**	**962**	**160**
3.0	1.99	2.6	1.5	2.32	6.5	967	161
2.5	1.99	1.6	2.0	2.32	8.9	976	163
2.0	1.98	0.6	2.5	2.31	11.0	988	165
1.5	1.98	-0.7	3.0	2.30	12.9	1005	168
4.0	2.01	6.1	0.0			1109	139
3.5	2.00	3.7	0.5	2.33	-0.1	972	162
3.0	2.00	2.5	1.0	2.32	3.7	968	161
2.5	1.99	1.5	1.5	2.32	6.5	975	162
2.0	1.98	0.4	2.0	2.31	8.9	987	164
1.5	1.98	-0.8	2.5	2.30	11.1	1005	168
1.0	1.97	-2.5	3.0	2.29	13.0	1034	172
0.5	1.97	-5.2	3.5	2.28	14.8	1087	181
0.0			4.0	2.27	18.2	1391	174

[a] Goodness-of-fit parameter. [b] Reduced goodness-of-fit parameter.
Best one- and two-shell fits are highlighted in bold.

Table 3.4: Fit Results of the EXAFS Data for EDTA-Treated Sample

O/N			S				
N	**R (Å)**	**σ^2 x 10^3 (Å^2)**	**N**	**R (Å)**	**σ^2 x 10^3 (Å^2)**	**F[a]**	**F'[b]**
6.0	2.07	12.2	0.0			944	125
5.5	2.07	11.5	0.0			947	118
5.0	2.04	8.4	0.5	2.32	-3.2	574	96
5.0	2.07	10.8	0.0			955	119
4.5	2.04	7.3	0.5	2.32	-3.4	564	94
4.0	2.03	6.6	1.0	2.32	-0.3	557	93
3.5	2.02	5.9	1.5	2.32	1.8	566	94
3.0	2.01	5.0	2.0	2.31	3.4	579	97
4.5	2.07	10.2	0.0			968	121
4.0	2.04	6.2	0.5	2.32	-3.5	557	93
3.5	2.03	5.4	1.0	2.32	-0.4	544	91
3.0	2.02	4.5	1.5	2.32	1.6	549	92
2.5	2.00	3.5	2.0	2.31	3.2	559	93
2.0	1.99	2.2	2.5	2.31	4.6	568	95
1.5	1.98	0.7	3.0	2.30	6.0	575	96
4.0	2.08	9.5	0.0			986	123
3.5	2.04	5.1	0.5	2.32	-3.7	555	93
3.0	2.03	4.1	1.0	2.32	-0.6	536	89
2.5	**2.01**	**3.1**	**1.5**	**2.31**	**1.4**	**537**	**90**
2.0	2.00	1.9	2.0	2.31	3.1	543	91
1.5	1.99	0.4	2.5	2.30	4.6	551	92
1.0	1.98	-1.6	3.0	2.30	6.0	555	93
0.5	1.96	-4.7	3.5	2.29	7.7	557	93
0.0			4.0	2.29	10.6	723	90

[a] Goodness-of-fit parameter. [b] Reduced goodness-of-fit parameter.
Best fit is highlighted in bold.

References

1. Ginsburg, H., R. Gorodetsky, and M. Krugliak, *The status of zinc in malaria (Plasmodium falciparum) infected human red blood cells: stage dependent accumulation, compartmentation and effect of dipicolinate.* Biochimica et Biophysica Acta (BBA) - Molecular Cell Research, 1986. **886**(3): p. 337.
2. Kidd, M.J. 2006, University of Michigan.
3. Wolford, J.L., *Zinc localization and quantitation in specialized cells and tissues*. 2006, Northwestern University.
4. McLaren, C.E., *Analysis of red blood cell volume distributions using the ICSH reference method: detection of sequential changes in distributions determined by hydrodynamic focusing.* Clinical and laboratory haematology, 1993. **15**(3): p. 173.
5. Finney, L.A., *Transition metal speciation in the cell: insights from the chemistry of metal ion receptors.* Science, 2003. **300**(5621): p. 931.
6. Outten, C.E., *Femtomolar sensitivity of metalloregulatory proteins controlling zinc homeostasis.* Science, 2001. **292**(5526): p. 2488.
7. Jiang, S., *Lack of Ca2+ involvement in thymocyte apoptosis induced by chelation of intracellular Zn2+*. Laboratory Investigation, 1995. **73**(1): p. 111.
8. Orrenius, S., et al., *The role of proteolysis in T cell apoptosis triggered by chelation of intracellular Zn2+*. Cell Death and Differentiation, 1997. **4**(1): p. 39.
9. Trager, W. and J. Jensen, *Human malaria parasites in continuous culture.* Science, 1976. **193**(4254): p. 673.
10. McMaster, W.H., *Compilation of X-ray cross sections*. 1969.
11. Weng, T.-C., G.S. Waldo, and J.E. Penner-Hahn, *A method for normalization of X-ray absorption spectra.* Journal of synchrotron radiation, 2005. **12**(4): p. 506.
12. Webb, S.M., *SIXPack: a Graphical User Interface for XAS Analysis Using IFEFFIT.* Physica Scripta, 2005. **115**: p. 1011-1014.
13. Clark-Baldwin, K., et al., *The limitations of X-ray absorption spectroscopy for determining the structure of zinc sites in proteins. When is a tetrathiolate not a tetrathiolate?* Journal of the American Chemical Society, 1998. **120**(33): p. 8401.
14. Teo, B.K., *EXAFS: Basic Principles and Data Analysis*. 1986, Berlin: Springer-Verlag.
15. Parkin, G., *Synthetic analogues relevant to the structure and function of zinc enzymes.* Chemical reviews, 2004. **104**(2): p. 699.
16. Vallee, B.L., *The biochemical basis of zinc physiology.* Physiological reviews, 1993. **73**(1): p. 79.
17. Penner-Hahn, J.E., *Characterization of "spectroscopically quiet" metals in biology.* Coordination Chemistry Reviews, 2005. **249**(1-2): p. 161.
18. Bunker, G., S. Hasnain, and D. Sayers, *X-Ray Absorption Fine Structure*. 1991, New York, NY: Ellis Horwood.
19. Stemmler, T.L., et al., *EXAFS Comparison of the Dimanganese Core Structures of Manganese Catalase, Arginase, and Manganese-Substituted Ribonucleotide Reductase and Hemerythrin.* Biochemistry, 1997. **36**(32): p. 9847.
20. Cotton, F.A., *Soft X-Ray Absorption Edges of Metal Ions in Complexes. III. Zinc (II) Complexes.* The Journal of chemical physics, 1958. **28**(1): p. 83.

21. Toftlund, H., et al., *Three overcrowded zinc(II) complexes with potentially hexadentate polypyridyl ligands.* Acta crystallographica. Section C, Crystal structure communications, 2008. **64**(5): p. m185.
22. Riggs-Gelasco, P.J., et al., *Reduced derivatives of the Mn cluster in the oxygen-evolving complex of photosystem II: An EXAFS study.* Journal of the American Chemical Society, 1996. **118**(10): p. 2387.
23. Penner-Hahn, J.E., *X-ray absorption spectroscopy in coordination chemistry.* Coordination Chemistry Reviews, 1999. **190-192**: p. 1101.
24. Wilker, J.J. and S.J. Lippard, *Modeling the DNA Methylphosphotriester Repair Site in Escherichia coli Ada. Why Zinc and Four Cysteines?* Journal of the American Chemical Society, 1995. **117**(33): p. 8682.
25. Suhy, D.A., et al., *Metallothionein Is Part of a Zinc-scavenging Mechanism for Cell Survival under Conditions of Extreme Zinc Deprivation.* J. Biol. Chem., 1999. **274**(14): p. 9183-9192.
26. Krungkrai, S.R., et al., *Characterisation of carbonic anhydrase in Plasmodium falciparum.* International Journal for Parasitology, 2001. **31**(7): p. 661.
27. Hamilton, A., et al., *Structurally simple farnesyltransferase inhibitors arrest the growth of malaria parasites.* Angewandte Chemie (International ed. in English), 2005. **44**(31): p. 4903.
28. Rosenberg, E., et al., *pfmdr2 Confers Heavy Metal Resistance to Plasmodium falciparum.* J. Biol. Chem., 2006. **281**(37): p. 27039-27045.
29. Vij, S. and A.K. Tyagi, *A20/AN1 zinc-finger domain-containing proteins in plants and animals represent common elements in stress response.* Functional & Integrative Genomics, 2008. **8**(3): p. 301-307.
30. Coulson, R.M.R., N. Hall, and C.A. Ouzounis, *Comparative Genomics of Transcriptional Control in the Human Malaria Parasite Plasmodium falciparum.* Genome Research, 2004. **14**(8): p. 1548-1554.

Chapter 4

X-Ray Fluorescence Imaging of Human KB Cells Undergoing Staurosporine-Induced Apoptosis

Introduction

Apoptosis, or programmed cell death, is the method by which multicellular organisms remove damaged or unneeded cells [1-5]. In addition to its role in normal ontogeny, apoptosis is important in disease pathology. Malignant tumors are characterized in part by their insensitivity to normal apoptotic stimuli [6, 7], and apoptosis has been implicated in neurodegenerative disease [8, 9].

Apoptosis proceeds by a variety of pathways, but is generally characterized by changes in plasma membrane composition, cysteine-aspartic acid protease (caspase) activation, DNA fragmentation and nuclear condensation as the cell breaks down into apoptotic bodies to facilitate absorption by the surrounding tissue [1, 5, 10]. One of the earliest markers for apoptosis is apoptotic volume decrease (AVD), a dramatic reduction in cell volume that occurs independently of the cell's regulatory osmotic response [11, 12]. Hessler *et al*. have used atomic force microscopy to study volume changes in KB (human epidermoid carcinoma) cells undergoing staurosporine-induced apoptosis. The authors found a 50% reduction in volume occurring within two hours after staurosporine exposure [12]. In contrast, many of the other classical markers for apoptosis, including phosphatidylserine translocation, caspase-3 activation, change in mitochondria membrane potential, DNA fragmentation, and plasma membrane blebbing, did not appear until at

least three hours after induction [12].

Apoptotic volume decrease has been attributed to water loss caused by efflux of small ions following apoptotic stimuli [13]. Potassium fluxes have been extensively studied, with the majority of groups reporting an efflux of potassium upon stimulation of apoptosis, independent of cell type or of apoptotic stimulus [13]. For example, L cells (mouse fibroblasts) exposed to the topoisomerase inhibitor VP-16 exhibited a decrease in intracellular K^+ from approximately 110 mM to approximately 50 mM over a period of three days [14], and the T lymphoma cell line CEM-C7A exhibited an approximately 40% decrease in total potassium (146 fmol/cell vs. 86 fmol/cell) over 48 hours after exposure to dexamethasone [15]. S49 Neo lymphoma cells exhibited a >90% decrease in potassium fluorophore PBFI-AM fluorescence 24 hours after exposure to dexamethasone or anisomycin, 8 hours after exposure to A23187 or thrapsigargin, and 6 hours after exposure to staurosporine [16]. Consistent with these observations, administration of potassium channel blocker tetraethylammonium (TEA) was shown to have a protective effect, delaying caspase activation and apoptosis in ceramide-exposed cultured cortical neurons [17]. It is generally accepted that potassium efflux is a necessary precursor to other key apoptotic events, since the binding of cytochrome c to apoptosis promoting factor (Apaf-1), caspase activation, and DNA fragmentation by the nuclease CAD have all been shown to be inhibited under high concentrations (>100 mM) of potassium [18, 19].

The link between apoptosis and cellular sodium and chloride fluxes has also received attention, though these have been less well-characterized compared to potassium efflux [13, 20]. Both sodium influx and efflux have been reported following apoptotic

stimulation, and whether sodium levels increase or decrease seems to depend on the specific cell line and apoptotic inducer that is used. In the study on S49 Neo lymphoma cells cited previously, cells exhibited a decrease in intracellular sodium levels in response to all inducers surveyed (dexamethasone, anisomycin, A23187, thapsigargin, and staurosporine), as judged by a decrease in the fluorescence signal from the sodium-specific fluorophore SBFI-AM [16]. In contrast, electron microprobe analysis of human monocytes induced with oxidized LDL exhibited an increase in sodium contents within 3 hours [21], and electron microprobe analysis of U937 monocytes also demonstrated an increase in sodium 90 minutes after exposure to UV light [22].

On the other hand, the majority of groups report chloride efflux upon induction of apoptosis. The electron microprobe analyses mentioned previously reported decreases in chloride contents [21, 22]. Furthermore, Jurkat T cells exhibited a reduction in intracellular chloride, as judged by a decrease in signal from the chloride fluorophore MEQ, when induced through UV-C exposure [23]. However, that same study also demonstrated no chloride loss when the extrinsic apoptotic pathway was induced though exposure to the Fas ligand [23]. Chloride efflux is generally thought to accompany potassium efflux in order to maintain electroneutrality [13]. Results vary as to whether or not chloride flux is necessary for the activation of apoptosis, and likely depends on the specific cell line and inducer used. The Cl^- channel blocker phloretin inhibited apoptosis in staurosporine-induced ECV304 (human endothelial) cells [24], though the Cl^- channel blockers DIDS, SITS, and NPPB were unable to prevent caspase activation or DNA fragmentation in cortical neurons exposed to staurosporine or ceramide [25].

Intracellular calcium has also been proposed to play a role in the onset and

regulation of apoptosis [10, 20]. There is a complex interplay between intracellular free calcium levels and the activation or inhibition of certain apoptotic pathways. An increase in intracellular free calcium has been noted under a variety of inducers, for cell lines as diverse as Jurkat T cells, neurons, and prostatic cancer cells [20]. Preventing this free calcium accumulation often has a protective effect. For example, depletion of media Ca^{2+} through administration of the calcium chelator quin-2 or through switching to a calcium-free medium prevented apoptosis in thymocytes [26]. In granulosa cells induced by serum withdrawal, apoptosis follows an immediate increase in intracellular free calcium, as determined by an increase in fluorescence signal from the calcium-specific fluorophore Fluo-4 AM, and apoptosis could be prevented by administering the calcium chelator BAPTA [27]. In cases where high intracellular free calcium promotes apoptosis, Ca^{2+} is thought to either act directly through activation of Ca^{2+}-dependent endonucleases and proteases, or indirectly through promoting permeability of the outer mitochondria membrane, releasing cytochrome c into the cytosol, where it can form the pro-apoptotic apoptosome through interaction with Apaf-1 [10]. In many cases, elevation of cytosolic Ca^{2+} is achieved through depletion of calcium stored in the endoplasmic reticulum (ER), and depletion of ER calcium may contribute to ER stress and activation of pro-caspase-12 [10, 28]. However, the link between elevated intracellular free calcium and apoptosis is not universal, as U937 monocytes were protected from apoptosis by stimulating Ca^{2+} influx with magnetic fields [29].

In addition to the bulk ions, certain transition metals, particularly zinc, have been implicated in the activation and regulation of apoptotic cell death. Both zinc excess and zinc deficiency potentiate cells for apoptosis, and mild zinc supplementation has a

protective effect for a variety of cell lines and inducers [30, 31]. Zinc is known to inhibit caspase-3 *in vitro* [32], an effect believed to be mediated through interaction with a catalytic sulfhydryl group [30], which partially explains its protective effect. The interaction of Zn^{2+} with sulfhydryl groups is also thought to help ameliorate oxidative stress by providing a barrier to disulfide formation [30]. Labile zinc pools associated with mitochondria have also received some attention, since high (10 mM) concentrations of zinc have been found to prevent cytochrome c release from mitochondria [33], although it is unknown if this phenomenon plays a role under biological conditions.

One common element of many of these studies is that ion-specific fluorophores are typically used to study the changes in ionic composition and distribution after induction of apoptosis. While this work has revealed much about the behavior of ions in cells, fluorophore studies suffer from two potential limitations. First, fluorophores are not completely element-specific. In one study on ionic fluxes after induction of apoptosis in mouse fibroblasts, cells with high Na^{+} (as judged by SBFI-AM fluorescence) had to be excluded from analysis, since the affinity of PBFI-AM for potassium is only 50% greater than that for sodium [14]. Furthermore, there is evidence that excitotoxicity in hippocampal neurons following ischemia, originally believed to be due to transient increases in Ca^{2+} as judged by increases in Calcium Green-1 fluorescence, may actually be caused by transient increases in Zn^{2+}, since administration of the intracellular zinc chelator TPEN has been shown to quench Calcium Green-1 fluorescence [34]. Secondly, fluorophores only give information about the solvent-accessible fraction of the ion under study. Tightly chelated or otherwise inaccessible ions cannot be detected. One alternative is to take advantage of the elements' intrinsic X-ray fluorescence, which allows sensitive

and specific elemental detection. Therefore, in order to gain a more complete picture of the bioinorganic chemistry of mammalian cells undergoing apoptosis, we imaged by X-ray fluorescence KB cells induced by staurosporine (STS), a potent kinase inhibitor.

Materials and Methods

Sample Preparation

KB cells (human epithelial carcinoma) were obtained from the American Type Culture Collection and grown directly on uncoated, 200-nm thick silicon nitride windows obtained from Structure Probe, Inc (West Chester, PA). The growth media was RPMI-1640, R 8758, obtained from Invitrogen (Carlsbad, CA). Cells were incubated at 30°C and 5% CO_2 for two days prior to treatment. After reaching maturity, cultures were treated with 2 μM staurosporine, obtained from BIOMOL International (Plymouth Meeting, PA), for 0, 30, 60, 90, or 140 minutes. At the designated times, the silicon nitride windows were dipped twice into potassium-free PBS solution (130 mM NaCl, 7 mM Na_2HPO_4, 3 mM $NaH_2PO_4 \cdot H_2O$, pH 7.4) and once into 120 mM ammonium carbonate solution (pH 9.0). These rinses were done to remove the excess media. After washing, samples were plunge frozen into liquid nitrogen-cooled liquid propane and lyophilized overnight. Ammonium carbonate is a volatile buffer that is removed during the freeze-drying step, leaving behind a clean background.

X-Ray Fluorescence Imaging

X-ray fluorescence imaging was performed at Sector 2-ID-E at the Advanced Photon Source at Argonne, IL. A Leica microscope (Leica Microsystems, Wetzlar,

Germany) was used to locate appropriate cells for imaging. Cells were selected for imaging if they appeared visually intact after plunge freezing and sufficiently isolated to define a region of interest (ROI) around individual cells during subsequent analysis. Undulator-derived X-rays were monochromatized to 10 keV incident energy using a single-bounce Si(111) monochromator and focused to a spot size of 0.5 μm horizontal by 0.3 μm vertical using Fresnel zone plate optics (X-radia, Concord, CT). Samples were raster-scanned through the X-ray beam using 0.5 μm horizontal and 0.3 μm vertical steps. Fluorescence spectra were collected for one second per pixel using a single-element Ge detector (Canberra Industries, Meriden, CT).

Data Analysis

Image processing and elemental quantification were performed using Maps software [35]. Normalized fluorescence intensities for each element at each pixel were converted to a two-dimensional concentration in micrograms per square centimeter by calibrating to the spectra obtained from the NIST thin-film standards NBS-1832 and NBS-1833 (National Institute of Standards and Technology, Gaithersberg, MD). Elemental levels were quantified by defining a region of interest (ROI) around a cell and another around a section of the background. The average concentrations in $\mu g/cm^2$ were calculated for both the cell and background ROIs. The average background concentration was subtracted from the average cell concentration, and the total elemental contents of each cell were calculated by multiplying the background-subtracted two-dimensional concentrations by the cell ROI area. Statistical significance of elemental levels relative to the control was determined using the Mann-Whitney *U* test [36], with $p < 0.05$ deemed

significant.

Propidium Iodide Staining

Propidium iodide (PI) was obtained from BioLegend (San Diego, CA). KB cells were incubated in well plates in RPMI 1640 media for two days at 30°C and 5% CO_2. Samples were exposed to 2 µM staurosporine for 0, 5, 30, 60, 90, or 120 minutes. Five minutes before each time point, samples were exposed to 5 µg/mL PI. Samples were illuminated with 488 nm light and photographed through a 562-588 nm band pass filter. The percentage of PI-stained cells was determined by inspection.

Results

Table 4.1 shows the control sample whole-cell concentrations of the elements surveyed in this study, and Table 4.2 shows the primary components of RPMI 1640 media for comparison. Fluorescence intensity in counts per second, normalized to the incident beam intensity, was converted to concentration in µg/cm^2 by comparison to the NIST thin-film standards 1832 and 1833. The elemental totals were determined by integrating over a region of interest (ROI) around the cell. The KB cell volume was taken to be 3 pL based on previous atomic force microscopy measurements [12]. Average metal concentrations tend to be conserved throughout a variety of cell types, except for certain specialized cells such as red blood cells [37]. The calculated K, Ca, Fe, Cu, and Zn concentrations are consistent with those determined for *Escherichia coli*; namely, >10 mM K, ~100 µM Ca, Fe, and Zn, and ~10 µM Cu [38]. Furthermore, the calculated Cl and K concentrations are close to the intracellular concentrations determined from

fluorophore studies, roughly 4-60 mM Cl and 130-150 mM K [20]. Taken together, these results confirm that the sample wash and plunge-freezing steps do not significantly perturb normal elemental concentrations.

Figures 4.1 through 4.5 show sample images for KB cells after 0, 30, 60, 90, and 140 minutes of STS exposure, respectively. The total numbers of cells at each time point were 9, 11, 10, 8, and 7, respectively, so these images together represent one third of all cells imaged. In general, phosphorous, sulfur, chloride, potassium, and zinc are all co-localized, and the maximum of these maps was taken to represent the nucleus. Iron tends to be localized and excluded from the nucleus. Since most cellular iron is located in the mitochondria [39], this localized iron was taken to represent the mitochondrial network. In most cases, calcium and copper tended not to be localized, but spread uniformly through the cytosol.

After 30 minutes of exposure to staurosporine, an apparent relocalization was observed in the calcium maps, with calcium aggregating and co-localizing with zinc (Figure 4.2). This phenomenon was observed in 6 out of 11 cells imaged, or roughly 50%. The hot spots in the calcium and zinc maps did not appear to localize to the nucleus or the mitochondrial network. The calcium:zinc mole ratio in these areas was calculated to be 1.9 ± 0.2 (standard error of the mean, n = 6), which was significantly higher than the whole-cell calcium:zinc mole ratio for these samples (0.8 ± 0.2, n = 6). Localization in the calcium and zinc maps was also observed at the 60 minute time point, although to a lesser extent than at the 30 minute time point. At 60 minutes, only 2 out of 10, or 20% of the cells imaged (both of which are shown in Figure 4.3), exhibited this localization. At 60 minutes, copper was found to co-localize with calcium and zinc. The calcium:zinc

mole ratio in these localized regions was determined to be 5 ± 1, and the calcium:copper mole ratio to be 18 ± 3, both considerably higher than the whole-cell ratios of 0.8 ± 0.1 and 10 ± 2, respectively.

Total potassium levels were found to decrease monotonically as a function of time after staurosporine exposure (Figure 4.6) and matched that of a 3 pL volume of RPMI 1640 media by the 140 minute time point. Potassium levels were significantly lower than the control ($p < 0.001$) at all time points. In contrast, chloride levels increased monotonically throughout the course of the experiment (Figure 4.7), matching that of a 3 pL volume of RPMI 1640 media by the final time point. Chloride levels were significantly higher than the control ($p < 0.05$) at all time points. The chloride-to-potassium ratio for each cell was also calculated in order to compare the ionic composition of each cell to the surrounding media without making any assumption about the cell volume. The result is shown in Figure 4.8. There is a statistically significant increase ($p < 0.001$) at the 30 minute time point compared to the control, and a monotonic increase throughout all time points surveyed, with a final chloride:potassium ratio of 19 ± 4, matching that of RPMI 1640 (chloride:potassium ratio of 20:1).

Total calcium levels were found to fluctuate throughout the course of the experiment (Figure 4.9). There is an initial, statistically significant ($p < 0.05$) increase in total calcium at 30 minutes following exposure to staurosporine, followed by a decrease between 30 and 90 minutes. At 60 minutes, total calcium levels match that of the control sample, and by 90 minutes total calcium levels are significantly below the control levels ($p < 0.05$). Total calcium increases between 90 and 140 minutes to a level significantly higher than the control ($p < 0.01$), with a final total matching that of a 3 pL volume of

RPMI 1640 media.

Both zinc (Figure 4.10) and iron (Figure 4.11) levels remained relatively constant over time, with no statistically significant differences from the control sample. This would seem to suggest that any functions these two metals may have during the early stages of apoptosis are dependent on re-localization of whatever metals are currently present, rather than influx or efflux of metal ions. In contrast, total copper exhibited a statistically significant increase at the 140-minute time point compared to the control ($p < 0.001$) (Figure 4.12).

Propidium iodide staining was carried out in order to assess membrane integrity of KB cells as a function of staurosporine exposure time. Example images from the control and 120 minute time points are shown in Figures 4.13 and 4.14, respectively. The percentage of cells exhibiting propidium iodide fluorescence at each time point is shown in Figure 4.15. In general, the percentage of PI-stainable cells did not vary significantly over time. The percentage of PI-stainable cells varied between zero and five percent, with two percent being typical. There were no significant differences in the fraction of PI-stainable cells for any of the time points surveyed compared to the control, except for the 30-minute time point, which exhibited a statistically significant ($p < 0.05$) decrease.

Discussion

In the work presented here, cellular potassium and chloride levels were altered in response to staurosporine exposure such that the molar ratio of chloride to potassium roughly matched that of the surrounding media by the 140-minute time point (Figure 4.8). This likely represents ion fluxes through membrane channels, since there

was no significant increase in the fraction of cells stainable by propidium iodide 120 minutes after staurosporine exposure (Figure 4.15), indicating that the membrane remained intact. For the 140-minute time point, the fact that there was no significant change in the total zinc and iron (Figures 4.10 and 4.11) provides further evidence against membrane disruption. Zinc and iron are concentrated roughly 100-fold over media levels, and most of the intracellular zinc and iron is tightly associated with proteins [38]. Although this tight association with proteins will lower the mobility of zinc and iron compared to the bulk ions, the fact that no significant losses in zinc and iron are seen throughout the course of the experiment suggests at least that there are no membrane ruptures large enough to allow proteins to leak into the media.

Thus, it appears as if the cytosol of KB cells exposed to staurosporine is gradually altered to match that of the surrounding media, even though the membrane remains intact. The remarkable feature about this is that KB cells may not be committed to apoptosis at this point. The factors which lead to commitment to apoptosis as opposed to survival or necrosis are not completely understood, but it is commonly believed that for many cell lines and apoptotic pathways the permeability transition of the outer mitochondrial membrane represents the point of no return [40, 41]. The mitochondrial lumen contains several pro-apoptotic factors, including cytochrome c, which can combine with Apaf-1 in the cytosol to form the apoptosome, thereby activating caspase-9, and Smac/DIABLO, which inhibits the anti-apoptotic IAP proteins [5, 10, 42]. For many apoptotic pathways, pores are formed in the outer mitochondrial membrane by oligomers of the Bcl-2 family proteins Bax and Bak [43], which releases these pro-apoptotic factors into the cytosol. The release of cytochrome c into the cytosol is often thought to

accompany a loss in the mitochondria membrane potential [44], and in KB cells treated with 1 μM staurosporine, no loss in mitochondria membrane potential was detected 3 hours after exposure [12]. Although cytochrome c release precedes mitochondria membrane potential loss for some cell lines and inducers [45], when HeLa cells—of which KB cells are a sub-line [46]—are exposed to 1 μM staurosporine, mitochondria membrane potential loss accompanies cytochrome c release, and neither event is observed until after 6 hours of treatment [45]. This suggests that if the increase in mitochondria outer membrane permeability is the point of no return for apoptotic cells, then after 2.5 hours, staurosporine-treated KB cells ought to be viable despite the fact that the cytosolic ionic composition has apparently equilibrated with the media.

The average total potassium concentration for the control cells was calculated to be 90 ± 7 mM, and the average total chloride concentration calculated to be 12 ± 3 mM. These numbers are similar to estimates of the K^+ and Cl^- concentrations for most cells (130-150 mM and 4-60 mM, respectively) using element-specific fluorophores [13, 20, 47]. This suggests either that there are few internal pools of these ions that are not accessible to fluorophores, or that both K^+ and Cl^- are relatively uniformly distributed through the cytosol. In line with several fluorophore studies of potassium fluxes during apoptosis, the work presented here finds that potassium decreases monotonically as a function of time after exposure to an apoptotic stimulus. In contrast, although the role of chloride in AVD and apoptosis has received less attention than the other bulk ions, the findings presented here differ from what is commonly observed. Jurkat T cells experience a decrease in chloride content over time, as measured by the fluorophore MEQ, after exposure to UV-C light [23]. Furthermore, electron microprobe studies of apoptotic

monocytes have demonstrated chloride loss under a variety of apoptotic stimuli [21, 22]. Chloride loss has commonly been attributed to co-transport with K^+ in order to maintain charge balance [13]. However, work presented here challenges that view.

Instead, we hypothesize that chloride fluxes depend upon the specific cell line, especially in regards to their membrane potential and free ion concentrations relative to the media. Assuming that potassium, sodium, and chloride represent the most important bulk ions, the membrane potential of a given cell, E_{rev}, depends upon the intracellular and extracellular concentrations of these ions as well as the membrane permeability to each ion type [47]. This is calculated using the Goldman-Hodgkin-Katz (GHK) voltage equation:

$$E_{rev} = \frac{RT}{F} \ln \frac{P_K[K]_o + P_{Na}[Na]_o + P_{Cl}[Cl]_i}{P_K[K]_i + P_{Na}[Na]_i + P_{Cl}[Cl]_o}$$

where P_X represents the permeability of the membrane to ion X, $[X]_o$ represents the extracellular concentration of ion X, and $[X]_i$ represents the intracellular concentration of ion X. R represents the gas constant, T represents the temperature, and F represents Faraday's constant. In addition, each ion X has an associated equilibrium potential E_X calculated from the Nernst equation:

$$E_X = \frac{RT}{z_X F} \ln \frac{[X]_o}{[X]_i}$$

where z_X is the charge on ion X and all other variables are defined as before. The equilibrium potential for ion X is the membrane potential at which the energy loss associated with moving an ion down a concentration gradient defined by $[X]_o$ and $[X]_i$ is exactly canceled by the energy gain associated with moving an ion with charge z_X across the voltage gradient E_X. As a result, there is no net movement of ion X across the

membrane when the membrane potential is equal to E_X and the outer and inner concentrations are $[X]_o$ and $[X]_i$, respectively. Alternatively, if the membrane potential were at voltage $V \neq E_X$ and the membrane permeability to ion X were increased, one would predict a net flow of X such as to move V closer to E_X. Similarly, in a real system in which Na^+, K^+, and Cl^- are all taken into account, if $E_{rev} \neq E_{Cl}$ and the membrane chloride permeability P_{Cl} is increased, the net flow of Cl^- would be such that E_{rev} is brought closer to E_{Cl}.

These ideas can be used to rationalize at least the initial chloride fluxes in KB cells as opposed to Jurkat T cells. For KB cells in RPMI 1640 media, $[Cl]_i$ is approximately 12 mM, and $[Cl]_o$ is 108 mM. At 30°C, this translates to E_{Cl} = -57.4 mV. The overall membrane potential of KB cells has been measured to be -13.4 mV at 30°C [48]. Thus, if the membrane permeability to chloride were increased, one would expect a net movement of Cl^- such as to bring E_{Cl} closer to E_{rev}, or in this case, a net movement of chloride into the cell. In Jurkat T cells, the intracellular chloride concentration has been calculated to be approximately 58 mM [23]. RPMI 1640 was the growth medium used in that experiment, so with $[Cl]_o$ = 108 mM, this translates to E_{Cl} = -16.2 mV at 30°C. The temperature-adjusted membrane potential for Jurkat T cells grown in RPMI 1640 media at 30°C is approximately -48.0 mV [49], so in this case increasing the membrane permeability to chloride would result in a net chloride efflux.

The loss in total calcium between 30 and 90 minutes after staurosporine exposure was unexpected. The majority of groups investigating the link between calcium signaling and apoptosis report an increase in intracellular labile calcium following apoptotic stimulation, a result attributed to either release of calcium from the endoplasmic

reticulum (ER) or to influx of extracellular Ca^{2+} [10, 20]. This may partially be due to differences in the technique used. Intracellular labile calcium is typically stored in the ER, where concentrations reach approximately 100 nM [20, 47]. In contrast, the average total calcium concentration, including bound and labile forms, is approximately 220 μM (Table 4.1). Thus, labile calcium represents only a small fraction of the total calcium content, and changes in this calcium pool are not necessarily indicative of changes in the global calcium concentration. This underscores the advantage of using both approaches, in order to obtain a more complete picture of how the calcium distribution changes over time. It is unknown why staurosporine-exposed KB cells should export calcium; however, it seems likely that this process may be crucially important to the cell, either as a stress response to staurosporine exposure or as a signaling event in apoptosis. At 90 minutes, total calcium levels are significantly below that of the control. In RPMI 1640 media, the Ca^{2+} concentration is 424 μM (Table 4.2). Thus, even if all cellular calcium were liberated from proteins, it would still have to be moved against a concentration gradient in order to achieve a net efflux. In addition, while plasma membrane depolarization is known to occur after induction of apoptosis for a variety of cell lines and inducers [50], a sign change in E_{rev} is not known to occur. This suggests that the calcium must also move against a negative voltage gradient, which suggests that calcium efflux is due to an active process, rather than passive. That the cell expends energy to accomplish this suggests that this phenomenon is significant in some way.

Co-localization of calcium and zinc was observed for some of the cells at 30 minutes, and co-localization of calcium, zinc, and copper at 60 minutes (Figures 4.2 and 4.3). The localized calcium, zinc, and copper do not appear to co-localize with the

nucleus. Furthermore, none of these elements co-localized with the iron, and since the iron is taken here as a mitochondria indicator, it is unlikely that this localization is related to the labile mitochondrial calcium and zinc pools thought to have a role in apoptosis. The reason for co-localization of these elements is unknown. The presence of zinc and copper often have an antagonistic relationship on calcium uptake and transport, and vice versa [51-54]. Given the calcium fluxes that are taking place during this time period (Figure 4.9), this may represent adventitious movement of zinc and copper as the cell mobilizes calcium.

Finally, comment should be made regarding the copper spike at the 140-minute time point (Figure 4.12). Although the connection between copper and apoptosis has not received as much attention as the link between zinc and apoptosis, it is known that both excess and deficiency of copper can induce apoptosis. Down-regulation of SOD1 has been linked to increased susceptibility to apoptosis [55]. On the other hand, copper is redox-active and potentially toxic. For example, incubation with 300 μM Cu^{2+} has been shown to induce apoptosis in cerebellar granular neurons through peroxide generation [56]. Thus, the copper spike at the 140-minute time point may plausibly represent an attempt by the cell to ameliorate oxidative stress through increased Cu/Zn-SOD production, or it may represent a side effect of staurosporine damage, e.g., extensive damage leading to deregulation of copper homeostasis, placing the cell under increased oxidative stress. It would be interesting to test whether or not chelation of media copper prior to this time point enhances apoptosis, or whether it has a protective effect.

Table 4.1: Whole-cell total elemental concentrations for human KB cells

Element	Concentration (mM)
P	25 (1)
S	22 (1)
Cl	12 (3)
K	90 (7)
Ca	0.22 (3)
Fe	0.09 (1)
Cu	0.014 (1)
Zn	0.37 (3)

Table 4.2: Primary components of RPMI 1640 media

Component	g/L	m.w. [g/mol]	conc. [mM]	Element	conc. [mM]
$Ca(NO_3)_2 \cdot 4H_2O$	0.1	236.06	0.42	Ca(II)	0.424
$MgSO_4$ (anh.)	0.04884	120.42	0.41	K+	5.365
KCl	0.4	74.55	5.37	Cl-	108.030
$NaHCO_3$	2.0	84.01	23.81	Na+	137.743
NaCl	6.0	58.44	102.66		
Na_2HPO_4 (anh.)	0.8	141.96	5.64		

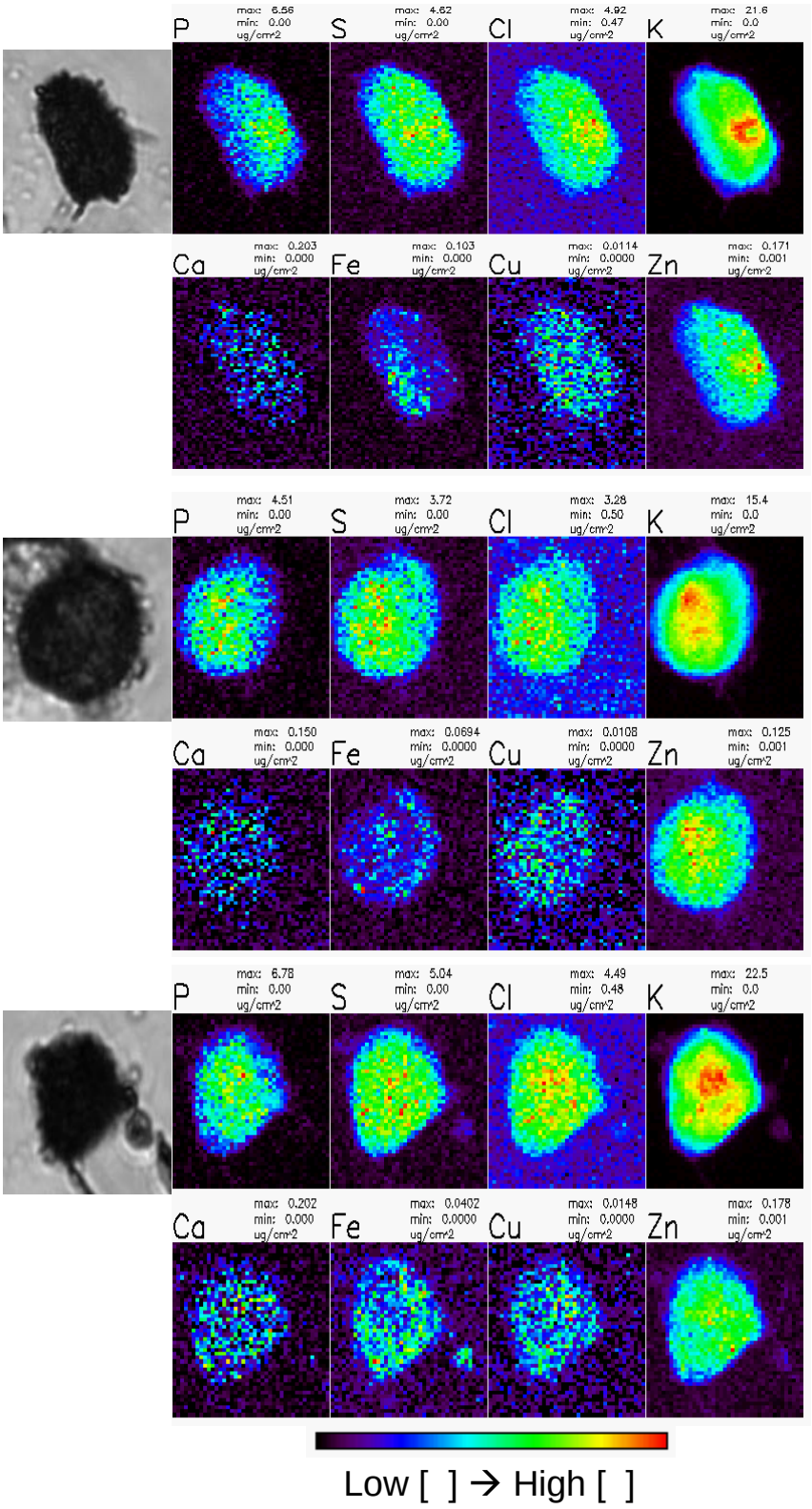

Figure 4.1: Sample XRF images for control sample.

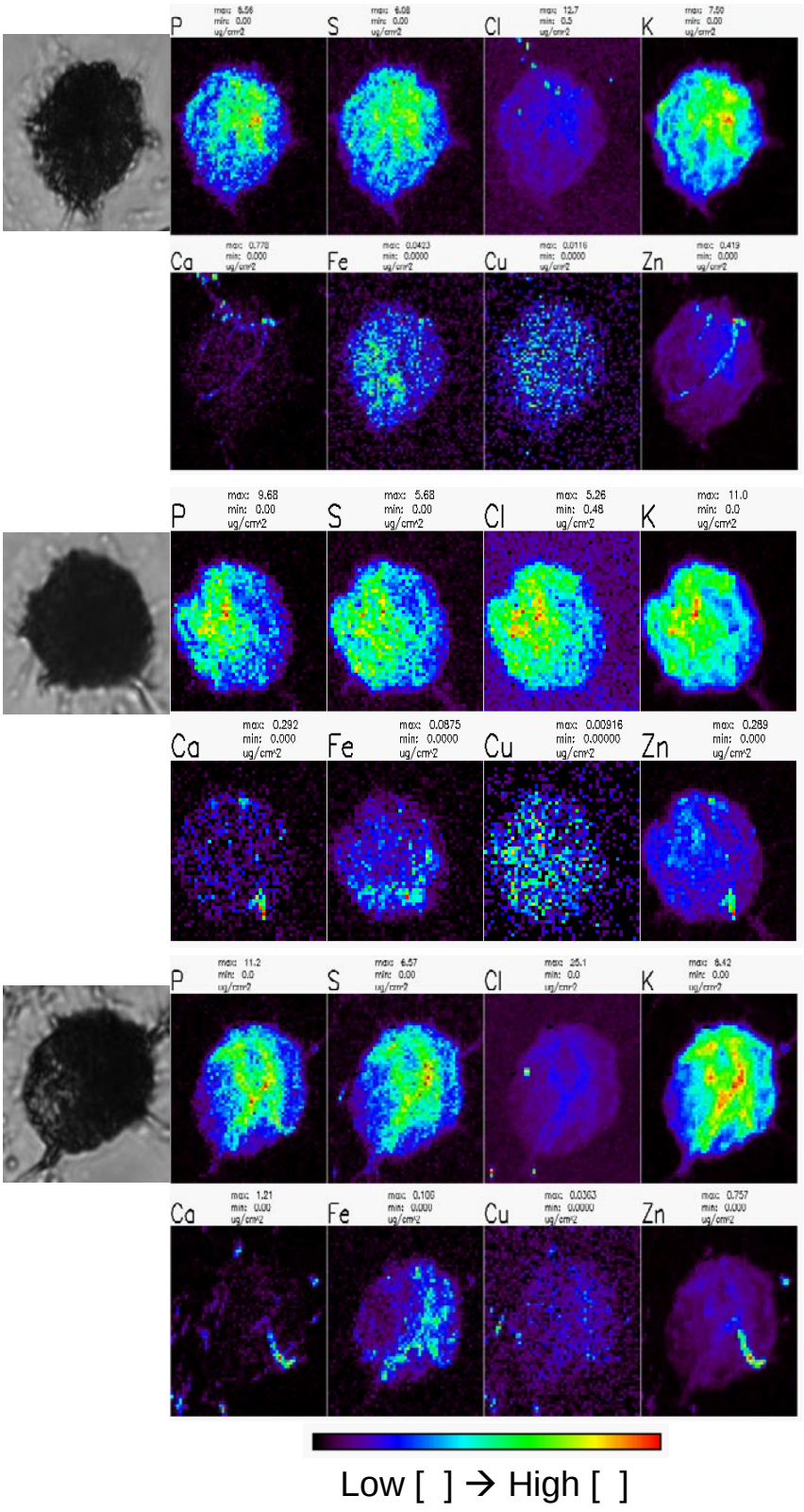

Figure 4.2: Sample XRF images after 30 minutes of STS exposure.

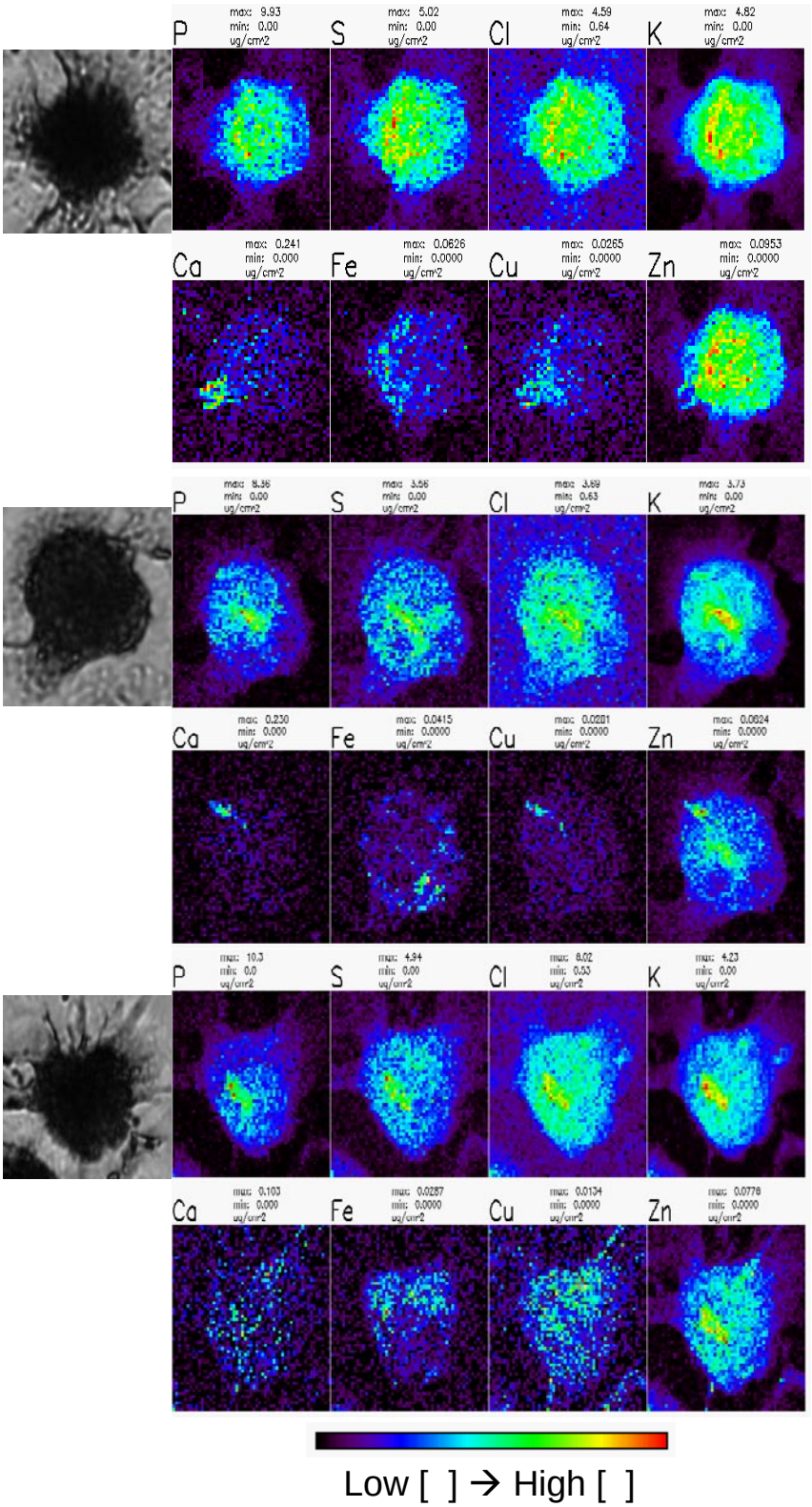

Figure 4.3: Sample XRF images after 60 minutes of STS exposure.

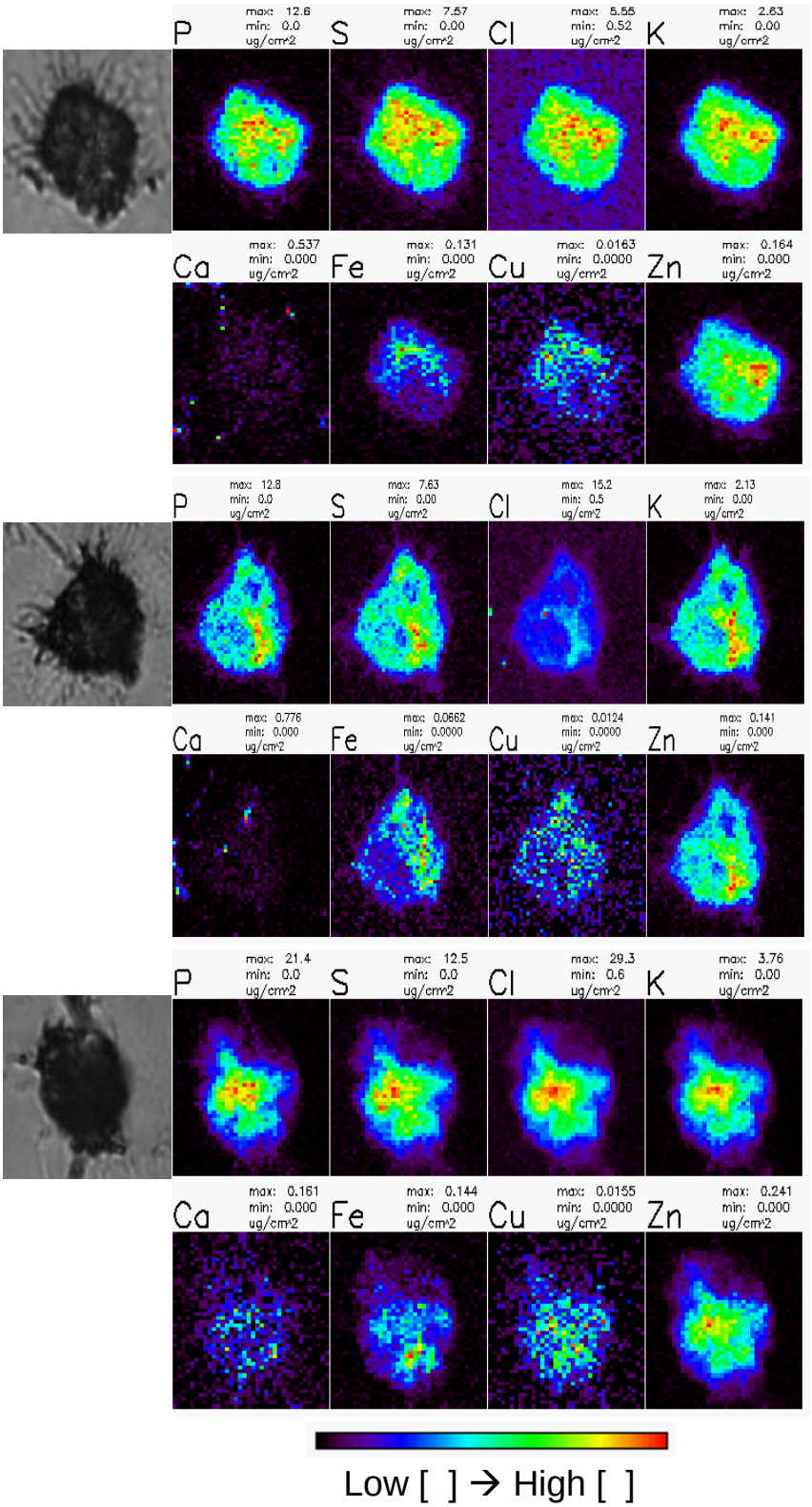

Figure 4.4: Sample XRF images after 90 minutes of STS exposure.

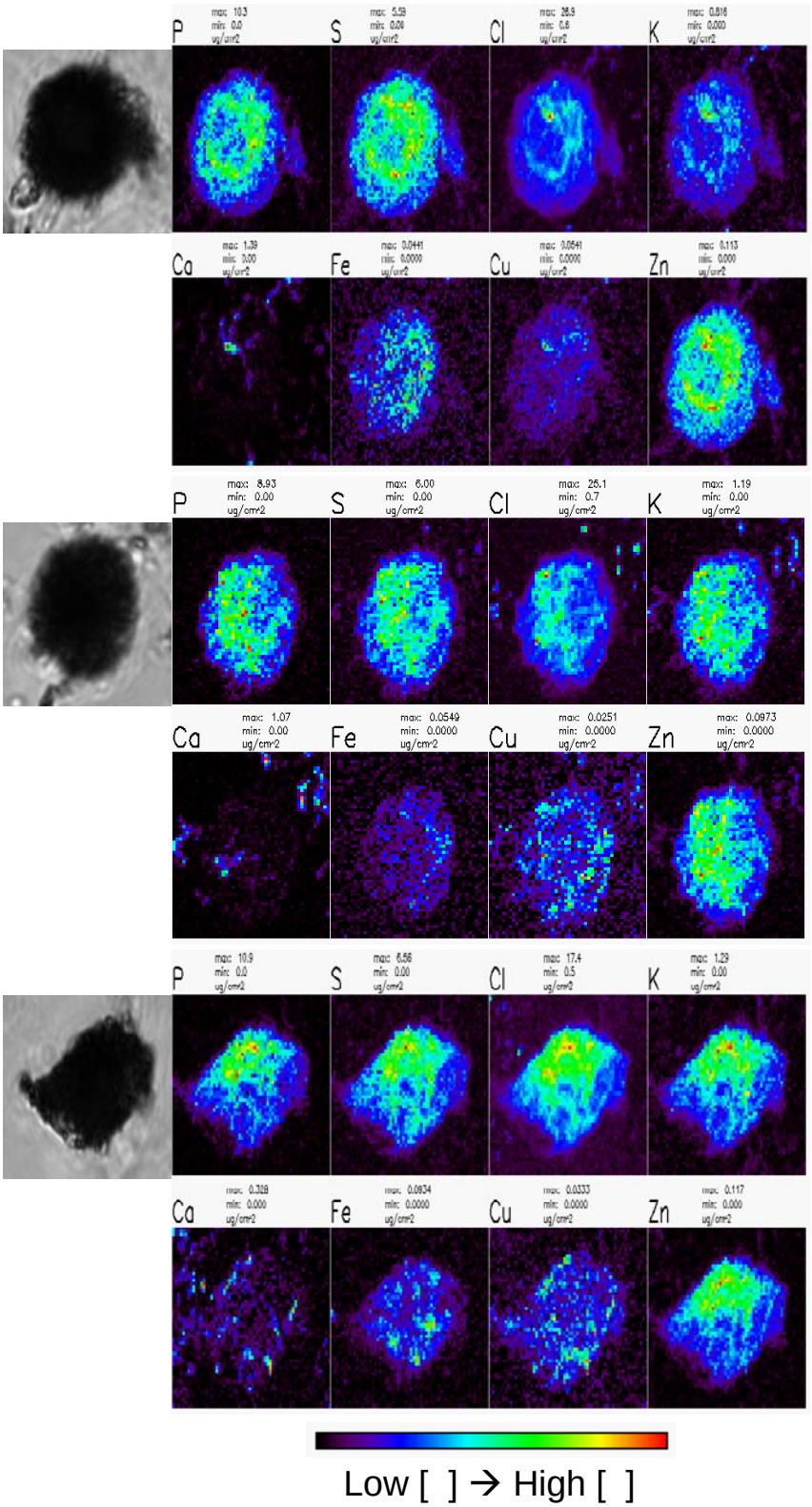

Figure 4.5: Sample XRF images after 140 minutes of STS exposure.

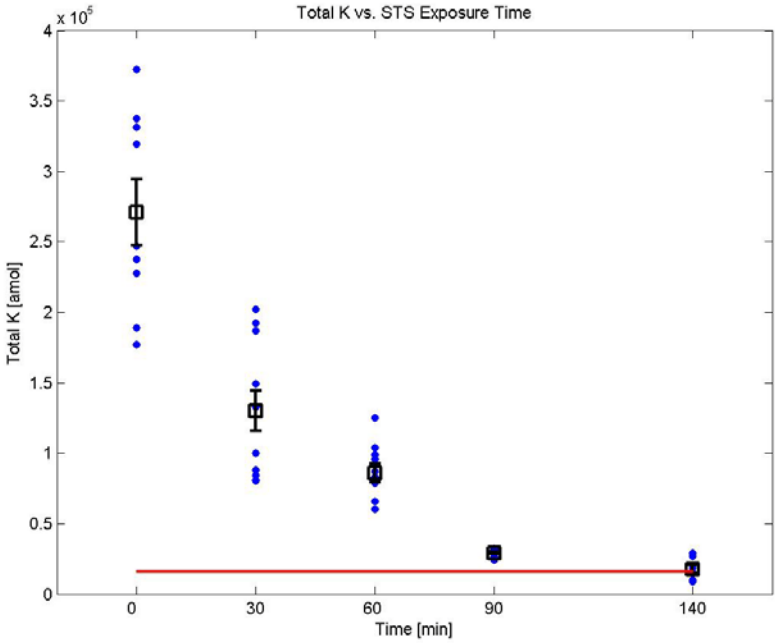

Figure 4.6: Total potassium levels as a function of staurosporine exposure. The blue points represent individual cells, while the black squares represent the average for that time point. Error bars represent one standard error of the mean. The red line represents the potassium contents of a 3 pL volume of RPMI 1640 media.

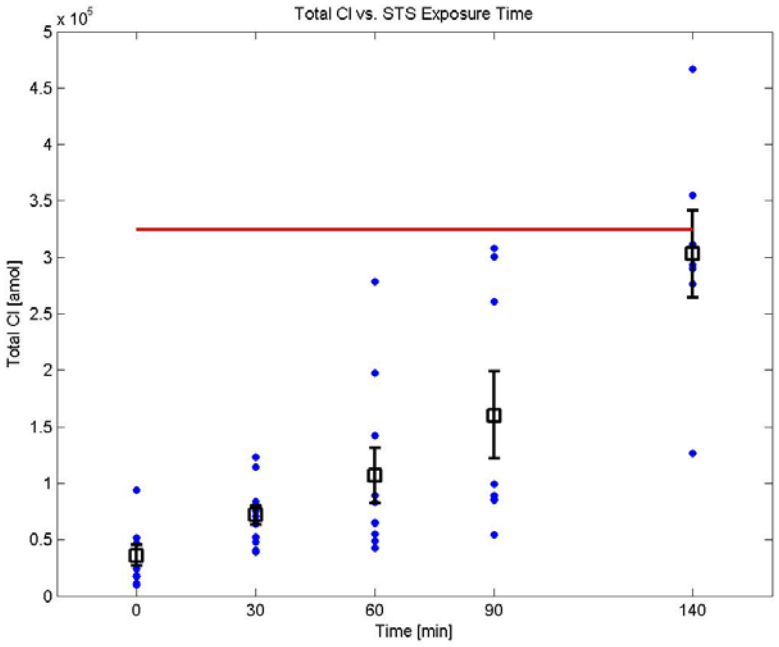

Figure 4.7: Total chloride levels as a function of staurosporine exposure. The blue points represent individual cells, while the black squares represent the average for that time point. Error bars represent one standard error of the mean. The red line represents the chloride contents of a 3 pL volume of RPMI 1640 media.

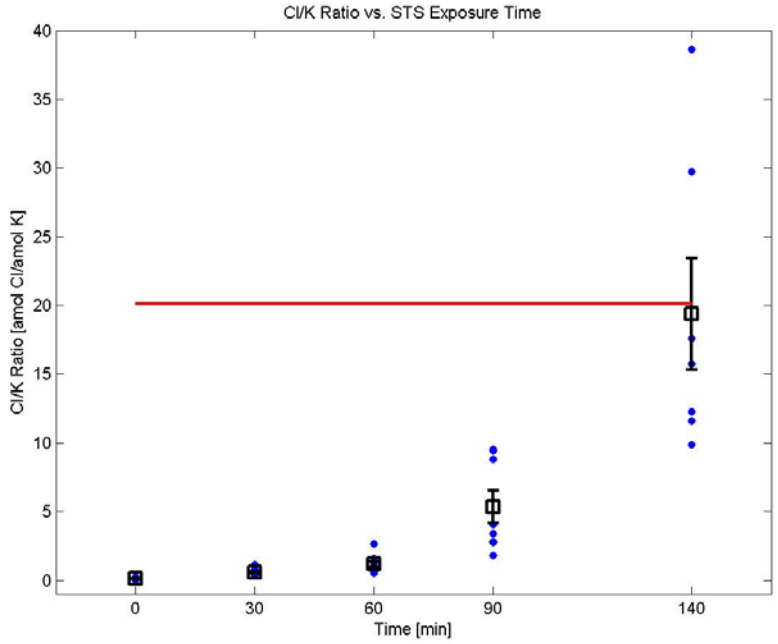

Figure 4.8: Chloride-to-potassium ratio as a function of staurosporine exposure. The blue points represent individual cells, while the black squares represent the average for that time point. Error bars represent one standard error of the mean. The red line represents the chloride-to-potassium ratio of RPMI 1640 media.

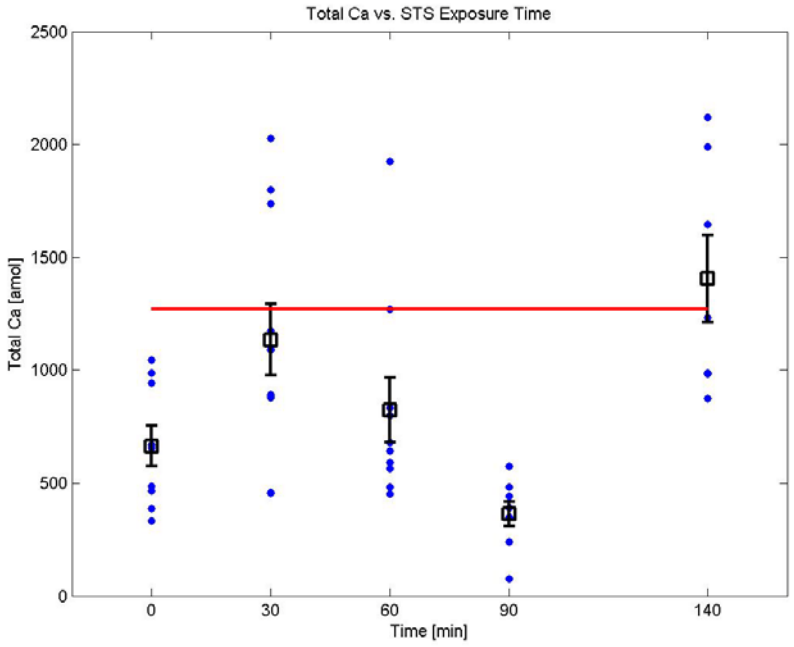

Figure 4.9: Total calcium levels as a function of staurosporine exposure. The blue points represent individual cells, while the black squares represent the average for that time point. Error bars represent one standard error of the mean. The red line represents the calcium contents of a 3 pL volume of RPMI 1640 media.

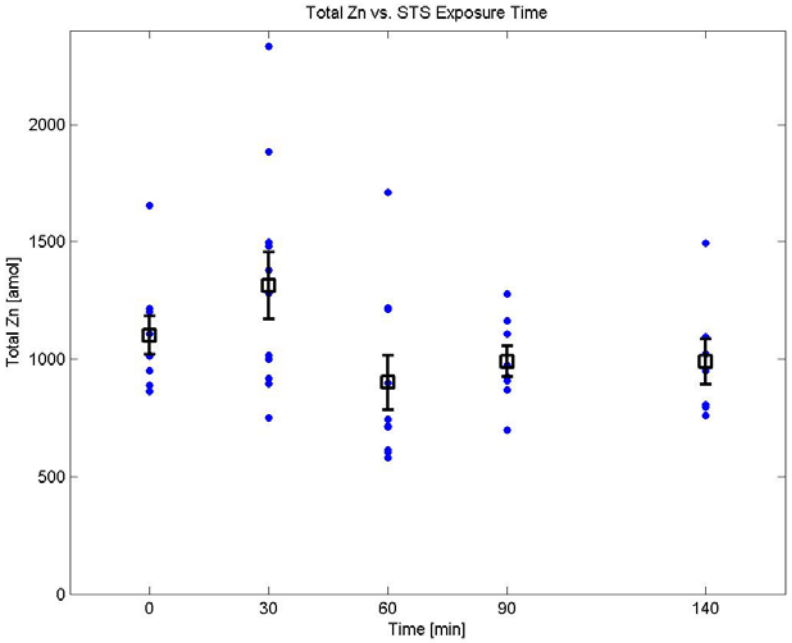

Figure 4.10: Total zinc levels as a function of staurosporine exposure. The blue points represent individual cells, while the black squares represent the average for that time point. Error bars represent one standard error of the mean.

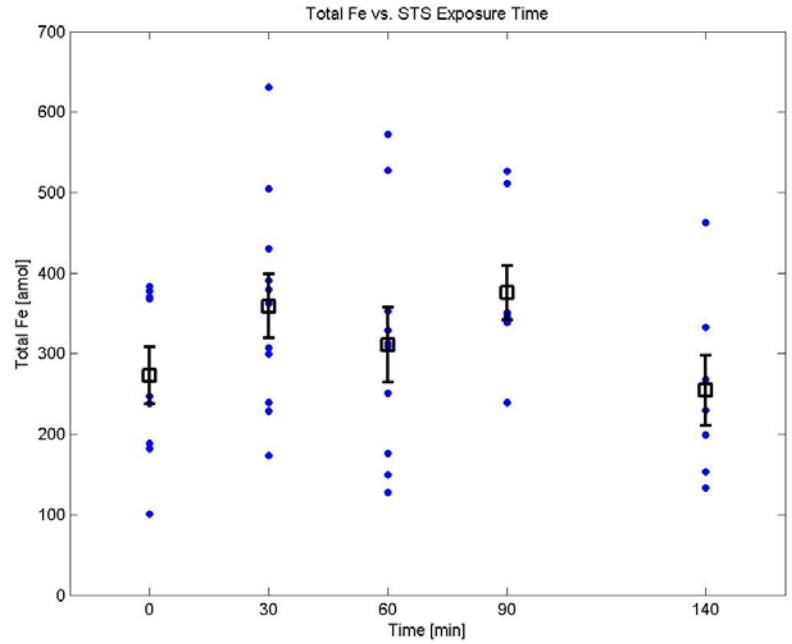

Figure 4.11: Total iron levels as a function of staurosporine exposure. The blue points represent individual cells, while the black squares represent the average for that time point. Error bars represent one standard error of the mean.

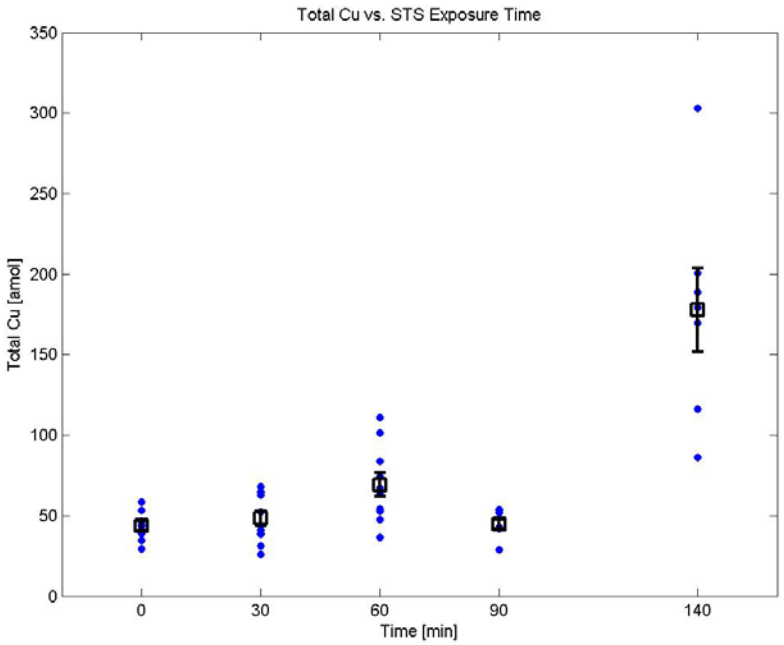

Figure 4.12: Total copper levels as a function of staurosporine exposure. The blue points represent individual cells, while the black squares represent the average for that time point. Error bars represent one standard error of the mean.

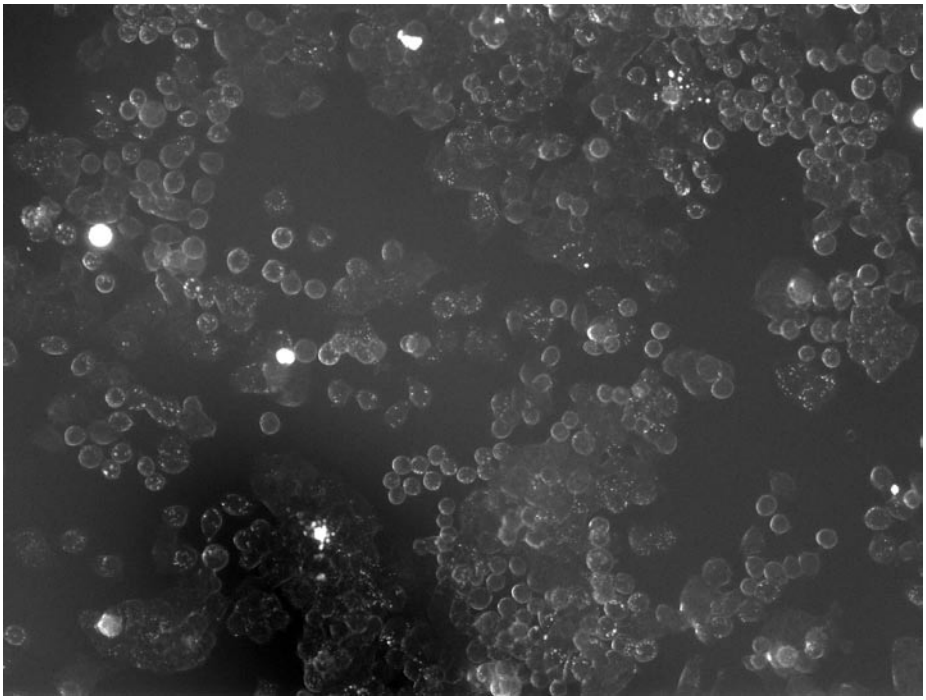

Figure 4.13: Propidium iodide fluorescence from an untreated culture.

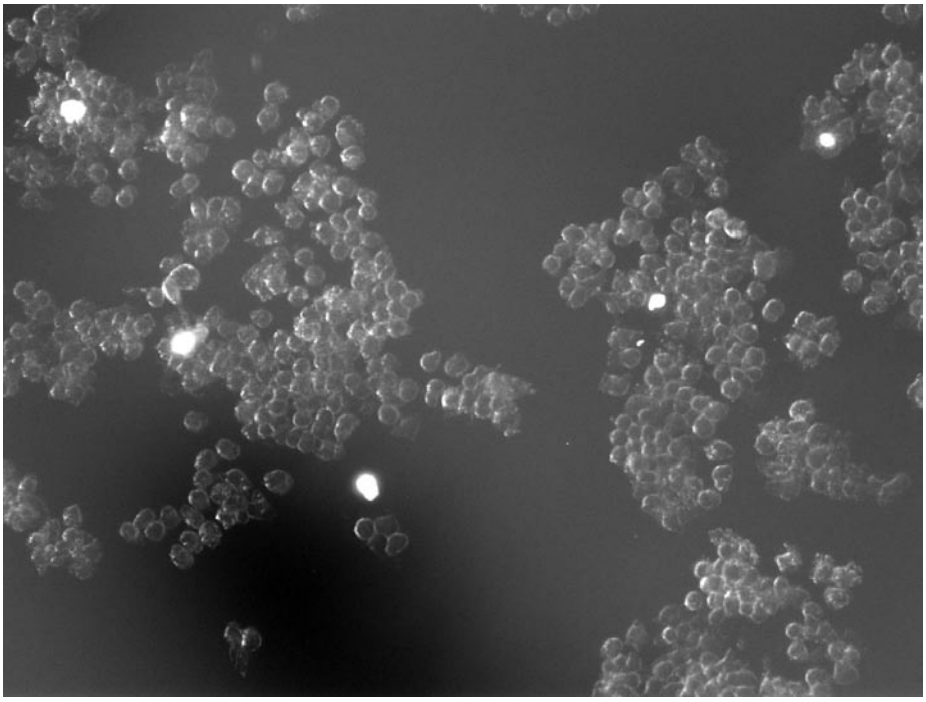

Figure 4.14: Propidium iodide fluorescence after 120 minutes of exposure to 2 μM STS.

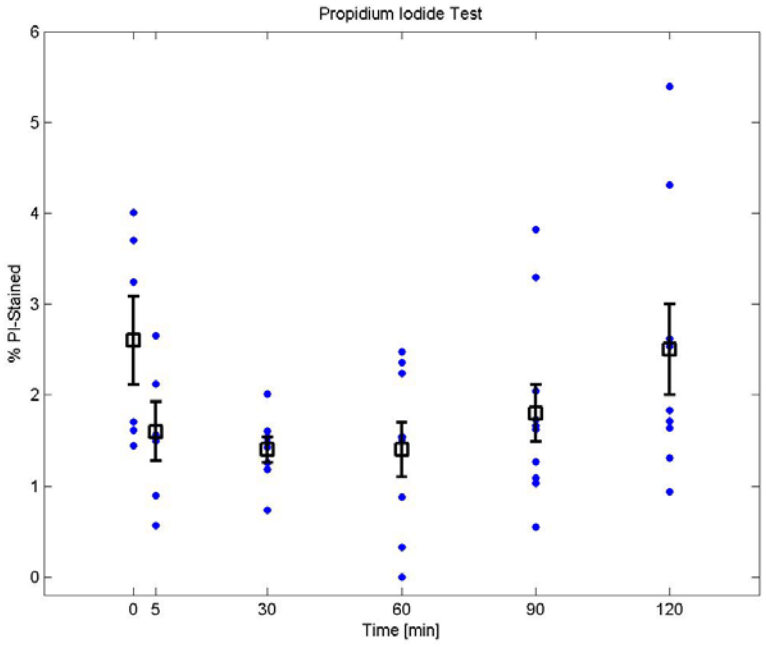

Figure 4.15: Percent KB cells stained by propidium iodide as a function of staurosporine exposure time.

References

1. Bowen, I.D., S.M. Bowen, and A.H. Jones, *Mitosis and Apoptosis: Matters of Life and Death*. 1998, London: Chapman & Hall.
2. Elmore, S., *Apoptosis: a review of programmed cell death.* Toxicologic pathology, 2007. **35**(4): p. 495.
3. Fadeel, B. and S. Orrenius, *Apoptosis: a basic biological phenomenon with wide-ranging implications in human disease.* Journal of internal medicine, 2005. **258**(6): p. 479.
4. Zhang, A., et al., *Apoptosis-a brief review.* Neuroembryology, 2004. **3**(1): p. 47.
5. Potten, C. and J. Wilson, *Apoptosis: The Life and Death of Cells*. 2005: Cambridge University Press.
6. Bold, R.J., P.M. Termuhlen, and D.J. McConkey, *Apoptosis, cancer and cancer therapy.* Surgical Oncology, 1997. **6**(3): p. 133.
7. Lee, J.M. and A. Bernstein, *Apoptosis, cancer and the p53 tumour suppressor gene.* Cancer and Metastasis Reviews, 1995. **14**(2): p. 149.
8. Friedlander, R.M., *Apoptosis and caspases in neurodegenerative diseases.* New England Journal of Medicine, The, 2003. **348**(14): p. 1365.
9. Mattson, M.P., et al., *Neurodegenerative disorders and ischemic brain diseases.* Apoptosis, 2001. **6**(1/2): p. 69.
10. Orrenius, S., B. Zhivotovsky, and P. Nicotera, *Regulation of cell death: the calcium–apoptosis link.* Nature Reviews. Molecular Cell Biology, 2003. **4**(7): p. 552.
11. Bortner, C.D. and J.A. Cidlowski, *Apoptotic volume decrease and the incredible shrinking cell.* Cell Death and Differentiation, 2002. **9**(12): p. 1307.
12. Hessler, J., et al., *Atomic force microscopy study of early morphological changes during apoptosis.* Langmuir, 2005. **21**(20): p. 9280.
13. Bortner, C.D. and Bortner, *Cell shrinkage and monovalent cation fluxes: role in apoptosis.* Archives of biochemistry and biophysics, 2007. **462**(2): p. 176.
14. Barbiero, G., et al., *Intracellular Ionic Variations in the Apoptotic Death of L Cells by Inhibitors of Cell Cycle Progression.* Experimental Cell Research, 1995. **217**(2): p. 410.
15. Benson, R.S., et al., *Characterization of cell volume loss in CEM-C7A cells during dexamethasone-induced apoptosis.* Am J Physiol Cell Physiol, 1996. **270**(4): p. C1190-1203.
16. Bortner, C.D., F.M. Hughes Jr, and J.A. Cidlowski, *A Primary Role for K+ and Na+ Efflux in the Activation of Apoptosis.* J. Biol. Chem., 1997. **272**(51): p. 32436-32442.
17. Yu, S.P., et al., *Role of the Outward Delayed Rectifier K+ Current in Ceramide-Induced Caspase Activation and Apoptosis in Cultured Cortical Neurons.* Journal of neurochemistry, 1999. **73**(3): p. 933.
18. Hughes Jr, F.M., *Intracellular K+ suppresses the activation of apoptosis in lymphocytes.* The Journal of biological chemistry, 1997. **272**(48): p. 30567.
19. Park, I.S., *Potassium efflux during apoptosis.* Journal of biochemistry and molecular biology, 2002. **35**(1): p. 41.

20. Yu, S., *Ion homeostasis and apoptosis.* Current opinion in cell biology, 2001. **13**(4): p. 405.
21. Skepper, J.N., et al., *Changes in elemental concentrations are associated with early stages of apoptosis in human monocyte-macrophages exposed to oxidized low-density lipoprotein: an X-ray microanalytical study.* The Journal of pathology, 1999. **188**(1): p. 100.
22. Fernández-Segura, E. and Fernandezsegura, *Changes in elemental content during apoptotic cell death studied by electron probe X-ray microanalysis.* Experimental cell research, 1999. **253**(2): p. 454.
23. Heimlich, G., *Selective role of intracellular chloride in the regulation of the intrinsic but not extrinsic pathway of apoptosis in Jurkat T-cells.* The Journal of biological chemistry, 2005. **281**(4): p. 2232.
24. Porcelli, A.M., et al., *Apoptosis induced by staurosporine in ECV304 cells requires cell shrinkage and upregulation of Cl− conductance.* Cell Death and Differentiation, 2004. **11**(6): p. 655.
25. Wei, L., et al., *Effects of chloride and potassium channel blockers on apoptotic cell shrinkage and apoptosis in cortical neurons.* Pflügers Archiv, 2004. **448**(3): p. 325.
26. McConkey, D.J., et al., *Glucocorticoids activate a suicide process in thymocytes through an elevation of cytosolic Ca2+ concentration.* Archives of biochemistry and biophysics, 1989. **269**(1): p. 365.
27. Lynch, K., et al., *Basic Fibroblast Growth Factor Inhibits Apoptosis of Spontaneously Immortalized Granulosa Cells by Regulating Intracellular Free Calcium Levels through a Protein Kinase C{delta}-Dependent Pathway.* Endocrinology, 2000. **141**(11): p. 4209-4217.
28. Nakagawa, T. and Yuan, *Caspase-12 mediates endoplasmic-reticulum-specific apoptosis and cytotoxicity by amyloid-β.* Nature, 2000. **403**(6765): p. 98.
29. Fanelli, C., et al., *Magnetic fields increase cell survival by inhibiting apoptosis via modulation of Ca2+ influx.* FASEB J., 1999. **13**(1): p. 95-102.
30. Truong-Tran, A.Q., et al., *The role of zinc in caspase activation and apoptotic cell death.* Biometals, 2001. **14**(3/4): p. 315.
31. Helmersson, A., S. von Arnold, and P.V. Bozhkov, *The level of free intracellular zinc mediates programmed cell death/cell survival decisions in plant embryos.* Plant Physiology, 2008. **147**(3): p. 1158.
32. Perry, D.K., *Zinc is a potent inhibitor of the apoptotic protease, caspase-3 A novel target for zinc in the inhibition of apoptosis.* The Journal of biological chemistry, 1997. **272**(30): p. 18530.
33. Zamzami, N., *Mitochondrial control of nuclear apoptosis.* The Journal of experimental medicine, 1996. **183**(4): p. 1533.
34. Stork, C.J. and Y.V. Li, *Intracellular Zinc Elevation Measured with a "Calcium-Specific" Indicator during Ischemia and Reperfusion in Rat Hippocampus: A Question on Calcium Overload.* J. Neurosci., 2006. **26**(41): p. 10430-10437.
35. Vogt, S., *MAPS: a set of software tools for analysis and visualization of 3D X-ray fluorescence data sets.* Journal de Physique IV (Proceedings), 2003. **104**(2): p. 635.

36. Sheskin, D., *Handbook of parametric and nonparametric statistical procedures, 3rd ed*. 2004, Boca Raton, FL: Chapman & Hall/CRC.
37. Wolford, J.L., *Zinc localization and quantitation in specialized cells and tissues*. 2006, Northwestern University.
38. Finney, L.A. and T.V. O'Halloran, *Transition Metal Speciation in the Cell: Insights from the Chemistry of Metal Ion Receptors.* Science, 2003. **300**(5621): p. 931-936.
39. Huang, X.-P., P.J. O'Brien, and D.M. Templeton, *Mitochondrial involvement in genetically determined transition metal toxicity: I. Iron toxicity.* Chemico-Biological Interactions, 2006. **163**(1-2): p. 68.
40. Keeble, J.A. and A.P. Gilmore, *Apoptosis commitment - translating survival signals into decisions on mitochondria.* Cell Res, 2007. **17**(12): p. 976.
41. Sheridan, C. and Sheridan, *Commitment in apoptosis: slightly dead but mostly alive.* Trends in cell biology, 2008. **18**(8): p. 353.
42. Adrain, C., E.M. Creagh, and S.J. Martin, *Apoptosis-associated release of Smac/DIABLO from mitochondria requires active caspases and is blocked by Bcl-2.* EMBO J, 2001. **20**(23): p. 6627.
43. Dejean, L.M., et al., *Regulation of the mitochondrial apoptosis-induced channel, MAC, by BCL-2 family proteins.* Biochimica et Biophysica Acta (BBA) - Molecular Basis of Disease, 2006. **1762**(2): p. 191.
44. Gottlieb, E., et al., *Mitochondrial membrane potential regulates matrix configuration and cytochrome c release during apoptosis.* Cell Death and Differentiation, 2003. **10**(6): p. 709.
45. Goldstein, J.C., et al., *The coordinate release of cytochrome c during apoptosis is rapid, complete and kinetically invariant.* Nat Cell Biol, 2000. **2**(3): p. 156.
46. Nelson-Rees, W. and R. Flandermeyer, *HeLa cultures defined.* Science, 1976. **191**(4222): p. 96.
47. Hille, B., *Ion Channels of Excitable Membranes*. 2001, Sunderland, MA: Sinauer Associates, Inc.
48. Redmann, K., C. Stolte, and D. Lders, *Membranpotential-Messungen an KB-Zellkulturen.* Die Naturwissenschaften, 1967. **54**(10): p. 255.
49. Tsien, R.Y., T. Pozzan, and T.J. Rink, *T-cell mitogens cause early changes in cytoplasmic free Ca 2+ and membrane potential in lymphocytes.* Nature, 1982. **295**(5844): p. 68.
50. Franco, R., C.D. Bortner, and J.A. Cidlowski, *Potential roles of electrogenic ion transport and plasma membrane depolarization in apoptosis.* Journal of Membrane Biology, 2006. **209**(1): p. 43.
51. Yamaguchi, M., *Regulatory effects of zinc and copper on the calcium transport system in rat liver nuclei. Relation to SH groups in the releasing mechanism.* Biochemical Pharmacology, 1993. **45**(4): p. 943.
52. Ohsumi, Y. and Y. Anraku, *Calcium transport driven by a proton motive force in vacuolar membrane vesicles of Saccharomyces cerevisiae.* J. Biol. Chem., 1983. **258**(9): p. 5614-5617.
53. Colvin, R.A., *Zinc inhibits Ca2+ transport by rat brain Na+/Ca2+ exchanger.* Neuroreport, 1998. **9**(13): p. 3091.

54. Baker, A.J.M., *The Uptake of Zinc and Calcium from Solution Culture by Zinc-Tolerant and Non-Tolerant Silene maritima with. In Relation to Calcium Supply.* The New phytologist, 1978. **81**(2): p. 321.
55. Troy, C.M., *Down-regulation of copper/zinc superoxide dismutase causes apoptotic death in PC12 neuronal cells.* Proceedings of the National Academy of Sciences of the United States of America, 1994. **91**(14): p. 6384.
56. Nishimura, T., et al., *Cellular prion protein regulates intracellular hydrogen peroxide level and prevents copper-induced apoptosis.* Biochemical and Biophysical Research Communications, 2004. **323**(1): p. 218.

Chapter 5

X-Ray Emission Spectroscopy of Zinc Active Site Mimics

Introduction

After iron, zinc is the most commonly used transition metal in biological systems [1], where it plays a variety of structural and functional roles. Its versatility is due to its redox-stability, its amphoterism, and its intermediate chemical hardness. However, these biological advantages also limit the number of techniques that can be used to study zinc active sites compared to other biologically-relevant transition metals such as iron, copper, and manganese. In particular, its $3d^{10}$, closed-shell configuration prohibits the use of EPR, MCD and UV/Vis spectroscopies for the study of Zn^{2+}-containing systems [2]. Cobalt or cadmium substitution is often used to obtain active site information using conventional spectroscopies; however, in some cases cobalt- or cadmium-substituted model compounds are not isostructural with the zinc complex [3, 4]. ^{67}Zn NMR offers one promising alternative, and has successfully been applied to distinguish between several active site mimics for carbonic anhydrase [5], including the protonated and deprotonated forms of the pyrazolylborate [$Tp^{t\text{-}Bu,Me}$]ZnOH [6], although to date useful information can only be obtained for highly-concentrated samples and highly symmetric zinc sites.

Typically, one must resort to X-ray techniques to study zinc in its native biological environment. Modern protein crystallography can in some cases yield atomic-resolution structures on the order of ~1 Å [7], which is sufficient to determine the

immediate interacting residues, assuming that the metal site from the crystalline structure is identical to the metal site in solution. X-ray absorption techniques can be used to determine electronic structure and geometry for metal sites where a crystal structure does not exist, or where there is concern that the crystallized protein's metal center may not be isostructural to the biological metal center. In particular, EXAFS—extended X-ray absorption fine structure—has been an important tool for obtaining high-resolution active site structures within 5 Å of the metal center, with an accuracy of approximately 0.02 Å and a precision of approximately 0.004 Å [2, 8]. However, even this technique suffers from certain limitations. In the EXAFS equation:

$$\chi(k) = -S_0^2 \times \sum_j \frac{N_j}{kR_j^2} |\, f(k)\,| \exp(\frac{-2R_j}{\lambda_e}) \exp(-2k^2\sigma_j^2) \sin(2kR_j + \varphi(k))$$

scatterer identity is encoded in the phase shift function $\varphi(k)$. Yet this function varies slowly with changes in the scatterer atomic number [9], which makes it impossible in practice to distinguish between scatterers with similar atomic numbers. This presents a problem for determining the active site structure for many enzymes, where the number of nearest-neighbor oxygen and nitrogen atoms may be known, but the nature of those ligands is subject to ambiguity (e.g., bidentate carboxylate vs. monodentate carboxylate plus water for farnesyl transferase [10], bound water vs. bound hydroxide at physiological pH for carbonic anhydrase [6]). Another sort of ambiguity exists for biological sites with mixed imidazole and thiolate ligation—although the phase shift functions $\varphi(k)$ are different enough in principle to distinguish between nitrogen and sulfur, the difference between the phase shifts for the two scatterers is approximately π for most of the k range, meaning that the signals from the two scatterers largely cancel out [11]. This has the effect of producing no resolvable peaks in the Fourier transform,

which makes the presence and degree of N/S mixture difficult to determine.

In order to address this issue, we investigated the use of high-resolution X-ray emission spectroscopy (XES) to obtain zinc active site information. Specifically, our aim was to detect the $K\beta_{1,3}$ (3p → 1s) satellite peaks, the $K\beta_{2,5}$ and Kβ'' transitions, where the $K\beta_{2,5}$ is the transition from the valence level to the metal 1s core hole, and the Kβ'' is a ligand-to-metal charge transfer transition [12]. For other metals, these peaks have previously been shown to be sensitive to oxidation state, spin state, chemical environment and geometry [12]. Since zinc coordination compounds have only one relevant oxidation and spin state, any observed changes in the $K\beta_{1,3}$ satellite peaks must be due to either ligand identity or geometry.

Our approach makes use of curved analyzer crystals in the Rowland circle geometry (Figure 5.1). In this setup, the sample, detector, and analyzer crystals are all situated on a circle, with the detector and sample equidistant from the analyzer crystals and with the analyzer crystal radius of curvature equal to the Rowland circle diameter [13]. The analyzer crystal identity and cut are chosen such that fluorescent X-rays from the sample are reflected towards the detector according to Bragg's law:

$$n\lambda = 2d \times \sin(\theta)$$

where n is the diffraction order, λ is the fluorescence wavelength, d is the spacing between two lattice planes, and θ is the angle between the incident ray and the crystal surface. Monochromatizing the fluorescent X-rays in this manner allows collection of very high resolution emission scans on the order of 1 eV, which allows collection of fluorescence from very weak transitions that would be unresolvable using a standard energy-dispersive detector. Figure 5.2 shows the improvement in resolution that results

from this experimental setup. A typical germanium detector has an energy resolution on the order of 150 eV [14]. Since the $K\beta_{2,5}$ and Kβ'' peaks lie within 100 eV of the $K\beta_{1,3}$ peaks and are 100 times less intense, these features would otherwise be completely obscured due to instrumental broadening.

In order to determine how ligand identity and geometry affect the position and intensity of the valence-to-core transitions, we measured the $K\beta_{2,5}$ spectra of a library of small, relatively well-characterized zinc compounds. Special attention is paid to zinc carboxylates, imidazoles, and thiolates, as these ligands are the most biologically relevant [1], although simpler structurally-characterized compounds such as the zinc halides were also included in order to aid identification of the main transitions and how these change with anion identity. Identification of the main peaks is also aided by comparison to electronic structure calculations. The sensitivity of these spectra to minute changes in the chemical environment is explored, and the features most relevant to biological zinc sites are determined. Finally, some comment is made on the feasibility of applying high-resolution XES to an actual biological sample in the near future.

Materials and Methods

Sample Preparation

Zinc oxide, zinc sulfide, zinc selenide, zinc fluoride, zinc bromide, zinc diethyldithiocarbamate, zinc nitrate hexahydrate, zinc sulfate heptahydrate, zinc perchlorate hexahydrate, zinc acetate dihydrate, zinc acrylate, zinc citrate dihydrate, zinc trifluoroacetate hydrate, zinc hexafluoroacetylacetonate dehydrate, zinc acetylacetonate hydrate, zinc stearate, zinc octaethylporphyrin, zinc tetraphenylporphyrin, and zinc

phthalocyanine were all obtained from Sigma-Aldrich (Milwaukee, WI). Zinc chloride was purchased from Mallinckrodt Baker, Inc. (Phillipsburg, NJ). Zinc perchlorate hexahydrate was purchased from Alfa Aesar (Ward Hill, MA).

Bis(2-aminopyridine-N)bis(benzoato-O)zinc [15], anhydrous zinc acetate [16], tetrakis(1-methylimidazole-N^3)zinc(II) diperchlorate [17], bis(benzoato-O)bis(thiourea-S)zinc(II) [18], (dipropionato-O)(dithiourea-S)zinc(II) [19], tetraethylammonium tetrathiolphenolatozinc(II) [20], and bis(1-methylimidazole)bis(thiophenolato)zinc(II) [21] were all synthesized according to literature procedures. Hexakis(1-methylimidazole-N^3)zinc(II) diperchlorate was synthesized according to a procedure for the analogous cobalt complex [22]. Zinc benzoate was prepared by adding 25 mL of 0.4 M sodium hydroxide solution to 1.22 g of benzoic acid (Sigma-Aldrich) under gentle heating and stirring until all benzoic acid was dissolved. To this was added a solution of 1.44 g of zinc sulfate hexahydrate in 10 mL of deionized water. A white solid precipitated immediately, which was collected and dried by suction filtration. Zinc propionate was prepared by adding 40 mL of 1 M sodium hydroxide to 3 mL of propionic acid, followed by addition of 2.72 g of zinc chloride. White crystals formed after 24 hours, which were collected and dried by suction filtration. Product was hot-filtered in deionized water and recrystallized overnight.

All synthesized compounds were submitted to Atlantic Microlab, Inc. (Norcross, GA) for CHN analysis, the results of which can be seen in Table 5.1. For the most part, all synthesized compounds were found to have close to the expected fractions of carbon, hydrogen, and nitrogen, with the exception of bis(benzoato-O)bis(thiourea-S)zinc(II) and tetraethylammonium tetrathiolphenolatozinc(II), which were found to differ from the

expected carbon contents by approximately 5%. However, these compounds were included for XES analysis since the EXAFS results confirmed that the local structure around the zinc site was likely accurate (see below). In addition, all zinc carboxylates and acetylacetonates were submitted for CHN analysis to assess their water content. Initial predicted values for percent carbon and hydrogen were generated by assuming all compounds were in their anhydrous form. The carboxylate:water stoichiometry was determined by minimizing the squared difference between the predicted and experimentally determined carbon and hydrogen percentages by allowing the number of waters to float. The number of water molecules per compound was then rounded to the nearest integer. The result can be seen in Table 5.2.

The zinc scorpionates $[Tm^{t\text{-}Bu}]ZnSPh$, $[Tm^{t\text{-}Bu}]ZnSCH_2C(O)N(H)Ph$, and $[Tp^{t\text{-}Bu,Me}]ZnOH$ were synthesized by Jonathan Melnick from the Parkin lab at Columbia University. All zinc scorpionates were prepared according to standard literature techniques [23, 24].

High-Resolution XES

X-ray emission spectra were measured at room temperature at beamline 6-2 at the Stanford Synchrotron Radiation Lightsource. Undiluted powder samples were packed into an aluminum sample mount and covered with Kapton tape. Samples were exposed to an incident beam with energy of 10.4 keV, focused to a spot size of 0.3 μm x 2.5 μm. Incident flux was calculated to be $3.8x10^{12}$ photons per second. In order to minimize the effects of radiation damage, the incident beam was focused onto a fresh spot on the sample for each scan. Fluorescence was collected using bent Ge(555) analyzer crystals in

a one-meter Rowland circle geometry, as described previously, and focused onto a single-element Ge detector. The experimental resolution was 1.6 eV on average, determined by fitting a Gaussian to the elastic scatter peak at various points of interest along the scan. This peak represents the monochrometer resolution convolved with the analyzer resolution. The monochrometer resolution was 1.1 eV, so assuming a Gaussian peak for both the monochrometer and the analyzer yields an analyzer resolution of 1.2 eV. Each sample had at least ten short-range scans taken between 9616.8 eV and 9674.4 eV, encompassing the $K\beta_{2,5}$ and Kβ'' peaks, and two long-range scans between 9534.9 eV and 9674.4 eV, encompassing both the $K\beta_{1,3}$ transition and the $K\beta_{2,5}$ region. The long-range scans provide both a means of energy calibration and a way to normalize the $K\beta_{2,5}$ region. All spectra were normalized to the maximum of the $K\beta_{1,3}$ peak. After normalization, the $K\beta_{2,5}$ spectrum was subjected to a peak-stripping algorithm [25] to remove distortion from the $K\beta_{1,3}$ tail. All spectra were plotted using Matlab. Peak centers, widths, and intensities were determined by fitting experimental peaks to Gaussian lineshapes using the 'fit' function from the Matlab Curve Fitting Toolbox. Two-Gaussian fits were employed for transitions with asymmetric lineshapes.

X-Ray Absorption Fine Structure (EXAFS) Spectroscopy

All synthesized samples were subjected to EXAFS analysis to confirm the local structure around the zinc site. EXAFS spectra were taken at beamline 9-3 at the Stanford Synchrotron Radiation Lightsource. Samples were diluted approximately ten-fold with boron nitride to reduce thickness effects and mounted in an aluminum sample holder with Kapton windows. Samples were placed in a He-cooled cryostat maintained at 12 K to

reduce thermal disorder. The incident beam was scanned between 9430 eV and 10325 eV using a Si(220) monochrometer in the $\varphi = 0^o$ orientation, with a rhodium-coated mirror upstream for harmonic rejection. The pre-edge region (9430 eV-9630 eV) was scanned in 10 eV steps, the edge region (9630 eV-9690 eV) in 0.35 eV steps, and the EXAFS region (between k = 1.62 $Å^{-1}$ and k = 13 $Å^{-1}$) in 0.05 $Å^{-1}$ steps. Integration times were 1 s per data point in the pre-edge and edge regions, and between 1s and 25 s (k^3-weighted) in the EXAFS region, for a total scan time of approximately 35 minutes per sweep. Three N_2-filled ion chambers were placed in the beam path, one prior to the cryostat in order to measure the incident beam intensity, and two placed after the cryostat. Sample absorption was measured as the negative logarithm of the ratio of the second and first ion chamber readings. Energy calibration was achieved by use of a zinc foil between the second and third ion chambers, with the first inflection point of the zinc foil scan defined to be 9659 eV.

Normalization, spline fitting, and Fourier transforms for EXAFS analysis were carried out using EXAFSPAK. The pre-edge region was fit to a linear polynomial, and the post-edge was fit to a cubic spline with three regions. The data were converted to k-space using the equation $k = [(8\pi^2 m_e/h^2)(E-E_0)]^{1/2}$, where the threshold energy, E_0, was taken to be 9666 eV. The k^3-weighted EXAFS were fit to the EXAFS equation over the k range of 2-12 $Å^{-1}$ with a non-linear least-squares algorithm. Single-shell fits were performed for every half-integer coordination number between 4 and 6, allowing the bond lengths and Debye-Waller factors to vary. The best fit was determined by the combination of parameters that minimize the sum of the squares of the differences between the data and the fit, subject to the usual constraints (e.g., no negative Debye-

Waller factors allowed, bond lengths must be appropriate for the corresponding coordination number). The results are shown in Table 5.3. In every case, the experimental bond lengths were identical to the literature values, providing further confirmation of sample integrity.

The above analysis was also performed on the zinc carboxylates and acetylacetonates in order to determine how their moisture content affects the coordination number. The results for single-shell N/O fits are shown in Table 5.4.

Electronic Structure Calculations

Ground-state density of states calculations were carried out for zinc oxide, zinc sulfide, zinc selenide, zinc fluoride, zinc chloride, and zinc bromide using DL Visualize and CRYSTAL98. Unit cell structures were taken from the literature [26]. DFT calculations were carried out using the PWGGA method. The basis sets were 86-411d31G for zinc, and Pople 3-21G for all other atom types. The Zn s, Zn p, and Zn d, and ligand DOS calculations were performed using CRYSTAL98. The energy scale of all DOS plots is defined relative to the Fermi energy by default, so all energies were shifted by 9659 eV, the zinc 1s binding energy, for comparison to experimental spectra. Further electronic structure calculations were carried out for the interaction of Zn(II) with tetrahedral formaldehyde, formate, thioformaldehyde, imidazole, and furan environments using StoBe software [27]. In addition, calculations were performed for a hexaqua zinc environment. Double-zeta valence polarization basis sets were used, with orbital contractions of (63321/531/311) for zinc, (6321/521/1) for sulfur, (621/41/1) for oxygen, nitrogen, and carbon, and (41/1*) for hydrogen.

Results

A summary of all peak positions, heights and intensities may be seen in Table 5.5. Comparisons of the high-resolution XES spectra for the zinc chalcogenides and zinc halides are shown in Figure 5.3 and Figure 5.4, respectively. One feature of note is the small peak at approximately 9652 eV, the position of which is relatively constant among the different chemical environments. This is further emphasized by comparing zinc compounds across rows, as depicted in Figure 5.5 and Figure 5.6. Just as the $K\beta_{1,3}$ transition is relatively independent of chemical environment (Figure 5.7), the relative insensitivity of the 9652 eV peak to the chemical environment suggests that this transition is a metal-metal transition rather than an MO-to-metal transition; thus, this peak is likely the Zn 3d → Zn 1s transition. Furthermore, this peak apparently arises primarily from direct quadrupole coupling of the Zn 1s and 3d, since it is essentially unchanged even in compounds with inversion symmetry. This can be seen, for example, in Figure 5.8, which shows a comparison of the $K\beta_{2,5}$ XES for tetrakis(1-methylimidazole-N^3) zinc(II) diperchlorate, hexakis(1-methylimidazole-N^3) zinc(II) diperchlorate, and zinc tetraphenylporphyrin. All three ligand sets bind zinc through nitrogen heterocycles, though all three differ in symmetry. Tetrakis(1-methylimidazole-N^3) zinc(II) diperchlorate is four-coordinate tetrahedral, hexakis(1-methylimidazole-N^3) zinc(II) diperchlorate is six-coordinate octahedral, and zinc tetraphenylporphyrin is four-coordinate square planar. The latter two have inversion symmetry, yet the intensity of the peak at 9652 eV only changes slightly, indicating a relatively low degree of p-d mixing. In contrast, for iron compounds the intensity of the 1s → 3d transition increases approximately three-fold as the symmetry around the iron

site changes from tetrahedral to octahedral, due to mixing of the Fe 3d and Fe 4p [28].

The main peak which appears between 9653 eV and 9659 eV is likely the transition from the highest occupied molecular orbital (HOMO) to the zinc 1s. Comparing ligands from the same group on the periodic table, the energy and intensity of this peak increases as the ligand atomic number increases (Figures 5.3 and 5.4). In contrast, the energy and intensity of this peak decrease as one proceeds from left to right across a row on the periodic table (Figures 5.5 and 5.6). Since the energy of the Zn 1s level is for the most part independent of the chemical environment, a lower HOMO → Zn 1s transition energy indicates that the HOMO is further from the Fermi level as the ligand identity changes from left to right across a row or from bottom to top along a column. This is similar to the periodic trend in ionization energy, which decreases from top to bottom along a column, and increases from left to right along a row. The intensity of these features likely indicates greater Zn 4p character in the ZnS and ZnSe HOMO compared to ZnO, or the $ZnBr_2$ and $ZnCl_2$ HOMO compared to ZnF_2. The Zn 4p lies significantly higher in energy than the O and F 2p, and any bonding molecular orbital formed between these two will have primarily ligand 2p character. As one proceeds from O to S and Se, or from F to Cl and Br, the ligand valence orbitals will be progressively higher in energy (i.e., closer to the Zn 4p), and the molecular orbitals will have increasing Zn 4p character, increasing the intensity of the HOMO → Zn 1s transition. This explains why the $K\beta_{2,5}$ intensity is lower in zinc chloride than in zinc sulfide, and zinc bromide than in zinc selenide.

In addition to the Zn 3d → Zn 1s and HOMO → Zn 1s transitions that make up the $K\beta_{2,5}$ region, there are two other sets of peaks of note in the XES spectra. The first are

a set of relatively low-intensity and low-energy peaks between 9635 eV and 9649 eV. The position of this peak depends upon the ligand identity and varies in the same way as the HOMO → Zn 1s transition, increasing in energy from zinc oxide to zinc selenide and from zinc fluoride to zinc bromide (Figures 5.3 and 5.4), and decreasing in energy from zinc sulfide to zinc chloride and from zinc selenide to zinc bromide (Figures 5.5 and 5.6). Similar peaks in Mn compounds have been identified as the Kβ'' peaks, the ligand-to-metal crossover transitions, since for Mn compounds with N, O, and F ligands, the relative positions of these peaks roughly correspond to the differences in N, O, and F 2s binding energy, and since the intensity of these peaks decrease exponentially with increasing bond length [29, 30].

The second set of notable peaks are a set of relatively low-intensity, high-energy peaks that sometimes appear at higher energy than the HOMO → Zn 1s transition, at 9662 eV and above. Similar peaks also appear in the Mn $K\beta_{2,5}$ region and have been assigned as a Mn 3p → Mn 1s transition for doubly-excited Mn, with both 1s and 2p holes [12]. This cannot be the case for the Zn compounds studied here, since the Zn 1s binding energy (9659 eV) plus the Zn 2p binding energy (1021 eV) is 10680 eV, and the incident energy used here is only 10400 eV. However, this is still likely to represent a multi-electron transition, for the following reasons. First, the peak in question has higher energy than the Zn 1s binding energy and appears under the edge of the corresponding XANES spectrum (Figure 5.9). Secondly, there is no corresponding feature in the density of states calculations (see below), which suggests that this peak does not correspond to a transition from any level that is occupied in the ground state.

The density of states calculations confirm the above peak assignments. Figure

5.10 shows a comparison between the zinc bromide XES spectrum and the corresponding density of states calculations. Here, the calculated density of states, with energies defined relative to the Fermi level, has been shifted by adding the Zn 1s binding energy, 9659 eV. The same energy shift was applied for all compounds. As expected, the Zn p density of states is greatest around the peak corresponding to the HOMO → Zn 1s transition. The Zn d density of states is sharply peaked around the peak near 9652 eV, confirming this assignment as the Zn 3d → Zn 1s transition. Finally, the ligand density of states is greatest around the small peak at 9647 eV, suggesting that this is the crossover peak for $ZnBr_2$. Comparisons between the XES spectra and the DOS calculations for $ZnCl_2$, ZnF_2, ZnSe, ZnS, and ZnO can be seen in Figures 5.11 through 5.15. Although the DOS calculations do not exactly reproduce the experimental spectra, especially for ZnF_2, the relative placements of the peaks are consistent for the most part, with one region with primarily ligand character corresponding to the crossover region, one region with primarily Zn d character corresponding to the Zn 3d → Zn 1s transition, and one region with primarily Zn p and ligand character corresponding to the HOMO → Zn 1s transition.

The XES spectra for the four-coordinate zinc carboxylates (anhydrous zinc acetate, zinc propionate, zinc benzoate, zinc acrylate, and zinc stearate—see Tables 5.1 through 5.4) are shown in Figure 5.16. These spectra all look similar, with three main peaks—a crossover peak between 9635.8 eV and 9637.6 eV, and two peaks in the $K\beta_{2,5}$ region. The $K\beta_{2,5}$ peaks consist of a shorter, broader peak centered between 9651.9 eV and 9652.2 eV, with a height of approximately 0.007 and an integrated intensity of approximately 0.18, and a taller, narrower peak centered between 9657.0 and 9657.4, with a height of approximately 0.01 and an integrated intensity of approximately 0.14.

The XES spectrum for zinc acetate dihydrate is qualitatively similar to the XES spectrum for anhydrous zinc acetate (Figure 5.17), despite the two having different ligation environments, with a visible crossover peak at 9636.8 eV, a shorter broad feature at 9651.9 eV, and a sharper peak at 9656.7 eV. The key difference between zinc acetate dihydrate and anhydrous zinc acetate seems to be a shift to 0.5 eV lower energy in both the crossover and HOMO → Zn 1s peaks in the dihydrate.

Comparing the zinc acetate dihydrate with its fluorinated form, zinc trifluoroacetate dihydrate (Figure 5.18), there are significant changes in both the crossover and $K\beta_{2,5}$ regions. The crossover energy decreases to 9634.5 eV, while the $K\beta_{2,5}$ region merges into a single peak with a maximum at 9653.7 eV and what appears to be a shoulder at 9657 eV. These observations can be rationalized by noting that fluorine is strongly electron-withdrawing, which would draw the carboxylate electrons tighter to the carboxylate and lower the frontier orbital energies [31]. Lowering the oxygen 2s and 2p orbital energies would also lower the energy of the crossover and HOMO → Zn 1s transitions.

The XES spectrum from zinc acetylacetonate hydrate is also somewhat similar to the XES spectra for most of the zinc carboxylates (Figure 5.19). Both types of compounds display a broad peak at approximately 9652 eV with similar height and integrated intensity. However, the peak at approximately 9657 eV is less intense than that found for the zinc carboxylates. Furthermore, the crossover peak is shifted to lower energy, 9635.5 eV. The fluorinated form shows a shift in intensity from the high energy peak to the lower-energy peak, similar to what was observed in zinc trifluoroacetate compared to zinc acetate (Figure 5.20).

Finally, mention should be made of the hydrated zinc salts, zinc nitrate hexahydrate, zinc perchlorate hexahydrate, and zinc sulfate heptahydrate. The XES spectra for all three are shown in Figure 5.21. All three spectra look similar, with a crossover peak between 9635.3 eV and 9636.3 eV, and a single peak in the $K\beta_{2,5}$ region centered at 9653.5 eV and a height of 0.013. The single $K\beta_{2,5}$ peak overlaps in energy with the peak assigned as the Zn 3d → Zn 1s transition for the other complexes. It is likely that this obscures the Zn 3d → Zn 1s peak for the aqueous complex. The relative insensitivity of these spectra to the anion identity suggests that these peaks are primarily due to the zinc-water interaction; that is, these spectra represent the XES spectra of hexaqua zinc. Since water is a stronger Lewis base than nitrate, perchlorate, and sulfate, it would be expected to constitute the inner coordination sphere for these three compounds [32].

The XES for many of the zinc compounds dominated by a zinc-nitrogen interaction has already been shown in Figure 5.9. Figure 5.22 shows the XES spectra for all of the zinc compounds with nitrogen-dominated environments. In contrast to the XES spectra for the zinc carboxylates, zinc acetylacetonates, and hydrated zinc salts, there is no visible crossover peak in these spectra. The $K\beta_{2,5}$ region is also qualitatively different. Whereas the zinc carboxylates showed two peaks with roughly equal integrated area, the two $K\beta_{2,5}$ peaks in zinc compounds dominated by nitrogen ligation are very unequal in intensity. The lower-energy Zn 3d → Zn 1s peak is located between 9651.5 eV and 9651.8 eV in all cases, with an integrated intensity that varies between 0.11 (for four-coordinate tetrahedral tetrakis(1-methylimidazole-N^3) zinc(II) diperchlorate) and 0.06 (for four-coordinate square-planar zinc octaethylporphyrin). The higher-energy

HOMO → Zn 1s transitions display a greater variety of lineshapes, but are generally located between 9655.8 eV and 9656.6 eV.

The XES spectra of the zinc-organosulfur complexes used in this study are shown in Figure 5.23. These are similar in overall shape to the XES spectra from zinc-imidazole complexes. As in the zinc imidazoles, there is no strong crossover peak present. The Zn 3d → Zn 1s transition is present between 9651.7 eV and 9651.9 eV, and the HOMO → Zn 1s transition is a tall, asymmetric peak with a maximum between 9658.3 eV and 9658.7 eV.

To summarize, the overall shape of the XES spectra seems to depend primarily on the ligand identity. Conversely, different ligand environments seem to have characteristic XES lineshapes. Figure 5.24 shows the XES spectra of three archetypical zinc environments used in this study, anhydrous zinc acetate, tetrakis(1-methylimidazole-N^3) zinc(II) diperchlorate, and tetraethylammonium tetrathiolphenolatozinc(II), plotted on the same scale to emphasize the differences in overall lineshape. The crossover peak is prominent only for the zinc carboxylate, and the occupied density of states seem to be distributed roughly equally between the low and high energy peaks of the $K\beta_{2,5}$ region. On the other hand, both the imidazole and thiolate environments have a relatively low-intensity, low energy peak in the $K\beta_{2,5}$ region located between 9651.5 eV and 9651.9 eV, with most of the $K\beta_{2,5}$ intensity around the high energy peak. In an imidazole environment, this high energy peak is symmetric and located between 9655.8 eV and 9656.6 eV, while the high energy $K\beta_{2,5}$ peak is asymmetric with a maximum between 9658.3 eV and 9658.7 eV in sulfur-dominated zinc sites.

Site symmetry also seems to have an effect. Comparing four-coordinate

tetrahedral anhydrous zinc acetate to six-coordinate octahedral zinc acetate dihydrate (Figure 5.17) and four-coordinate tetrahedral tetrakis(1-methylimidazole-N^3) zinc(II) diperchlorate to six-coordinate octahedral hexakis(1-methylimidazole-N^3) zinc(II) diperchlorate (Figure 5.8), one observes a slight decrease in both energy and intensity of the high energy peak in the $K\beta_{2,5}$ region for the octahedral complex. Quantitative fits of the low-energy peak show that it decreases in integrated intensity by approximately 20% as one proceeds from a four-coordinate tetrahedral site to one with inversion symmetry if one fits the $K\beta_{2,5}$ region and sums over the low-energy peak. However, geometric effects seem to be secondary for the biologically relevant ligands—the overall shape depends primarily on chemical identity of the nearest neighbors.

Mention should be made of those compounds with mixed ligation environments. Figure 5.25 shows the XES spectrum of (dipropionato-O)(dithiourea-S)zinc(II), along with zinc propionate and zinc tetrathiophenol for comparison. Zinc tetrathiourea was not prepared for this study; however, exploiting the general similarity between the XES spectra of zinc sites in primarily sulfur environments (Figure 5.23) should allow some useful comparisons to be made. In the (dipropionato-O)(dithiourea-S)zinc(II) spectrum, all features are intermediate between the zinc propionate and zinc tetrathiophenol spectra. The crossover peak is present, but has roughly half the intensity as found in zinc propionate, the intensities of both $K\beta_{2,5}$ peaks are intermediate between the zinc propionate and zinc tetrathiophenol $K\beta_{2,5}$ peaks, and the high energy $K\beta_{2,5}$ peak lies between the zinc propionate and zinc tetrathiophenol high-energy $K\beta_{2,5}$ peak in energy (9658.0 eV, compared to 9657.0 eV and 9658.2 eV, respectively). Except for the intensity of the high energy $K\beta_{2,5}$ peak, many features of the (dipropionato-O)(dithiourea-

S)zinc(II) spectrum can even be approximated as a linear combination of the zinc propionate and zinc tetrathiophenol spectra (Figure 5.26). Thus, (dipropionato-O)(dithiourea-S)zinc(II), which has zinc coordinating two propionate anions and two thiourea molecules, has an XES spectrum with features characteristic of both zinc carboxylates and sulfur-rich zinc sites, namely the crossover peak and the broad, intense low energy $K\beta_{2,5}$ peak characteristic of zinc carboxylates, and the sharp high energy $K\beta_{2,5}$ peak characteristic of sulfur-rich zinc sites. The XES spectrum of bis(benzoato-O) bis(thiourea-S)zinc(II), which has zinc coordinating two benzoate anions and two thiourea molecules, is similar in shape (Figure 5.27).

The XES spectrum of bis(2-aminopyridine-N)bis(benzoato-O)zinc(II), which has zinc interacting with two benzoate anions and two 2-aminopyridine molecules, is compared to the XES spectrum of bis(benzoato-O)bis(thiourea-S)zinc(II) in Figure 5.28. Both spectra have some features in common, including the crossover peak and the broad low energy $K\beta_{2,5}$ peak characteristic of zinc carboxylates. However, the two are distinguished by the high energy $K\beta_{2,5}$ peak, which is located at 9657.2 eV in bis(2-aminopyridine-N)bis(benzoato-O)zinc(II) and 9658.0 eV in bis(benzoato-O) bis(thiourea-S)zinc(II). Thus, it appears that XES can distinguish between nitrogen and sulfur ligands in this case.

Bis(1-methylimidazole)bis(thiophenolato)zinc(II), which has zinc interacting with two 1-methylimidazole molecules and two thiophenolate anions, has a $K\beta_{2,5}$ region that is split into three peaks, as seen in Figure 5.29. As in most of the other compounds, there is a low-intensity Zn 3d → Zn 1s peak at 9652.0 eV. However, the high-energy region is split into two peaks, one at 9655.7 eV and one at 9658.5 eV, which while not exactly

equal to the maxima found in the tetra(1-methylimidazole) and tetrathiophenol complexes (9656.3 eV and 9658.6 eV, respectively) are close to the ranges presented above for the high-energy peak in nitrogen-rich and sulfur-rich zinc sites (9655.8 eV to 9656.6 eV and 9658.3 eV to 9658.7 eV, respectively). Furthermore, this spectrum can be approximated as a linear combination of the spectra from the tetra(1-methylimidazole) and tetrathiophenol complexes (Figure 5.30). Thus, it appears—based on Figures 5.24, 5.28, and 5.29—that XES can distinguish between oxygen, nitrogen, and sulfur ligands in mixed chemical environments, and that these spectra can be described, or at least approximated, as linear combinations of the spectral components for each ligand.

In order to gain a better understanding of the XES lineshapes, and the zinc carboxylate and acetylacetonate lineshapes in particular, quantum chemical calculations were carried out on several model zinc coordination complexes. Six different four-coordinate ligand sets were chosen—formaldehyde, methanol, formate, thioformaldehyde, imidazole, and furan. For the zinc-formate interaction, the Zn-O distance was taken to be 2.04 Å, a typical zinc-aspartate distance in biological systems [33]. The Zn-O-C angle was chosen to be 124°, and the zinc was placed in the plane defined by the formate anion (so that the Zn-O-C-H dihedral angle was 0°). Methanol and formaldehyde were built by modifying the formate template as needed. Thioformaldehyde was built to be structurally similar to formaldehyde, except with a Zn-S distance of 2.30 Å. The zinc-imidazole model was built such that the Zn-N distance was 2.00 Å (a typical zinc-histidine interaction distance [33]), the two carbons immediately bound to the interacting nitrogen were equidistant from the zinc, and the zinc lay in the plane defined by the imidazole molecule. Furan was generated by

replacing the nitrogens in imidazole with an interacting oxygen and a carbon, without changing the bond length. In each case, one ligand was generated and the S_4 symmetry operations were applied in order to generate a tetrahedral complex, on which orbitals and energies were calculated. In addition to the four-coordinate models described above, a calculation was performed on a six-coordinate, hexaqua zinc model with a Zn-O distance of 2.093 Å [34]. The input models can be seen in Figure 5.31. All orbitals beyond the Zn 3p were considered frontier orbitals. For each calculation, the percent Zn 4p and 3d character were determined for each frontier orbital. The percent contributions were summed over all the frontier orbitals and the contributions of the Zn 4p and 3d were expressed as a fraction of the overall Zn 4p or 3d occupation. Stick spectra were then generated showing fraction of overall Zn 4p or 3d occupation as a function of orbital energy.

The stick spectrum calculated for thioformaldehyde is shown in Figure 5.32. The zinc 3d and 4p are well-separated—orbitals that have some contribution from the zinc tend to either have a contribution from the zinc 3d or the zinc 4p, but not both. Most of the energy levels with significant Zn 3d contribution tend to cluster around -20 eV, and most of the contribution from the Zn 4p comes from one orbital at approximately -15 eV, a shift of approximately 5 eV. For this compound, the Zn 3d orbitals do not show significant mixing with the Zn 4p. This is similar to what is seen in the XES spectra of sulfur-rich zinc sites (Figure 5.23)—the Zn 3d → Zn 1s peak occurs at 9651 eV, while the HOMO → Zn 1s peak has a maximum at approximately 9658 eV. A similar situation exists for the tetra-imidazole calculation (Figure 5.33). The total contribution from the zinc 4p and 3d is spread out over a wider variety of orbitals, but the zinc 3d levels tend to

cluster at approximately -18 eV, while most of the zinc 4p contribution occurs at one molecular orbital with energy of approximately -15 eV. The energy difference between the Zn 3d cluster and the orbital with maximum Zn 4p contribution is smaller than in the Zn-thioformaldehyde calculation, which is consistent with what is seen experimentally (Figures 5.22 and 5.25, and Table 5.5).

In contrast to the zinc-thioformaldehyde calculation, in the zinc-formaldehyde interaction the contributions from the Zn 3d and 4p are spread out over a much greater variety of energy levels (Figure 5.34). The high-energy levels with significant Zn 4p character are closer to the Zn 3d cluster, and there appears to be a greater degree of p-d mixing. Similarly-high levels of p-d mixing are calculated for the zinc-methanol interaction (breaking the C=O π bond), or if formate is substituted (Figures 5.35 and 5.36, respectively). The same trend is found when comparing the zinc-imidazole interaction (Figure 5.33) to the zinc-furan interaction (Figure 5.37). The zinc-furan cluster used in this study is isostructural and isoelectronic to the zinc-imidazole cluster, so the differences seen here are likely due to the interacting oxygen itself. This, combined with the higher levels of p-d mixing predicted for such diverse ligands as formate, formaldehyde, and methanol, suggest that the relatively intense Zn 3d $\rightarrow$ Zn 1s peak and the relatively weak HOMO $\rightarrow$ Zn 1s peak (compared to other compounds) may be due to the oxygen frontier orbitals being low enough in energy to interact with both the Zn 3d and the Zn 4p. Further evidence for this is seen in the calculation for hexaqua zinc, shown in Figure 5.38. The stick spectrum is qualitatively similar to the XES spectra for the hydrated zinc salts shown in Figure 5.21. None of the calculated molecular orbitals exhibit any p-d mixing, consistent with the centrosymmetry of hexaqua zinc. However,

the molecular orbitals formed with the zinc 4p are close in energy to the zinc 3d.

Discussion

EXAFS is a powerful technique for obtaining high-resolution active site structures. However, due to the relative insensitivity of the scattering phase shift function $\varphi(k)$, which gives EXAFS its chemical sensitivity, nitrogen and oxygen scatterers cannot be readily distinguished. Furthermore, although sulfur can be readily distinguished from oxygen and nitrogen using EXAFS, in sites with mixed sulfur/low-Z ligation the relative numbers of each type of scatterer can be difficult to determine due to destructive interference between the sulfur and low-Z scattering contributions. Furthermore, since the scattering amplitude is much greater for sulfur scatterers than nitrogen and oxygen scatterers [9], it is sometimes difficult to distinguish between ZnS_4 and ZnS_3N sites [11, 35]. For example, EXAFS analysis suggested that the primary zinc-binding site in 5-aminolaevulinate dehydratase (ALAD) bound zinc through four cysteines, whereas the crystal structure suggests that zinc is bound through three cysteines, leaving one slot open for interaction with substrate and water [36].

In contrast, data presented here suggest that X-ray emission spectroscopy can readily distinguish between ligation possibilities, through the unique lineshapes of the $K\beta_{2,5}$ and Kβ'' regions. The crossover peak seems to be absent in sites dominated by zinc-imidazole or zinc-sulfur interactions, so this feature can be exploited to decide between a model where the zinc interacts with the solvent versus one where zinc interacts with a histidine, cysteine, or methionine, assuming that there is no aspartate or glutamate already present. Furthermore, the high-energy peak of the $K\beta_{2,5}$ region is sharp for both

nitrogen-rich and sulfur-rich sites, but its position depends on the ligand chemical identity. This feature can also be exploited to distinguish between ZnS_4 and ZnS_3N models.

The unique lineshapes also open up the possibility of performing site-selective EXAFS on biological systems. In this kind of experiment, the analyzer crystals are set to collect fluorescence at one specific wavelength, while the incident energy is scanned across the zinc edge as in a normal EXAFS experiment. If the sample contains multiple metal sites and one of these sites fluoresces very strongly at a certain wavelength, performing an EXAFS experiment while the analyzer crystals are tuned to that specific wavelength will enhance the contribution from that site only. If all metal sites in the sample contribute to the $K\beta_{2,5}$ fluorescence but to different extents at different wavelengths, the contributions from the two zinc sites can be separated by measuring the EXAFS at multiple emission energies and performing singular value decomposition on the resulting data set. Based on the results presented here, for zinc sites the presence of glutamate, aspartate, and water ligands will make the crossover region and low-energy $K\beta_{2,5}$ peak relatively more intense, whereas different energy ranges in the high-energy end of the $K\beta_{2,5}$ peak will be more sensitive to zinc-imidazole or zinc-cysteine interaction. This would allow the study of proteins with multiple zinc sites *in situ*. For example, alcohol dehydrogenase contains two zinc sites—a catalytic site that binds two cysteines, a histidine, and a water molecule, and a structural site that binds four cysteines [1]. In principle, site-specific EXAFS would be able to determine high-resolution structures for both zinc sites simultaneously by taking advantage of the differences in the crossover and high-energy $K\beta_{2,5}$ regions that histidine and water ligation would produce.

Currently, applying valence-to-core XES to biological systems presents a challenge due to the relatively low fluorescence intensities of rare events. The XES spectra here were collected on undiluted powder samples, and each spectrum took roughly an hour to acquire, including both short-range and long-range scans. The densities and molecular weights of most solid zinc samples translate to an effective concentration of 1-10 M. On the other hand, many biological samples of interest may be concentrated to mM-range levels at best, so acquiring a spectrum with a similar signal-to-noise ratio would require about 1000 hours of beam time. However, there are measures that can be taken to reduce this time significantly. The first is to increase the incident flux impinging upon the sample, which can be done by increasing the synchrotron storage ring current. The current operating ring current at the Stanford Synchrotron Radiation Lightsource is 100 mA. Upgrades are underway to increase this to 500 mA in the near future [37]. Since photon flux is proportional to ring current [38], this should increase the incident flux by a factor of five. The second measure that can be taken is to add more analyzer crystals to the array. When the measurements presented here were taken, the analyzer crystal array could hold up to 14 crystals. However, due to availability only three Ge(555) crystals were actually used. Using 14 Ge(555) would increase the fluorescence collected by roughly a factor of four. If both measures are adopted, a biological sample could be collected within approximately 50 hours, with roughly the same signal to noise ratio as the data presented here.

Table 5.1: CHN Analysis of Synthesized Compounds

	Expected			Found		
Compound	**% C**	**% H**	**% N**	**% C**	**% H**	**% N**
Tetrakis(1-Methylimidazole-N^3) Zinc(II) Diperchlorate	32.4	4.1	18.9	33.8	4.3	19.6
Hexakis(1-Methylimidazole-N^3) Zinc(II) Diperchlorate	38.1	4.8	22.2	37.9	4.7	22.1
Anhydrous Zinc Acetate	26.2	3.3	0.0	25.3	3.4	0.0
Zinc Propionate	34.1	4.8	0.0	32.9	4.7	0.0
Zinc Benzoate	54.7	3.3	0.0	53.1	3.2	0.0
Bis(Benzoato-O)Bis(Thiourea-S) Zinc(II)	41.8	3.9	12.2	35.6	3.3	10.4
Bis(Benzoato-O)Bis(2-Aminopyridine) Zinc (II)	58.1	4.5	11.3	57.9	4.4	11.3
Bis(Propionato-O)Bis(Thiourea-S) Zinc(II)	26.4	5.0	15.4	25.4	4.8	14.8
Bis(1-Methylimidazole)Bis(Thiophenolato) Zinc(II)	53.6	5.0	12.5	53.5	4.9	12.4
Tetraethylammonium Tetrathiolphenolato Zinc(II)	59.1	6.8	4.3	54.5	7.4	3.6

Table 5.2: CHN Analysis of Zinc Carboxylates and Acetylacetonates

	Expected (Anh.)		Found			Hydrated Form	
Compound	**% C**	**% H**	**% C**	**% H**	**Est. # H2O**	**% C**	**% H**
Zinc Acetate	26.2	3.3	21.8	4.5	2	21.9	4.6
Zinc Acrylate	34.7	2.9	34.8	2.9	0	34.7	2.9
Zinc Citrate	25.1	1.8	23.5	2.4	2	23.6	2.3
Zinc Stearate	68.4	11.2	66.3	10.9	0	68.4	11.2
Zinc Trifluoroacetate	16.5	0.0	13.4	2.0	4	13.2	2.2
Zinc Acetylacetonate	45.6	5.4	42.3	5.6	1	42.7	5.7
Zinc Hexafluoroacetylacetonate	25.1	0.4	22.8	1.1	2	23.3	1.2

Table 5.3: Best Fits for EXAFS of Synthesized Compounds

Compound	Shell	N	R (Å)	σ^2 x 10^3 (Å^2)	Lit R (Å)	Ref
Tetrakis(1-Methylimidazole-N[3]) Zinc(II) Diperchlorate	N/O	4.0	1.986	4.8	1.991 (2)	[17]
Hexakis(1-Methylimidazole-N[3]) Zinc(II) Diperchlorate	N/O	6.0	2.177	4.3	2.18 (3)	[22]
Anhydrous Zinc Acetate	N/O	4.0	1.957	4.9	1.957 (7)	[16]
Zinc Propionate	N/O	4.0	1.954	4.7	1.953	[39]
Zinc Benzoate	N/O	4.0	1.950	3.4	1.95	[40]
Bis(Benzoato-O)Bis(Thiourea-S) Zinc(II)	N/O	2.0	1.963	3.6	1.964 (2)	[18]
	S	2.0	2.372	3.6	2.367 (2)	
Bis(Benzoato-O)Bis(2-Aminopyridine) Zinc (II)	N/O	4.0	2.009	6.6	1.99 (9)	[15]
Bis(Propionato-O)Bis(Thiourea-S) Zinc(II)	N/O	2.0	1.979	3.3	1.97 (2)	[19]
	S	2.0	2.331	4.1	2.33 (1)	
Bis(1-Methylimidazole) Bis(Thiophenolato) Zinc(II)	N/O	2.5	2.046	3.3	2.05 (1)	[21]
	S	2.0	2.300	3.9	2.300 (2)	
Tetraethylammonium Tetrathiolphenolato Zinc(II)	S	4.0	2.361	4.2	2.36 (2)	[20]

Table 5.4: Best Fits for EXAFS of Zinc Carboxylates and Acetylacetonates

Compound	N	R (Å)	σ^2 x 10^3 (Å^2)
Zinc Acrylate	4.0	1.968	3.9
Zinc Citrate	4.5	2.037	6.0
Zinc Stearate	4.0	1.957	2.6
Zinc Trifluoroacetate	5.5	2.088	5.4
Zinc Acetylacetonate	5.0	2.016	3.9
Zinc Hexafluoroacetylacetonate	6.0	2.075	3.7

Table 5.5: Positions and Intensities for XES Peaks

Chemical Class	Material	Zn Environment	Peak	Position (eV)	Intensity
Chalcogenides	Zinc Oxide	4-coordinate tetrahedral	Crossover	9639.0	0.033
			3d→1s	9651.4	0.075
			HOMO→1s	9656.4	0.249
	Zinc Sulfide	4-coordinate tetrahedral	Crossover	9649.3	0.032
			3d→1s	9651.8	0.034
			HOMO→1s	9657.9	0.258
	Zinc Selenide	4-coordinate tetrahedral	Crossover	9649.1	0.026
			3d→1s	9651.7	0.031
			HOMO→1s	9658.3	0.253
Halides	Zinc Fluoride	6-coordinate octahedral	Crossover	9632.7	0.022
			3d→1s	N/A	
			HOMO→1s	9653.3	0.276
	Zinc Chloride	4-coordinate tetrahedral	Crossover	9646.1	0.017
			3d→1s	9651.7	0.050
			HOMO→1s	9656.9	0.233
	Zinc Bromide	4-coordinate tetrahedral	Crossover	9646.7	0.012
			3d→1s	9651.8	0.048
			HOMO→1s	9657.5	0.230
Carboxylates	Anhydrous Zinc Acetate	4-coordinate tetrahedral	Crossover	9637.3	0.014
			3d→1s	9652.0	0.166
			HOMO→1s	9657.2	0.149
	Zinc Propionate	4-coordinate tetrahedral	Crossover	9637.6	0.014
			3d→1s	9651.9	0.148
			HOMO→1s	9657.0	0.146
	Zinc Benzoate	4-coordinate tetrahedral	Crossover	9637.3	0.012
			3d→1s	9652.2	0.202
			HOMO→1s	9657.4	0.121
	Zinc Acrylate	4-coordinate tetrahedral	Crossover	9635.9	0.011
			3d→1s	9652.2	0.181
			HOMO→1s	9657.4	0.134
	Zinc Stearate	4-coordinate tetrahedral	Crossover	9635.8	0.010
			3d→1s	9652.0	0.172
			HOMO→1s	9657.4	0.136
	Zinc Citrate Hydrate	4-5-coordinate	Crossover	9635.7	0.010
			3d→1s	9652.1	0.147
			HOMO→1s	9657.1	0.137

Chemical Class	Material	Zn Environment	Peak	Position (eV)	Intensity
Carboxylates (continued)	Zinc Acetate Dihydrate	6-coordinate pseudo-octahedral	Crossover	9636.8	0.019
			3d→1s	9651.9	0.143
			HOMO→1s	9656.7	0.158
	Zinc Trifluoroacetate Dihydrate	6-coordinate	Crossover	9634.5	0.011
			3d→1s	N/A	
			HOMO→1s	9653.7	0.257
Acetylacetonates	Zinc Acetylacetonate Hydrate	5-coordinate	Crossover	9635.5	0.007
			3d→1s	9652.3	0.169
			HOMO→1s	9657.6	0.103
	Zinc Hexafluoro-acetylacetonate Dihydrate	6-coordinate	Crossover	9634.9	0.008
			3d→1s	9652.3	0.151
			HOMO→1s	9657.2	0.088
Hydrated Salts	Zinc Nitrate Hexahydrate	6-coordinate octahedral	Crossover	9636.3	0.016
			3d→1s	N/A	
			HOMO→1s	9653.5	0.298
	Zinc Perchlorate Hexahydrate	6-coordinate octahedral	Crossover	9635.4	0.013
			3d→1s	N/A	
			HOMO→1s	9653.5	0.282
	Zinc Sulfate Hexahydrate	6-coordinate octahedral	Crossover	9635.3	0.015
			3d→1s	N/A	
			HOMO→1s	9653.5	0.297
Nitrogen-Rich	Zinc Tetra-methylimidazole	4-coordinate tetrahedral	Crossover	N/A	
			3d→1s	9651.8	0.106
			HOMO→1s	9656.3	0.235
	Zinc Hexa-methylimidazole	6-coordinate octahedral	Crossover	N/A	
			3d→1s	9651.7	0.085
			HOMO→1s	9655.8	0.209
	Zinc Tetraphenyl-porphyrin	4-coordinate square planar	Crossover	N/A	
			3d→1s	9651.7	0.084
			HOMO→1s	9656.4	0.195
	Zinc Octaethyl-porphyrin	4-coordinate square planar	Crossover	N/A	
			3d→1s	9651.7	0.061
			HOMO→1s	9656.6	0.199
	Zinc Phthalo-cyanine	4-coordinate square planar	Crossover		
			3d→1s	9651.5	0.078
			HOMO→1s	9656.2	0.218

Chemical Class	Material	Zn Environment	Peak	Position (eV)	Intensity
Sulfur-Rich	Zinc Tetrathiophenol	4-coordinate tetrahedral	Crossover	N/A	
			3d→1s	9651.3	0.047
			HOMO→1s #1	9657.4	0.195
			HOMO→1s #2	9658.6	0.084
	TmZnPMA	4-coordinate pseudo-tetrahedral	Crossover	N/A	
			3d→1s	9651.2	0.054
			HOMO→1s #1	9657.3	0.203
			HOMO→1s #2	9658.5	0.063
	TmZnSPh	4-coordinate pseudo-tetrahedral	Crossover	N/A	
			3d→1s	9651.4	0.055
			HOMO→1s #1	9657.4	0.215
			HOMO→1s #2	9658.7	0.074
	Zinc Diethyl-dithiocarbamate	4-coordinate tetrahedral	Crossover	N/A	
			3d→1s	9651.4	0.049
			HOMO→1s #1	9657.6	0.182
			HOMO→1s #2	9658.3	0.089
Mixed Coordination	Zinc $(Propionate)_2$ $(Thiourea)_2$	4-coordinate 2 O, 2 S	Crossover	9637.6	0.009
			3d→1s	9652.7	0.142
			HOMO→1s	9658.0	0.188
	Zinc $(Benzoate)_2$ $(Thiourea)_2$	4-coordinate 2 O, 2 S	Crossover	9638.1	0.009
			3d→1s	9652.9	0.142
			HOMO→1s	9658.0	0.162
	Zinc $(Benzoate)_2$ $(Aminopyridine)_2$	4-coordinate 2 O, 2 N	Crossover	9638.1	0.011
			3d→1s	9652.8	0.150
			HOMO→1s	9657.2	0.152
	TpZnOH	4-coordinate 1 O, 3 N	Crossover	9638.6	0.014
			3d→1s	9652.0	0.109
			HOMO→1s	9656.7	0.229
	Zinc $(Thiophenol)_2$ $(Methylimidazole)_2$	4-coordinate 2 N, 2 S	Crossover	N/A	
			3d→1s	9652.0	0.081
			HOMO→1s #1	9655.7	0.079
			HOMO→1s #2	9658.5	0.150

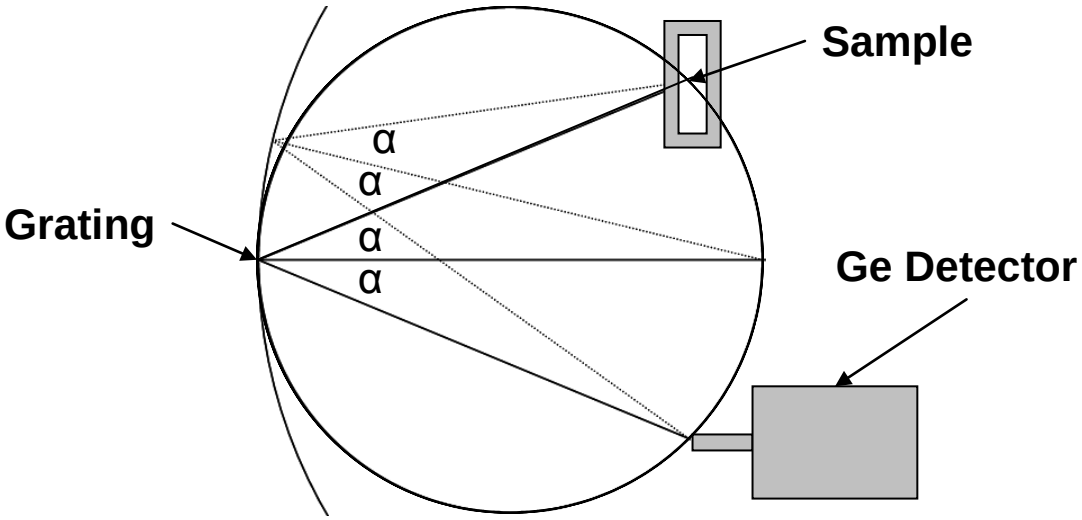

Figure 5.1: Schematic of Rowland circle geometry.

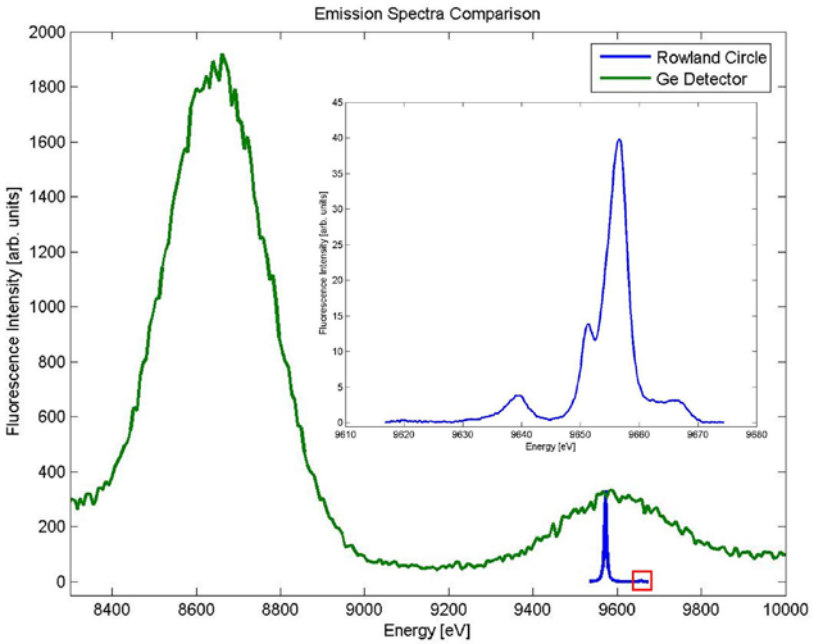

Figure 5.2: Comparison between zinc emission spectra. The green line shows a fragment of a typical X-ray emission spectrum, as detected by a standard energy-dispersive Ge detector, after excitation with a 12 keV incident beam. The peak at 8637 eV is the zinc Kα fluorescence, and the peak at 9572 eV is the $K\beta_{1,3}$ fluorescence. The blue line depicts the $K\beta_{1,3}$ fluorescence as detected by the experimental setup described in this paper. At this scale, the $K\beta_{2,5}$ fluorescence can barely be seen at approximately 9656 eV. The insert shows a blow-up of the red box around the high energy side of the $K\beta_{1,3}$ spectrum, showing the detail of the $K\beta_{2,5}$ and Kβ'' peaks.

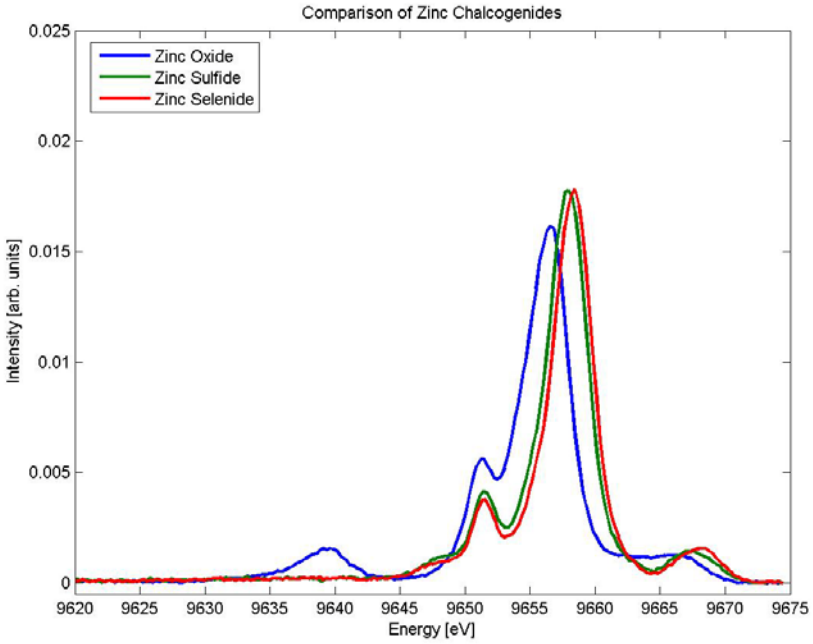

Figure 5.3: XES of Zinc Chalcogenides.

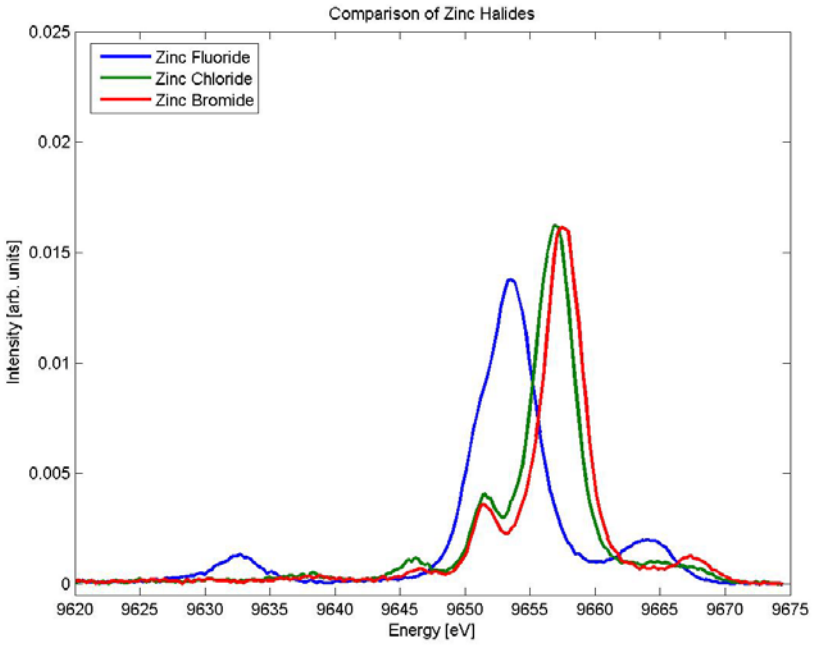

Figure 5.4: XES of Zinc Halides.

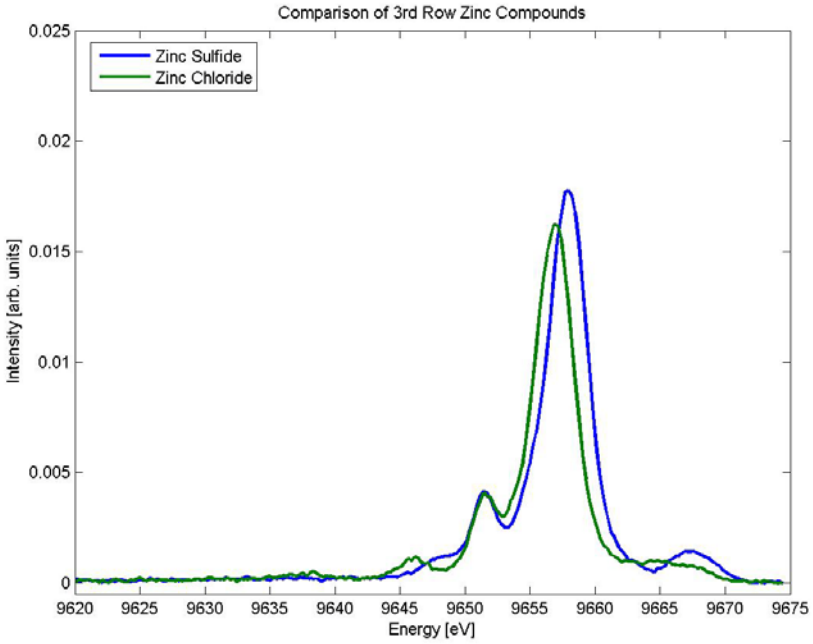

Figure 5.5: XES of 3rd-Row Zinc Salts.

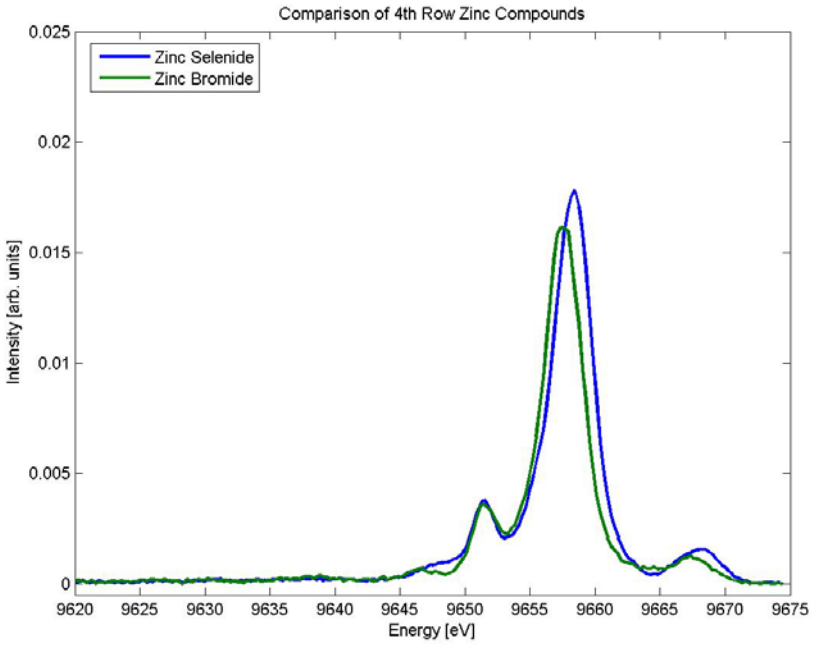

Figure 5.6: XES of 4th-Row Zinc Salts.

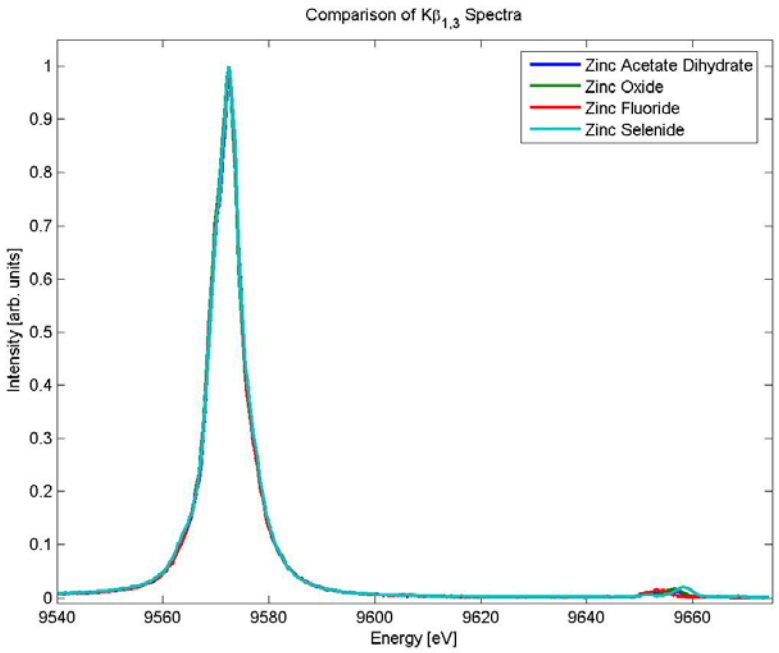

Figure 5.7: Comparison of $K\beta_{1,3}$ spectra of various zinc compounds. The large peak at 9572 eV is the zinc 3p→1s transition. The $K\beta_{2,5}$ region is visible at the high energy side of the spectrum.

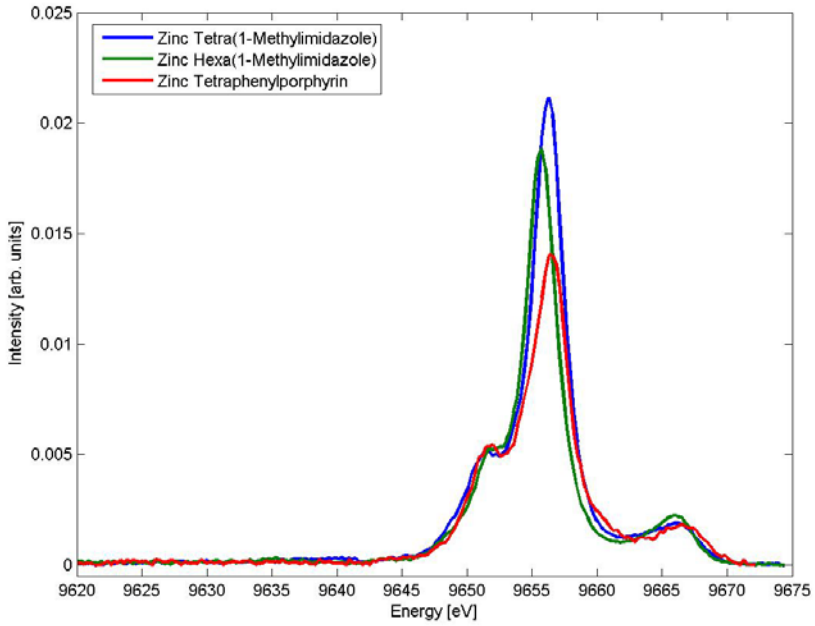

Figure 5.8: Variation of XES with geometry.

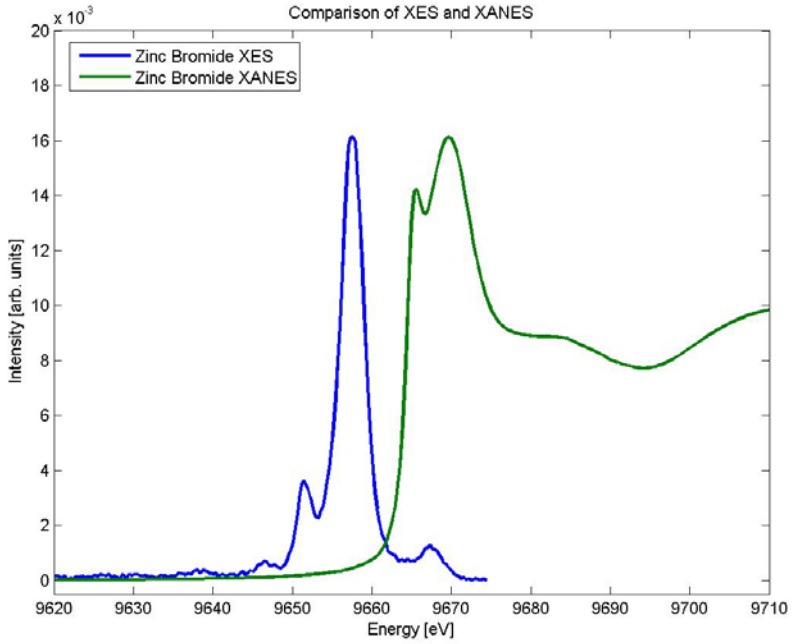

Figure 5.9: Comparison of XES and XANES for zinc bromide. Both plots have been scaled so that the maximum intensities coincide to aid comparison.

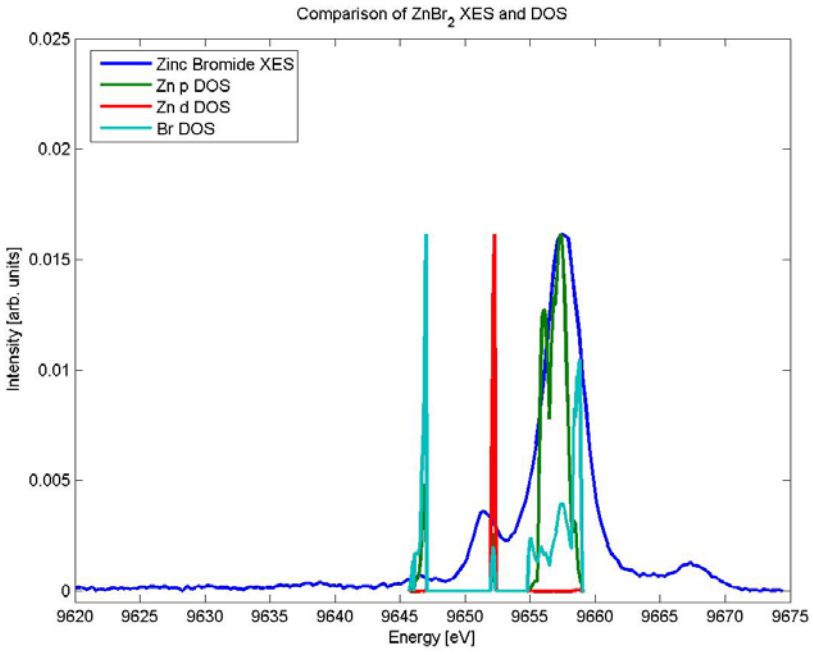

Figure 5.10: Comparison between XES and DOS calculations for $ZnBr_2$. The DOS has been scaled to the $K\beta_{2,5}$ maximum and shifted by the Zn 1s binding energy (9659 eV).

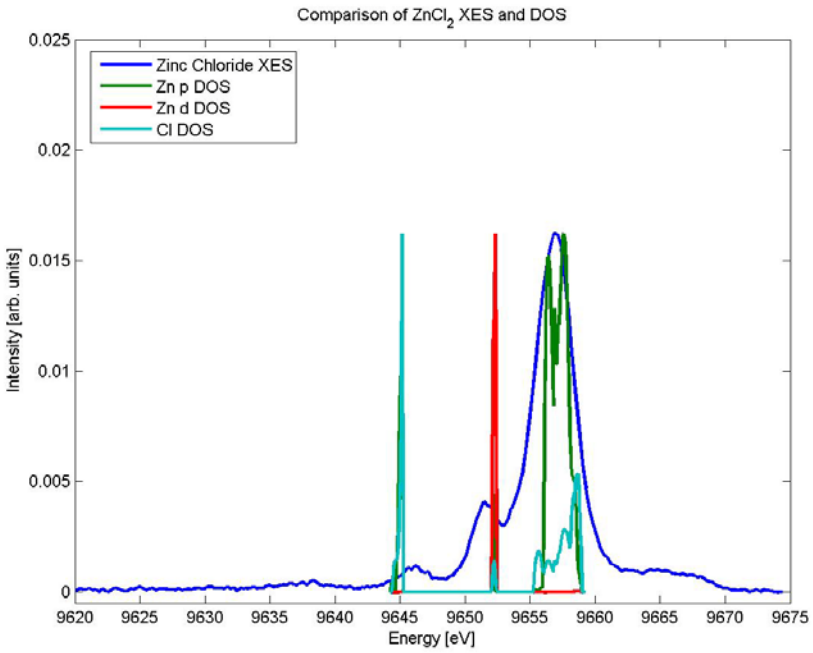

Figure 5.11: Comparison between XES and DOS calculations for $ZnCl_2$. The DOS has been scaled to the $K\beta_{2,5}$ maximum and shifted by the Zn 1s binding energy (9659 eV).

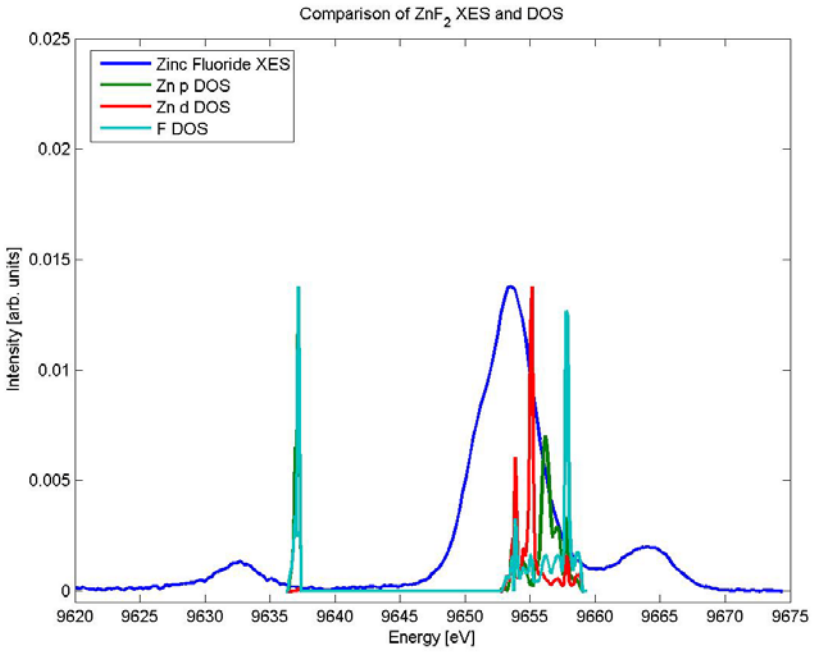

Figure 5.12: Comparison between XES and DOS calculations for ZnF_2. The DOS has been scaled to the $K\beta_{2,5}$ maximum and shifted by the Zn 1s binding energy (9659 eV).

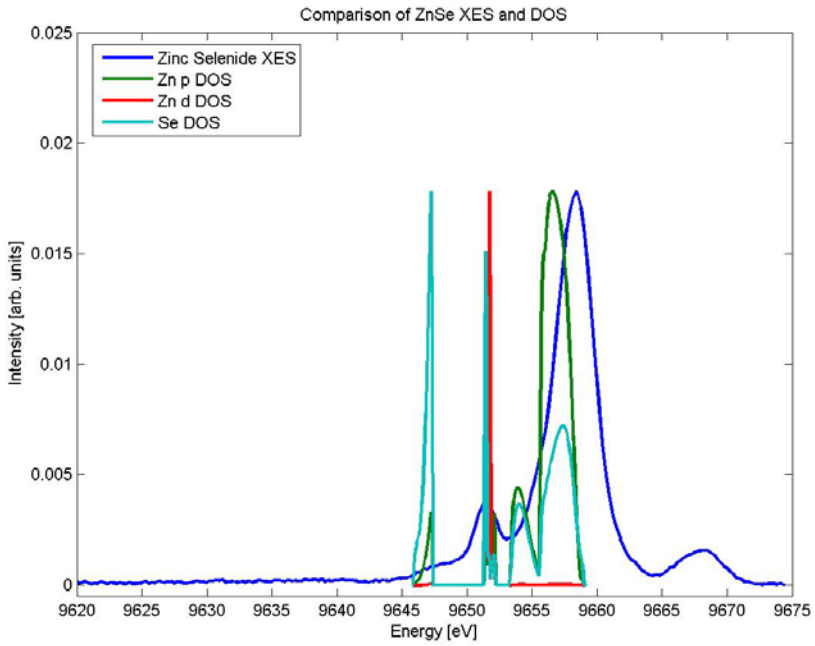

Figure 5.13: Comparison between XES and DOS calculations for ZnSe. The DOS has been scaled to the $K\beta_{2,5}$ maximum and shifted by the Zn 1s binding energy (9659 eV).

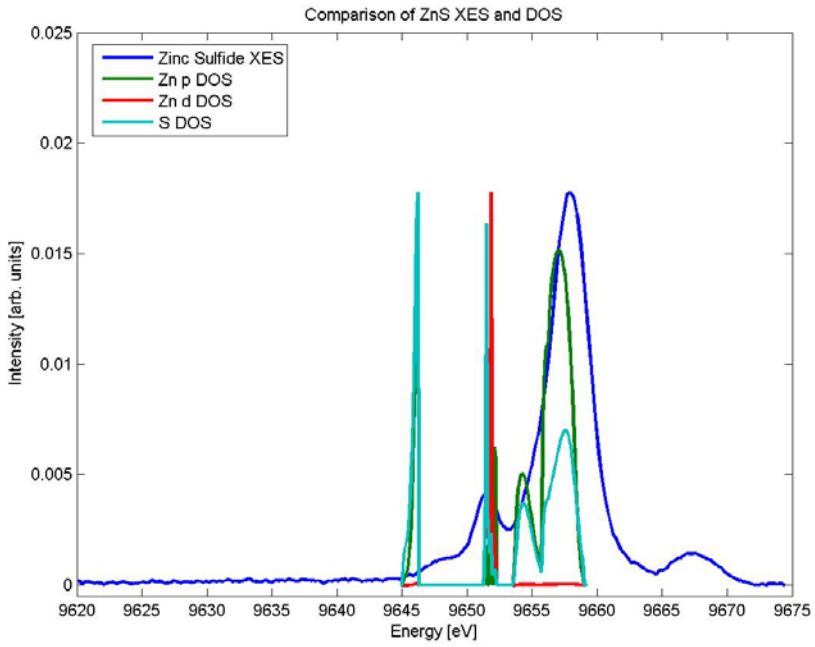

Figure 5.14: Comparison between XES and DOS calculations for ZnS. The DOS has been scaled to the $K\beta_{2,5}$ maximum and shifted by the Zn 1s binding energy (9659 eV).

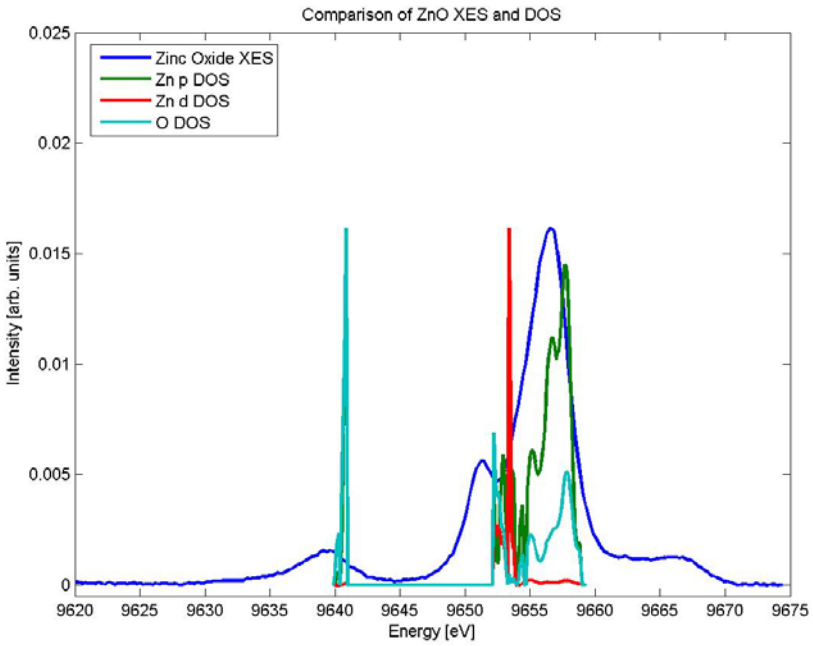

Figure 5.15: Comparison between XES and DOS calculations for ZnO. The DOS has been scaled to the $K\beta_{2,5}$ maximum and shifted by the Zn 1s binding energy (9659 eV).

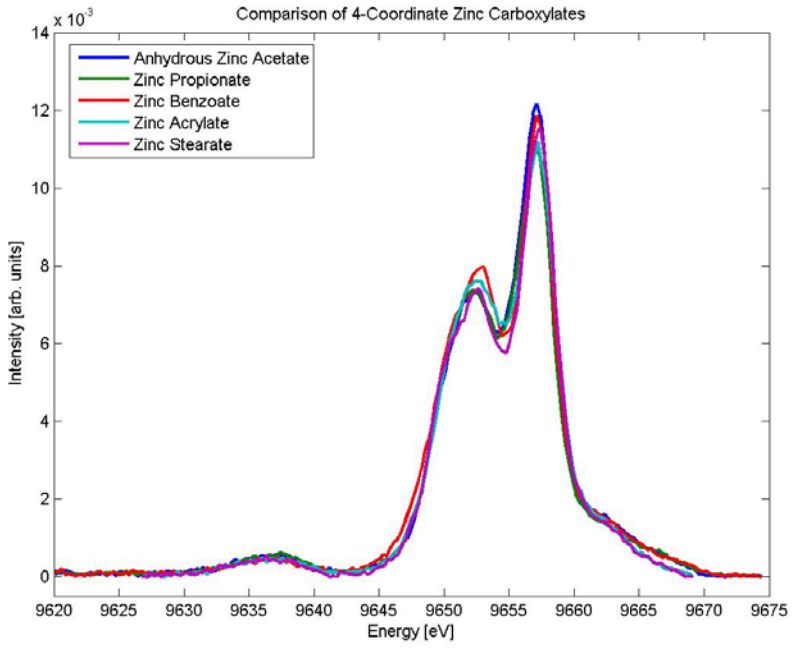

Figure 5.16: Comparison of XES for 4-coordinate zinc carboxylates.

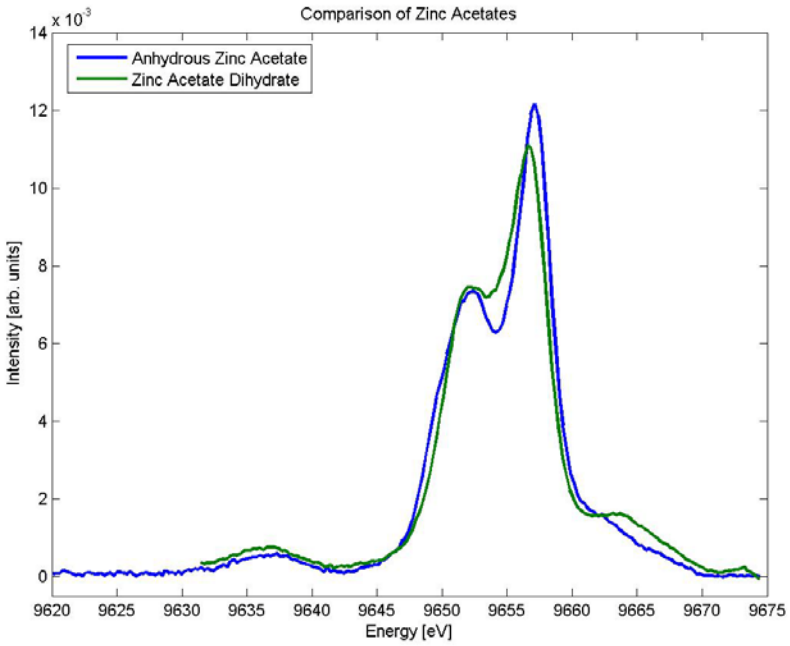

Figure 5.17: Comparison of XES for anhydrous zinc acetate and the corresponding dihydrate.

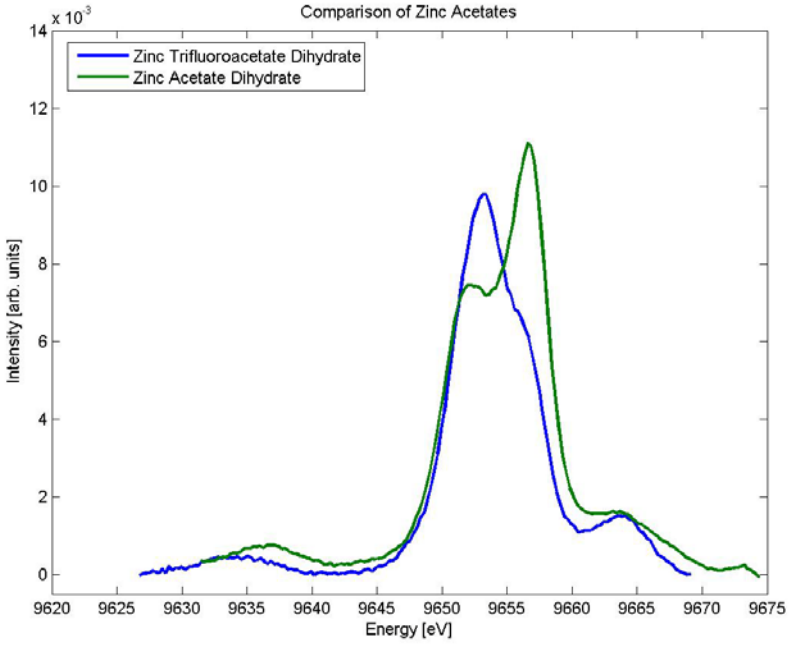

Figure 5.18: Comparison of zinc acetate dihydrate with fluorinated form.

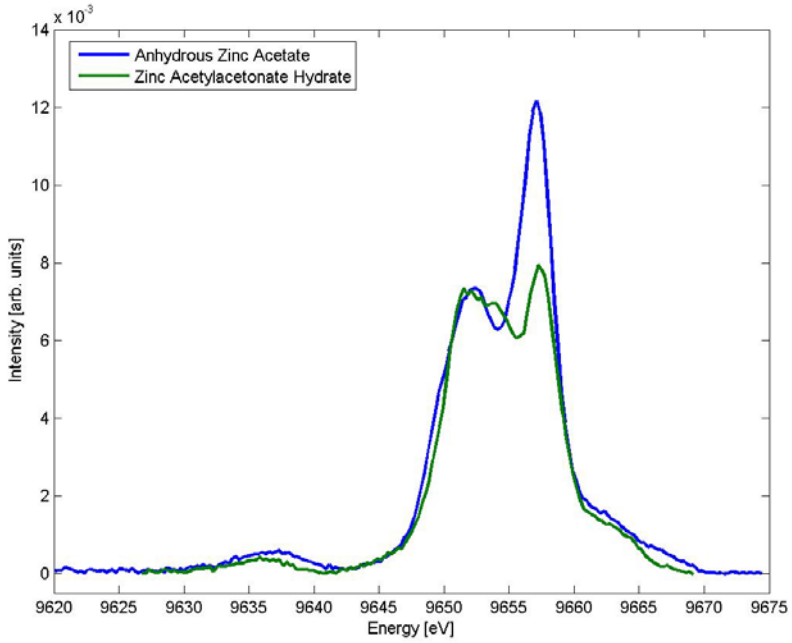

Figure 5.19: Comparison of zinc acetate and zinc acetylacetonate.

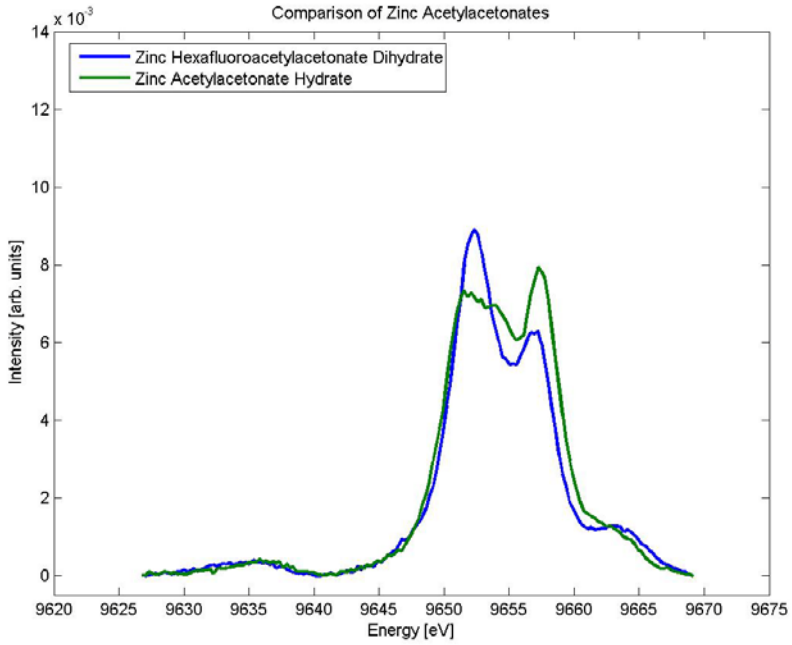

Figure 5.20: Comparison of zinc acetylacetonates.

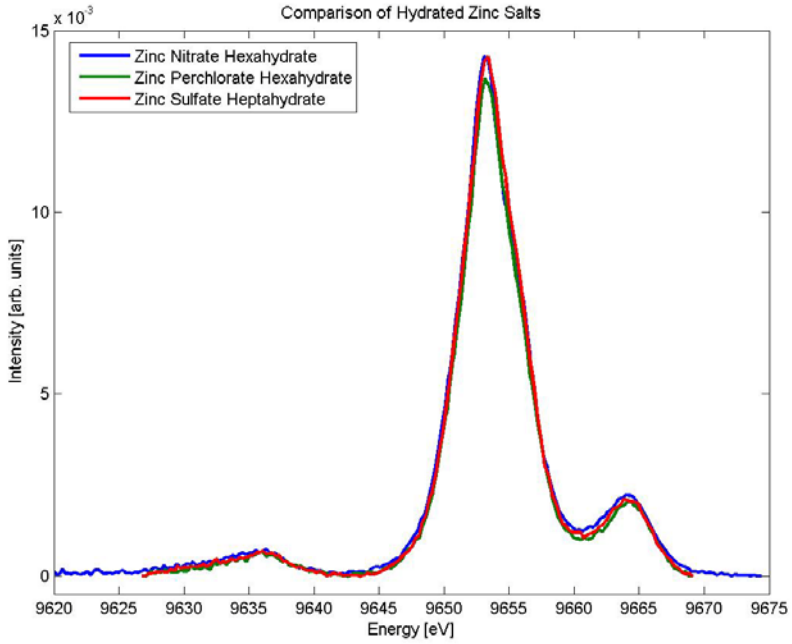

Figure 5.21: XES of hydrated zinc salts.

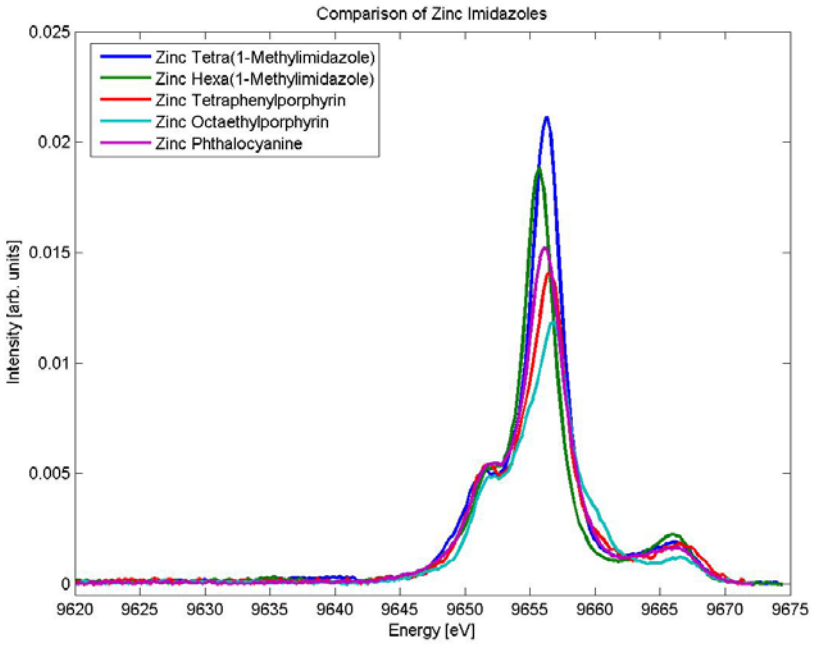

Figure 5.22: Comparison of zinc compounds dominated by Zn-N ligation.

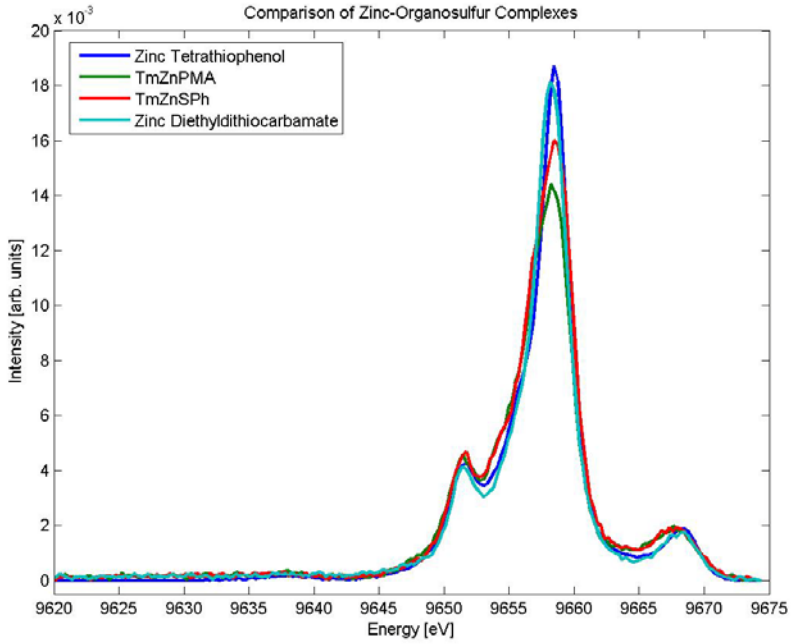

Figure 5.23: XES of zinc-organosulfur complexes. Here, "TmZnPMA" = $[Tm^{t\text{-}Bu}]ZnSCH_2C(O)N(H)Ph$ and "TmZnSPh" = $[Tm^{t\text{-}Bu}]ZnSPh$.

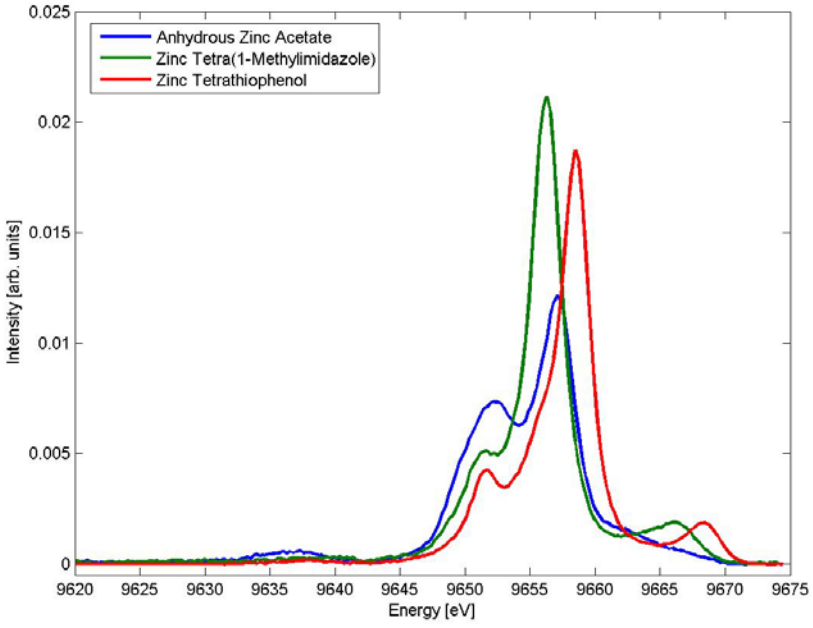

Figure 5.24: XES comparison of zinc compounds in carboxylate, imidazole, and thiolate environments.

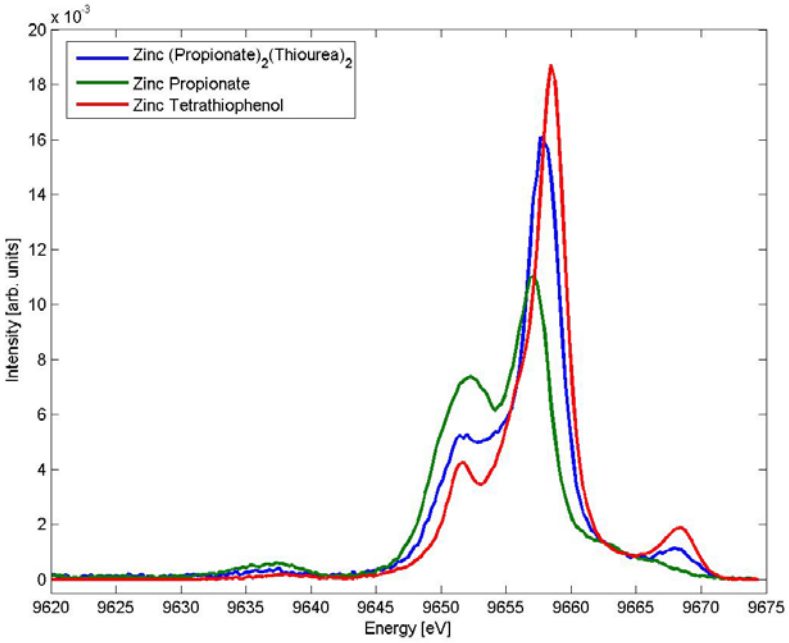

Figure 5.25: XES of (dipropionato-O)(dithiourea-S)zinc(II).

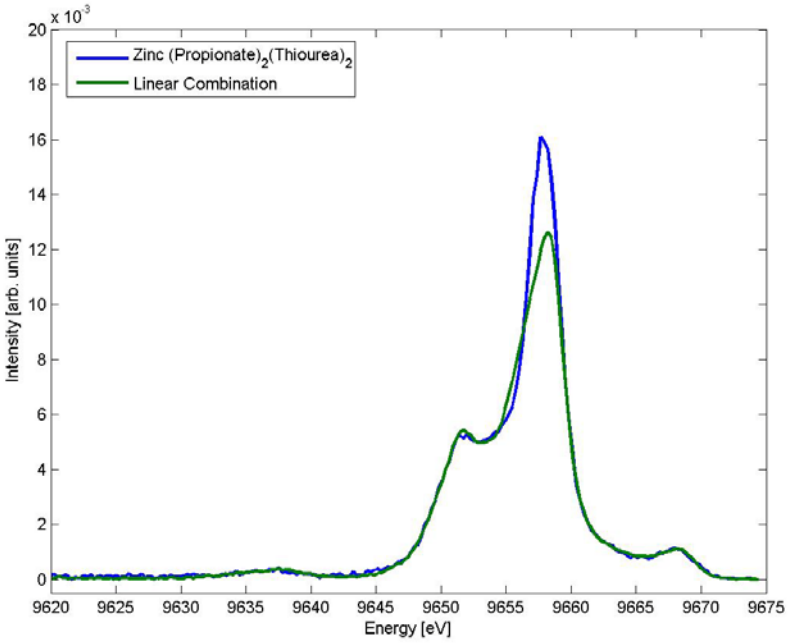

Figure 5.26: XES of (dipropionato-O)(dithiourea-S)zinc(II) and fit. The fit consists of 50% of the zinc propionate spectrum and 50% of the zinc tetrathiophenol spectrum.

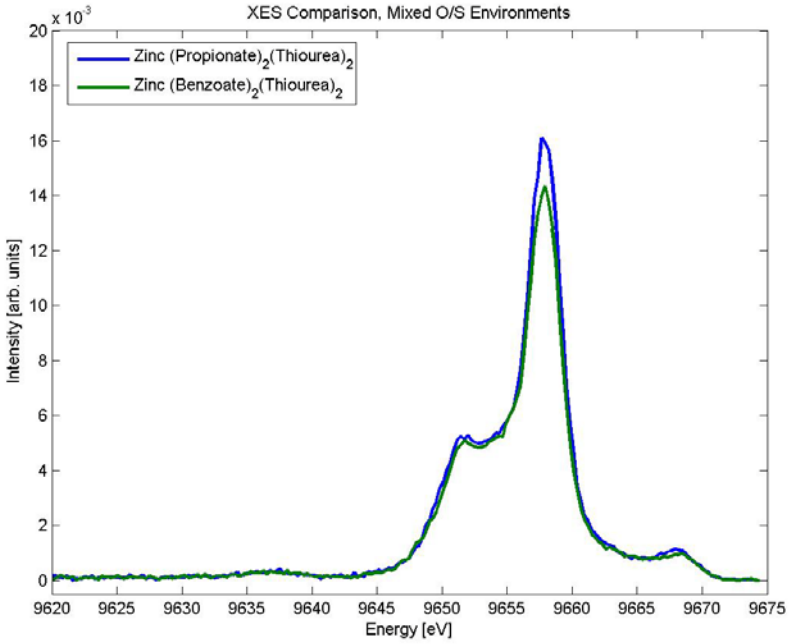

Figure 5.27: XES comparison of mixed oxygen/sulfur zinc environments.

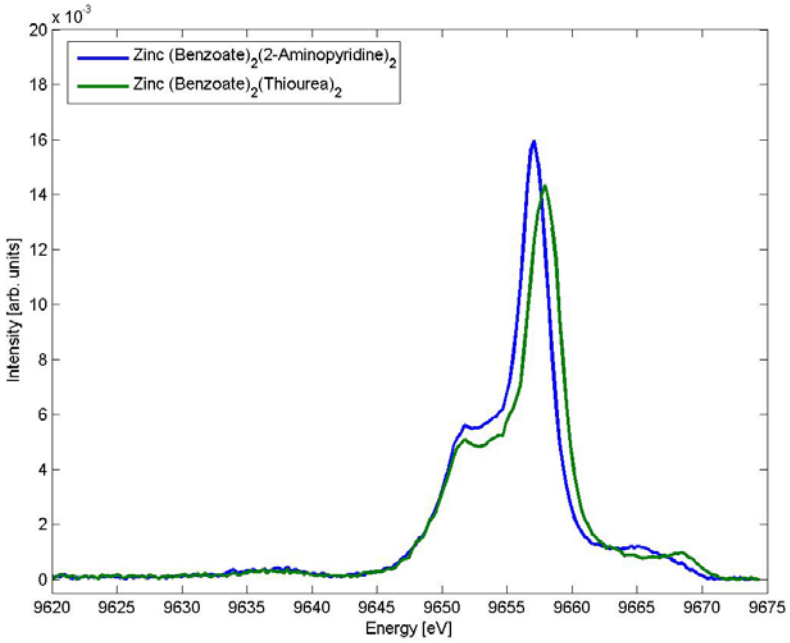

Figure 5.28: XES comparison of bis(2-aminopyridine-N)bis(benzoato-O)zinc(II) and bis(benzoato-O)bis(thiourea-S)zinc(II).

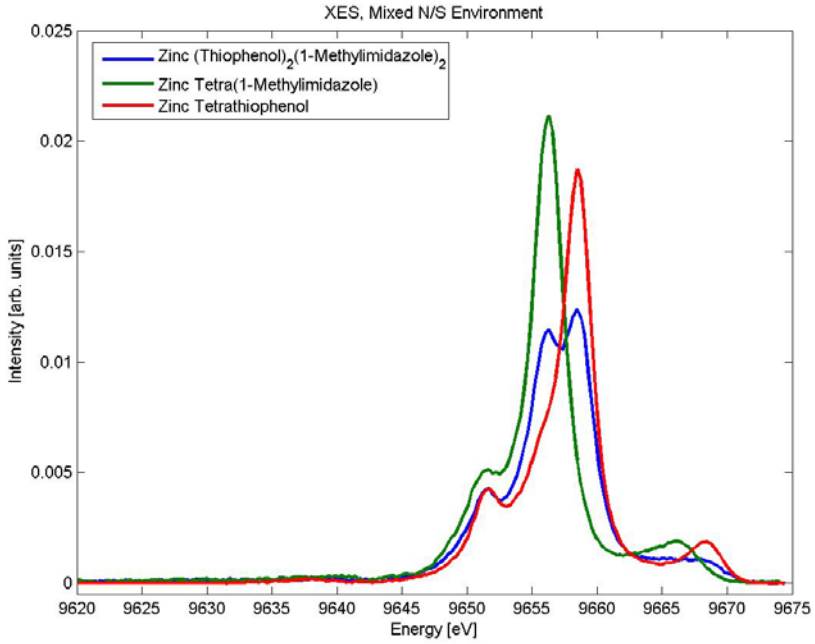

Figure 5.29: XES of bis(1-methylimidazole)bis(thiophenolato)zinc(II).

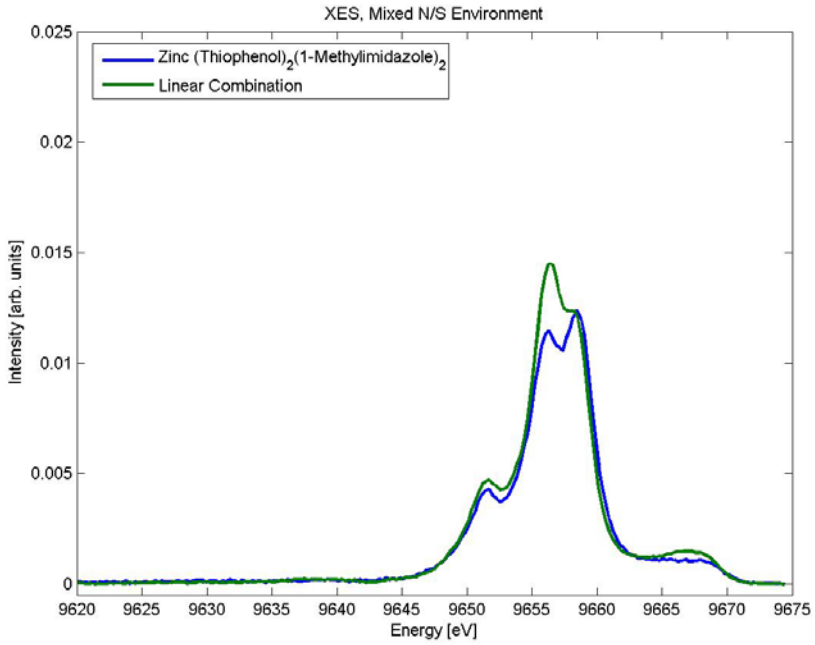

Figure 5.30: XES of bis(1-methylimidazole)bis(thiophenolato)zinc(II) and fit. The fit consists of 50% of the zinc tetra(1-methylimidazole) spectrum and 50% of the zinc tetrathiophenol spectrum.

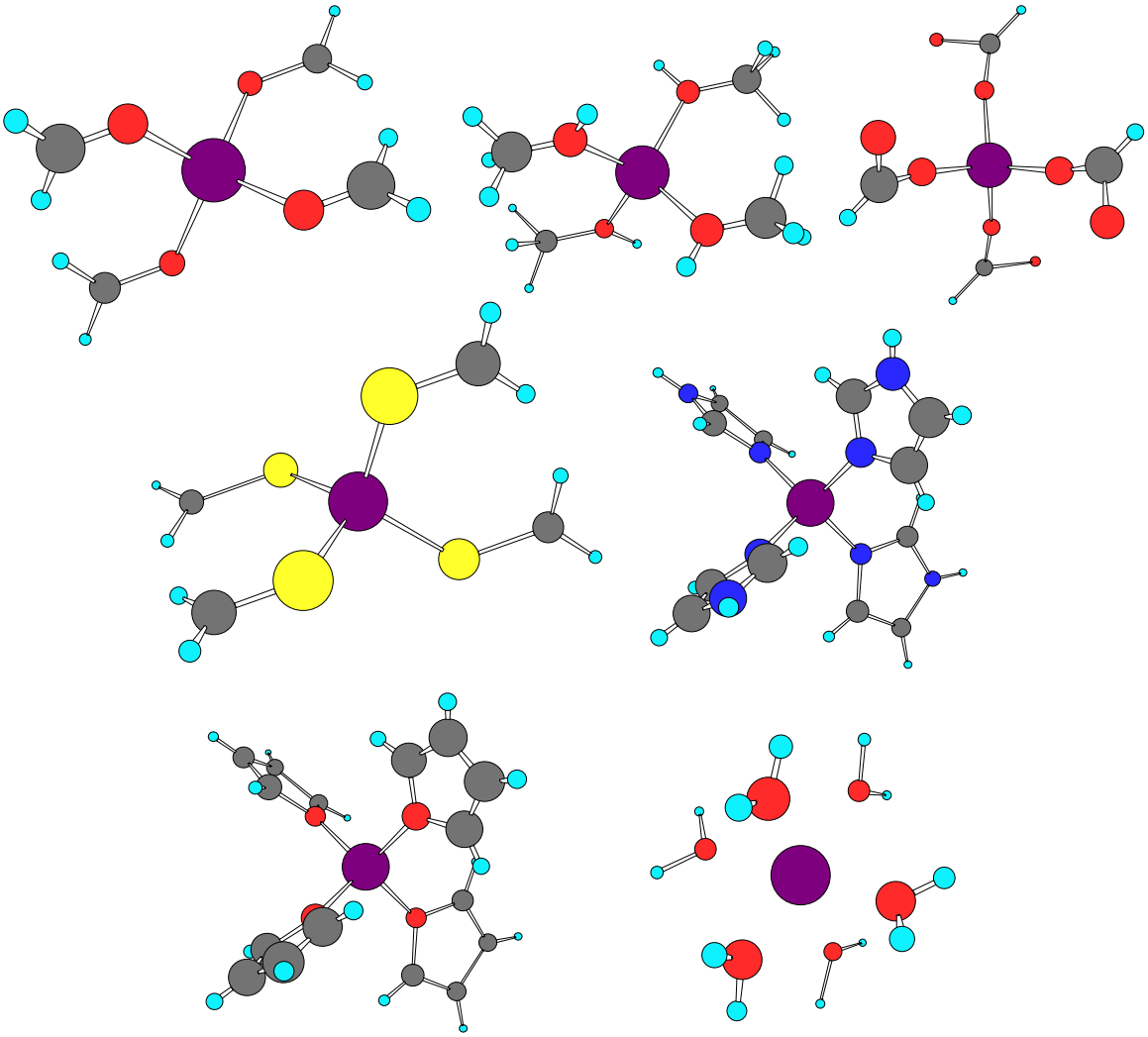

Figure 5.31: Input models used in cluster calculations. Here, grey represents carbon, red represents oxygen, light blue represents hydrogen, dark blue represents nitrogen, yellow represents sulfur, and dark purple represents zinc. The ligands sets are (from left to right):
Top row: Formaldehyde, methanol, formate
Middle row: Thioformaldehyde, imidazole
Bottom row: furan, water

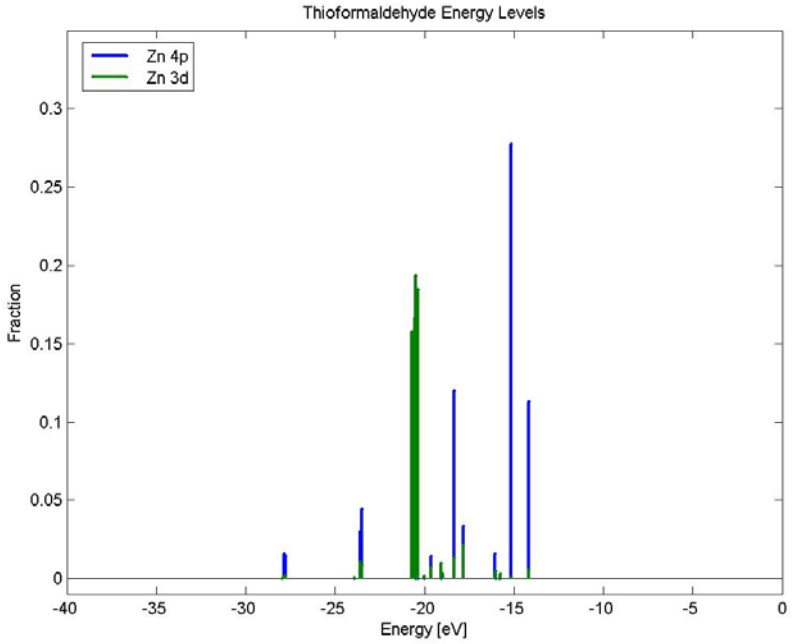

Figure 5.32: Stick spectrum for thioformaldehyde ligation.

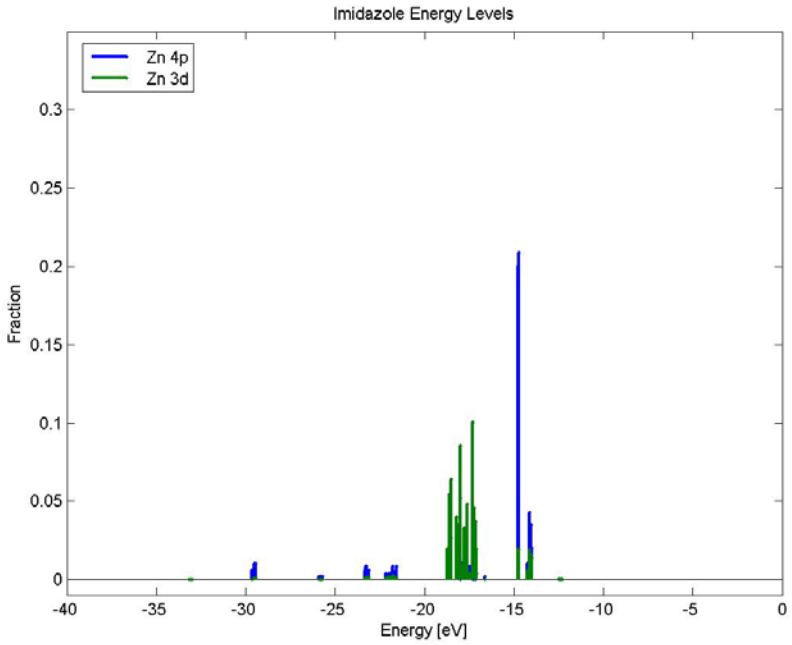

Figure 5.33: Stick spectrum for imidazole ligation.

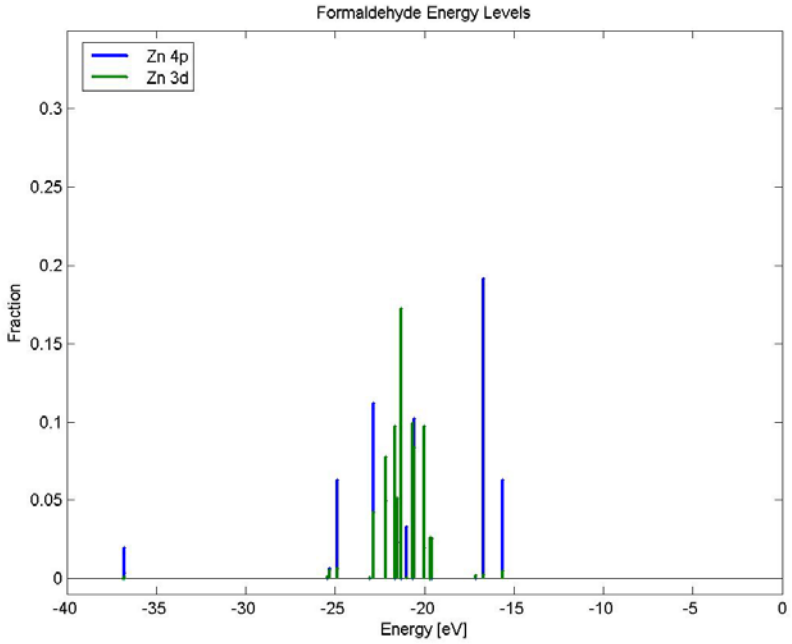

Figure 5.34: Stick spectrum for formaldehyde ligation.

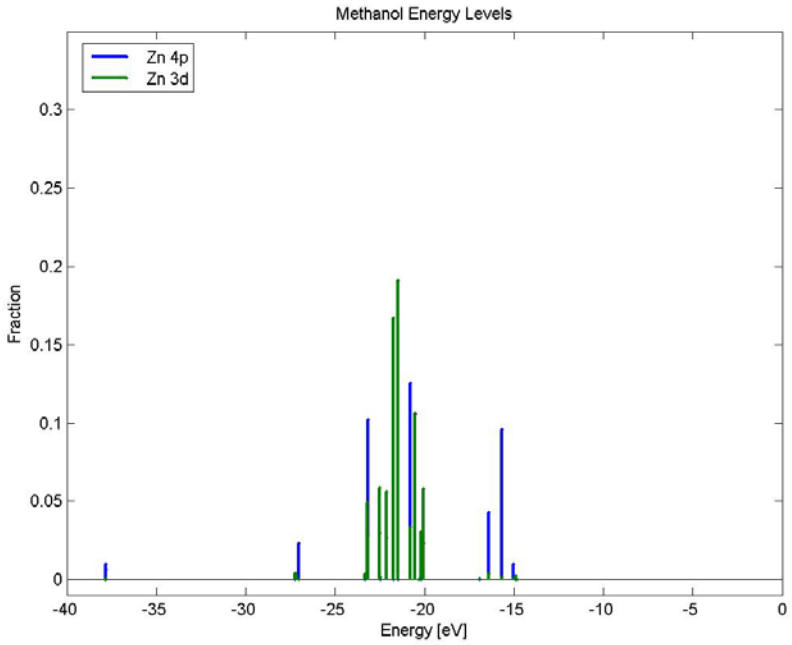

Figure 5.35: Stick spectrum for methanol interaction.

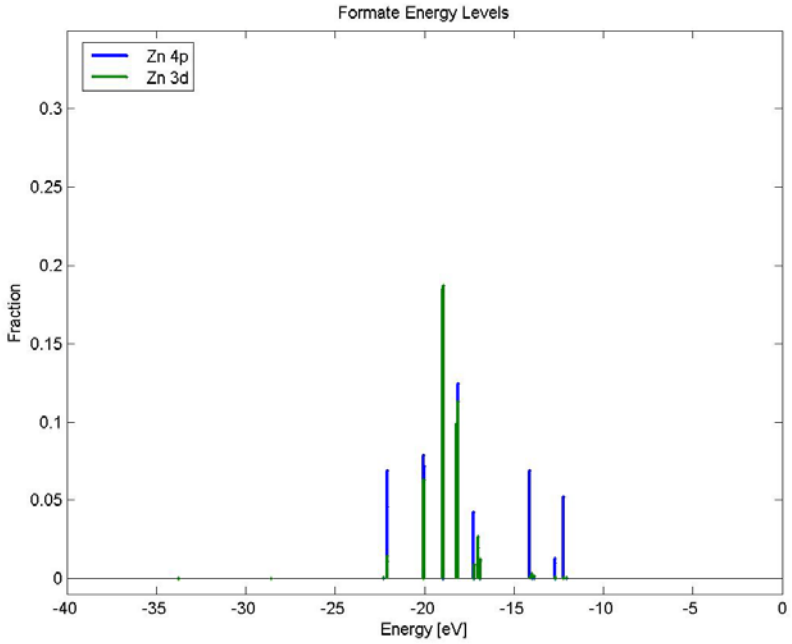

Figure 5.36: Stick spectrum for formate interaction.

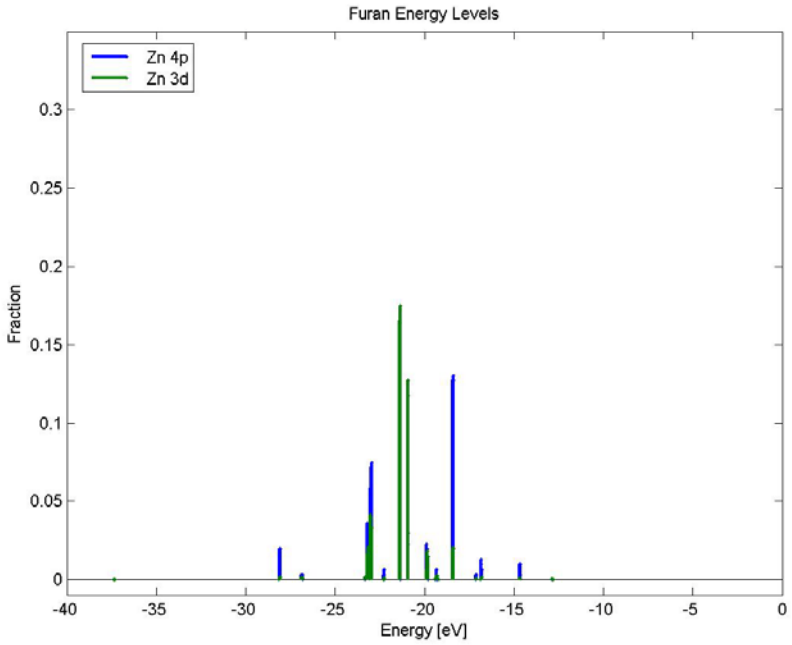

Figure 5.37: Stick spectrum for furan interaction.

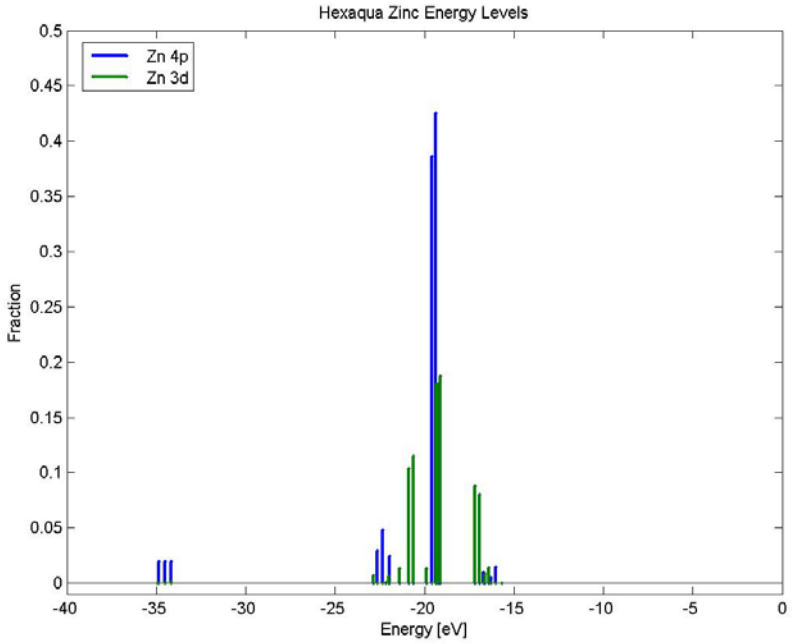

Figure 5.38: Stick spectrum for hexaqua zinc.

References

1. Vallee, B.L., *The biochemical basis of zinc physiology*. Physiological reviews, 1993. **73**(1): p. 79.
2. Penner-Hahn, J.E., *Characterization of "spectroscopically quiet" metals in biology*. Coordination Chemistry Reviews, 2005. **249**(1-2): p. 161.
3. Kremer-Aach, A., et al., *Cobalt as a Probe for Zinc in Metalloenzyme Model Compounds? A Comparison of Spectroscopic Features and Coordination Geometry of Four- and Five-Coordinate Complexes. Crystal and Molecular Structures of [Co(eta(3)-Tp(Ph))(eta(2)-Tp(Ph))], [(eta(3)-Tp(Ph))Zn(anthranilate)], and [(eta(3)-Tp(Ph))M(eta(2)-acac)] (Tp(Ph) = Hydrotris(3-phenylpyrazol-1-yl)borate, acac = Pentane-2,4-dionate, and M = Zn, Co).* Inorganic chemistry, 1997. **36**(8): p. 1552.
4. Kimblin, C., et al., *Bis (mercaptoimidazolyl)(pyrazolyl) hydroborato Complexes of Zinc, Cadmium, and Cobalt: Structural Evidence for the Enhanced Tendency of Zinc in Biological Systems to Adopt Tetrahedral M [S4] Coordination.* Inorganic chemistry, 2000. **39**(19): p. 4240.
5. Lipton, A.S., et al., *Solid-State 67Zn NMR Spectroscopic Studies and ab Initio Molecular Orbital Calculations on a Synthetic Analogue of Carbonic Anhydrase.* Journal of the American Chemical Society, 2003. **125**(13): p. 3768.
6. Lipton, A.S., R.W. Heck, and P.D. Ellis, *Zinc Solid-State NMR Spectroscopy of Human Carbonic Anhydrase: Implications for the Enzymatic Mechanism.* Journal of the American Chemical Society, 2004. **126**(14): p. 4735.
7. Strange, R.W., M. Ellis, and S.S. Hasnain, *Atomic resolution crystallography and XAFS.* Coordination Chemistry Reviews, 2005. **249**(1-2): p. 197.
8. Riggs-Gelasco, P.J., et al., *Reduced derivatives of the Mn cluster in the oxygen-evolving complex of photosystem II: An EXAFS study.* Journal of the American Chemical Society, 1996. **118**(10): p. 2387.
9. Teo, B.K., *EXAFS: Basic Principles and Data Analysis*. 1986, Berlin: Springer-Verlag.
10. Kelly, R.A., *Structural, Spectroscopic, and Mechanistic Studies of Zinc Alkyl Transfer Enzymes*. 2007, University of Michigan.
11. Clark-Baldwin, K., et al., *The limitations of X-ray absorption spectroscopy for determining the structure of zinc sites in proteins. When is a tetrathiolate not a tetrathiolate?* Journal of the American Chemical Society, 1998. **120**(33): p. 8401.
12. Bergmann, U., et al., *High-resolution X-ray spectroscopy of rare events: a different look at local structure and chemistry.* Journal of Synchrotron Radiation, 2001. **8**(2): p. 199.
13. Born, M. and E. Wolf, *Principles of Optics*. 7th ed. 2005: Cambridge University Press.
14. Thompson, A., et al., *X-Ray Data Booklet*, ed. U.o.C. Lawrence Berkeley National Laboratory, Berkeley, CA. 2001.
15. Raj, S.S. and S. Raj, *Bis (2-aminopyridine-N) bis (benzoato-O) zinc.* Acta crystallographica. Section C, Crystal structure communications, 2000. **56**(7): p. 742.

16. Clegg, W., I.R. Little, and B.P. Straughan, *Monoclinic anhydrous zinc (II) acetate.* Acta crystallographica. Section C, Crystal structure communications, 1986. **42**(12): p. 1701.
17. Chen, X.M., et al., *Tetrakis (1-methylimidazole-N3) zinc (II) Diperchlorate.* Acta crystallographica. Section C, Crystal structure communications, 1996. **52**(10): p. 2482.
18. Cernak, J., et al., *Bis (benzoato-O) bis (thiourea-S) zinc (II).* Acta crystallographica. Section C, Crystal structure communications, 1995. **51**(3): p. 392.
19. Smolander, K., et al., *Monomeric (dipropionato-O)(dithiourea-S)zinc(II).* Acta crystallographica. Section C, Crystal structure communications, 1994. **56**(7): p. 742.
20. Wilker, J.J. and S.J. Lippard, *Alkyl transfer to metal thiolates: kinetics, active species identification, and relevance to the DNA methyl phosphotriester repair center of Escherichia coli Ada.* Inorganic chemistry, 1997. **36**(6): p. 969.
21. Wilker, J.J., *Modeling the DNA Methylphosphotriester Repair Site in Escherichia coli Ada. Why Zinc and Four Cysteines?* Journal of the American Chemical Society, 1995. **117**(33): p. 8682.
22. Marzotto, A., et al., *Structure of hexakis (methylimidazole) cobalt (II) dichloride dihydrate,[Co (CH3-C3H3N2) 6] Cl2. 2H2O.* Acta crystallographica. Section C, Crystal structure communications, 1989. **45**(4): p. 582.
23. Alsfasser, R., et al., *A mononuclear zinc hydroxide complex stabilized by a highly substituted tris (pyrazolyl) hydroborato ligand: analogies with the enzyme carbonic anhydrase.* Inorganic chemistry, 1991. **30**(21): p. 4098.
24. Melnick, J.G., et al., *Thiolate exchange in [TmR]ZnSR' complexes and relevance to the mechanisms of thiolate alkylation reactions involving zinc enzymes and proteins.* Journal of Inorganic Biochemistry, 2006. **100**(5-6): p. 1147.
25. Van Grieken, R.E. and A.A. Markowicz, eds. *Handbook of X-Ray Spectrometry*. 2002, Marcel Dekker: New York, NY.
26. Wyckoff, R.W.G., *Crystal Structures*. 2nd ed. Vol. 1. 1963, New York: John Wiley & Sons.
27. Hermann, K., et al. 2009. p. StoBe-deMon, version 3.0.
28. Roe, A.L., et al., *X-ray absorption spectroscopy of iron-tyrosinate proteins.* Journal of the American Chemical Society, 1984. **106**(6): p. 1676.
29. Glatzel, P. and U. Bergmann, *High resolution 1s core hole X-ray spectroscopy in 3d transition metal complexes—electronic and structural information.* Coordination chemistry reviews, 2005. **249**(1-2): p. 65.
30. Bergmann, U., et al., *Chemical dependence of interatomic X-ray transition energies and intensities - a study of Mn K[beta]" and K[beta]2, 5 spectra.* Chemical Physics Letters, 1999. **302**(1-2): p. 119.
31. Chambers, R.D., *Fluorine in Organic Chemistry*. 2004, Hoboken, NJ: Wiley-Blackwell.
32. Cotton, F.A., *Soft X-Ray Absorption Edges of Metal Ions in Complexes. III. Zinc (II) Complexes.* The Journal of chemical physics, 1958. **28**(1): p. 83.

33. Harding, M.M., *The geometry of metal-ligand interactions relevant to proteins.* Acta crystallographica. Section D, Biological crystallography, 1999. **55**(8): p. 1432.
34. Rudolph, W.W. and C.C. Pye, *Zinc (II) Hydration in Aqueous Solution: A Raman Spectroscopic Investigation and An ab initio Molecular Orbital Study of Zinc (II) Water Clusters.* Journal of Solution Chemistry, 1999. **28**(9): p. 1045.
35. Guo, J., et al., *X-ray and Visible Absorption Spectroscopy of Wild-Type and Mutant T4 Gene 32 Proteins: His64, not His81, Is the Non-Thiolate Zinc Ligand.* Journal of the American Chemical Society, 2002. **117**(37): p. 9437.
36. Erskine, P.T., et al., *X-ray structure of 5-aminolaevulinate dehydratase, a hybrid aldolase.* Nature structural biology, 1997. **4**(12): p. 1025.
37. Safranek, J. *Spear3 accelerator physics update*. in *Particle Accelerator Conference, 2007 IEEE*. 2007.
38. Wiedemann, H., *Synchrotron Radiation*. 2002, New York, NY: Springer.
39. Ishioka, T., *Vibrational spectra and structures of zinc carboxylates I. Zinc acetate dihydrate.* Spectrochimica acta. Part B, Atomic spectroscopy, 1998. **54**(12): p. 1827.
40. Sarret, G., et al., *Structural Determination of Zn and Pb Binding Sites in Penicillium chrysogenum Cell Walls by EXAFS Spectroscopy.* Environmental Science & Technology, 1998. **32**(11): p. 1648.

Chapter 6

Summary and Future Directions

The Role of Zinc in Malaria

Due to the emergence of drug-resistant strains of the malaria parasite *Plasmodium falciparum* [1], there is much interest in discovering alternative treatment strategies. Since red blood cells infected with *P. falciparum* accumulate zinc approximately threefold over normal erythrocyte levels [2-4], and since zinc levels are tightly regulated within the cell, one possible approach is to prevent zinc uptake through the use of metal chelators. The O'Halloran lab at Northwestern University has found that a 0.5 μM concentration of the high-affinity, membrane-permeable chelator TPEN was sufficient to reduce parasitemia by 50%, whereas a much greater concentration (~350 μM) of the high-affinity, membrane-impermeable chelator EDTA caused no measurable reduction in infection levels, despite media zinc concentrations on the order of 1 μM.

X-ray fluorescence imaging results indicated that both 0.5 μM TPEN and 350 μM EDTA were able to prevent zinc uptake in schizont-stage infected erythrocytes. Furthermore, the chelator-treated samples seemed to have consumed a significantly greater percentage of the host cytosol, as judged by the percent total iron present in the hemozoin crystal. We hypothesized that increased cytosol consumption was one of the methods by which zinc-deprived parasites coped with zinc starvation. Furthermore, in contrast to earlier reports that the parasite did not utilize a significant fraction of the host cell zinc, based on the Zn/Fe ratio of the hemozoin crystal, XRF imaging data suggested

that the host cell zinc had undergone processing by the parasite, at least in the chelator-treated samples. This was hypothesized to be another method by which parasites coped with extracellular zinc deprivation.

Since the zinc levels, phosphorous levels, and percentage of host cell cytosol consumed were identical between the TPEN-treated and EDTA-treated samples, X-ray absorption spectroscopy was carried out in order to determine the essential difference between the two. While the TPEN-treated sample was found to have a similar average zinc environment compared to the untreated schizont-stage and uninfected samples, the EDTA-treated sample had an average zinc site with significantly higher sulfur content. We hypothesized that these sulfur-rich sites represented essential zinc finger proteins, and that exposure to TPEN prevented these sites from being filled. However, it is unknown at this time whether the failure to deliver zinc to these sulfur-rich sites is the cause of parasite death, or if parasite death causes failure of proper zinc delivery.

Several open questions remain regarding zinc homeostasis in *Plasmodium falciparum*. Since 350 μM EDTA was able to abolish zinc uptake while having no discernable effect on parasite viability, the question remains as to why the untreated parasite imports the excess zinc. Only subtle differences in the XANES and no differences in the EXAFS fits were observed between the untreated schizont-stage infected and the untreated uninfected samples, despite almost three quarters of the total zinc in the former being newly imported by the parasite from the medium. A more refined technique is required to determine the distribution of zinc among the possible zinc sites in both cases. Since both the genome and proteome of *P. falciparum* have been determined [5, 6], it seems feasible to carry out a metallome study at this point. The

protein gel imaging technique currently under development at the Advanced Photon Source should aid in this analysis [7]. Studies of how the metallome changes in response to EDTA or TPEN treatment should also provide confirmation or refutation of the hypothesis that the sulfur-rich sites present in the EDTA-treated samples represent zinc finger proteins.

The Bioinorganic Chemistry of Apoptosis

Small ion fluxes, particularly of potassium, but also of sodium and chloride, have been extensively studied in relation to their role in the early stages of apoptosis [8]. Changes in calcium and zinc have also received much attention [9, 10]. One common theme to these studies is that ion fluxes are often measured using element-specific fluorophores. However, this approach has two potential drawbacks. First, the elemental specificity of a given fluorophore is sometimes questionable. Crosstalk between ions and fluorophores can make quantitation difficult. Secondly, element-specific fluorophores only probe the labile fraction of each element. While this likely constitutes the majority of the small ions potassium, sodium and chloride, labile calcium and labile zinc make up only a small fraction of their respective totals, as calcium and zinc are normally found tightly associated to proteins or other macromolecules. In order to address these issues, as well as to elucidate possible roles for iron, copper, and zinc in the early stages of apoptosis, we undertook to image staurosporine-induced KB cells using X-ray fluorescence.

It was found that the average whole-cell potassium and chloride concentrations roughly matched cellular concentrations calculated from optical fluorophores, confirming

that the bulk of potassium and chloride in the cell is solvent-accessible. Consistent with previous studies using a variety of cell lines and inducers, results presented here indicate a decrease in total potassium as a function of time after staurosporine exposure. In contrast, we observed an increase in chloride over time, which contradicts the results found for other cell lines and inducers. While chloride has been proposed to be obligated to exit the cell with potassium in order to maintain electroneutrality, we proposed instead that the initial chloride fluxes are more dependent on how the resting chloride potential compares to the overall membrane potential, and is probably dependent on cell line, media, and apoptotic inducer. Confirming this hypothesis, of course, would require a comprehensive study of a variety of cell lines, inducers, and growth conditions, combining the results of both electrophysiology measurements and whole-cell chloride measurements.

In addition to the unexpected chloride increases, we observed an unexpected decrease in calcium 90 minutes after staurosporine exposure, and an increase in total copper at the 140-minute time point. It is currently unknown what purpose these fluxes serve; however, the decrease in calcium strikes us as significant, because it appears to be moving against both concentration and electrochemical gradients, indicating active transport by the cell. In addition, it is unknown whether or not these unusual calcium and copper fluxes are pro-apoptotic or anti-apoptotic in function. However, administration of calcium efflux inhibitors, such as bepridil or caloxin, should shed some light on the function of the calcium decrease. In addition, the use of a chelator that preferentially binds copper, such as trientine, should help to determine whether or not copper import has a protective effect.

XES of Zinc Active Site Mimics

Although EXAFS is a powerful technique for yielding high-resolution zinc active site structures, and is one of the few techniques available for studying zinc metalloproteins, it suffers from some significant drawbacks [11, 12]. EXAFS is unable to distinguish between oxygen and nitrogen ligands, which means that some of the most significant biological zinc ligands—namely, aspartate, glutamate, histidine, and water—are completely indistinguishable using this technique. Secondly, the fact that photoelectrons scattered from nitrogen and sulfur ligands are almost exactly out of phase for much of the useful *k* range means that the presence and degree of N/S mixing can sometimes be difficult to determine.

We investigated the use of valence-to-core X-ray emission spectroscopy in order to distinguish between these different ligation environments. Specifically, we were interested in the $K\beta_{1,3}$ satellite peaks, the $K\beta_{2,5}$ (HOMO → Zn 1s) and Kβ'' (ligand valence → Zn 1s) transitions. Detecting these transitions depended upon the use of bent analyzer crystals in the Rowland circle geometry, which yield a resolution of approximately 1.2 eV [13]. Since these transitions involve ligand valence orbitals and molecular orbitals formed between the zinc and ligand valence orbitals, XES was expected to be highly sensitive to chemical environment [14].

Indeed, it was found that zinc carboxylates, zinc imidazoles, and zinc thiolates all had unique and characteristic lineshapes, and that spectra derived from compounds with mixed ligation would be qualitatively reproduced by linear combinations of component spectra. Unlike EXAFS, X-ray emission spectroscopy should have little trouble distinguishing a bound carboxylate from a bound imidazole, and should be able to

distinguish the presence of a lone histidine in a $(Cys)_3(His)_1$ site. The unique lineshapes of zinc carboxylates, zinc imidazoles, and zinc thiolates also open up the possibility of site-selective EXAFS in proteins with multiple zinc-binding sites.

Currently, expected fluorescence intensities are too low to collect the $K\beta_{2,5}$ peak on a solution-phase biological sample with the type of signal-to-noise ratios presented here for the solid model compounds. A 1 mM sample would require roughly 1000 hours of beamtime. However, planned upgrades at the Stanford Synchrotron Radiation Lightsource should increase the storage ring current from 100 mA to 500 mA. This, combined with increasing the number of curved Ge(555) analyzer crystals used, can increase fluorescence intensity by up to a factor of 20, reducing the time needed to collect the $K\beta_{2,5}$ spectrum for a solution-phase biological sample to the neighborhood of 50 hours.

In the meantime, it would be interesting and helpful to collect $K\beta_{2,5}$ spectra for zinc compounds with lower symmetry than those collected here, as well as collecting spectra on lyophilized, well-characterized protein samples, in order to test some of the expectations of the capabilities of high-resolution XES.

References

1. Foley, M., *Quinoline antimalarials mechanisms of action and resistance and prospects for new agents.* Pharmacology & therapeutics, 1998. **79**(1): p. 55.
2. Wolford, J.L., *Zinc localization and quantitation in specialized cells and tissues*. 2006, Northwestern University.
3. Kidd, M.J. 2006, University of Michigan.
4. Ginsburg, H., R. Gorodetsky, and M. Krugliak, *The status of zinc in malaria (Plasmodium falciparum) infected human red blood cells: stage dependent accumulation, compartmentation and effect of dipicolinate.* Biochimica et Biophysica Acta (BBA) - Molecular Cell Research, 1986. **886**(3): p. 337.
5. Bahl, A., *PlasmoDB: the Plasmodium genome resource. A database integrating experimental and computational data.* Nucleic Acids Research, 2003. **31**(1): p. 212.
6. Florens, L., et al., *A proteomic view of the Plasmodium falciparum life cycle.* Nature, 2002. **419**(6906): p. 520.
7. Finney, L.A. *High-Throughput Metalloproteomics: X-Ray Fluorescence Imaging Paired with Electrophoresis*. in *Annual Meeting of the American Electrophoresis Society (AES)*. 2008. Philadelphia, PA.
8. Bortner, C.D. and Bortner, *Cell shrinkage and monovalent cation fluxes: role in apoptosis.* Archives of biochemistry and biophysics, 2007. **462**(2): p. 176.
9. Orrenius, S., B. Zhivotovsky, and P. Nicotera, *Regulation of cell death: the calcium–apoptosis link.* Nature Reviews. Molecular Cell Biology, 2003. **4**(7): p. 552.
10. Truong-Tran, A.Q., *Cellular Zinc Fluxes and the Regulation of Apoptosis/Gene-Directed Cell Death 1*. Journal of Nutrition, The, 2000. **130**(5): p. 1459.
11. Penner-Hahn, J.E., *X-ray absorption spectroscopy in coordination chemistry.* Coordination Chemistry Reviews, 1999. **190-192**: p. 1101.
12. Penner-Hahn, J.E., *Characterization of "spectroscopically quiet" metals in biology.* Coordination Chemistry Reviews, 2005. **249**(1-2): p. 161.
13. Bergmann, U. and S.P. Cramer. *Proceedings of SPIE: High-resolution large-acceptance analyzer for x-ray fluorescence and Raman spectroscopy*. 1998. San Diego, CA.
14. Bergmann, U., et al., *High-resolution X-ray spectroscopy of rare events: a different look at local structure and chemistry.* Journal of Synchrotron Radiation, 2001. **8**(2): p. 199.